Etude de l'interaction entre endommagement ductile et striction dans les tôles minces : application à la prédiction de la formabilité.

Muhammad Waqar Nasir

HESAM UNIVERSITÉ

Arts et Métiers Sciences et Technologies

ÉCOLE DOCTORALE SCIENCES DES MÉTIERS DE L'INGÉNIEUR
[Laboratoire d'Étude des Microstructures et de Mécanique des Matériaux – Campus de Metz]

THÈSE

présentée par : **Muhammad Waqar NASIR**

soutenue le : **18 Mai 2021**

pour obtenir le grade de : **Docteur d'HESAM Université**

préparée à : **École Nationale Supérieure d'Arts et Métiers**

Spécialité : **Mécanique et Matériaux**

Investigation of the interaction between ductile damage and necking in predicting sheet metal formability

THÈSE dirigée par :
M. ABED-MERAIM Farid

et co-encadrée par :
M. CHALAL Hocine

Jury

M. Pierre-Olivier BOUCHARD, Professeur, CEMEF, Mines ParisTech	Président
M. Lionel LEOTOING, Maître de Conférences HDR, LGCGM, INSA de Rennes	Rapporteur
M. Jean-Philippe PONTHOT, Professeur, LTAS, Université de Liège	Rapporteur
Mme Marion MARTINY, Professeure, LEM3, Université de Lorraine	Examinatrice
M. Laurent TABOUROT, Professeur, SYMME, Université Savoie Mont Blanc	Examinateur
M. Farid ABED-MERAIM, Professeur, LEM3, Arts et Métiers	Examinateur
M. Hocine CHALAL, Maître de Conférences, LEM3, Arts et Métiers	Examinateur

T H È S E

Dedication

To my beloved parents who helped me in all things great and small
To my wife and daughter who encouraged me to pursue my PhD
To my dear supervisors for their guidance
To all my dear friends for their help

Acknowledgments

First and foremost, I would like to thank my supervisors for their dedicated support, kind guidance and encouragement. I sincerely thank the director of my thesis, Prof. Farid ABED-MERAIM, for providing me valuable advices, guidance and feedback throughout this project. I would like to thank my co-supervisor, Dr. Hocine CHALAL, for his responsible supervision, meticulous guidance and kind assistance. Without them, it is impossible for me to complete this thesis on time. It was a really great pleasure for me to work with them for three years. Their guidance helped me in all the time of research and writing of this thesis.

Besides my advisor, I would like to thank the rest of my thesis committee: Prof. Marion MARTINY and Dr. Mohamed BEN BETTAIEB, for their insightful comments and encouragement. Without their precious support it would not be possible to conduct this research.

I would like to thank the Higher Education Commission Pakistan (HEC Pakistan) who granted the scholarship to support my PhD studies in France under HRDI-UESTP Faculty Development Program. I would also like to thank my employer, University of Engineering and Technology Lahore (UET Lahore) who granted me study leave to pursue my PhD.

I also deeply thank Prof. Pierre-Olivier BOUCHARD from Mines ParisTech for being the president of my Ph.D. thesis committee. I would like to express my gratitude to my reviewers, Prof. Jean-Philippe PONTHOT from Université de Liège and Assoc. Prof. Lionel LEOTOING from INSA de Rennes, for their insightful comments and academic reports. I am deeply grateful to Prof. Marion MARTINY from Université de Lorraine and Prof. Laurent TABOUROT from Université Savoie Mont Blanc for accepting the invitation and spending their precious time to attend my thesis defense. I am honored to be able to invite these famous, charming and knowledgeable professors as the referees. I sincerely appreciate their insightful, valuable and constructive comments.

I would like to thank all my colleagues in our lab for the stimulating discussions, and also my Pakistani friends with whom I shared the most memorable moments.

I express my sincere gratitude to all my family members, particularly my parents, spouse and daughter for all the unconditional support throughout writing this thesis and my life in general. There are no words for me to be able to express my utmost gratitude and thanks to them for their great sacrifices, support and encouragement.

Contents

List of Tables

List of Figures

Part I: English version

Introduction

General context of the thesis

With the advancements in the field of manufacturing processes, sheet metal forming is found to be of utmost importance in many industries, such as automotive, packaging, aerospace, beverages, food processing, home appliances, etc. In sheet metal forming process, the desired parts are produced when the raw material undergoes large plastic deformations without material removal. Usually, almost all of the raw material is used in the forming process with a very high production rate. Therefore, the process is well suited for mass production and can be fully automated.

The increasing costs of raw materials and the major global concerns for reducing the CO_2 emissions lead to the pressing demand of lightweight structures. The development of lightweight structures will eventually bring about the reduction in the material usage, transportation cost and energy consumption at the same time. In this context, the automotive industry is playing a vital role. The increased competition in automotive manufacturing companies leads, on the one hand, to the development of more advanced and lightweight materials. On the other hand, it requires the design of relevant forming processes and tools, in order to produce defect-free structures. Springback, wrinkling, diffuse necking as well as localized necking, which is precursor to fracture, are some of the main defects observed during the forming processes, which limit the formability of thin sheet metals and ultimately affect the productivity. Therefore, the in-depth understanding of these defects and the capability of their accurate prediction during plastic deformation are crucial, in order to increase the productivity of the forming processes. In this regard, the use of numerical simulations is found to be a very cost-effective and efficient procedure. The recent advances in the field of constitutive modeling, which enable the accurate simulation of the mechanical behavior of a large variety of materials under complex loading conditions, represent an important prerequisite for the development of such efficient numerical tools. Concurrently, significant efforts have been made in the literature to predict the occurrence of plastic instabilities that limit the material formability. Therefore, for the optimization of sheet

metal forming processes, advanced constitutive models should be combined with theoretical and numerical criteria that are relevant to the prediction of plastic instabilities.

Objectives of the thesis

In the context of thin sheet metal forming, the concept of forming limit diagram (FLD) is crucial, as it provides the limits to the deformations that sheet metals can withstand without the occurrence of undesirable defects. The experimental determination of forming limit diagrams is a costly and time-consuming process and the results often suffer from the lack of reproducibility. The objectives of the thesis fall under the scope of theoretical and numerical predictions of FLDs, which leads to a very cost-effective procedure as compared to experimental measurements. For this purpose, the present thesis first aims to model the mechanical behavior of ductile materials commonly used in sheet metal forming processes. Some well-established phenomenological elastic–plastic constitutive models, which have been developed in the literature for porous materials, are recalled and presented in this manuscript. Among these constitutive models, only those based on the micromechanical analysis of porous media, and more specifically Gurson-based damage models, are considered in the present contribution. Various extensions of the original Gurson damage model, such as through the incorporation of material anisotropy, void size, void nucleation, void coalescence, and non-associative plasticity will be considered, and their effects on the sheet metal formability will be discussed. As to the prediction of plastic instability, both diffuse and localized necking criteria, which are based on the bifurcation theory and multi-zone (initial imperfection) approach, will be implemented and compared to each other. For comparison purposes, the plastic instability criteria will be coupled with the same constitutive models. An important objective of this thesis is to investigate the most critical destabilizing mechanisms associated with the constitutive model, which promote the initiation of plastic instability.

Once the proposed numerical tool implemented and validated, this approach can be used in future works for the development of new grades of metallic materials with improved mechanical properties (e.g., strength and ductility), while respecting the new regulations related to the CO_2 emissions, comfort and lighter structures.

Structure of the thesis

The present manuscript is organized into four chapters, which are discussed as follows:

In the first chapter, a general overview of the sheet metal forming processes, their applications and the main defects induced during the forming processes are presented. Thereafter, the concept and the historical background of the forming limit diagram (FLD) are recalled, followed by the description of various experimental procedures and theoretical/numerical tools developed in the literature for the determination of FLDs. Chapter 1 also encompasses state of the art of ductile damage theories and plastic instability criteria for the prediction of diffuse and localized necking.

The second chapter is devoted to the coupling of Gurson–Tvergaard–Needleman (GTN) damage model with four bifurcation-based criteria for the prediction of FLDs. The effects on the prediction of FLDs of destabilizing mechanisms related to non-associative plasticity and non-normality of the plastic flow rule will be investigated.

The third chapter deals with the comparative analysis of the bifurcation theory and the multi-zone (initial imperfection) approach used for the prediction of localized necking. In this comparative study, the GTN damage model is coupled with the initial imperfection approach and both geometric and material initial imperfections are considered. The sensitivity analysis of FLDs to various imperfection types is also investigated.

The fourth chapter deals with the implementation of an extended version of the GTN damage model, which incorporates void size effect. The void-size dependent GTN model is coupled with the bifurcation theory, and the resulting numerical tool is used to predict the FLD of Al5754 aluminum.

Finally, general conclusion will be drawn based on the studies carried out in the thesis, followed by some perspectives and future developments.

Chapter 1

State of the art on formability limits of sheet metals

1.1 Introduction

Sheet metal forming is one of the most widely used manufacturing processes. High production rates and low material loss make it a competitive process for many applications, such as manufacturing of automotive body parts, packaging industry, household appliances and utensils. This process involves large plastic deformations of sheet metals in order to manufacture sheet metal parts for different applications. A general overview of the sheet metal forming operations, their applications and the commonly observed defects are discussed hereafter.

1.1.1 Sheet metal forming operations and applications

In sheet metal forming, a thin sheet metal (also known as a blank) is deformed plastically with the help of a punch and die tools. Generally, sheet metal forming operations take place at room temperature; however, in order to decrease the forming forces acting on the forming tools and to increase the formability of sheet metals, forming operations are also performed at elevated temperatures. Sheet metal forming operations can be broadly categorized into either cutting, bending, or drawing. In the cutting process, also known as shearing, a large amount of shear load is applied, which plastically deforms the sheet metal and eventually cut it in several parts. Cutting is used in sheet metal forming to produce holes, create a perimeter or to simply cut larger sheet parts into smaller ones. Sheet metal bending is normally used to produce V-shape, U-shape or a groove around an axis. The drawing process is used to produced box shaped, cup shaped and complex curved or concave parts. Beverage cans, processed food storage cans, kitchen sinks, and automotive body panels are some of the examples that are produced by the drawing process. Another process similar to the drawing is the hydroforming, in which the force on the sheet metal is applied with the help of pressurized fluid. This process turns out to be particularly suitable for the forming of tubular parts. Various sheet metal forming operations discussed above are illustrated in Fig. 1.1.

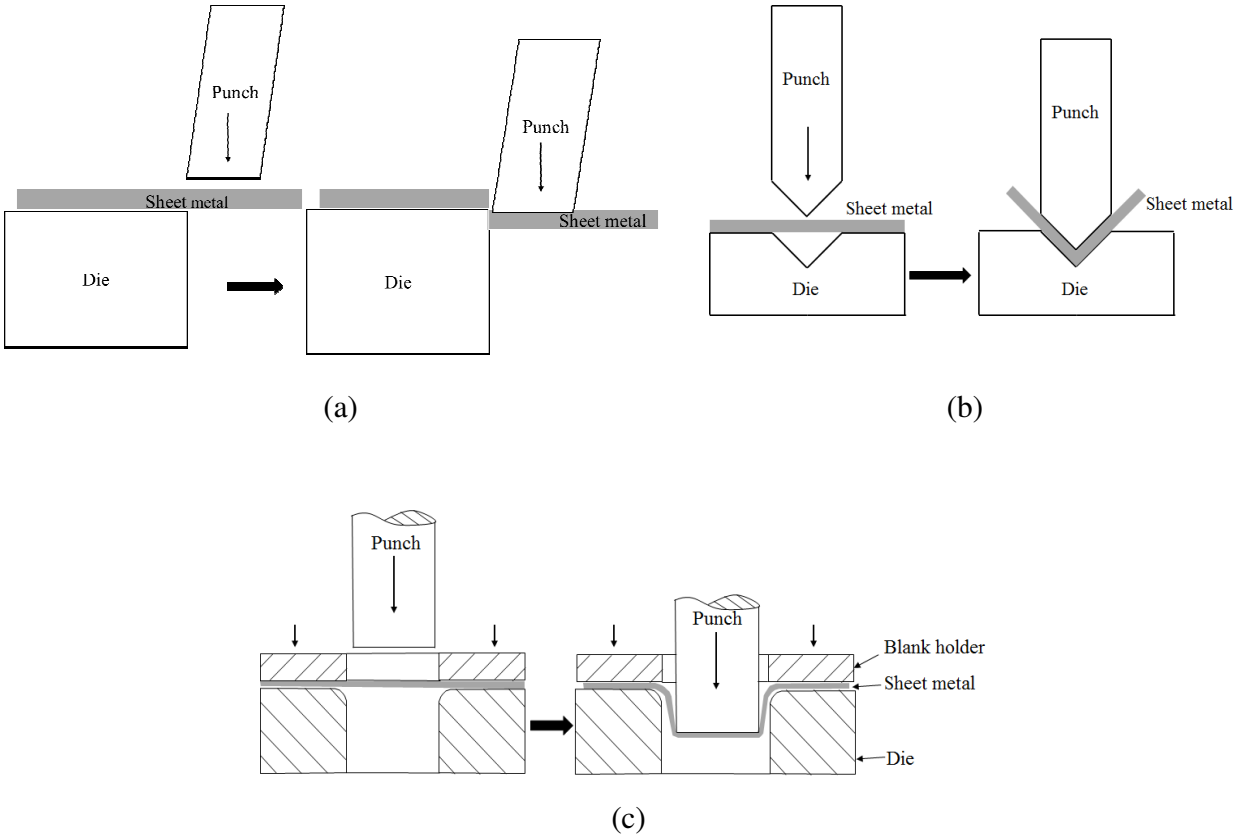

Figure 1.1. Illustration of various sheet metal forming operations: (a) Cutting, (b) bending and (c) deep drawing.

Recent advancements in the forming processes led to the development of a rather new process, known as incremental forming (IF) process. Single point incremental forming (SPIF) process is the specific type of IF process, in which a hemispherical tool (typically 5 mm to 20 mm in diameter) is controlled by a CNC machine for local plastic deformation of the sheet metal. The tool is moved over the entire specimen in several passes to obtain the final shape. The fine controlled tool movements allow producing complex geometries with a single generic tool. Moreover, it has been observed experimentally that higher formability of the sheet metal is achieved in IF as compared to traditional drawing or stretching processes. The SPIF process is schematically represented in Fig. 1.2.

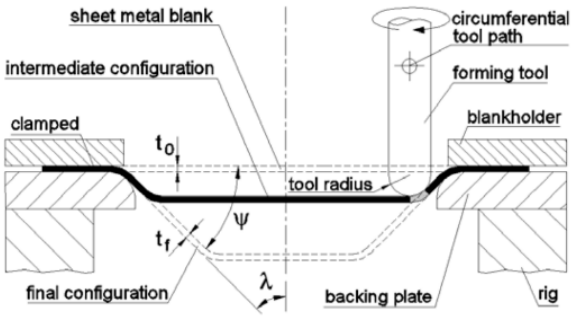

Figure 1.2. Schematic presentation of single point incremental forming (SPIF) process (from Silva et al., 2009).

1.1.2 Materials commonly used in sheet metal forming

With the implementation of new regulations on the CO2 emission, fuel consumption, safety standards and comfort, new grades of materials are continuously being developed with enhanced mechanical properties. In this regard, advanced aluminum alloys are found to be emerging materials for the automotive bodies. However, it has been observed that the formability of aluminum alloys is low, especially during cold forming processes (Mohamed and Ismail, 2016). 5xxx series of aluminum alloys have comparatively good formability at room temperature, though their strength is low. On the other hand, 6xxx and 7xxx series of aluminum alloys have higher strength; but, they generally require elevated temperatures for the forming operations. However, hot forming is a complex process that generally requires expensive equipment (Harrison et al., 2013).

Over the past few decades, significant improvements have been made in the composition and the mechanical properties of steel grades. The overall spectrum of the steel grades used in the automotive industry can be broadly categorized into three types, depending on their tensile strength: mild steel (MS), high strength steel (HSS), and advanced/ultra-high strength steel (AHSS/UHSS). In order to compare the mechanical properties of these steel grades, a graph showing the percentage of elongation (%) versus tensile strength (MPa) is generally plotted as shown in Fig. 1.3. The steel grades that are present on the furthest left in Fig. 1.3 (i.e., interstitial-free (IF) steel or mild steel (MS)) have low strength and high ductility. By contrast, the steel grades on the right (i.e., martensitic steel (MART)) have high strength, but they are difficult to be drawn into desired shapes. An ideal material is the one having perfect balance of ductility and

strength. In Fig. 1.3, these materials are present near the center (i.e., dual-phase (DP) steels, transformation-induced plasticity (TRIP) steels, twinning-induced plasticity (TWIP) steels, complex phase (CP) steels). Fig. 1.4 depicts the relative use of steels and aluminum alloys in typical automotive bodies.

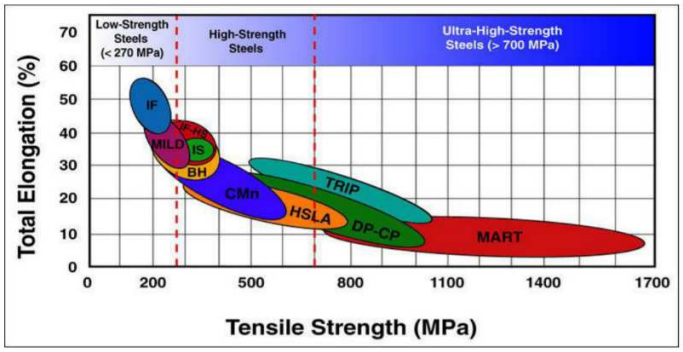

Figure 1.3. Comparison of the mechanical properties of different steel grades used in automotive bodies (Ballay and Monoši, 2017).

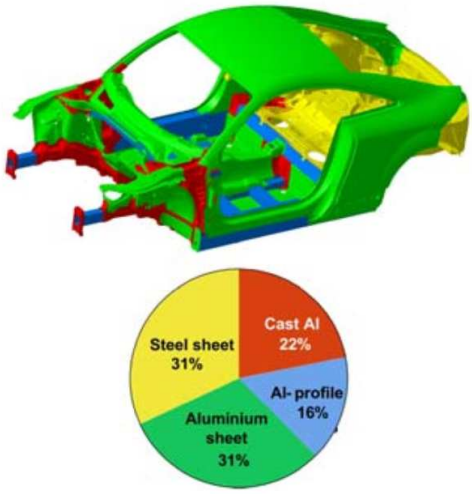

(a)

Figure 1.4. Percentages of steel and aluminum alloys used in typical automotive bodies (Tisza, 2013).

1.1.3 Common defects associated with sheet metal forming processes

Sheet metal forming processes typically have very high production rates; however, the defects involved during these forming processes are the main reasons for the obtained material scrap. The common defects observed during sheet metal forming processes are recalled in what follows.

1.1.3.1 Wrinkling

Wrinkling is one of the primary defects observed in deep drawing of sheet metals. Wrinkling may appear in the flange, wall or on the main body of drawn object, as shown in Fig. 1.5. Wrinkling in the walls occurs when the diameters of the punch and the die cavity are too large. On the other hand, when the diameters of punch and die cavity are too small, wrinkling or tearing may occur in the main body because of the high values of stresses. Wrinkling can be minimized by adjusting some of the process parameters, such as the application of variable blank holder pressure (pneumatically or hydraulically) during the deep drawing process, minimizing the asymmetry and complexity of the blank, splitting the single deep drawing process into multi-step deep drawing processes, minimizing the excess material in the initial blank geometry. Also, reducing the friction between the blank and tools can help to avoid the occurrence of wrinkling.

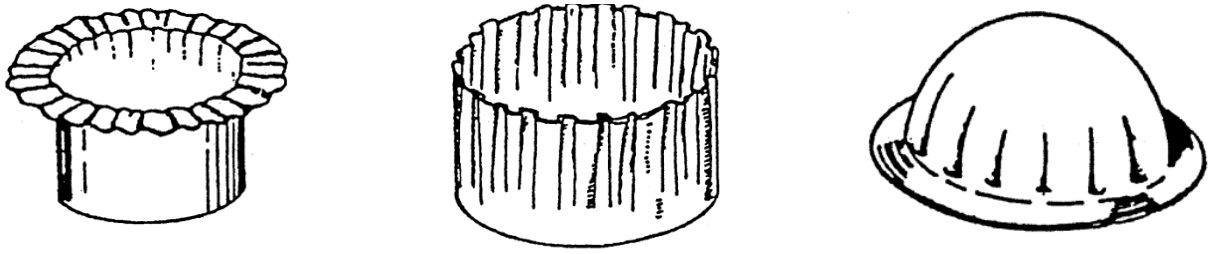

(a) (b) (c)

Figure 1.5. Occurrence of wrinkles in the: (a) flange, (b) walls, and (c) main body, during the deep drawing process (Banabic, 2010).

1.1.3.2 Fracture

Fracture occurs during sheet metal forming when the strains developed in the blank exceed the limit strains, and thus the material completely loses its stress carrying capacity. Several factors contribute to the development of fracture within the sheet metal. However, the clearance

between the die and the punch is the most significant. If the clearance is too large or too small, the sheet metal may crack during the forming process. Fracture mostly occurs near the punch corner in the deep drawing process, because the material points in this region are subjected to severe strain-path loading. Two illustrations of the occurrence of fracture at the bottom of a circular cup and the corner of a square cup during deep drawing processes are shown in Fig. 1.6.

(a) (b)

Figure 1.6. (a) Bottom fracture in the circular cup, and (b) corner fracture in the square cup, during deep drawing process (Banabic, 2010).

1.1.3.3 Necking

Necking occurs as a result of material instability when the decrease in thickness takes place in a greater proportion, as compared to the increase in strength due to strain hardening. Necking can be classified as either diffuse necking or localized necking. Diffuse necking can be interpreted as the progressive evolution of a homogenous strain state towards a quasi-homogenous or heterogenous strain state. Diffuse necking is initiated when the maximum load force is reached and is generally not critical in the forming process of thin sheet metals. However, diffuse necking is often precursor to localized necking, which is more critical than the former one. Localized necking is characterized by the occurrence of a local decrease in thickness of the sheet in the form of a localized band. Localized necking is usually followed by the final fracture, whereby a crack develops inside the region of the localized band. The occurrence of diffuse and localized necking also depends on the initial thickness of the sheet metal (see, e.g., Col, 2011). For instance, Fig. 1.7 illustrates the occurrence of necking and fracture for two sheet metals having different thicknesses. When the thickness of the sheet metal is significant with respect to its length and width, diffuse necking initiates, which is then followed by the occurrence of

localized necking, and eventually fracture (see Fig. 1.7a). However, for very thin sheet metals, diffuse necking is not the significant mechanism, and localized necking is directly followed by fracture (see Fig. 1.7b).

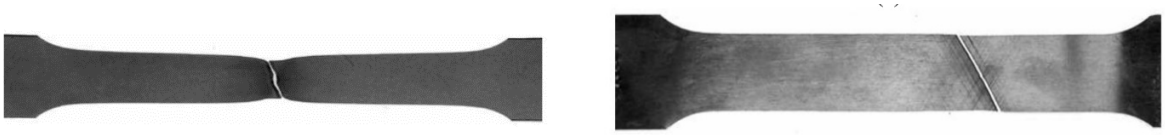

(a) (b)

Figure 1.7. Occurrence of necking and fracture in (a) thick sheet and (b) very thin sheet (Col, 2011).

1.2 Concept of forming limit diagrams

Accelerated development of sheet metal forming processes has been observed in the ninetieth century. In order to characterize the formability limits of sheet metals, various researchers have developed laboratory tests in the beginning of the twentieth century. Among the tests of assessment of sheet metal formability, the first laboratory test was proposed by Erichsen (1914), who developed the Erichsen deep drawing test, as illustrated in Fig. 1.8. Using this test, the sheet metal specimens are plastically deformed until fracture, with the help of a hemispherical punch. The formability limit is characterized by the depth in millimeters of the indentation produced in the sheet metal, also commonly known as Erichsen index. Similar tests have also been proposed later by Olsen (1920), Sachs (1930), Jovignot (1930), Fukui (1938), Loxley and Swift (1945), Guyot (1962) and Hecker (1974).

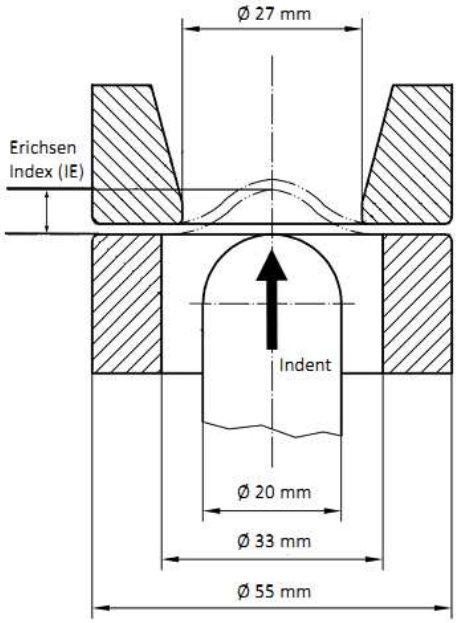

Figure 1.8. Schematic illustration of the Erichsen deep drawing test for the assessment of sheet metal formability (Sorce et al., 2019).

The limit dome height test, proposed by Ghosh (1975), is very similar to the Erichsen test. However, in the former test, the heights of the deformed specimens are plotted as a function of minor strains developed at the fracture point. A typical limiting curve obtained from the limit dome height test is shown in Fig. 1.9.

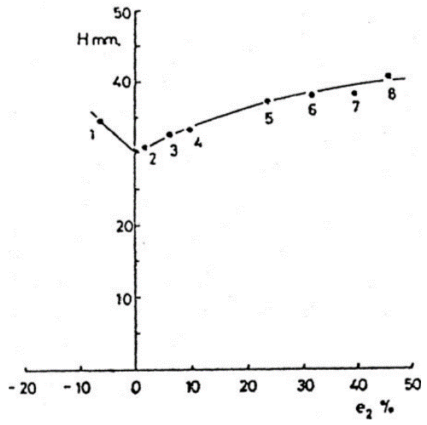

Figure 1.9. A typical limit dome height curve (Pearce, 1978).

Gensamer (1946) laid the foundation of forming limit diagram based on the measurements of local deformations. The diagram proposed by Gensamer (1946) to characterize the formability limits is in fact the mirror image of the present form of forming limit diagram (see Banabic et al., 2019). The original and the mirrored image of the diagram proposed by Gensamer (1946) are represented in Fig. 1.10.

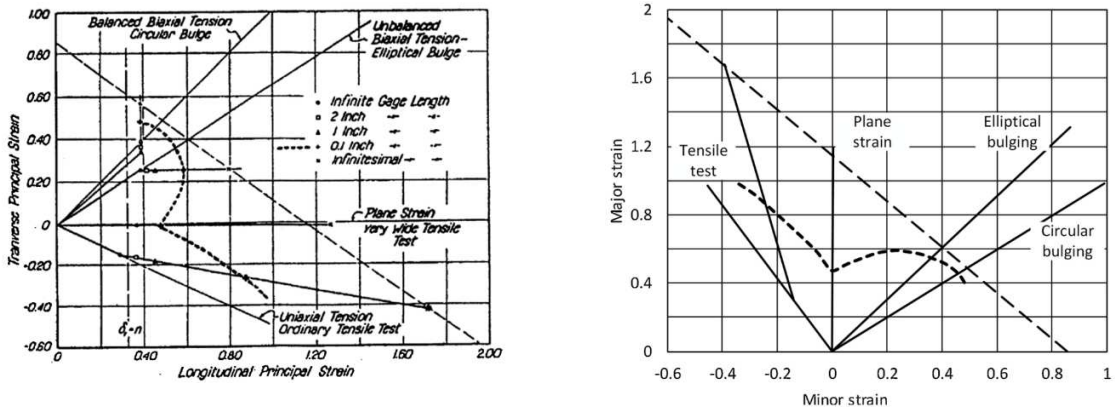

(a) (b)

Figure 1.10. (a) Forming limit diagram obtained by Gensamer (1946) and (b) its mirrored image (Banabic et al., 2019).

Based on the concept of forming limit diagram introduced by Gensamer (1946), Keeler and Backofen (1963) calculated the principal strains ε_1 and ε_2 at the failure of the sheet metals subjected to biaxial expansion (i.e., $\varepsilon_1 > 0$ and $\varepsilon_2 > 0$). ε_1 and ε_2 are commonly known as the major and minor strains, respectively. The forming limit diagrams (FLD) presented by Keeler (1965), based on the measurements of minor and major strains, are depicted in Fig. 1.11a. Note that the FLD shown in Fig. 1.11a is only limited to the positive minor strains. Later, Goodwin (1968) extended the FLD for the negative minor strains (i.e., $\varepsilon_2 < 0$ and $\varepsilon_1 > 0$). The complete FLD obtained by Goodwin (1968) is represented in Fig. 1.11b.

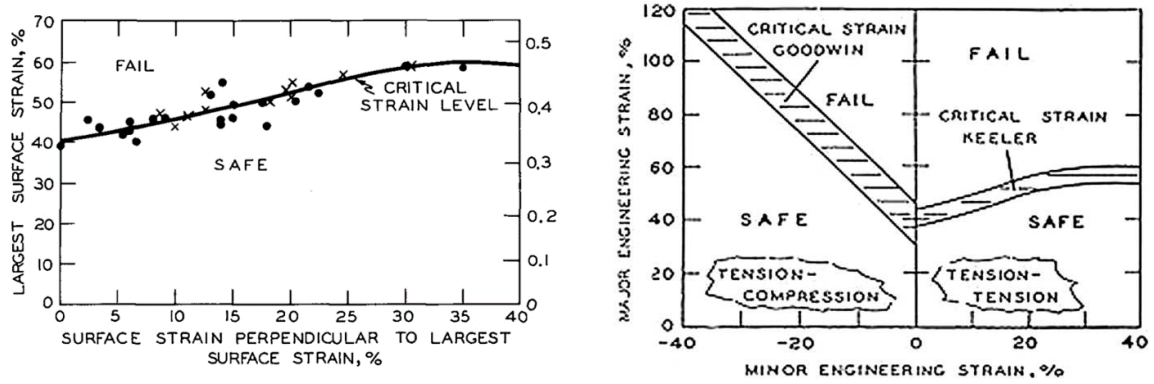

(a) (b)

Figure 1.11. Forming limit diagrams proposed by: (a) Keeler (1965) and (b) Goodwin (1968).

In a typical FLD, the limit strains are measured at the onset of diffuse or localized necking. However, the concepts of fracture forming limit curve (FFL) (see, e.g., Song et al., 2017) and wrinkling forming limit curve have also been introduced by some researchers, for which the limit strains are measured at the onset of final fracture and wrinkling, respectively. Fig. 1.12 represents the typical shapes of the FLD, FFL and wrinkling forming limit curve on the major and minor strain axes.

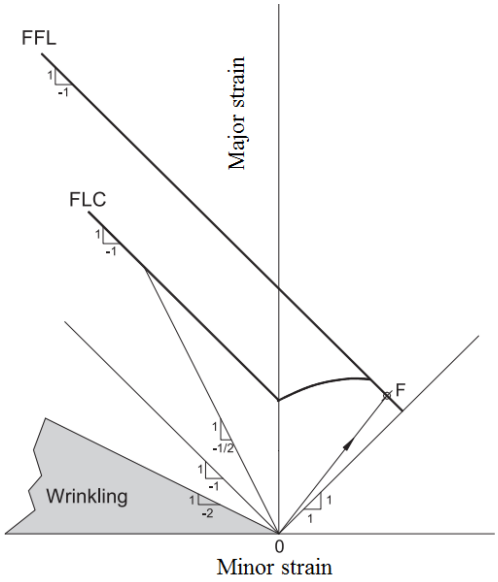

Figure 1.12. Schematic presentation of fracture forming limit curve (FFL), forming limit diagram (FLD) and wrinkling forming limit curve (Martins et al., 2014).

The assumption of proportional strain loading is generally followed for the determination of FLDs. However, in practice, strains do not remain necessarily proportional during the forming processes. For instance, many manufacturing processes involve multi-stage forming, which ultimately results in an overall non-proportional strain-path ratio. It has been shown in the literature that the strain-based FLDs are very sensitive to the loading paths (see, e.g., Hiwatashi et al., 1998; Kuroda and Tvergaard, 2000). For this purpose, some researches (see, e.g., Arrieux, 1995, 1997; Stoughton, 2000) transformed the strain-based FLD into the principal stress space by using suitable constitutive assumptions. It has been shown in their investigation that different strain-based FLDs (i.e., corresponding to the as-received sample and pre-strained sample) converged to nearly unique FLD in the principal stress space. Fig. 1.13a represents the strain-based FLDs for 2008-T4 aluminum subjected to different magnitudes of pre-strains. Fig. 1.13b

shows the transformed FLDs into the principal stress space obtained by Stoughton (2000). Note that the stress-based FLDs remain approximately the same for all the considered values of pre-strains. Therefore, stress-based FLD appears to be an attractive alternative for the prediction of the formability of sheet metals subjected to non-proportional loading paths.

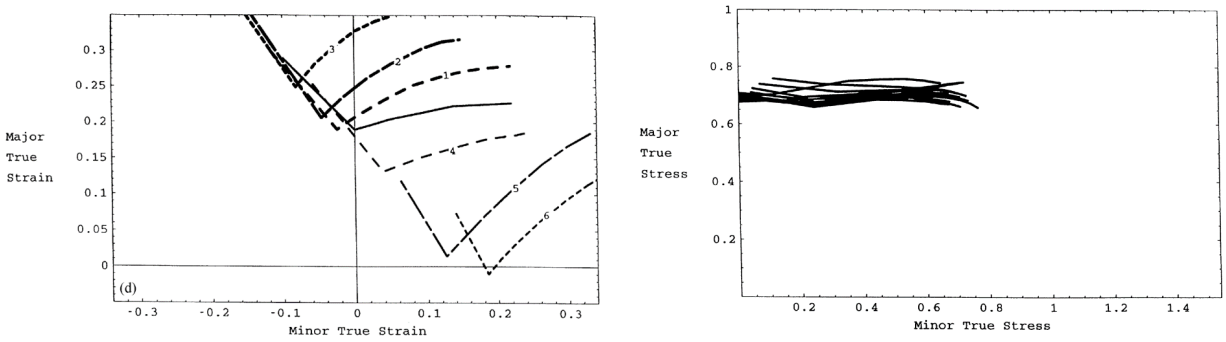

(a) (b)

Figure 1.13. (a) Strain-based FLDs of 2008-T4 aluminum under different levels of pre-strains and (b) transformed FLDs into the principal stress space (Stoughton, 2000).

1.2.1 Experimental determination of FLDs

Since the introduction of FLD by Keeler (1965) and Goodwin (1968), several experimental procedures have been proposed to determine the FLDs of thin sheet metals. Among them, the uniaxial tensile tests, hydraulic bulge tests, and punch tests are of key importance.

Rectangular sheet metal specimens are used in the uniaxial tensile test, as shown in Fig. 1.14. Different values of the notch radii are used in order to generate various strain-path ratios. The major disadvantage of this uniaxial tensile test is that it only allows the determination of the left-hand side of the FLD (i.e., $\varepsilon_2 < 0$ and $\varepsilon_1 > 0$). Nevertheless, there are several advantages, such as the sheet metal specimens remain planar during the deformation, thereby the strain measurements are easy. Moreover, due to their simple shapes, the specimens are easy to manufacture.

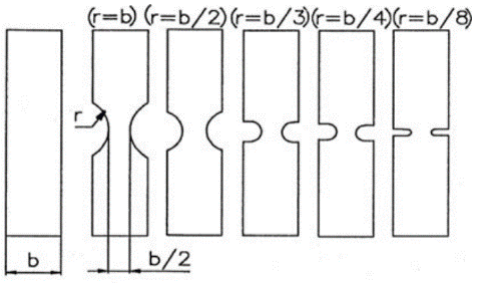

Figure 1.14. Rectangular sheet metal specimens for the determination of FLD using uniaxial tensile tests (Banabic, 2010).

For the hydraulic bulge test, hydraulic pressure is applied to plastically deform the sheet metal specimens through elliptical dies (see Fig. 1.15). Various values of strain-path ratios are obtained by using different values of the major and minor radii of the ellipse. The disadvantage of this test is that only the right-hand side of FLD can be determined (i.e., $\varepsilon_2 > 0$ and $\varepsilon_1 > 0$). Moreover, due to the presence of curvature in the deformed specimen, strain measurements are subjected to unavoidable errors. Nevertheless, the main advantage is the absence of friction due to contact in the area of interest, since no punch is used during the forming process.

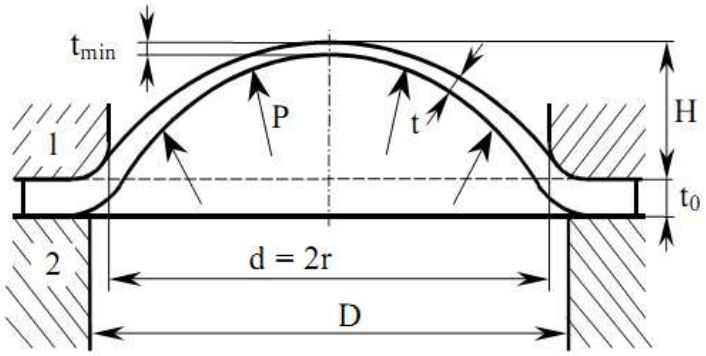

Figure 1.15. Schematic illustration of the hydraulic bulge test (Gagov et al., 2005)

Unlike the hydraulic bulge test, sheet metal specimens are plastically deformed using a punch in the Keeler test, Marciniak test, Nakazima test and Hasek test. In the Keeler test, a spherical punch is used to deform the sheet metal specimens. Different values of strain-path ratios are obtained by using different radii of the spherical punch. The typical punch geometries used in the Keeler test are shown in Fig. 1.16. Unlike the Keeler test, a single punch geometry is used in the Hecker test. However, different loading paths are produced by using different amounts of lubricant between the specimen and the punch.

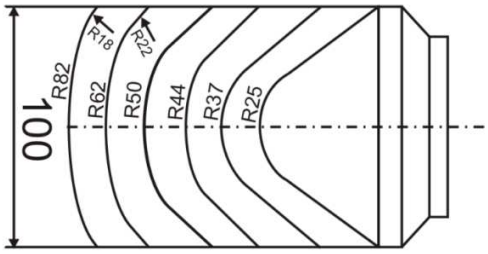

Figure 1.16. Different geometries of the spherical punch used in the Keeler test (Quaak, 2008).

Marciniak (1965) proposed a deep drawing test for the experimental determination of the FLDs. An intermediate spacer with a circular hole is placed between the sheet metal specimen and the hollow flat punch. Schematic illustration of the Marciniak test is presented in Fig. 1.17. The vertical force of the punch is converted into the planar biaxial force on the specimen due to the presence of friction between the intermediate spacer and the specimen. It has been observed that tearing occurs in the flat bottom region of the drawn cup with the use of an intermediate spacer. Different cross section shapes (e.g., rectangular, elliptical, circular, etc.) of the punch can be used in order to obtain various strain-path ratios. However, the Marciniak test suffers from two major drawbacks, i.e., the FLDs can only be obtained for the biaxial expansion domain (i.e., $\varepsilon_1 > 0$ and $\varepsilon_2 > 0$) and the manufacturing of complex punch shapes is a costly and time-consuming process. To overcome these drawbacks, Raghavan (1995) proposed the use of different geometries of the intermediate spacer and the specimen. With the right selection of the spacer and the specimen geometries, any strain-path ratio between uniaxial tension and balanced biaxial tension can be reproduced.

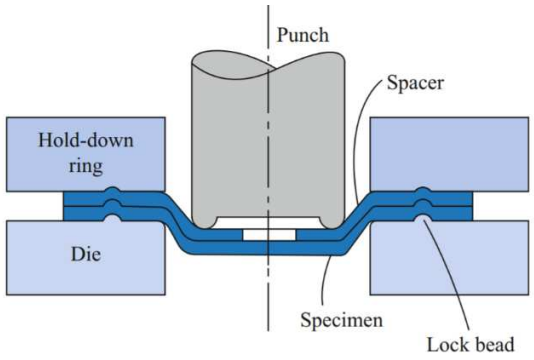

Figure 1.17. Schematic illustration of the Marciniak deep drawing test for the determination of FLDs (Bhaduri, 2018).

In Nakazima test, a hemispherical punch is used to draw rectangular sheet metal specimens through a circular die (see, e.g., Nakazima and Kikuma, 1967; Nakazima et al., 1968; Garcia et al., 2006). All the loading paths between uniaxial tension and balanced biaxial tension are obtained by varying the specimen width and the friction force between the punch and the specimen. Fig. 1.18a illustrates the schematic view of the Nakazima deep drawing test, while the geometry of the sheet metal specimen, as recommended by ISO 12004-2 (2008), is presented in Fig. 1.18b. Hasek (1973) proposed the use of circular sheet metal specimens instead of

rectangular ones, as shown in Fig. 1.19, for materials that exhibit the wrinkling phenomenon during deep drawing.

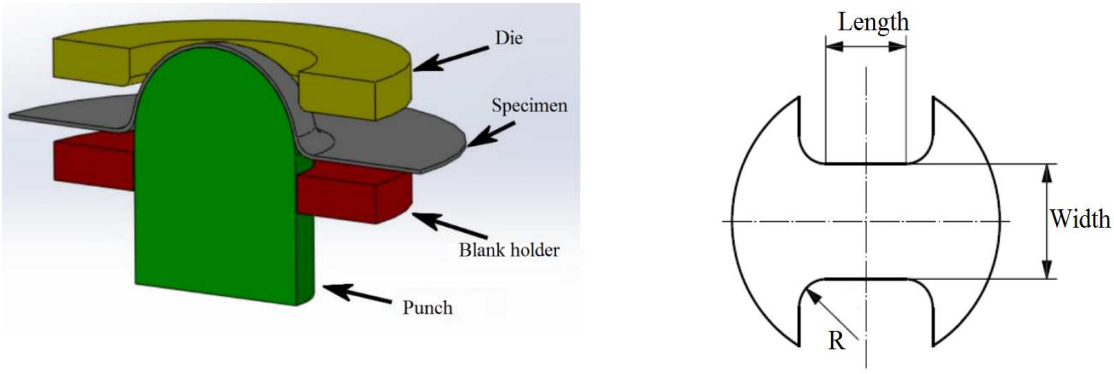

(a) (b)

Figure 1.18. Schematic illustration of the Nakazima deep drawing test (left) and geometry of the sheet metal specimen recommended by ISO 12004-2 (2008) (right).

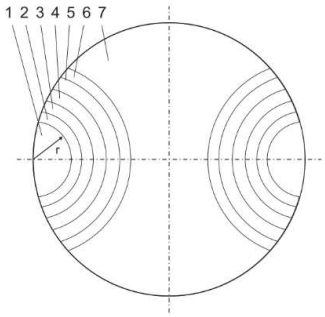

Figure 1.19. Geometries of the circular sheet metal specimens proposed by Hasek (1973).

Figure 1.20 compares the typical shapes of FLDs, obtained by using different experimental procedures described above. Note that the complete FLDs are presented for Nakazima test and Hasek test. The use of Marciniak test or hydraulic bulge test is suitable for materials in which the friction forces are significant. Uniaxial test is recommended when cost effectiveness and quick estimate of the limit strains are needed. Nakazima test and Hasek tests are preferred when the complete range of FLDs is required.

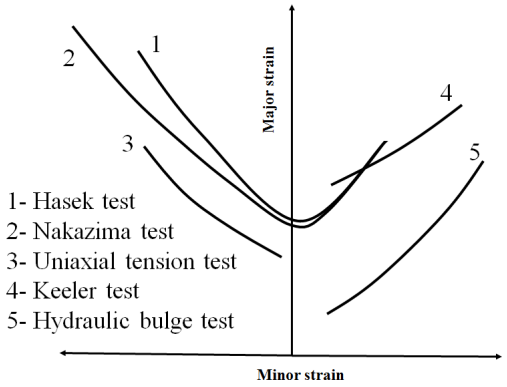

Figure 1.20. Comparison of the forming limit curves obtained by using different experimental procedures (Hasek, 1978).

The sheet metal specimens are generally marked with fine grid patterns, which serves as a relatively simple method for the strain measurements. Fig. 1.21 represents the circular grid pattern typically used on the surface of sheet metal specimens. The circles become ellipses after plastic deformations, and the measurements of the major and minor axes of the deformed ellipses are used to calculate the major and minor strains, respectively.

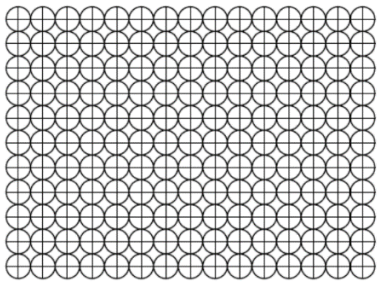

Figure 1.21. Circular grid pattern recommended by ISO 12004-1 (2008) for the surface marking of sheet metal specimens.

With the advancement in the field of image processing and machine vision, various methods have been developed, which incorporate the use of video-cameras for the strain measurements. Among them, the method proposed by team "SOLLAC" (see, Marron et al., 1997) is worth mentioning, whereby necking is identified by the accelerated increase in the strain rate. In the same framework, the working group IDDRG (International Deep Drawing Research Group) has greatly contributed to the development of numerical and experimental methods for the detection of the onset of necking in thin sheet metals (see, e.g., Hotz, 2006). Their methods are very robust and have been used by many commercial companies.

Despite all the advancements and the efforts made for the experimental determination of FLDs, these methods are rarely used in the industry because of their major disadvantages, such as high cost of the tests and low reproducibility of the results. Nevertheless, these methods are widely used in the research community as a benchmark to validate the newly developed numerical tools for the theoretical and numerical predictions of FLDs.

1.2.2 Theoretical predictions of FLDs

The theoretical prediction of FLDs requires the combination of two key components, i.e., constitutive models and instability criteria. The constitutive models allow reproducing the essential physical phenomena that occur within the material for a specific loading condition. The instability criteria are coupled with the constitutive models to predict the occurrence of plastic instabilities (diffuse or localized necking) for a given loading path. The coupling of the constitutive model and the plastic instability criterion for the prediction of FLD is schematically represented in Fig. 1.22. After selecting a constitutive model, which depends on the material under investigation, the material points are subjected to the boundary conditions corresponding to various proportional loading paths ranging from uniaxial tension to balanced biaxial tension. Based on the known stress–strain state at the beginning of each loading increment, elastic–plastic calculations are performed according to the selected constitutive model to calculate the updated values of stresses, strains, and internal variables. At the end of each loading increment, the plastic instability criterion is evaluated. If the criterion is satisfied, the simulation is stopped, and the values of the principal strains at that loading increment are considered as the limit strains, which

are used to plot the FLD. However, if the criterion is not satisfied, the material points are subjected to a next loading increment and the elastic–plastic calculations are performed again.

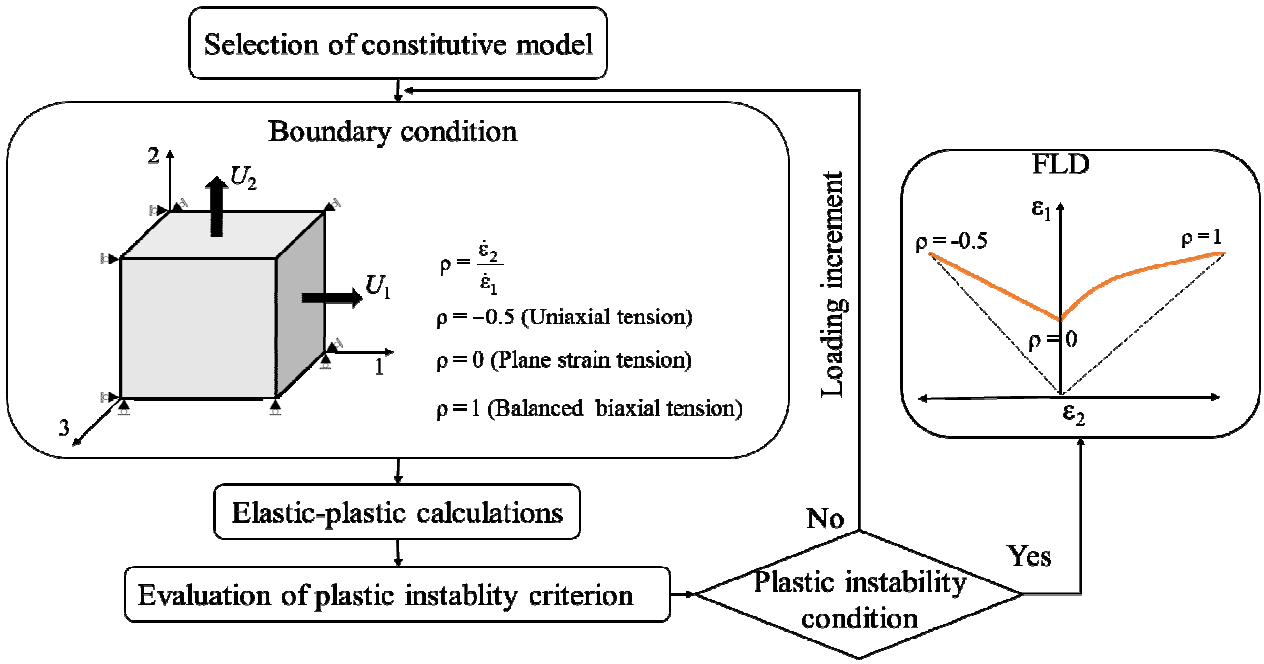

Figure 1.22. A general algorithm used for the theoretical prediction of FLDs.

1.2.3 Applications of the FLDs

The concept of forming limit diagram is found to be very useful in industrial applications. FLDs can be used to select a suitable material for a specific application. For this purpose, the designer first calculates all the strains that may be produced inside the sheet metal during a specific forming process. These strains are then plotted on the FLDs of the candidate materials. The material for which the forming limit curve lies above the maximum strain points can be considered as the suitable material for that application. Additionally, FLDs can also be used to compare the formability of sheet metals made up of the same material and having different thicknesses.

1.3 Ductile damage models: state of the art

Constitutive modeling of metallic materials plays an important role in the numerical simulation of forming processes. The constitutive models incorporate various physical phenomena taking place inside the material during the deformation, such as strain hardening,

anisotropy, softening, etc. Strain hardening is produced due to the interaction of dislocations with each other, which ultimately reduce their mobility. In case of isotropic strain hardening, the increase in the material strength is the same in all directions. Several phenomenological laws have been developed in the literature to model isotropic hardening. Among them, Swift's, Voce's, Hollomon's and Ludwig's hardening laws are widely used. In case of kinematic strain hardening, the plastic deformation causes an increase in strength in one direction, while a decrease in strength in the other direction is observed. Commonly used phenomenological laws for kinematic strain hardening include Prager's law and Armstrong–Frederick's law. The grains in the sheet metals arrange in some preferred orientations, due to the rolling processes during manufacturing, which results in directional variation of the material yield strength and plastic flow. This directional variation of the mechanical properties is defined as the material anisotropy and is usually characterized by the Lankford (anisotropy) coefficients (see, Lankford et al., 1950).

In addition to the elastic–plastic constitutive models, material softening (i.e., gradual degradation of the mechanical properties) plays an important role in the prediction of plastic instabilities. In this context, two damage theories have been developed in the literature over the past few decades, i.e., micromechanical constitutive models and phenomenological constitutive models. Since the main motivation of the present thesis is to investigate the forming processes of thin sheet metals, which undergo large plastic deformations; therefore, prior to the description of these two damage theories, kinematics of large deformations is presented in what follows.

1.3.1 Kinematics of large deformations

The kinematics of large deformations is based on the multiplicative decomposition of the deformation gradient $\mathbf{F}$ into its elastic and plastic parts, which was initially proposed by Lee (1969) as follows:

$$\mathbf{F} = \mathbf{F}^e \cdot \mathbf{F}^p , \tag{1.1}$$

where $\mathbf{F}^e$ and $\mathbf{F}^p$ are the elastic and plastic parts of the deformation gradient, respectively. The multiplicative decomposition is schematically illustrated in Fig. 1.23, where a line element $d\mathbf{X}$ is first plastically deformed from an initial configuration to an intermediate configuration $d\bar{\mathbf{x}}$ according to the deformation gradient $\mathbf{F}^p$. Then, the elastic deformation gradient $\mathbf{F}^e$ brings the

line element $d\bar{\mathbf{x}}$ elastically to its final configuration $d\mathbf{x}$. If the element is subjected to elastic unloading from its final configuration to its intermediate configuration, then the element in the intermediate configuration is considered to be stress free. Additionally, it should be noted that the intermediate configuration and hence the multiplicative decomposition are not unique.

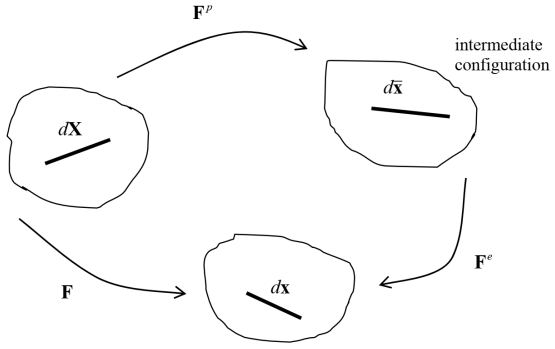

Figure 1.23. Demonstration of the multiplicative decomposition of the deformation gradient $\mathbf{F}$ (Kelly, 2019).

The expression for the velocity gradient tensor **G** is given by:

$$\mathbf{G} = \dot{\mathbf{F}} \cdot \mathbf{F}^{-1}. \tag{1.2}$$

By using the multiplicative decomposition of deformation gradient (see Eq. (1.1)), the velocity gradient can be expanded as follows:

$$\mathbf{G} = \dot{\mathbf{F}}^e \cdot \left(\mathbf{F}^e\right)^{-1} + \mathbf{F}^e \cdot \dot{\mathbf{F}}^p \cdot \left(\mathbf{F}^p\right)^{-1} \cdot \left(\mathbf{F}^e\right)^{-1}. \tag{1.3}$$

By using the left polar decomposition, the elastic part of the deformation gradient $\mathbf{F}^e$ can be expressed as:

$$\mathbf{F}^e = \mathbf{V}^e \cdot \mathbf{R}, \tag{1.4}$$

where $\mathbf{R}$ is the orthogonal rotation matrix and $\mathbf{V}^e$ is the symmetric left Cauchy stretch tensor. The stretch is defined as the ratio of the final element length to the original element length. The rotation matrix $\mathbf{R}$ satisfies the following identity:

$$\mathbf{R}^{\mathrm{T}} = \mathbf{R}^{-1}. \tag{1.5}$$

In cold forming processes of metallic materials, the elastic part of the deformation gradient $\mathbf{F}^e$ typically involves large rotations with very small elastic strains. This simplifying assumption implies that the final configuration and elastically relaxed configuration (i.e., intermediate configuration) in Fig. 1.23 remain very close to each other except rotations. In this case, the stretch tensor $\mathbf{V}^e$ can be simply written as:

$$\mathbf{V}^e = \mathbf{I} + \mathbf{e}, \tag{1.6}$$

where $\mathbf{I}$ is the second-order identity tensor and $\mathbf{e}$ is the elastic strain tensor such that its norm is very small as compared to unity. By substituting Eqs. (1.4) and (1.6) into Eq. (1.3), and by limiting the polynomial expansion of $\left(\mathbf{F}^e\right)^{-1}$ to the first order, the velocity gradient can be evaluated as:

$$\mathbf{G} = \dot{\mathbf{R}} \cdot \mathbf{R}^{\mathrm{T}} + \overset{\nabla}{\mathbf{e}} + \mathbf{R} \cdot \dot{\mathbf{F}}^p \cdot \left(\mathbf{F}^p\right)^{-1} \cdot \mathbf{R}^{\mathrm{T}}, \tag{1.7}$$

where

$$\overset{\nabla}{\mathbf{e}} = \dot{\mathbf{e}} + \mathbf{e} \cdot \left(\dot{\mathbf{R}} \cdot \mathbf{R}^{\mathrm{T}}\right) - \left(\dot{\mathbf{R}} \cdot \mathbf{R}^{\mathrm{T}}\right) \cdot \mathbf{e}, \tag{1.8}$$

is the objective time derivative of $\mathbf{e}$ calculated by using $\dot{\mathbf{R}} \cdot \mathbf{R}^{\mathrm{T}}$ as the spin tensor. The velocity gradient $\mathbf{G}$ can be additively decomposed into its symmetric and anti-symmetric parts as follows:

$$\mathbf{G} = \mathbf{D} + \mathbf{W}, \tag{1.9}$$

where $\mathbf{D}$ and $\mathbf{W}$ are the strain rate tensor and the spin tensor, respectively. Their expressions are:

$$\mathbf{D} = \frac{1}{2}\left(\mathbf{G} + \mathbf{G}^T\right), \tag{1.10}$$

and

$$\mathbf{W} = \frac{1}{2}\left(\mathbf{G} - \mathbf{G}^T\right). \tag{1.11}$$

By using Eq. (1.7), the strain rate tensor and the spin tensor can be evaluated as:

$$\mathbf{D} = \overset{\nabla}{\mathbf{e}} + \mathbf{D}^p , \tag{1.12}$$

and

$$\mathbf{W} = \dot{\mathbf{R}} \cdot \mathbf{R}^{\mathrm{T}} + \mathbf{W}^p , \tag{1.13}$$

where $\mathbf{D}^p$ and $\mathbf{W}^p$ are the plastic strain rate tensor and the plastic spin tensor, respectively. Their expressions are:

$$\mathbf{D}^p = \mathbf{R} \cdot \hat{\mathbf{D}}^p \cdot \mathbf{R}^{\mathrm{T}} , \tag{1.14}$$

and

$$\mathbf{W}^p = \mathbf{R} \cdot \hat{\mathbf{W}}^p \cdot \mathbf{R}^{\mathrm{T}} , \tag{1.15}$$

where $\hat{\mathbf{D}}^p$ and $\hat{\mathbf{W}}^p$ are the symmetric and anti-symmetric parts of the plastic velocity gradient.

In order to ensure frame invariance of the rate constitutive equations within the framework of large strains, objective derivatives of tensor-valued variables must be used, such as that given in Eq. (1.8). This approach simplifies the numerical implementation of these constitutive equations into finite element codes. For instance, consider a second-order tensor $\mathbf{A}$ and its objective derivative $\overset{\nabla}{\mathbf{A}} = \dot{\mathbf{A}} + \mathbf{A} \cdot \boldsymbol{\Omega} - \boldsymbol{\Omega} \cdot \mathbf{A}$ associated with the rotation matrix $\mathbf{T}$, such that $\boldsymbol{\Omega} = \dot{\mathbf{T}} \cdot \mathbf{T}^{\mathrm{T}}$ is a skew-symmetric spin tensor. In this case, the time derivative of tensor $\mathbf{A}$ rotated by an amount $\mathbf{T}$ (i.e., $\hat{\mathbf{A}} = \mathbf{T}^{\mathrm{T}} \cdot \mathbf{A} \cdot \mathbf{T}$) is given by:

$$\dot{\hat{\mathbf{A}}} = \dot{\mathbf{T}}^{\mathrm{T}} \cdot \mathbf{A} \cdot \mathbf{T} + \mathbf{T}^{\mathrm{T}} \cdot \dot{\mathbf{A}} \cdot \mathbf{T} + \mathbf{T}^{\mathrm{T}} \cdot \mathbf{A} \cdot \dot{\mathbf{T}} , \tag{1.16}$$

or equivalently,

$$\dot{\hat{\mathbf{A}}} = \mathbf{T}^{\mathrm{T}} \cdot \overset{\nabla}{\mathbf{A}} \cdot \mathbf{T} . \tag{1.17}$$

Different objective derivatives have been proposed in the literature, which make the large strain formulation of rate constitutive equations similar in form to a small strain formulation. These objective derivatives depend on the choice of the rotation matrix $\mathbf{T}$ and the polar decomposition of the deformation gradient $\mathbf{F}$. One possible choice is to consider the anti-symmetric part of the velocity gradient (i.e., $\mathbf{\Omega} = \mathbf{W}$), which results in the well-known Jaumann objective rate. Another possible choice arises by the left polar decomposition of the deformation gradient i.e., $\mathbf{F} = \mathbf{V} \cdot \mathbf{R}$, and considering $\mathbf{R}$ as a rotation matrix (i.e., $\mathbf{T} = \mathbf{R}$), which results in Green–Naghdi objective rate.

1.3.2 Micromechanical constitutive models

McClintock (1968) and Rice and Tracey (1969) observed that fracture in porous ductile materials frequently takes place owing to large growth and eventually coalescence of voids. They studied the kinematics of isolated voids present inside an infinite block of rigid-plastic material. Both cylindrical and spherical void shapes were considered, and it was found that void growth strongly depends on the hydrostatic stress component. Moreover, when the value of hydrostatic stress is large, the change in volume of voids is significantly more than the change in their shape. Rice and Tracey (1969) proposed the following expression for the growth of spherical voids subjected to remote strain fields:

$$\frac{\mathrm{dR}}{\mathrm{R}} = \zeta \exp\left(\frac{3\Sigma_{\mathrm{m}}}{2\bar{\sigma}}\right) \mathrm{d}\bar{\varepsilon}^{\mathrm{p}}, \tag{1.18}$$

where R is the void radius, Σ_{m} is the hydrostatic stress, $\bar{\sigma}$ is the yield strength, $\bar{\varepsilon}^{\mathrm{p}}$ is the equivalent plastic strain and ζ is a constant, which depends on the material microstructure. Rice and Tracey (1969) proposed a value of ζ equal to 0.283. However, several researches (see, e.g., Marino et al., 1985) proposed different values for the parameter ζ, depending on the distribution and initial dimensions of voids. Note that Eq. (1.18) shows that the void growth is an exponential function of the hydrostatic stress. In order to take into account the effect of strain hardening, Beremin (1981) heuristically extended the Rice and Tracey model by replacing $\bar{\sigma}$ in Eq. (1.18) with the von Mises equivalent stress Σ_{eq}. Additionally, Eq. (1.18) can be used in conjunction

with elastic–plastic constitutive equations to predict ductile fracture when the void radius reaches a critical value (Beremin, 1981).

1.3.2.1 Gurson damage model

Gurson (1977) developed a macroscopic yield function for porous ductile materials by following the homogenization theory. Fig. 1.24 represents the shapes of the voids and the representative volume elements (RVEs) considered in the limit analyses performed by Gurson (1977), which led to the following yield function:

$$\Phi = \left(\frac{\Sigma_{eq}}{\bar{\sigma}} \right)^2 + 2f \cosh\left(\frac{3\kappa\Sigma_m}{2\bar{\sigma}} \right) - 1 - f^2 = 0, \tag{1.19}$$

where f is the porosity or void volume fraction, defined as the ratio of void volume to the RVE volume. The value of parameter κ is equal to 1 for spherical geometry of the void and RVE, while it is equal to $\sqrt{3}$ for cylindrical geometry. $\bar{\sigma}$ is the yield stress of the matrix material, which was considered as rigid-plastic in the original Gurson (1977) model, and Σ_{eq} is the von Mises equivalent stress. It should be noted that the yield function in Eq. (1.19) reduces to the von Mises yield criterion when the porosity is equal to 0. Note also that the porosity f is the only microstructural variable involved in the Gurson damage model.

(a) (b)

Figure 1.24. Cylindrical (left) and spherical (right) geometries for the void and the RVE considered by Gurson (1977).

Yield surfaces for the Gurson damage model are presented in Fig. 1.25 for different values of the void volume fraction f. In Fig. 1.25a, the normalized yield surfaces are plotted in the

principal stress space, while in Fig. 1.25b, the normalized yield surfaces are plotted in hydrostatic stress and equivalent stress plane. Note that, for $f = 0$, pressure independent von Mises yield surface is recovered from the Gurson damage model, whereas for $f > 0$, pressure (hydrostatic stress) dependent yield surfaces are obtained. Also note that, as the value of porosity increases, the yield surface shrinks in size, which represents the degradation of material strength with the void growth.

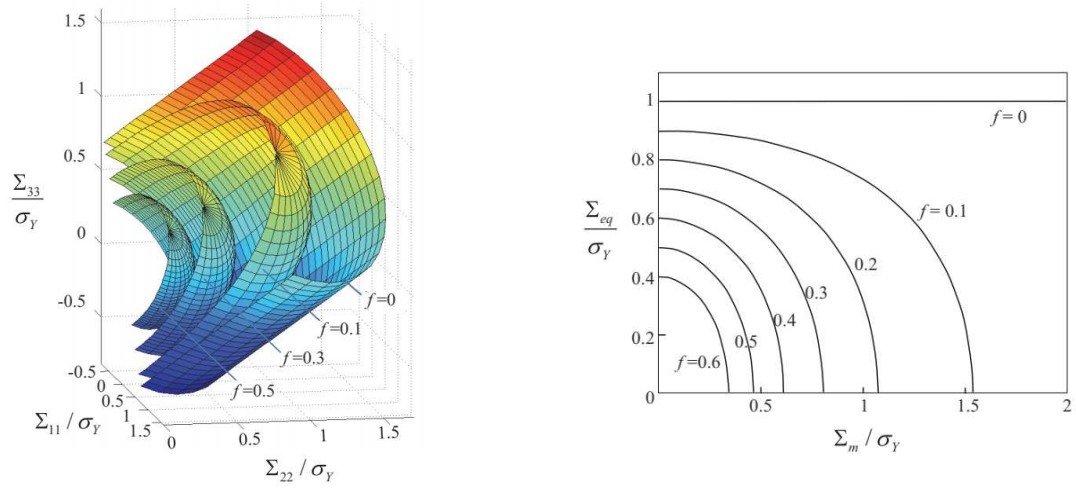

(a) (b)

Figure 1.25. Normalized yield surfaces for the Gurson damage model in three-dimensional principal stress space (left) and hydrostatic stress and equivalent stress plane (right) (Li and Wang, 2008).

The microstructural variable (i.e., porosity f), involved in the Gurson damage model, is assumed to evolve with the plastic deformation. Depending on the material under investigation, the initial value of porosity (i.e., f_0) is treated as a material parameter. The dense matrix material of the RVE is considered to be incompressible. Therefore, the total change in the RVE volume during the plastic deformation is solely attributed to the change in the void volume. If ω and Ω represent the volumes of the void and the RVE, respectively, then, the evolution of the porosity can be evaluated as:

$$\dot{f} = \frac{\mathrm{d}}{\mathrm{d}t}\left(\frac{\omega}{\Omega}\right) = \left(\frac{\dot{\omega}}{\dot{\Omega}} - \frac{\omega}{\Omega}\right)\frac{\dot{\Omega}}{\Omega}, \tag{1.20}$$

where $\dot{\omega} = \dot{\Omega}$. Therefore, Eq. (1.20) can be simplified as:

$$\dot{f} = (1 - f)\mathbf{D}^{\mathrm{p}} : \mathbf{I}, \tag{1.21}$$

where $\mathbf{D}^{\mathrm{p}}$ represents the macroscopic plastic strain rate tensor, and $\mathbf{I}$ is the second-order identity tensor. $\mathbf{D}^{\mathrm{p}}$ can be evaluated from the yield function (i.e., Eq. (1.19)) by using the normality rule. Therefore, the evolution of porosity only depends on the macroscopic yield function. The use of a single microstructural variable, i.e. porosity, is generally sufficient for the modeling of isotropic damage. However, for anisotropic damage theory, incorporation of other microstructural variables, such as void shape and void orientation, is necessary.

1.3.2.2 Extensions in the Gurson damage model

The original Gurson model described above does not incorporate the elasticity, strain hardening of the dense matrix material, void nucleation, void coalescence, void shape and void size effects. In order to implement the Gurson damage model into finite element codes, and to establish a good correlation between experimental and numerical results, several heuristic extensions of the original Gurson model have been proposed. These extensions are discussed in what follows.

1.3.2.2.1 Strain/work hardening

In the original Gurson model (i.e., Eq. (1.19)), the matrix material is considered to be rigid-plastic with the yield strength $\bar{\sigma}$ having a constant value. In order to incorporate the phenomenon of strain/work hardening in the Gurson model, the constant yield strength $\bar{\sigma}$ is heuristically replaced by a function $\bar{\sigma}\left(\bar{\varepsilon}^{\mathrm{p}}\right)$, where $\bar{\varepsilon}^{\mathrm{p}}$ is the equivalent plastic strain of the fully dense matrix material. Various isotropic hardening laws have been proposed in the literature. The most widely used isotropic hardening laws are presented below:

$$
\begin{aligned}
&\overline{\sigma}(\overline{\varepsilon}^{\mathrm{p}}) = \overline{\sigma}_0 + K\left(\overline{\varepsilon}^{\mathrm{p}}\right)^n && \text{(Ludwig's hardening law)},\\
&\overline{\sigma}(\overline{\varepsilon}^{\mathrm{p}}) = K\left(\overline{\varepsilon}^{\mathrm{p}} + \varepsilon_0\right)^n && \text{(Swift's hardening law)},\\
&\overline{\sigma}(\overline{\varepsilon}^{\mathrm{p}}) = \overline{\sigma}_0 + R_{\mathrm{sat}}\left(1-\exp(-\mathrm{C_R}\overline{\varepsilon}^{\mathrm{p}})\right) && \text{(Voce's hardening law)},\\
&\overline{\sigma}(\overline{\varepsilon}^{\mathrm{p}}) = \overline{\sigma}_0\left(1+\frac{\overline{\varepsilon}^{\mathrm{p}}}{\overline{\sigma}_0 / E}\right)^n && \text{(Power}-\text{hardening law)},
\end{aligned}
\tag{1.22}
$$

where $\overline{\sigma}_0$ is the initial yield strength, while K, ε_0, n, R_{sat} and $\mathrm{C_R}$ are the material hardening parameters. The evolution of the equivalent plastic strain (i.e., $\dot{\overline{\varepsilon}}^{\mathrm{p}}$) is related to the evolution of the macroscopic plastic strain via the equivalence relationship of the plastic work rate as follows:

$$
(1-f)\overline{\sigma}\dot{\overline{\varepsilon}}^{\mathrm{p}} = \boldsymbol{\Sigma} : \mathbf{D}^{\mathrm{p}}. \tag{1.23}
$$

It has been demonstrated by Devaux et al. (1997) that the evolution of the porosity in the original Gurson model only depends on the initial value of the porosity, stress triaxiality ratio and the equivalent plastic strain. Additionally, Chalal and Abed Meraim (2015) have also shown that the evolution of porosity is independent of the strain hardening exponent. However, the unit-cell studies performed by Koplik and Needleman (1988) have shown the effect of strain hardening on the evolution of porosity. For this purpose, Leblond et al. (1995) and Lacroix et al. (2016) have extended the original Gurson model by incorporating two internal variables (i.e., Σ_1 and Σ_2) instead of one (i.e., $\overline{\sigma}$) to define the isotropic strain hardening. The modified yield function is expressed as follows:

$$
\Phi = \left(\frac{\Sigma_{\mathrm{eq}}}{\Sigma_1}\right)^2 + 2f\cosh\left(\frac{3\Sigma_{\mathrm{m}}}{2\Sigma_2}\right) - 1 - f^2 = 0. \tag{1.24}
$$

In their extended version, the spherical RVE is divided into several layers and the terms Σ_1 and Σ_2 depend on the yield strengths and the local porosities of each layer. Therefore, the expressions of Σ_1 and Σ_2 involved complex numerical integration (see Lacroix et al., 2016). It has been shown that the extended Gurson-based layered model can reproduce the phenomenon of ratcheting of porosity under cyclic loading, which was not the case with the original Gurson

model. The model has been further extended by Morin et al. (2017) to incorporate kinematic hardening in addition to the isotropic hardening.

1.3.2.2.2 Correction factors

Based on micromechanical analyses of periodic distributions of spherical and cylindrical voids, Tvergaard (1981) introduced the so-called void interaction parameters (i.e., q_1, q_2 and q_3) in the original Gurson model. The improved Gurson model for spherical voids can be expressed as follows:

$$\Phi = \left(\frac{\Sigma_{\text{eq}}}{\bar{\sigma}}\right)^2 + 2q_1 f \cosh\left(\frac{3q_2\Sigma_{\text{m}}}{2\bar{\sigma}}\right) - 1 - q_3 f^2 = 0. \tag{1.25}$$

The typical values of the void interaction parameters are $q_1 = 1.5$, $q_2 = 1$ and $q_3 = q_1^2 = 2.25$. However, unit-cell studies have shown that the values of these parameters depend on the void shape and the loading conditions. Therefore, some researchers calibrated these parameters based on the strain hardening (see Faleskog et al., 1998), stress triaxiality, or lode parameters (see, e.g., Vadillo and Fernández-Sáez, 2009; Vadillo et al., 2016). Therefore, it can be concluded that the *q*-parameters do not simply reflect the effects of void interactions but, as a whole, represent the inherent inaccuracies associated with the Gurson damage model.

Some empirical yield functions have also been developed in the literature for porous sintered ductile materials. The expressions for these yield functions are almost similar to that of the original Gurson damage model. For instance, the yield function developed by Shima and Oyane (1976) can be written as follows:

$$\Phi = \left(\frac{\Sigma_{\text{eq}}}{\bar{\sigma}}\right)^2 + 6.2 f^{1.028} \left(\frac{\Sigma_{\text{m}}}{\bar{\sigma}}\right)^2 - (1-f)^5 = 0. \tag{1.26}$$

The yield function expressed in Eq. (1.26) was empirically fitted for sintered copper; however, reasonably accurate results were also obtained for sintered aluminum and sintered iron. Later, many experimental evidences (see, e.g., Doraivelu et al., 1984; Becker and Needleman, 1986; Becker et al., 1988) have shown that, for all porous ductile materials including the sintered

metals, the yield function defined in Eq. (1.25) could accurately predict the material response by selecting the specific values of the parameters q_1 and q_2.

1.3.2.2.3 Void nucleation

Nucleation of new voids takes place inside the porous material during plastic deformation due to particle fracture or debonding of the particle-matrix interface. The exact mechanism depends on the hardness of the dense matrix material (Babout et al., 2004). The micrographs obtained from X-ray tomography for both the hard and the soft materials are presented in Fig. 1.26. It can be observed from Fig. 1.26 that particle cracking is the dominant mechanism for void nucleation when the hardness of the matrix material is large, while decohesion of particle-matrix is more favorable for soft matrix materials.

(a) (b)

Figure 1.26. Void nucleation mechanisms: particle cracking for hard matrix material (left) and particle-matrix decohesion for soft matrix material (right) (Babout et al., 2004).

By treating the void nucleation as a mechanism not directly linked with the void growth, the total evolution of the porosity $\dot{f}$ during the plastic deformation is given by the sum of porosity evolution due to void growth $\dot{f}_{\mathrm{g}}$ and that due to void nucleation $\dot{f}_{\mathrm{n}}$:

$$\dot{f} = \dot{f}_{\mathrm{g}} + \dot{f}_{\mathrm{n}}, \tag{1.27}$$

where the void growth term $\dot{f}_{\mathrm{g}}$ is already defined in Eq. (1.21). As to the void nucleation term, i.e., $\dot{f}_{\mathrm{n}}$, various phenomenological models have been developed in the literature. As an example, Fig. 1.27 graphically represents the three typical void nucleation models, i.e., cluster void nucleation, continuous void nucleation, and statistical void nucleation. In Fig. 1.27, "X" represents some strain or stress related quantity, which controls the void nucleation mechanism. In the cluster void nucleation model, when X reaches a critical value, e.g., X_1, the first population of voids are nucleated, as shown in Fig.1.27a. Similarly, second or third population of voids are nucleated corresponding to X_2, and X_3, respectively. Indeed, the cluster void nucleation model is frequently considered in the Gurson damage model in the form of an initial porosity. The continuous void nucleation model assumes that the void nucleation rate, with respect to the nucleation controlling quantity X, is constant. This model is less commonly used; however, it accurately predicts the void nucleation mechanism for some materials (see, e.g., Zhang and Niemi, 1994a, 1994b). The statistical approach to model the void nucleation mechanism is the most sophisticated approach, which assumes that the void nucleation amplitude is maximum at a critical value X_c. The phenomenological statistical void nucleation model proposed by Needleman and Rice (1978) and Chu and Needleman (1980) is widely used in conjunction with the Gurson damage model, and is expressed as follows:

$$\dot{f}_{\mathrm{n}} = A_N \dot{\bar{\varepsilon}}^{\mathrm{p}} + B_N \left(\dot{\Sigma}_{\mathrm{m}} + \dot{\bar{\sigma}} \right), \tag{1.28}$$

with

$$A_N = \frac{f_N}{s_N \sqrt{2\pi}} \exp\left(-\frac{1}{2} \left(\frac{\bar{\varepsilon}^{\mathrm{p}} - \varepsilon_N}{s_N} \right)^2 \right), \tag{1.29}$$

and

$$B_N = \frac{f_N}{s_N \bar{\sigma}_0 \sqrt{2\pi}} \exp\left(-\frac{1}{2} \left(\frac{\bar{\sigma} + \Sigma_{\mathrm{m}} - \sigma_N}{\bar{\sigma}_0 s_N} \right)^2 \right), \tag{1.30}$$

where A_N and B_N represent the amplitudes of strain- and stress-controlled nucleation, respectively. When $A_N > 0$ and $B_N = 0$, void nucleation is strain-controlled, while it is stress-controlled for $A_N = 0$ and $B_N > 0$. f_N is the Gaussian amplitude, which represents the void volume fraction of the cavities that are likely to nucleate, σ_N and ε_N are, respectively, the mean stress and mean strain for nucleation, and s_N is the standard deviation for the normal distribution curve. From Eqs. (1.29-1.30), it can be observed that maximum amplitude for stress- and strain-controlled nucleation takes place when $\bar{\sigma} + \Sigma_m = \sigma_N$ and $\bar{\varepsilon}^p = \varepsilon_N$, respectively. It has been shown in the literature that the strain- and stress-controlled void nucleation in the Gurson model lead to significantly different predictions of the ductility limits. More specifically, the dependence of stress-controlled void nucleation amplitude on the mean Cauchy stress makes the plastic flow non-normal, which promotes early flow localization. This aspect and its effect on the prediction of FLDs will be numerically detailed in Chapter 2.

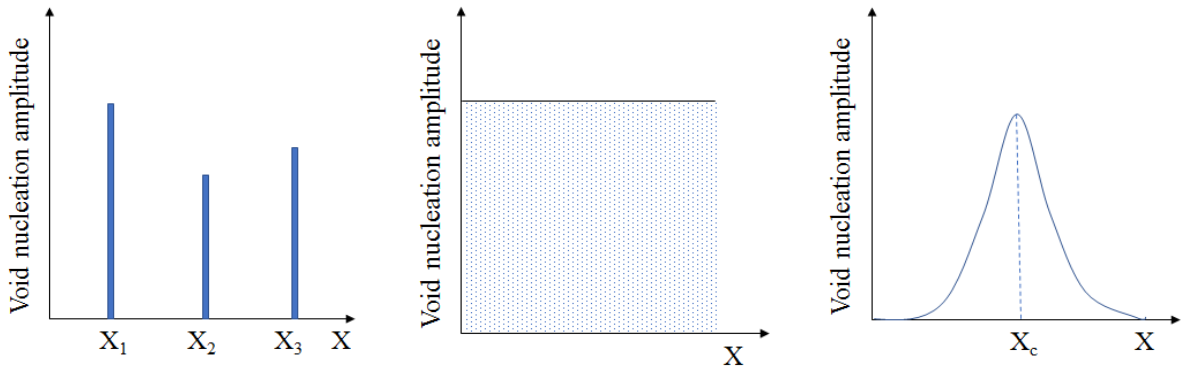

(a) (b) (c)

Figure 1.27. Typical void nucleation models: (a) cluster void nucleation, (b) continuous void nucleation, and (c) statistical void nucleation.

1.3.2.2.4 Void Coalescence

Due to the mechanisms of void growth and void nucleation during the plastic deformation, the voids that are close to each other overcome the inter-void spacing and merge into one another. This phenomenon is known as void coalescence. During the void coalescence, the plastic flow

becomes localized in the inter-void matrix, which ultimately leads to ductile failure of the porous material. Experiments have shown the evidences that after a certain amount of plastic deformation, the void growth does not remain stable, and rapid decay of load carrying capacity of the material is observed. Unit-cell studies have also established the evidences of transition from diffuse to localized plastic flow in the inter-void spacings. There are three commonly observed modes of void coalescence, which are depicted in Fig. 1.28. The first and the most common mode of void coalescence is through the local necking of inter-void ligament, also known as "coalescence in layers". The second mode of void coalescence takes place due to local plastic instability of the matrix material between the adjacent voids in the form of micro-shear bands. This mode of void coalescence significantly decreases the ductility limit, since the micro-shear bands could appear between the voids that are still quite apart from each other. The third mode of void coalescence, i.e., "necklace coalescence" or "coalescence in columns" is more favorable at low values of stress triaxiality ratio. In this mode, the voided column is produced along the loading direction. Necklace coalescence is quite common in steel having MnS inclusions; however, it does not significantly affect the ductility limits.

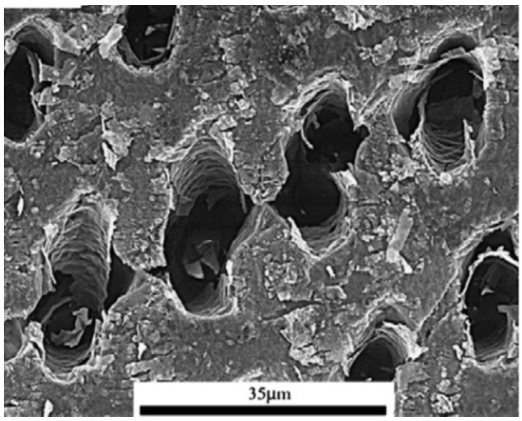

(a)

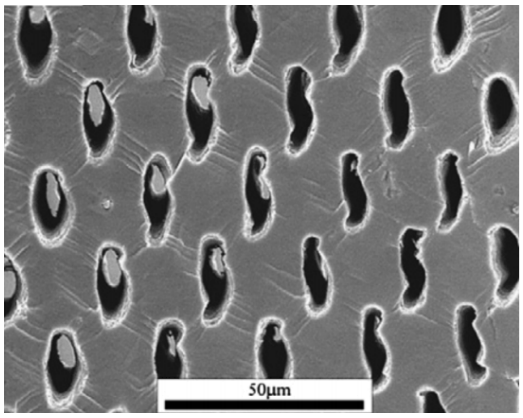

(b)

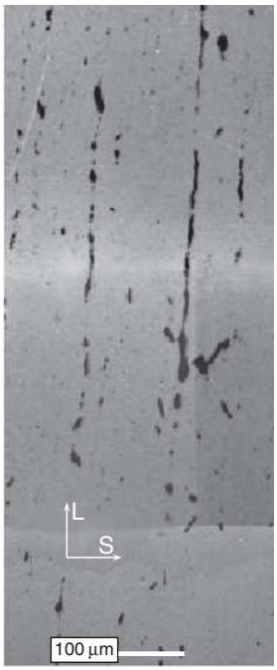

(c)

Figure 1.28. Modes of void coalescence: (a) coalescence in layers, (b) coalescence in micro-shear bands, and (c) coalescence in columns (Weck et al., 2006).

According to the Gurson model, the final failure is predicted when the material completely loses its load carrying capacity. From Eq. (1.25), the value of porosity corresponding to the final failure can be calculated as $f = 1/q_1$. Indeed, at this value of porosity, the Gurson yield surface depicted in Fig. 1.25 reduces to a point. However, Brown and Embury (1973) have proposed that the actual failure of the material takes place at the onset of void coalescence and the value of porosity, i.e., $f = 1/q_1$, is unrealistically high. For this purpose, Tvergaard (1982) and Tvergaard and Needleman (1984) proposed the well-known Gurson–Tvergaard–Needleman (GTN) model for void coalescence by introducing the concept of effective porosity (i.e., $f^*(f)$) in the Gurson damage model. Their model predicts the complete loss of load carrying capacity of the material, even when the porosity values are not unrealistically high. Accordingly, the yield function in Eq. (1.25) is heuristically modified by replacing the porosity with an effective porosity as follows:

$$\Phi = \left(\frac{\Sigma_{\text{eq}}}{\overline{\sigma}} \right)^2 + 2q_1 f^* \cosh\left(\frac{3q_2 \Sigma_{\text{m}}}{2\overline{\sigma}} \right) - 1 - q_3 f^{*2} = 0, \tag{1.31}$$

where the effective porosity is defined as:

$$f^* = f_{\text{cr}} + \delta_{\text{GTN}}(f - f_{\text{cr}}), \tag{1.32}$$

where f_{cr} and δ_{GTN} are material parameters, defined as the critical porosity and the accelerating factor, respectively. The onset of the void coalescence regime is marked when the value of porosity becomes equal to the critical porosity. Accelerating factor can be expressed as follows:

$$\delta_{\text{GTN}} = \begin{cases} 1 & \text{for } f \le f_{\text{cr}} \\ \dfrac{f_{\text{F}} - f_{\text{cr}}}{f_{\text{R}} - f_{\text{cr}}} & \text{for } f_{\text{cr}} < f \le f_{\text{R}} \end{cases}, \tag{1.33}$$

where f_{F} represents the maximum admissible value of the effective porosity, i.e., $f_{\text{F}} = q_1 + \sqrt{q_1^2 - q_3} \big/ q_3$, and f_{R} is the actual value of porosity at final fracture.

Thomason (1985) proposed a phenomenological model for the coalescence in layer mode. A square representative volume element (RVE) having a cylindrical void was considered, as shown in Fig. 1.29. The matrix material surrounding the void is considered rigid, while the kinematically admissible velocity fields were considered in the inter-void spacing. The following closed-form expression was developed for the limit load necessary for the onset of void coalescence:

$$\Sigma_{33}^{\max} = \overline{\sigma}\left(1 - \pi\chi^2\right)\left(\alpha \left(\frac{\chi^{-1} - 1}{w} \right)^2 + \beta\sqrt{\frac{1}{\chi}} \right) = \text{C}_f, \tag{1.34}$$

where $\alpha = 0.1$, $\beta = 1.2$ and $\Sigma_{33}^{\max}$ represents the maximum axial stress under axisymmetric loading. Nguyen et al. (2020) heuristically extended an axisymmetric coalescence criterion for general stress state by incorporating the maximum principal stress in the coalescence criterion. The extended coalescence criterion for the general stress state writes:

$$\max\left(\mu^{\boldsymbol{\Sigma}}\right) = \mathrm{C}_f\,, \tag{1.35}$$

where $\max\left(\mu^{\boldsymbol{\Sigma}}\right)$ denotes the maximum eigenvalue of stress tensor $\boldsymbol{\Sigma}$. χ is the measure of inter-void ligament size ratio. For Gurson-type models, this ratio is given as, see Zhang et al. (2000):

$$\chi = \frac{\sqrt[3]{\dfrac{6f}{\pi}\exp(\varepsilon_1+\varepsilon_2+\varepsilon_3)}}{\sqrt{\exp(\varepsilon_2+\varepsilon_3)}}\,, \tag{1.36}$$

where $\varepsilon_1, \varepsilon_2$ and ε_3 are the principal strains, such that $\varepsilon_1 > \varepsilon_2 > \varepsilon_3$. w is the height to diameter ratio of the cylindrical void. Based on unit-cell studies, Pardoen and Hutchinson (2000) extended Thomason (1985) coalescence criterion for general spheroidal void by defining w as the void aspect ratio. Additionally, the coefficients α and β are defined as a function of isotropic hardening exponent:

$$\begin{aligned} &\alpha = 0.1 + 0.217n + 4.83n^2, \\ &\beta = 1.24. \end{aligned} \tag{1.37}$$

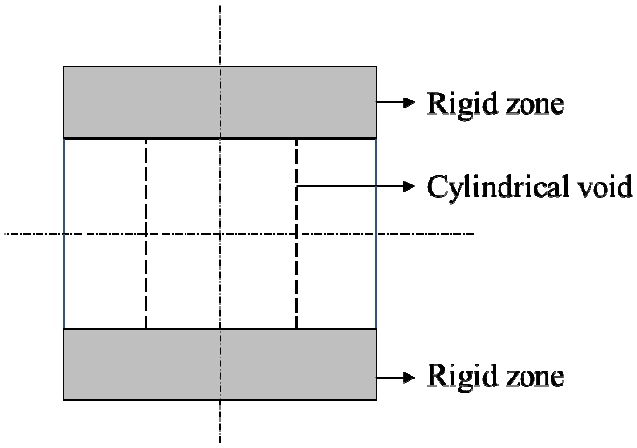

Figure 1.29. Square representative volume element with a cylindrical void assumed for the development of Thomason coalescence criterion (Benzerga and Leblond, 2010).

Gologanu (1997) and Gologanu et al. (2001a) further extended the Thomason (1985) coalescence criterion for the combined tension and shear loadings. The Thomason coalescence criterion fails to predict the onset of coalescence for the penny shaped flat voids i.e., $w \to \infty$. For

this purpose, Benzerga (2002) proposed a coalescence criterion by assuming a cylindrical RVE with a spheroidal void. Benzerga's coalescence criterion provides a better estimate of the upper bound for the critical load as compared to the Thomason (1985) coalescence criterion. The critical condition proposed by Benzerga (2002) for the onset of coalescence is as follows:

$$\Sigma_{33}^{\max} = \bar{\sigma}\left(1-\pi\chi^2\right)\left(0.1\left(\frac{\chi^{-1}-1}{w^2+0.1\chi^{-1}+0.02\chi^{-2}}\right)^2+1.3\sqrt{\frac{1}{\chi}}\right)=\mathrm{C}_f\,. \tag{1.38}$$

Benzerga (2002) also developed the following yield function for post-coalescence regime:

$$\Phi=\frac{\Sigma_{\mathrm{eq}}}{\bar{\sigma}}+\frac{3\left|\Sigma_{\mathrm{m}}\right|}{2\bar{\sigma}}-\frac{3\mathrm{C}_f}{2\bar{\sigma}}=0\,. \tag{1.39}$$

Gologanu et al. (2001b) modeled the "coalescence in column" mode by considering a cylindrical void present inside a cylindrical RVE, which is subjected to predominant lateral stress under arbitrary axisymmetric loadings. Tekoglu (2015) extended the Thomason (1985) and Benzerga (2002) coalescence criteria by considering two populations of voids. Keralavarma and Chockalingam (2016) incorporated the plastic anisotropy and void shape effects for the development of coalescence criterion using the Gurson-based model. Gallican and Hure (2017) proposed a coalescence criterion that also incorporates the effect of void size. Recently, Torki et al. (2017) proposed a coalescence criterion for arbitrary loadings, which also provides an upper bound for the cases involving shear loadings.

Despite all the research work carried out in the literature for the development of coalescence criteria, the current practice is still based on the phenomenological coalescence criterion proposed by Tvergaard and Needleman (1984), because in the latter, the material parameters are easy to calibrate. When coupled with the Gurson damage model, the combined model is generally referred to as the Gurson–Tvergaard–Needleman (GTN) damage model.

1.3.2.2.5 Void shape and shear extensions

The original Gurson model was developed by considering a spherical void present inside a spherical RVE. Additionally, the voids are assumed to remain spherical even after plastic deformation. Consequently, the Gurson model incorporates only one microstructural variable,

i.e., porosity. This assumption is valid under high values of stress triaxiality ratio. However, for low values of stress triaxiality ratio, experiments have revealed that the void shape changes from spherical to general spheroids. In this regard, Gologanu et al. (1993, 1994) proposed their macroscopic yield functions by considering the prolate and oblate ellipsoidal voids present inside the confocal RVEs. In contrast to the Gurson damage model, their yield functions incorporate three microstructural variables, i.e., void aspect ratio, porosity, and major axis of the ellipsoidal void. These void shape dependent yield functions are commonly known as Gologanu–Leblond–Devaux (GLD) models. Similar to the Gurson damage model, Benzerga (2000) proposed several extensions in the GLD model, such as elasticity, isotropic hardening, and void interaction parameters. It should be noted that the results obtained from both the Gurson and GLD models coincide for sufficiently high values of stress triaxiality ratios. However, for low values of stress triaxiality ratios, the Gurson damage model overestimates the evolution of porosity, as compared to the GLD model. For instance, in the particular case of uniaxial tension, the GLD model predicts no change in the porosity; however, only void shape (aspect ratio) changes with the plastic deformation (see Benzerga and Leblond, 2010). Recently, Madou and Leblond (2012a, 2012b, 2013) and Madou et al. (2013) further extended this approach to general spheroidal void shapes.

The unit-cell studies carried out by Zhang et al. (2001) and Dæhli et al. (2018) have shown that the lode parameter, which depends on the third invariant of the Cauchy stress tensor, has strong influence on the void shape evolution. Moreover, this effect is more prominent at low values of stress triaxiality ratio. In this regard, some researchers have proposed the shear extensions in the Gurson damage model (see, e.g., Xue, 2008; Nahshon and Hutchinson, 2008; Zhou et al., 2014). In these extensions, in addition to the void growth and void nucleation, a shear damage term is heuristically incorporated in the porosity evolution relationship, which depends on the third stress invariant. It should be noted that, after the heuristic shear extension, the porosity loses its true meaning of void volume fraction, and rather represents a general variable of damage.

1.3.2.2.6 Void size

Since porosity is the only microstructural variable in the original Gurson model, therefore, the Gurson yield surface does not depend on the void size. However, experimental investigations (see, e.g., Fleck et al., 1994; Schlu et al., 1996; Begley and Hutchinson, 1998; Fu and Chan, 2011; Chentouf et al., 2017; Li et al., 2018) and unit-cell studies (see, e.g., Liu et al., 2003; Mi et al., 2011; Monchiet and Bonnet, 2013; Brach et al., 2016) have revealed that the material strength increases with the decrease in the void size.

In this context, Dormieux and Kondo (2010) extended the Gurson damage model to take into account the effect of void size by considering a hypothetical membrane surrounding the nano-void. Their yield function incorporates a non-dimensional parameter, which depends on the void size. Dormieux and Kondo (2013) and Brach et al. (2017) further extended the void-size dependent yield function for non-linear porous plastic materials by using non-linear homogenization techniques. Later, Monchiet and Kondo (2013) extended the model by incorporating the effect of void shape in addition to the void size. Monchiet and Bonnet (2013) also proposed a Gurson-based model that incorporates the void size effect by using the strain gradient plasticity approach. Their yield function is applicable for the micro-voids; however, the proposed model does not capture the void size effects at low values of stress triaxiality ratio. Based on the Taylor dislocation plasticity model, Wen et al. (2005) proposed a void size dependent yield function for micron and sub-micron void sizes. Their yield function is also sensitive to the variation of void size for both low and high values of stress triaxiality ratio. Note however that the resulting yield function can only be expressed in a parametric form, which leads to its complex numerical implementation.

1.3.2.2.7 Anisotropy

The experimental characterization of sheet metals reveals significant anisotropic behavior, due to the rolling processes involved in their manufacturing. In the original Gurson model, the dense matrix behavior was considered to be isotropic, and defined by the classical isotropic J_2 flow theory of plasticity. In order to extend the Gurson model for anisotropic plastic materials, Benzerga and Besson (2001) considered the Hill'48 plasticity model (see Hill, 1948) for the

dense matrix, which is the straightforward extension of J_2 flow theory for anisotropic materials. They came up with the following macroscopic yield function:

$$\Phi = \left(\frac{\Sigma_{\text{eq}}}{\overline{\sigma}} \right)^2 + 2q_1 f^* \cosh\left(\frac{3q_2 \Sigma_{\text{m}}}{\eta \overline{\sigma}} \right) - 1 - q_3 f^{*2} = 0 , \tag{1.40}$$

where

$$\Sigma_{\text{eq}} = \sqrt{F\left(\Sigma_{22} - \Sigma_{33}\right)^2 + G\left(\Sigma_{33} - \Sigma_{11}\right)^2 + H\left(\Sigma_{11} - \Sigma_{22}\right)^2 + 2L\,\Sigma_{23}^2 + 2M\,\Sigma_{31}^2 + 2N\,\Sigma_{12}^2} , \tag{1.41}$$

and F, G, H, L, M, N and η are the anisotropy material parameters, which depend on the Lankford coefficients (see Benzerga and Besson, 2001). It is noteworthy that the original Gurson model is recovered from Eq. (1.40) for $\eta = 2$, $F = G = H = 0.5$ and $L = M = N = 1.5$. Similar approaches have been followed by Monchiet et al. (2008) and Morin et al. (2015), where void shape dependent Gurson-based models have been extended for anisotropic materials by considering the Hill'48 plasticity model for the dense matrix. Some researchers have heuristically extended the Gurson model for anisotropic materials by replacing the equivalent stress term (i.e., Σ_{eq}) in the Gurson yield function, with the corresponding equivalent stress function for anisotropic materials. For instance, Morin et al. (2018a) have incorporated Yld2004-18p (see Barlat et al., 2005) non-quadratic equivalent stress function for anisotropic materials into the GTN damage model.

1.3.3 Phenomenological constitutive models

The concept of phenomenological constitutive model based on the continuum damage mechanics (CDM) is widely used in the literature to model the degradation of the load carrying capacity of ductile materials. In the CDM theory, a damage variable is introduced in the elastic–plastic constitutive equations, which results in gradual softening in the material stress–strain response. This concept was initially proposed by Kachanov (1958), and subsequently extended by Rabotnov (1969), Lemaitre (1992), Maire and Chaboche (1997), Brünig (2002), Bouchard et al. (2011) and Doghri (2013). The damage variable is defined as the surface density of cracks, which are assumed to exist on the surface of an RVE. Depending on the

anisotropy and softening behavior, the damage variable may be a scalar or a tensor quantity. Three alternative approaches have been developed in the literature in the context of CDM theory, i.e., stress equivalence principle, strain equivalence principle, and energy equivalence principle. The strain equivalence principle, proposed by Lemaitre (1971), is widely used as compared to the other hypotheses, and employs the concept of effective stress. Fig. 1.30 represents an RVE, which is considered in the CDM theory for the description of damage variable. A_o represents the total surface area, while A_d represents the damaged (cracked) area. The damage variable along the normal vector **n** is defined as:

$$d(\mathbf{n}) = \frac{A_d}{A_o}, \tag{1.42}$$

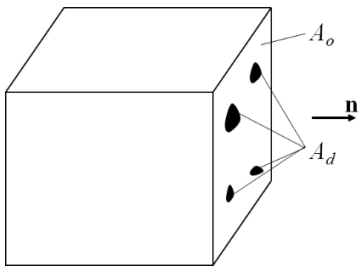

Figure 1.30. Schematic illustration of cracks on the surface of an RVE.

When the damage variable $d(\mathbf{n})$ depends on the orientation of the normal vector **n**, the damage is considered as anisotropic, and must be represented by a second- or fourth-order tensor. However, when microcracks and cavities are uniformly distributed in all directions, then a scalar $d = d(\mathbf{n})$ completely characterizes the damage of the RVE. The effective stress $\tilde{\boldsymbol{\Sigma}}$, which will be subsequently employed in the description of the yield function for the damaged material, is defined as follows:

$$\tilde{\boldsymbol{\Sigma}} = \frac{\boldsymbol{\Sigma}}{1-d}, \tag{1.43}$$

where $\tilde{\boldsymbol{\Sigma}}$ is the effective stress tensor in the undamaged material (i.e., acting on area $A_o - A_d$) and $\boldsymbol{\Sigma}$ is the Cauchy stress tensor in the damaged material (i.e., acting on area A_o). The value of the

damage variable $d=0$ corresponds to the virgin material, while $d=1$ corresponds to the completely damaged material. The yield function can be expressed as:

$$\Phi = \Sigma_{eq}\left(\tilde{\boldsymbol{\Sigma}}\right) - \bar{\sigma} = 0, \tag{1.44}$$

where $\Sigma_{eq}\left(\tilde{\boldsymbol{\Sigma}}\right) = J_2\left(\tilde{\boldsymbol{\Sigma}}\right) = \sqrt{3\tilde{\boldsymbol{\Sigma}} : \tilde{\boldsymbol{\Sigma}}/2}$ is the von Mises norm of the effective stress tensor. By using a hypoelastic law for the effective stress rate tensor, the Cauchy stress rate tensor can be derived from Eq. (1.43) as:

$$\dot{\boldsymbol{\Sigma}} = (1-d)\mathbf{C}^{e} : \left(\mathbf{D} - \mathbf{D}^{p}\right) - \frac{\dot{d}}{1-d}\boldsymbol{\Sigma}, \tag{1.45}$$

where $\mathbf{C}^{e}$ is the fourth-order tensor of elasticity constants, and $\mathbf{D}$ is the macroscopic strain rate tensor. In the Lemaitre damage model, the evolution of the damage variable depends on the amount of strain energy density release Y_e and the equivalent plastic strain rate, as follows:

$$\dot{d} = \begin{cases} \dfrac{1}{(1-d)^{\beta}}\left(\dfrac{Y_e - Y_{ei}}{S}\right)^{s}\dot{\lambda} & \text{if } Y_e \geq Y_{ei} \\ 0 & \text{otherwise} \end{cases}, \tag{1.46}$$

where

$$Y_e = \frac{J_2}{2E}\left[\frac{1}{2}(1+\nu) + 3(1-2\nu)\left(\frac{tr\left(\tilde{\boldsymbol{\Sigma}}\right)}{3J_2}\right)^{2}\right], \tag{1.47}$$

and β, s, S and Y_{ei} are the material damage parameters.

1.4 Prediction of the occurrence of necking: state of the art

In order to predict the occurrence of plastic instabilities inside the material during the deformation, the constitutive models are coupled with plastic instability criteria. Various theoretical and numerical plastic instability criteria have been proposed in the literature over the past few decades. These criteria either predict the occurrence of diffuse necking or localized

necking. Diffuse necking can be interpreted as the progressive evolution of a homogenous strain state towards a quasi-homogenous or heterogenous strain state. This phenomenon of plastic instability is generally not critical in the forming processes of thin sheet metals. However, diffuse necking is often precursor of localized necking, which is more critical than the former. It has been widely established that the formability of thin sheet metals is generally limited by the occurrence of localized necking. Localized necking is characterized by the local decrease in thickness of a sheet metal in the form of a localized band. The plastic instability criteria are broadly classified into four categories.

1.4.1 Principle of maximum force

The first category of plastic instability criteria is based on the maximum load principle, which was first proposed by Considère (1885) for the prediction of diffuse necking in the particular case of uniaxial tension. According to this criterion, diffuse necking is detected when the maximum force point is reached during the uniaxial tensile test. Considère's criterion has been subsequently extended to in-plane biaxial loading by Swift (1952), and was successfully used to predict the occurrence of diffuse necking in the right-hand side of the FLD. Concurrently, Hill (1952) proposed an alternative criterion for the prediction of localized necking, which is based on the bifurcation theory, also known as Hill's zero extension theory. Since Hill's criterion can only predict localized necking on the left-hand side of the FLD (i.e., from uniaxial tension to plane-strain tension), it has generally been used in conjunction with Swift's criterion to predict the complete FLD. Hora et al. (1996), and later Mattiasson et al. (2006), extended Considère's and Swift's criteria in order to take into account strain-path changes in the prediction of localized necking.

1.4.2 Bifurcation theory

The second category of plastic instability criteria is based on the bifurcation theory. Drucker (1956) and later Hill (1958) laid the foundations of general bifurcation theory for the prediction of diffuse necking. This theory requires the positiveness of the second-order work for non-bifurcation state. This criterion provides the lower bound for the occurrence of diffuse or localized necking, and is found to be too conservative for practical applications. A similar, however less conservative criterion for the prediction of diffuse necking, known as the limit-point

bifurcation criterion, was proposed by Valanis (1989). This criterion predicts the occurrence of diffuse necking corresponding to the stationary value of the first Piola–Kirchhoff stress, which in turn requires the singularity of the elasto-plastic tangent modulus. On the basis of the bifurcation theory, Rudnicki and Rice (1975), Stören and Rice (1975) and Rice (1976) developed a plastic instability criterion for the prediction of localized necking in the form of a planar shear or necking band. This criterion for strain localization corresponds to the loss of ellipticity of the partial differential equations governing the associated boundary value problem. Subsequently, Bigoni and Hueckel (1991) and Neilsen and Schreyer (1993) proposed an alternative more conservative criterion for the prediction of flow localization, as compared to the loss of ellipticity criterion, namely loss of strong ellipticity criterion. Based on these bifurcation theories, closed-form analytical solutions for the prediction of strain localization were also derived within the framework of small strains (see, e.g., Doghri and Billardon, 1995; Loret and Rizzi, 1997a, 1997b; Rizzi and Loret, 1997; Sánchez et al., 2008). The major downside of the bifurcation-based plastic instability criteria is that these criteria are only applicable for strain-rate independent materials. Moreover, within the framework of associative plasticity and smooth yield function, the prediction of localized necking in the right-hand side of FLD (i.e., biaxial stretching) requires the material softening phenomenon, which can be achieved by coupling the elastic–plastic constitutive equations with ductile damage models.

1.4.3 Multi-zone (initial imperfection) approach

The third category of plastic instability criteria was popularized by Marciniak and Kuczyński (1967), and is commonly known as M–K initial imperfection approach or simply M–K approach. In the M–K approach, an initial heterogenous region is assumed inside the sheet metal with slightly degraded mechanical properties. Therefore, in the M–K approach, the sheet metal under investigation consists of two zones, i.e., the safe (or homogenous) zone and the defected zone. In the original Marciniak and Kuczyński (M–K) model, the initial heterogeneity was assumed in the form of a narrow band of reduced thickness (i.e., geometric imperfection). Later, Marciniak (1968) introduced the band inclination angle, which enables the M–K model to predict realistic limit strains on the left-hand side of FLD. Moreover, Hutchinson and Neale (1978) extended the M–K model by allowing the imperfection band rotation during the plastic deformation. The M–K approach has also been extended for visco-plastic materials by Marciniak

et al. (1973). Yamamoto (1978) introduced the concept of initial heterogeneity of the mechanical properties (i.e., material imperfection) within a narrow imperfection band. The M–K model has been successfully coupled with various constitutive models, including ductile damage models, and has been widely used for the prediction of FLDs (see, e.g., Mesrar et al., 1998; Ding et al., 2015). An extensive review on the M–K model and its coupling with various forms of equivalent stresses, polycrystalline yield surfaces, and ductile damage models has recently been presented by Banabic (2010a) and Banabic et al. (2019).

The coupling of ductile damage models with the M–K imperfection approach could improve the overall predictions of FLDs with respect to experiments (see, e.g., Hu et al., 1998). Using an elastic–plastic–damage model combined with the M–K approach, initial imperfection could be introduced in the form of an imperfection band with reduced thickness; increased value of damage; different set of hardening parameters, or any combination of imperfections that results in reduced hardening slope within the imperfection band, as compared to the homogeneous zone. In the pioneering work of Yamamoto (1978), the original Gurson model was coupled with the M–K model, in which the initial imperfection was introduced in the localization band as a slightly higher value of initial porosity, as compared to the homogeneous zone. Ductility limits for two strain paths, i.e. axisymmetric uniaxial tension and plane-strain tension, were analyzed. Needleman and Triantafyllidis (1978) extended the approach of Yamamoto (1978) by considering more strain paths on the right-hand side of the FLD and allowing for the change in thickness of the imperfection band due to plastic deformation. This approach has been further extended by incorporating the effect of void nucleation (Chu and Needleman, 1980). A similar approach has been followed by Saje et al. (1982) and Pan et al. (1983) for axisymmetric tension and plane-strain tension by incorporating the strain-rate sensitivity and the effect of stress triaxiality during necking. Several applications of the approach combining the M–K method with damage models for the prediction of ductility limits have been presented in the literature over the last two decades. For instance, Huang et al. (2000), Simha et al. (2007), Liu et al. (2012), Hosseini et al. (2017) and Morin et al. (2018b) considered the material imperfection in the form of initial porosity in Gurson-based damage models. Additionally, combination of material and geometric imperfections has been considered in some investigations (see, e.g., Hu et al., 1998; Ragab and Saleh, 2000; Ragab et al., 2002; Zadpoor et al., 2009; Hu et al., 2017). Son and Kim (2003) investigated the effect of void shape on the FLDs by using the M–K model combined with

the Gologanu–Leblond–Devaux (GLD) damage model for prolate ellipsoidal voids. Chien et al. (2004) implemented the combined material and geometric imperfections for the accurate modeling of shear and necking modes.

1.4.4 Linear perturbation theory

The last category of plastic instability criteria is based on the linearized theory of stability and the associated perturbation analysis. The linear perturbation theory can be used to predict both diffuse and localized necking, and is a good alternative to the bifurcation theory in the particular case of strain-rate dependent materials (see, e.g., Fressengeas and Molinari, 1987; Dudzinski and Molinari, 1991; Toth et al., 1996).

1.5 Modeling of necking criteria based on bifurcation theory

The brief literature review on the plastic instability criteria developed over the past few decades has been discussed in the previous section. Among the bifurcation theories, the General bifurcation criterion and limit-point bifurcation criterion are mostly used to predict diffuse necking, while loss of ellipticity criterion and loss of strong ellipticity criterion are used to predict localized necking. In the present section, first of all, these bifurcation criteria are presented in their general theoretical framework. Then, some theoretical links are established between these bifurcation criteria, in order to classify them according to the order of prediction of the plastic instabilities. Finally, these plastic instability criteria are reformulated in the plane-stress framework, which is more relevant to thin sheet metals.

1.5.1 General bifurcation (GB) criterion

Drucker (1956) and Hill (1958) proposed a general criterion for non-bifurcation state applicable to rate-independent materials. In order to develop the mathematical relationship for general bifurcation criterion, consider a solid domain Ω_S with its boundary denoted by $\partial\Omega_B$. The boundary $\partial\Omega_B$ is divided into two parts, i.e., $\partial\Omega_1$ and $\partial\Omega_2$, such that:

$$\partial\Omega_1 \cup \partial\Omega_2 = \partial\Omega_B \text{ and } \partial\Omega_1 \cap \partial\Omega_2 = \varnothing . \tag{1.48}$$

The solid domain Ω_S is subjected to body forces $\boldsymbol{F}_v$; while the boundary $\partial\Omega_1$, having a normal unit vector represented by **n**, is subjected to surface traction $\boldsymbol{T}_s$; and the boundary $\partial\Omega_2$ is associated with the velocity fields $\boldsymbol{V}$. The quasi-static equilibrium equation and the boundary conditions can be written in the following rate form:

$$\begin{aligned} &\operatorname{div}\dot{\mathbf{B}}+\dot{\boldsymbol{F}}_v=\mathbf{0} \text{ on } \Omega_S, \\ &\dot{\mathbf{B}}\cdot\mathbf{n}=\dot{\boldsymbol{T}}_s \text{ on } \Omega_1, \\ &\boldsymbol{v}=\boldsymbol{V} \text{ on } \Omega_2, \end{aligned} \tag{1.49}$$

where $\mathbf{B}$ is the first Piola–Kirchhoff stress tensor, which is related to the deformation gradient $\mathbf{F}$ through the following constitutive rate relationship:

$$\dot{\mathbf{B}}=\mathbf{L}^{\mathrm{B}}:\dot{\mathbf{F}}, \tag{1.50}$$

where $\mathbf{L}^{\mathrm{B}}$ is defined as the fourth-order tangent modulus. Consider that $\left(\dot{\mathbf{B}}^1,\dot{\mathbf{F}}^1\right)$ and $\left(\dot{\mathbf{B}}^2,\dot{\mathbf{F}}^2\right)$ are two distinct solutions of the boundary value problem (i.e., Eq. (1.49)) at the occurrence of bifurcation. By applying the principle of virtual power and after some mathematical developments, it can be shown that the general condition for uniqueness of solution of the boundary value problem can be mathematically expressed as the positiveness of the second-order work:

$$\int_{\Omega_S}\left(\Delta\dot{\mathbf{B}}:\Delta\dot{\mathbf{F}}\right)d\mathrm{V}>0, \tag{1.51}$$

where $\Delta\dot{\mathbf{B}}=\dot{\mathbf{B}}^1-\dot{\mathbf{B}}^2$. By substituting Eq. (1.50) into Eq. (1.51), the non-bifurcation condition can be written as:

$$\int_{\Omega_S}\left(\Delta\dot{\mathbf{F}}:\mathbf{L}^{\mathrm{B}}:\Delta\dot{\mathbf{F}}\right)d\mathrm{V}>0, \tag{1.52}$$

where Ω_S represents the solid (structure) volume in its undeformed configuration. It should be noted that the non-bifurcation condition stated in Eq. (1.52) excludes all of the geometric as well as material instabilities. Therefore, in order to restrict the criterion for the prediction of only material plastic instabilities, a local formulation is used as follows:

$$\Delta\dot{\mathbf{F}} : \mathbf{L}^{B} : \Delta\dot{\mathbf{F}} > 0 . \tag{1.53}$$

Eq. (1.53) is a sufficient condition for the homogenous strain state for rate-independent materials, which requires the positiveness of all the eigenvalues associated with the symmetric part of the tangent modulus $\mathbf{L}^{B}$. In practice, the occurrence of diffuse necking is numerically detected when the minimum eigenvalue associated with the symmetric part of tangent modulus $\mathbf{L}^{B}$ becomes non-positive. Additionally, the general bifurcation criterion provides the lower bound for the occurrence of diffuse or localized necking.

1.5.2 Limit-point bifurcation (LPB) criterion

Following the above general bifurcation (GB) criterion, it has been observed that the predicted limit strains are too low in some practical applications (see, e.g., Abed-Meraim et al., 2014). As an alternative, Valanis (1989) introduced a less conservative criterion, as compared to the GB criterion, named as the limit-point bifurcation (LPB) criterion. According to this criterion, diffuse necking takes place when the first Piola–Kirchhoff stress attains a stationary state, i.e.,

$$\dot{\mathbf{B}} = \mathbf{L}^{B} : \dot{\mathbf{F}} = \mathbf{0} , \tag{1.54}$$

which suggests that bifurcation is associated with the singularity of the tangent modulus $\mathbf{L}^{B}$, i.e., $\det\left(\mathbf{L}^{B}\right) = 0$, or equivalently, when one of its eigenvalues becomes equal to zero. It is noteworthy that, in the case of small strains, associative flow rules and undamaged material, the general bifurcation criterion and limit-point bifurcation criterion predict equivalent limit strains, due to the symmetry of the involved tangent modulus.

1.5.3 Loss of ellipticity (LOE) criterion

Stören and Rice (1975) and Rice (1976) investigated the occurrence of localized necking in the form of a localization band, across which the velocity gradient is discontinuous. This

localization bifurcation corresponds to the loss of ellipticity (LOE) of the partial differential equations that govern the associated boundary value problem. The localization band is described by a planar discontinuity band defined by its normal unit vector **n**, as schematically illustrated in Fig. 1.31. The equilibrium of forces can be expressed in terms of jump of nominal stress rate tensor across the localization band, as follows:

$$\mathbf{n} \cdot [\![\dot{\mathbf{N}}]\!] = \mathbf{0}, \tag{1.55}$$

with

$$[\![\dot{\mathbf{N}}]\!] = \dot{\mathbf{N}} - \dot{\mathbf{N}}^{\mathrm{B}}, \tag{1.56}$$

where $\dot{\mathbf{N}}^{\mathrm{B}}$ and $\dot{\mathbf{N}}$ represent the nominal stress rate tensor inside and outside the narrow localization band, respectively. The abrupt jump in the velocity gradient, across the localization band, can be expressed by using Maxwell's compatibility equation:

$$[\![\mathbf{G}]\!] = \dot{\boldsymbol{\gamma}} \otimes \mathbf{n}, \tag{1.57}$$

with

$$[\![\mathbf{G}]\!] = \mathbf{G} - \mathbf{G}^{\mathrm{B}}, \tag{1.58}$$

where $\mathbf{G}^{\mathrm{B}}$ and $\mathbf{G}$ represent the velocity gradient inside and outside the narrow localization band, respectively. The vector $\dot{\boldsymbol{\gamma}} = [\![\mathbf{G}]\!] \cdot \mathbf{n}$ is the jump amplitude vector, which describes the localization mode (e.g., shear bifurcation mode when $\dot{\boldsymbol{\gamma}} \perp \mathbf{n}$). The constitutive relationship between the nominal stress rate tensor $\dot{\mathbf{N}}$ and the velocity gradient $\mathbf{G}$ is defined as:

$$\dot{\mathbf{N}} = \mathbf{L} : \mathbf{G}, \tag{1.59}$$

where $\mathbf{L}$ is a fourth-order tensor, defined as elastic–plastic tangent modulus. By substituting Eq. (1.59) into Eq. (1.55), the equilibrium equation can be expanded as:

$$\mathbf{n} \cdot [\![\mathbf{L} : \mathbf{G}]\!] = \mathbf{0}. \tag{1.60}$$

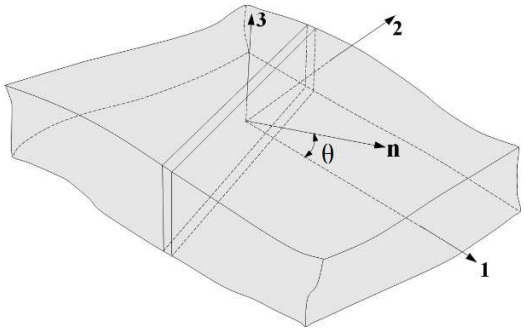

Figure 1.31. Schematic illustration of a localization band within a sheet metal.

By assuming that the elastic–plastic tangent modulus $\mathbf{L}$ is continuous across the narrow localization band before the onset of flow localization, Eq. (1.60) can be written as:

$$\mathbf{n}\cdot\left(\mathbf{L}:[\![\mathbf{G}]\!]\right)=\mathbf{0}. \tag{1.61}$$

Finally, by substituting the compatibility equation Eq. (1.57) into Eq. (1.61), one obtains:

$$\mathbf{n}\cdot\left(\mathbf{L}:\left(\dot{\boldsymbol{\gamma}}\otimes\mathbf{n}\right)\right)=\mathbf{0}, \tag{1.62}$$

or equivalently,

$$\left(\mathbf{n}\cdot\mathbf{L}\cdot\mathbf{n}\right)\cdot\dot{\boldsymbol{\gamma}}=\mathbf{0}. \tag{1.63}$$

The above equation is an eigenvalue problem and a non-trivial solution of Eq. (1.63) only exists when the acoustic tensor $\mathbf{Q}=\mathbf{n}\cdot\mathbf{L}\cdot\mathbf{n}$ becomes singular, i.e.,

$$\det\left(\mathbf{Q}\right)=\det\left(\mathbf{n}\cdot\mathbf{L}\cdot\mathbf{n}\right)=0. \tag{1.64}$$

Eq. (1.64) represents a necessary condition for the prediction of localized necking according to the loss of ellipticity criterion. In practice, localization bifurcation is predicted numerically during the process of loading when the minimum value of the acoustic tensor determinant, for all possible orientations of the normal **n** to the localization band, becomes non-positive.

1.5.4 Loss of strong ellipticity (LOSE) criterion

Similar to the loss of ellipticity criterion, Bigoni and Zaccaria (1992) and Bigoni (1996) proposed the loss of strong ellipticity criterion for the prediction of localized necking. It can be demonstrated that the loss of strong ellipticity criterion is a special case of the general bifurcation criterion. Indeed, in the latter theory, no restrictive condition is imposed on the form of the velocity gradient $\dot{\mathbf{F}}$ (see Eq. (1.53)). However, if the compatibility condition proposed by Neilsen and Schreyer (1993) is imposed on the velocity gradient, then the loss of strong ellipticity criterion is recovered from the general bifurcation criterion. The loss of strong ellipticity criterion states that localized necking does not take place as long as the following condition holds:

$$\begin{aligned} &\dot{\boldsymbol{\gamma}} \cdot \left(\mathbf{n} \cdot \mathbf{L} \cdot \mathbf{n} \right) \cdot \dot{\boldsymbol{\gamma}} > 0, \\ &\dot{\boldsymbol{\gamma}} \cdot \left(\mathbf{Q} \right) \cdot \dot{\boldsymbol{\gamma}} > 0, \end{aligned} \tag{1.65}$$

where the acoustic tensor $\mathbf{Q} = \mathbf{n} \cdot \mathbf{L} \cdot \mathbf{n}$ is the same as that defined in the loss of ellipticity criterion. Practically, loss of strong ellipticity condition is equivalent to the condition of positive definiteness of the acoustic tensor **Q**, which requires the positiveness of all the eigenvalues of the symmetric part of the acoustic tensor **Q**.

It is interesting to note that, within the framework of small strains, associative plastic flow rule, and with no coupling to damage, the acoustic tensor is symmetric and therefore, both loss of ellipticity criterion and loss of strong ellipticity criterion predict equivalent FLDs.

1.5.5 Theoretical classification of the bifurcation criteria

In this subsection, a theoretical classification for the bifurcation-based plastic instability criteria, according to their order of prediction of necking, is established. For this purpose, let us consider a matrix **K** and its symmetric part (i.e., $\mathbf{K}^{\mathrm{sym}} = \tfrac{1}{2}(\mathbf{K} + \mathbf{K}^{\mathrm{T}})$, where $\mathbf{K}^{\mathrm{T}}$ denotes the transpose of matrix **K**). It has been shown in the literature (see, e.g., Abed-Meraim, 1999) that the real parts of the eigenvalues $\mu_i^{\mathbf{K}}$ of matrix **K** are bounded by the minimum and the maximum eigenvalue of its symmetric part ($\mathbf{K}^{\mathrm{sym}}$):

$$\min_{Sp(\mathbf{K}^{\mathrm{sym}})} \left(\mu_i^{\mathbf{K}^{\mathrm{sym}}} \right) \leq \underset{Sp(\mathbf{K})}{Re} \left(\mu_i^{\mathbf{K}} \right) \leq \max_{Sp(\mathbf{K}^{\mathrm{sym}})} \left(\mu_i^{\mathbf{K}^{\mathrm{sym}}} \right), \tag{1.66}$$

where $\underset{Sp(\mathbf{K})}{Re}\left(\mu_i^{\mathbf{K}}\right)$ represent the real parts of the eigenvalues $\mu_i^{\mathbf{K}}$ $(1 \le i \le n)$ of matrix $\mathbf{K}$, while $\min\limits_{Sp(\mathbf{K}^{\mathrm{sym}})}\left(\mu_i^{\mathbf{K}^{\mathrm{sym}}}\right)$ and $\max\limits_{Sp(\mathbf{K}^{\mathrm{sym}})}\left(\mu_i^{\mathbf{K}^{\mathrm{sym}}}\right)$ denote the smallest and the largest eigenvalue of matrix $\mathbf{K}^{\mathrm{sym}}$. Based on Eq. (1.66), the following inequalities can be derived, which involve the eigenvalues of the tangent modulus $\mathbf{L}^{\mathrm{B}}$ and the acoustic tensor $\mathbf{Q}$ and of their symmetric parts $\mathbf{L}^{\mathrm{B}^{\mathrm{sym}}}$ and $\mathbf{Q}^{\mathrm{sym}}$, respectively:

$$\min_{Sp(\mathbf{L}^{\mathrm{B}\,\mathrm{sym}})}\left(\mu_i^{\mathbf{L}^{\mathrm{B}\,\mathrm{sym}}}\right) \le \underset{Sp(\mathbf{L}^{\mathrm{B}})}{Re}\left(\mu_i^{\mathbf{L}^{\mathrm{B}}}\right), \tag{1.67}$$

$$\min_{Sp(\mathbf{Q}^{\mathrm{sym}})}\left(\mu_i^{\mathbf{Q}^{\mathrm{sym}}}\right) \le \underset{Sp(\mathbf{Q})}{Re}\left(\mu_i^{\mathbf{Q}}\right). \tag{1.68}$$

According to Eq. (1.67), the singularity of the tangent modulus $\mathbf{L}^{\mathrm{B}}$ cannot occur before the loss of positive definiteness of the symmetric part of the tangent modulus $\mathbf{L}^{\mathrm{B}}$. This mathematical property implies that, for the prediction of diffuse necking, the GB criterion is more conservative than the LPB criterion. Similarly, Eq. (1.68) implies that the singularity of the acoustic tensor $\mathbf{Q}$ cannot occur before the loss of positive definiteness of the symmetric part of tensor $\mathbf{Q}$. In other words, for the prediction of localized necking, the LOSE criterion is more conservative than the LOE criterion.

From the above discussion, the following theoretical classification of the bifurcation-based criteria can be established (see also Fig. 1.32):

- The GB criterion provides a lower bound for the occurrence of any type of necking (diffuse or localized necking);
- The LOE criterion provides an upper bound for the occurrence of localized necking;
- The LPB criterion is less conservative than the GB criterion;
- The LOSE criterion is more conservative than the LOE criterion.

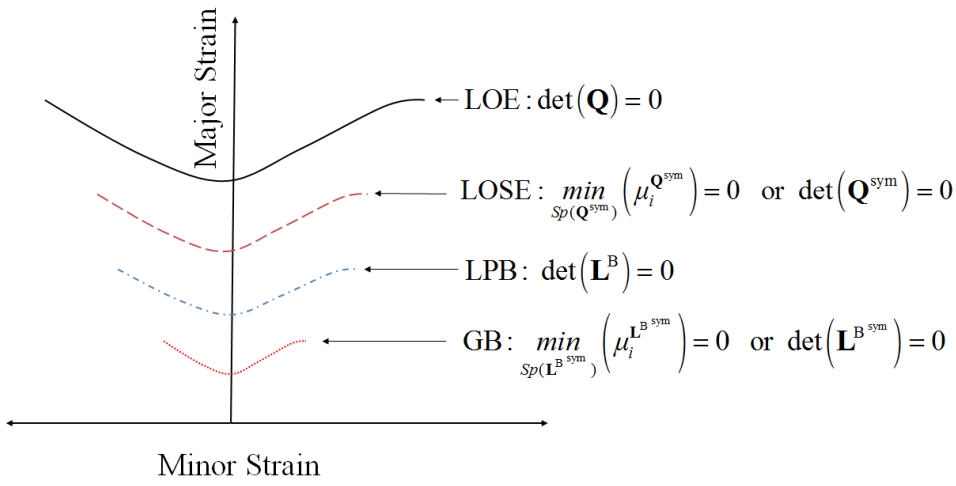

Figure 1.32. Illustration of the theoretical classification of the four bifurcation-based criteria.

1.5.6 Plane-stress framework

It should be recalled that the present thesis is primarily devoted to the prediction of forming limit diagrams for thin sheet metals. Therefore, the plastic instability criteria, discussed in the previous sections, must be implemented by assuming the plane-stress condition. For this purpose, the elastic–plastic tangent modulus $\mathbf{L}$, which is required in the formulation of LOE criterion and LOSE criterion, is reformulated for the plane-stress condition in what follows. As to the general bifurcation criterion and limit-point bifurcation criterion, the tangent modulus $\mathbf{L}^{\mathrm{B}}$ involved in their formulations is related to the elastic–plastic tangent modulus $\mathbf{L}$ by the following relationship:

$$L^{B}_{ijkl} = L_{jikl}\,. \tag{1.69}$$

The plane-stress condition for the nominal stress rate tensor $\dot{\mathbf{N}}$ and velocity gradient $\mathbf{G}$ can be written as follows:

$$\dot{N}_{i3} = \dot{N}_{3i} = 0 \quad \text{with} \quad i = 1,2,3\,, \tag{1.70}$$

and

$$G_{i3} = G_{3i} = 0 \quad \text{with} \quad i = 1,2\,. \tag{1.71}$$

By substituting Eqs. (1.71-1.72) into Eq. (1.59), the non-zero components of nominal stress rate tensor are obtained as:

$$\dot{N}_{ij} = L_{ijkl} G_{kl} + L_{ij33} G_{33} \quad \text{with i, j, k, l} = 1,2 \,. \tag{1.72}$$

The expression for the nominal stress rate component in the thickness direction is given by:

$$\dot{N}_{33} = L_{33kl} G_{kl} + L_{3333} G_{33} \quad \text{with k, l} = 1,2 \,. \tag{1.73}$$

By substituting $\dot{N}_{33} = 0$ in Eq. (1.73) for plane-stress condition, the velocity gradient in the thickness direction is obtained as:

$$G_{33} = -\frac{L_{33kl}}{L_{3333}} G_{kl} \quad \text{with k, l} = 1,2 \,. \tag{1.74}$$

Finally, by substituting Eq. (1.74) into Eq. (1.72), the nominal stress rate tensor for plane-stress condition is given by the following expression:

$$\dot{N}_{ij} = \left(L_{ijkl} - \frac{L_{ij33} L_{33kl}}{L_{3333}} \right) G_{kl} \quad \text{with i, j, k, l} = 1,2 \,, \tag{1.75}$$

or equivalently

$$\dot{N}_{ij} = L^{PS}_{ijkl} G_{kl} \quad \text{with i, j, k, l} = 1,2 \,. \tag{1.76}$$

From the comparison of Eq. (1.75) and Eq. (1.76), the elastic–plastic tangent modulus for the plane-stress condition $\mathbf{L}^{PS}$ is obtained in terms of the three-dimensional elastic–plastic tangent modulus $\mathbf{L}$ as follows:

$$L^{PS}_{ijkl} = L_{ijkl} - \frac{L_{ij33} L_{33kl}}{L_{3333}} \,. \tag{1.77}$$

It should be noted that under plane-stress formulation, the normal unit vector to the localization band lies in the plane of the sheet metal and is defined with a band orientation angle θ (see Fig. 1.31).

1.6 Conclusion

This chapter first dealt with a general overview on sheet metal forming processes, their applications and the common defects involved during plastic deformation. Indeed, the formability of thin sheet metals is limited due to the initiation of these defects. Among these defects, the occurrence of diffuse and localized necking is of key importance and needs in-depth understanding. Then, the concept of forming limit diagram (FLD) and its developments over the past few decades have been summarized, which serves as an important tool to characterize the formability of thin sheet metals. It is followed by a brief introduction of various experimental and theoretical procedures developed in the literature for the determination of FLDs. It has been demonstrated that the theoretical prediction of FLDs, which requires the coupling of advanced constitutive models with plastic instability criteria, is a cost-effective procedure as compared to the experimental one. In this regard, a literature review on the micromechanical constitutive models and phenomenological constitutive models has been presented. However, particular attention has been devoted to Gurson-based damage models, which have been developed over the past four decades. As to the prediction of plastic instabilities, various diffuse and localized necking criteria and their classification have been presented. These plastic instability criteria are broadly classified into four categories, i.e., criteria based on the principle of maximum force, bifurcation theory, multi-zones (initial imperfection) approach, and theory of linear stability. The mathematical foundations of the bifurcation-based plastic instability criteria have been presented, which will be used in the following chapters for the prediction of FLDs. Two of the bifurcation criteria, i.e., general bifurcation criterion and limit-point bifurcation criterion, predict the occurrence of diffuse necking, while the loss of ellipticity criterion and the loss of strong ellipticity criterion predict the occurrence of localized necking. These criteria are first formulated within the framework of large strain and fully three-dimensional approach. However, the necessary modification in the elastic–plastic tangent modulus for the plane-stress condition is also presented. The theoretical classification of the resulting bifurcation-based plastic instability criteria has also been established, which shows that the general bifurcation criterion is more

conservative than the limit-point bifurcation criterion, and provides the lower bound for the occurrence of diffuse or localized necking. Additionally, the loss of ellipticity criterion is less conservative than the loss of strong ellipticity criterion, and provides an upper bound for the occurrence of localized necking.

Chapter 2

Gurson–Tvergaard–Needleman (GTN) model coupled with bifurcation theory

2.1 Introduction

In this chapter, the four bifurcation-based necking criteria presented in the previous Chapter are coupled with the GTN damage model for the prediction of diffuse and localized necking. The resulting constitutive equations and instability criteria are implemented into the finite element code ABAQUS/Standard. The constitutive equations are formulated within the framework of large deformations and fully three-dimensional approach. Since the developed numerical tools have intended applications mainly for thin sheet metals; therefore, the plane-stress conditions are considered within the instability criteria. The present chapter focuses on the effect of destabilizing mechanisms, due to non-associative plasticity and non-normal plastic flow rule, on the prediction of forming limit diagrams (FLDs). Several variants of the GTN model are combined with the bifurcation criteria for the prediction of FLDs for fictitious materials. The order of the predicted FLDs, using the four plastic instability criteria, is compared with the theoretical hierarchical classification established in the previous Chapter in Section 1.5.

2.2 GTN constitutive equations for anisotropic materials

In the following sections, Hill (1948) quadratic yield function, which is the straightforward extension of J_2 flow theory for anisotropic materials, is used in conjunction with the GTN yield surface Φ_Y (see Eq. (1.31)). The expression for the Hill'48 equivalent stress is given as follows:

$$\Sigma_{eq} = \sqrt{F_Y \left(\Sigma_{22} - \Sigma_{33}\right)^2 + G_Y \left(\Sigma_{33} - \Sigma_{11}\right)^2 + H_Y \left(\Sigma_{11} - \Sigma_{22}\right)^2 + 2L_Y \Sigma_{23}^2 + 2M_Y \Sigma_{31}^2 + 2N_Y \Sigma_{12}^2}, \quad (2.1)$$

where F_Y, G_Y, H_Y, L_Y, M_Y and N_Y are material anisotropy parameters, which are experimentally identified using initial yield stresses along various orientations with respect to the rolling direction. Within the framework of non-associative flow rule, the plastic flow is assumed to be controlled by a plastic potential Φ_P, which is different from the yield surface Φ_Y. Note that in

the case of undamaged material and associative flow rule (AFR), the plastic potential Φ_P and the yield surface Φ_Y coincide, while they do not coincide in the case of undamaged material and non-associative flow rule (NAFR). In the present contribution, the mathematical form of the plastic potential Φ_P is similar to that of the undamaged part of the yield surface Φ_Y (i.e. $\Phi_P = \left(\frac{\Sigma_{peq}}{\overline{\sigma}} \right)^2 - 1 \leq 0$), for which the Hill'48 anisotropy coefficients F_p, G_p, H_p, L_p, M_p and N_p are experimentally identified using strain *r*-values (i.e., Lankford coefficients). Therefore, the expression for the macroscopic plastic strain rate tensor $\mathbf{D}^p$ is given by the following flow rule:

$$\mathbf{D}^p = \dot{\lambda} \frac{\partial \Phi_P}{\partial \boldsymbol{\Sigma}} = \dot{\lambda} \mathbf{V}_p , \tag{2.2}$$

where $\dot{\lambda}$ is the plastic multiplier, and $\mathbf{V}_p$ represents the direction of the plastic flow. Considering isotropic strain hardening for the fully dense matrix material, the rate form for the flow stress can be evaluated as:

$$\dot{\overline{\sigma}}(\overline{\varepsilon}^p) = \frac{\partial \overline{\sigma}}{\partial \overline{\varepsilon}^p} \dot{\overline{\varepsilon}}^p = h(\overline{\varepsilon}^p) \dot{\overline{\varepsilon}}^p , \tag{2.3}$$

where $h(\overline{\varepsilon}^p) = \partial \overline{\sigma} / \partial \overline{\varepsilon}^p$ is the plastic hardening slope of the fully dense matrix material, which depends on the isotropic strain hardening law considered in the constitutive equations. By using Eq. (1.23), the equivalent plastic strain rate $\dot{\overline{\varepsilon}}^p$ can be expressed as follows:

$$\dot{\overline{\varepsilon}}^p = \frac{\boldsymbol{\Sigma} : \mathbf{D}^p}{(1-f)\overline{\sigma}} . \tag{2.4}$$

It should be noted that in the GTN damage model, the evolution of porosity is due to the combined effect of the void growth, void nucleation and void coalescence mechanisms. Their expressions are given by Eqs. (1.21) and (1.27–1.33).

Within the co-rotational material frame, the Cauchy stress rate tensor is expressed using the following hypoelastic law:

$$\dot{\boldsymbol{\Sigma}} = \mathbf{C}^{\mathrm{e}} : \left(\mathbf{D} - \mathbf{D}^{\mathrm{p}} \right) = \mathbf{C}^{\mathrm{e}} : \left(\mathbf{D} - \dot{\lambda} \mathbf{V}_{\mathrm{p}} \right) = \mathbf{C}^{\mathrm{ep}} : \mathbf{D} , \tag{2.5}$$

where $\mathbf{C}^{\mathrm{e}}$ is the fourth-order tensor of the elasticity constants and $\mathbf{C}^{\mathrm{ep}}$ is the elastic–plastic tangent modulus, which is determined hereafter. To derive the expressions of the plastic multiplier $\dot{\lambda}$ and the analytical elastic–plastic tangent modulus $\mathbf{C}^{\mathrm{ep}}$, the yield function Φ_{Y} and the plastic multiplier $\dot{\lambda}$ are written in a well-known form of Kuhn–Tucker relationship as follows:

$$\Phi_{\mathrm{Y}} \le 0, \;\; \dot{\lambda} \ge 0, \;\; \Phi_{\mathrm{Y}} \dot{\lambda} = 0 . \tag{2.6}$$

The above relation implies that, when $\Phi_{\mathrm{Y}} \le 0$, no plastic flow occurs (i.e., $\dot{\lambda} = 0$), while a strict plastic loading (i.e., $\dot{\lambda} > 0$) necessarily implies that $\dot{\Phi}_{\mathrm{Y}} = 0$. The latter condition is known as the consistency condition and can be expanded as follows:

$$\dot{\Phi}_{\mathrm{Y}} = \left(\frac{\partial \Phi_{\mathrm{Y}}}{\partial \boldsymbol{\Sigma}} + \frac{\partial \Phi_{\mathrm{Y}}}{\partial f^{*}} \frac{\partial f^{*}}{\partial f} \frac{B_N}{3} \mathbf{I} \right) : \dot{\boldsymbol{\Sigma}} + \left(\frac{\partial \Phi_{\mathrm{Y}}}{\partial \overline{\sigma}} + \frac{\partial \Phi_{\mathrm{Y}}}{\partial f^{*}} \frac{\partial f^{*}}{\partial f} \left(\frac{A_N}{h} + B_N \right) \right) \dot{\overline{\sigma}} + \left(\frac{\partial \Phi_{\mathrm{Y}}}{\partial f^{*}} \frac{\partial f^{*}}{\partial f} \right) \dot{f} \; = 0 . \tag{2.7}$$

The different partial derivatives involved in the above equation can be evaluated as follows:

$$\begin{aligned}
&\frac{\partial \Phi_{\mathrm{Y}}}{\partial \boldsymbol{\Sigma}} = \frac{2\Sigma_{\mathrm{eq}}}{\overline{\sigma}^2} \frac{\partial \Sigma_{\mathrm{eq}}}{\partial \boldsymbol{\Sigma}} + \frac{q_1 q_2 f^{*}}{\overline{\sigma}} \sinh\left(\frac{3 q_2 \Sigma_{\mathrm{m}}}{2\overline{\sigma}} \right) \mathbf{I} , \\
&\frac{\partial \Phi_{\mathrm{Y}}}{\partial f^{*}} = 2 q_1 \cosh\left(\frac{3 q_2 \Sigma_{\mathrm{m}}}{2\overline{\sigma}} \right) - 2 q_3 f^{*} , \\
&\frac{\partial \Phi_{\mathrm{Y}}}{\partial \overline{\sigma}} = -\frac{2\Sigma_{\mathrm{eq}}^2}{\overline{\sigma}^3} - \frac{3 q_1 q_2 f^{*} \Sigma_{\mathrm{m}}}{\overline{\sigma}^2} \sinh\left(\frac{3 q_2 \Sigma_{\mathrm{m}}}{2\overline{\sigma}} \right) , \\
&\frac{\partial f^{*}}{\partial f} = \delta_{\mathrm{GTN}} \; .
\end{aligned} \tag{2.8}$$

By substituting the expressions for the time rates of porosity, yield stress, and the Cauchy stress tensor, along with Eq. (2.2) into the consistency condition (i.e. Eq. (2.7)), the final expression for the plastic multiplier $\dot{\lambda}$ can be given as:

$$\dot{\lambda} = \frac{\mathbf{M} : \mathbf{C}^{\mathrm{e}} : \mathbf{D}}{\mathrm{H}_{\lambda}}, \tag{2.9}$$

where

$$\mathbf{M} = \frac{\partial \Phi_{\mathrm{Y}}}{\partial \boldsymbol{\Sigma}} + \frac{B_N}{3} \frac{\partial \Phi_{\mathrm{Y}}}{\partial f^*} \frac{\partial f^*}{\partial f} \mathbf{I}. \tag{2.10}$$

and

$$\mathrm{H}_{\lambda} = \mathbf{M} : \mathbf{C}^{\mathrm{e}} : \mathbf{V}_{\mathrm{p}} - \frac{h\left(\boldsymbol{\Sigma} : \mathbf{V}_{\mathrm{p}}\right)}{(1-f)\overline{\sigma}} \left[\frac{\partial \Phi_{\mathrm{Y}}}{\partial \overline{\sigma}} + \delta_{GTN} \left(\frac{A_N}{h} + B_N \right) \frac{\partial \Phi_{\mathrm{Y}}}{\partial f^*} \right] - \delta_{GTN} (1-f) \frac{\partial \Phi_{\mathrm{Y}}}{\partial f^*} \left(\mathbf{V}_{\mathrm{p}} : \mathbf{I} \right). \tag{2.11}$$

Finally, by substituting Eq. (2.9) into Eq. (2.5), the expression for the analytical elastic–plastic tangent modulus $\mathbf{C}^{\mathrm{ep}}$ can be derived as follows:

$$\mathbf{C}^{\mathrm{ep}} = \mathbf{C}^{\mathrm{e}} - \tau \frac{\left(\mathbf{C}^{\mathrm{e}} : \mathbf{V}_{\mathrm{p}}\right) \otimes \left(\mathbf{M} : \mathbf{C}^{\mathrm{e}}\right)}{\mathrm{H}_{\lambda}} = \mathbf{C}^{\mathrm{e}} - \tau \frac{\mathbf{P} \otimes \mathbf{Q}}{\mathrm{H}_{\lambda}}. \tag{2.12}$$

where $\tau = 1$ for plastic loading and 0 otherwise.

2.3 Numerical implementation and validation

2.3.1 Time integration scheme

The constitutive equations for the GTN damage model are implemented into the FE code ABAQUS/Standard using a user-defined material (UMAT) subroutine. Large strains and fully three-dimensional approach are considered in the formulation and its numerical implementation. The Jaumann objective rate of the Cauchy stress tensor is used in order to maintain material objectivity.

It can be observed that the evolution of the stress state and internal variables can be represented by a general differential equation in the generic form:

$$\dot{\boldsymbol{x}} = \boldsymbol{g}_{\boldsymbol{x}}(\boldsymbol{x}), \tag{2.13}$$

where vector $\boldsymbol{x}$ encompasses all GTN model variables to be updated at the end of each loading increment. In this work, an explicit time integration scheme, specifically, the fourth-order Runge–Kutta method is adopted. With this explicit time integration scheme, a reasonable compromise can be achieved in terms of accuracy, computational cost, and convergence (see Mansouri et al., 2014).

2.3.2 Numerical validations

In this subsection, the numerical validations of the implemented constitutive equations and the time integration scheme are outlined. The numerical validation is carried out in two steps. First, the numerical results corresponding to a uniaxial tensile test for the original isotropic GTN damage model, predicted with the present UMAT, are compared with those obtained from the built-in isotropic GTN damage model available in ABAQUS/Standard. Then, the numerical implementation of the undamaged anisotropic plastic behavior is validated through comparisons to reference results available in the literature, since the present anisotropic GTN damage model is not available in ABAQUS/Standard.

2.3.2.1 Validations of GTN damage model

For the numerical validations of the present model, simulations of a uniaxial tension test with the original isotropic GTN model are carried out. Note that the original isotropic GTN model is recovered from the anisotropic one when the Lankford coefficients are set to 1 and when $F_{\mathrm{Y}} = G_{\mathrm{Y}} = H_{\mathrm{Y}} = 0.5$ and $L_{\mathrm{Y}} = M_{\mathrm{Y}} = N_{\mathrm{Y}} = 1.5$. Only void growth and strain-controlled nucleation (without coalescence) are considered in the simulations. The material parameters used in the simulations are summarized in Tables 2.1 and 2.2. Stress–strain curves as well as porosity evolution are shown in Fig. 2.1, for both the developed UMAT subroutine and the built-in ABAQUS model. As observed, the results predicted with the UMAT are in excellent agreement with those of ABAQUS built-in model, which allows validating the numerical implementation of the original isotropic GTN model.

Table 2.1. Elastic–plastic material parameters used in the simulations.

E (GPa)	ν	K (MPa)	n	ε_0
70	0.33	371.2	0.17	0.00324

Table 2.2. GTN damage parameters for strain-controlled nucleation.

f_0	f_N	ε_N	s_N	q_1	q_2	q_3
0.01	0.25	0.27	0.1	1.5	1	2.15

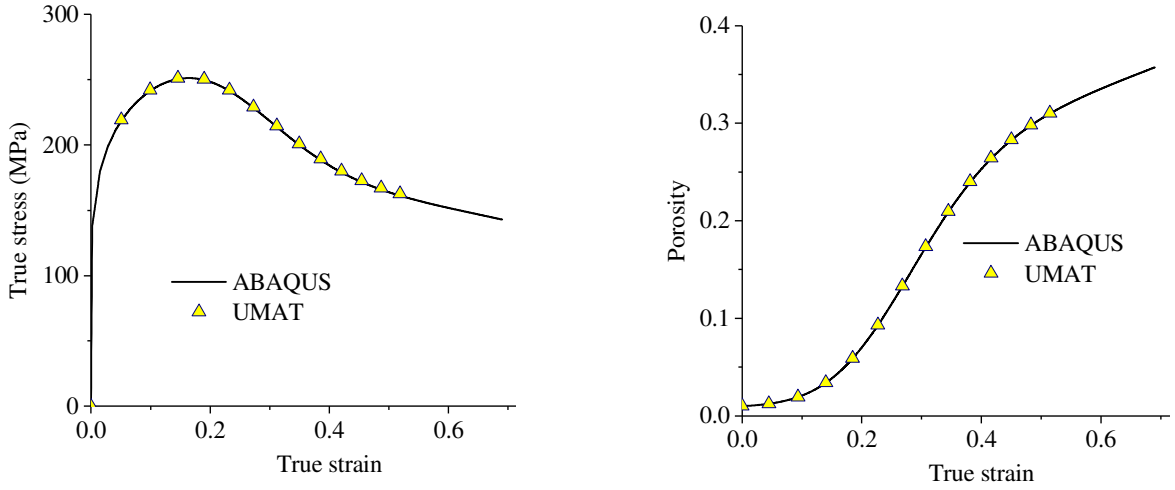

Figure 2.1. Comparison between the built-in ABAQUS GTN model and the developed UMAT subroutine, with strain-controlled nucleation, in terms of true stress–strain curves (left) and porosity evolution (right), for a uniaxial tension test.

In order to achieve qualitative validations, specifically intended to strain- and stress-controlled nucleation, stress–strain curves are plotted for a uniaxial tension test with the GTN damage parameters listed in Table 2.3 and 2.4, respectively. Note that the initial porosity is taken to be zero in order to focus attention on the void nucleation mechanism (without coalescence regime).

Table 2.3. GTN damage parameters for strain-controlled nucleation.

f_0	f_N	ε_N	s_N	q_1	q_2	q_3
0	0.25	0.27	0.1	1.5	1	2.15

Table 2.4. GTN damage parameters for stress-controlled nucleation.

f_0	f_N	σ_N (MPa)	s_N	q_1	q_2	q_3
0	0.25	400	1	1.5	1	2.15

For strain-controlled nucleation, f_N, ε_N and s_N are varied, one at a time, while the remaining parameters are kept constant (see Table 2.3). The resulting stress–strain curves for

uniaxial tension are plotted in Fig. 2.2, along with the stress–strain curve corresponding to undamaged isotropic elastic–plastic model. From this figure, it can be observed that large values of f_N and small values of s_N increase the nucleation amplitude (see A_N in Eq. (1.29)), which consequently accelerates the softening regime (see Figs. 2.2a and 2.2c). On the other hand, the nucleation parameter ε_N controls the onset of void nucleation; therefore, large values of ε_N delay the material softening (see Fig. 2.2b). Note that the undamaged isotropic elastic–plastic material response is recovered from strain-controlled nucleation for $f_N = 0$, or for large values of s_N or ε_N.

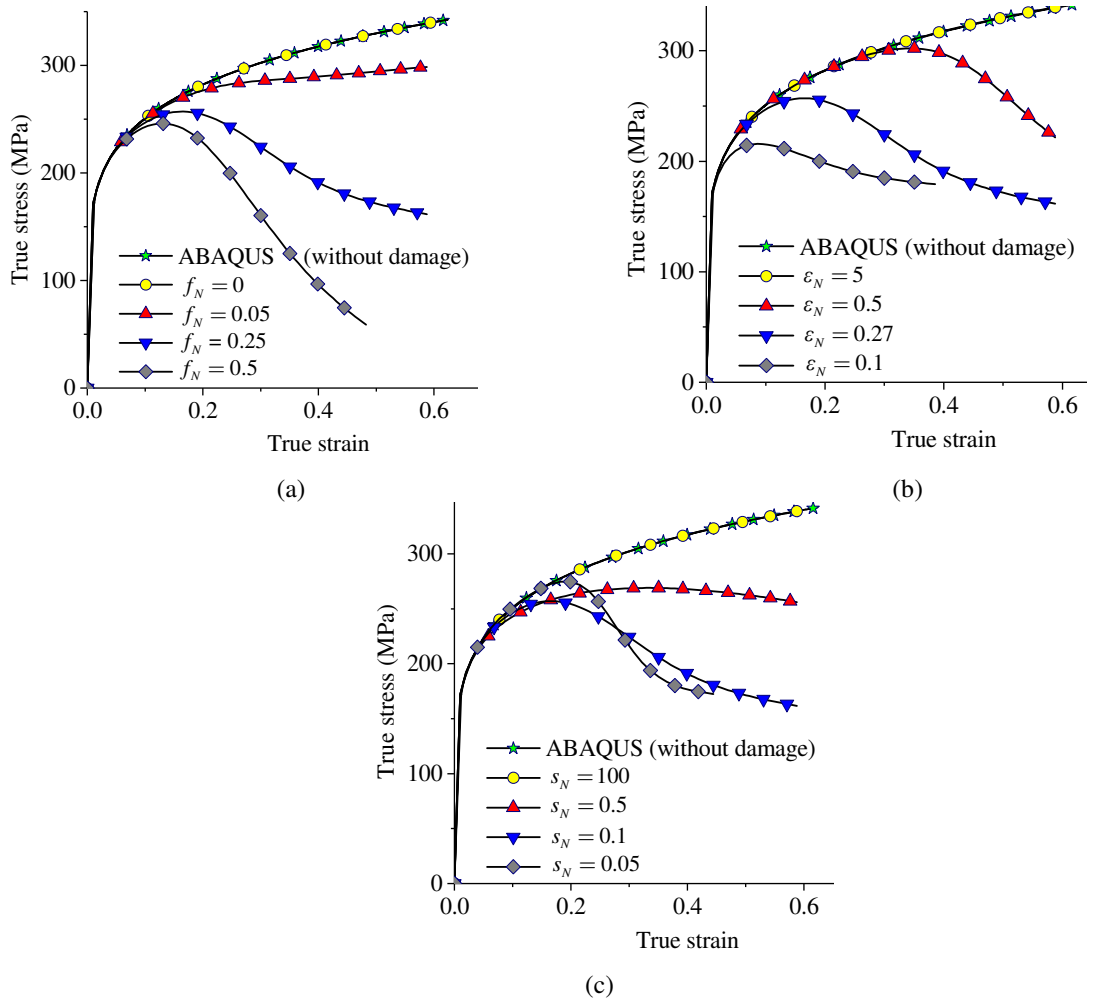

Figure 2.2. Comparisons in terms of true stress–strain curves between the GTN damage model using strain-controlled nucleation (UMAT subroutine) and undamaged isotropic elastic–plastic model (ABAQUS built-in model) under uniaxial tension. Investigation of the effect of void nucleation parameters (a) f_N, (b) ε_N, and (c) s_N.

For stress-controlled nucleation, the reference set of nucleation parameters is reported in Table 2.4. In this sensitivity analysis, f_N, σ_N and s_N are varied, one at a time, while the remaining parameters in Table 2.4 are kept constant. The resulting stress–strain curves for uniaxial tension are presented in Figs. 2.3a, 2.3b and 2.3c, respectively, along with the stress–strain curve corresponding to undamaged isotropic elastic–plastic model. Similar trends are observed when varying the stress-controlled nucleation parameters, as for the case of strain-controlled nucleation parameters, with an undamaged isotropic elastic–plastic material response recovered from stress-controlled nucleation for $f_N = 0$ or for large values of s_N or σ_N.

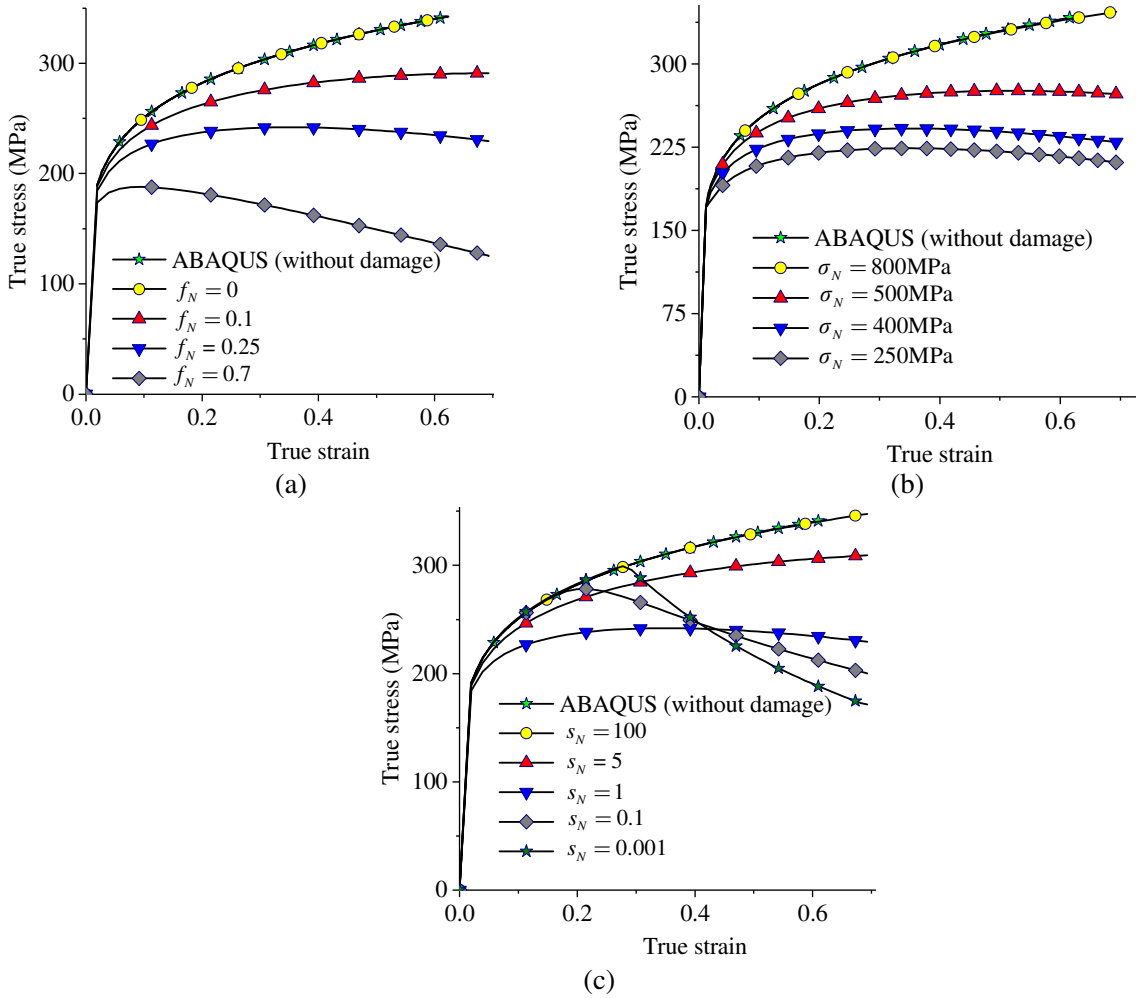

Figure 2.3. Comparisons in terms of true stress–strain curves between the GTN-damage model using stress-controlled nucleation (UMAT subroutine) and undamaged isotropic elastic–plastic model (ABAQUS built-in model) under uniaxial tension. Investigation of the effect of void nucleation parameters (a) f_N, (b) σ_N, and (c) s_N.

2.3.2.2 Validation of Hill'48 anisotropic behavior

In order to account for the plastic anisotropy of the material, the original isotropic GTN plastic yield surface is modified by introducing the Hill'48 equivalent stress instead of the von Mises one (see Eq. (2.1)). In order to validate the numerical implementation of the anisotropic material behavior, the results predicted for uniaxial flow properties, i.e., normalized flow stresses and *r*-values as functions of the tensile angle orientation with respect to the rolling direction, are shown in Fig. 2.4, along with the reference results reported by Neto et al. (2018). These types of numerical results are usually used to identify the anisotropy coefficients of the material. The Hill'48 anisotropy coefficients used in the simulations are listed in Table 2.5. It can be seen from Fig. 2.4 that the predicted results are in excellent agreement with the reference ones, which validates the present implementation for the whole anisotropic behavior (i.e., *r*-values and flow stresses).

Table 2.5. Hill'48 anisotropy coefficients used in the simulations (Neto et al. (2018)).

F	*G*	*H*	*L*	*M*	*N*
0.5688	0.5848	0.4152	1.5	1.5	1.8226

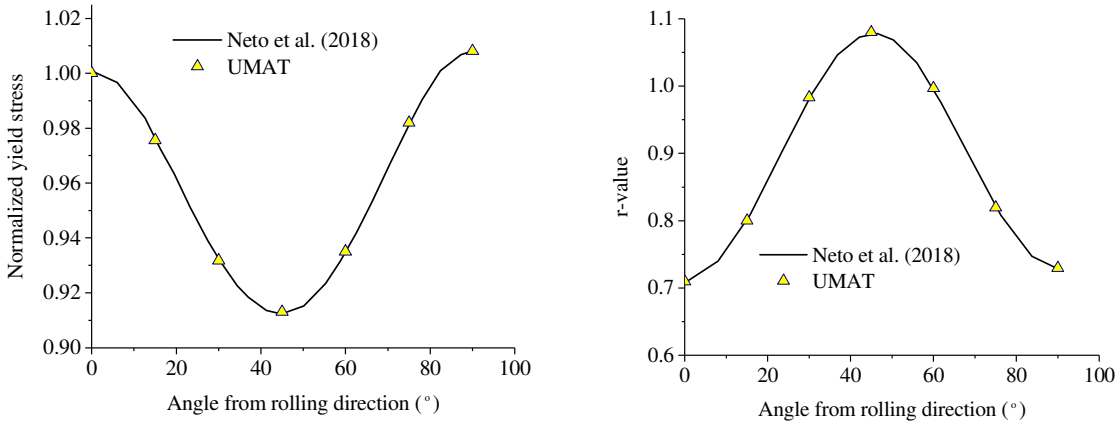

Figure 2.4. Validation of the anisotropic behavior: normalized flow stresses (left), and *r*-values (right) under uniaxial tension.

In addition to the above results, validations in terms of yield locus and stress–strain curves for uniaxial tension tests at 0° and 90° from the rolling direction are also presented Fig. 2.5, which are compared with those obtained with the built-in Hill'48 model available in ABAQUS.

The material parameters used in the simulations are listed in Table 2.6. Again, the numerical results provided by the UMAT subroutine and the built-in ABAQUS model coincide.

Table 2.6. Hill'48 anisotropy coefficients and Voce's hardening parameters used in the simulations.

F	G	H	L	M	N	$\bar{\sigma}_0$(MPa)	R_{sat} (MPa)	C_R
0.7	0.48	0.52	1.5	1.5	1.265	124.2	167	9.5

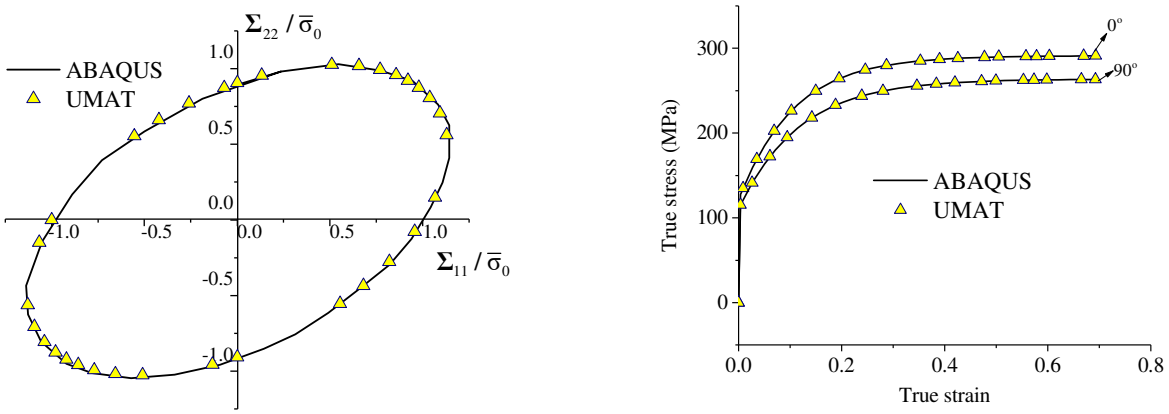

Figure 2.5. Hill'48 normalized yield surface (left), and uniaxial tensile stress–strain curves at 0° and 90° from the rolling direction.

2.4 Prediction of necking using the GTN model and bifurcation criteria

In the present investigation, the GTN elastic–plastic–damage model is coupled with the bifurcation-based plastic instability criteria for the prediction of forming limit diagrams (FLDs). The mathematical foundations of the bifurcation-based plastic instability criteria, as well as their classification in terms of order of prediction of critical necking strains, can be found in Chapter 1.

The nominal stress tensor $\mathbf{N}$, the first Piola–Kirchhoff stress tensor $\mathbf{B}$, and the Cauchy stress tensor $\boldsymbol{\Sigma}$ are related by the following classical relationships:

$$\mathbf{F}\cdot\mathbf{B}^{\mathrm{T}} = J\,\boldsymbol{\Sigma} = \mathbf{F}\cdot\mathbf{N}\,, \tag{2.14}$$

where J is called the Jacobian, defined as the determinant of the deformation gradient $\mathbf{F}$, i.e., $J = \det(\mathbf{F})$. Note that the nominal stress tensor and the first Piola–Kirchhoff stress tensor are the transpose of each other (i.e., $\mathbf{N} = \mathbf{B}^{\mathrm{T}}$). By taking the time derivative of Eq. (2.14) and rearranging, the expression of the nominal stress rate tensor can be evaluated as follows:

$$\dot{\mathbf{N}} = J\mathbf{F}^{-1} \cdot \left(\mathrm{tr}(\mathbf{D})\boldsymbol{\Sigma} + \dot{\boldsymbol{\Sigma}} - \mathbf{G} \cdot \boldsymbol{\Sigma} \right). \tag{2.15}$$

Following an updated Lagrangian approach, i.e., $J = 1$ and $\mathbf{F} = \mathbf{I}$, the expression of the nominal stress rate tensor can be simplified as:

$$\dot{\mathbf{N}} = \dot{\boldsymbol{\Sigma}} + \mathrm{tr}(\mathbf{D})\boldsymbol{\Sigma} - \mathbf{G} \cdot \boldsymbol{\Sigma}. \tag{2.16}$$

For the sake of material objectivity, the Jaumann objective rate of the Cauchy stress tensor has been used in the present work. Therefore, the hypoelastic law for large strains, as defined in Eq. (2.5) using the co-rotational material frame, can be expressed in a fixed reference frame as follows:

$$\dot{\boldsymbol{\Sigma}}^{\mathrm{J}} = \mathbf{C}^{\mathrm{e}} : \left(\mathbf{D} - \mathbf{D}^{\mathrm{p}} \right) = \mathbf{C}^{\mathrm{ep}} : \mathbf{D}, \tag{2.17}$$

where $\dot{\boldsymbol{\Sigma}}^{\mathrm{J}}$ represents the Jaumann objective rate of the cauchy stress tensor, which is defined by the following relationship:

$$\dot{\boldsymbol{\Sigma}}^{\mathrm{J}} = \dot{\boldsymbol{\Sigma}} - \mathbf{W} \cdot \boldsymbol{\Sigma} + \boldsymbol{\Sigma} \cdot \mathbf{W}, \tag{2.18}$$

where $\mathbf{W}$ is the spin tensor, which is defined as the skew-symmetric part of the velocity gradient **G**. Finally, by combining Eqs. (2.16–2.18), the expression of the nominal stress rate tensor can be obtained as:

$$\dot{\mathbf{N}} = \mathbf{C}^{\mathrm{ep}} : \mathbf{D} + \mathrm{tr}(\mathbf{D})\boldsymbol{\Sigma} - \mathbf{D} \cdot \boldsymbol{\Sigma} - \boldsymbol{\Sigma} \cdot \mathbf{W}. \tag{2.19}$$

From the comparison of Eqs. (2.19) and (1.59), the expression of the tangent modulus $\mathbf{L}$ can be derived as:

$$\mathbf{L} = \mathbf{C}^{\mathrm{ep}} + \mathbf{C}_1 - \mathbf{C}_2 - \mathbf{C}_3, \tag{2.20}$$

where the analytical elastic–plastic tangent modulus $\mathbf{C}^{ep}$ is given by Eq. (2.12), while $\mathbf{C}_1$, $\mathbf{C}_2$ and $\mathbf{C}_3$ are composed of convective stress components, which are induced by the large strain framework. Their expressions depend only on Cauchy stress components, and are given by the following expressions:

$$\begin{aligned} C_{1ijkl} &= \Sigma_{ij}\delta_{kl}, \\ C_{2ijkl} &= \frac{1}{2}\left(\Sigma_{jk}\delta_{il} + \Sigma_{jl}\delta_{ik}\right), \\ C_{3ijkl} &= \frac{1}{2}\left(\Sigma_{ik}\delta_{jl} - \Sigma_{il}\delta_{jk}\right), \end{aligned} \tag{2.21}$$

where

$$\delta_{ij} = \begin{cases} 1 & \text{for } i = j \\ 0 & \text{for } i \neq j \end{cases}. \tag{2.22}$$

In order to investigate plastic instabilities that are inherent to the material alone, which exclude all structural (geometric) effects, a single finite element with one integration point (specifically, C3D8R solid element in ABAQUS) is used in the simulations, which results in a homogenous strain state in the material prior to the occurrence of plastic instability. Boundary conditions corresponding to in-plane biaxial stretching are applied to the finite element, in order to generate various proportional loading paths with constant strain-path ratios ranging from uniaxial tension to balanced biaxial tension. The single finite element, specifically C3D8R solid element in ABAQUS, is shown in Fig. 2.6 along with the associated boundary conditions. U_1 and U_2 represent the prescribed displacements along the major and minor directions, respectively. In order to maintain a constant strain-path ratio throughout the loading, the minor displacement U_2 is defined as a function of the major displacement U_1 via a user-defined displacement (DISP) subroutine. The instability criteria are implemented into ABAQUS via a user-defined output variables (UVARM) subroutine. It should be noted that the full GTN damage model is not available in the ABAQUS/Standard finite element code. Indeed, only the Gurson model, including void growth and strain-controlled nucleation mechanisms, is available in ABAQUS/Standard code. Moreover, the non-associative flow rule and stress-controlled

nucleation are not available in ABAQUS/Standard, which has motivated in part our own implementation of the extended GTN model in ABAQUS/Standard via UMAT subroutine. Note that at the end of each loading increment, when the equilibrium condition is satisfied, the updated tangent modulus $\mathbf{C}^{ep}$ as well as the associated internal variables are transferred from the UMAT subroutine to the UVARM subroutine, where the calculations of elastic–plastic tangent moduli (i.e., $\mathbf{L}$ and $\mathbf{L}^{B}$) are performed and the plastic instability criteria are evaluated.

The effects of non-associative plasticity with non-normal plastic flow on the prediction of plastic instabilities are investigated hereafter. The elasticity constants and Ludwig's isotropic hardening parameters for fictitious material used for the simulations are listed in Table 2.7.

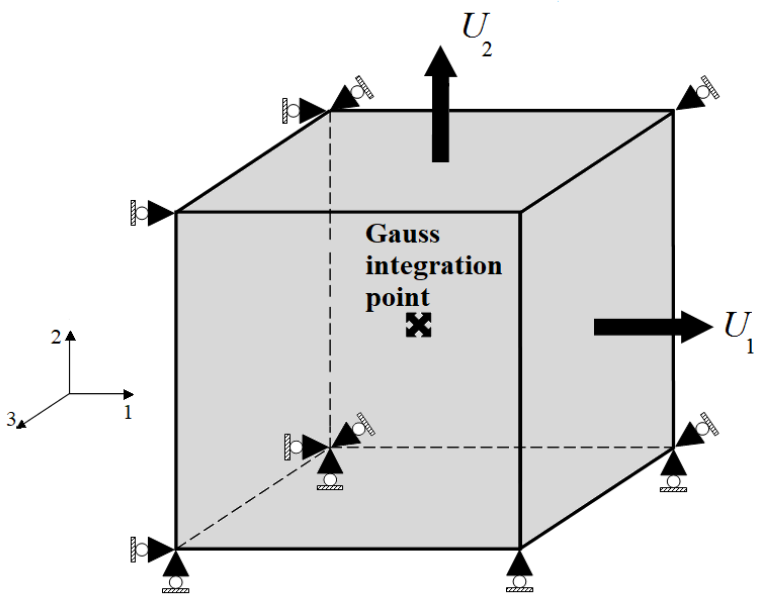

Figure 2.6. Presentation of a single finite element (C3D8R) and the associated boundary conditions.

Table 2.7. Elasticity constants and Ludwig's isotropic hardening parameters.

E (GPa)	ν	K (MPa)	n	$\overline{\sigma}_0$ (MPa)
210	0.3	443.59	0.219	300

2.4.1 Undamaged anisotropic elastic–plastic model

In this section, an undamaged elastic–plastic model with Hill'48 plastic anisotropy is considered for the prediction of FLDs. For this purpose, the initial porosity f_0 and the Gaussian amplitude f_N, involved in the constitutive equations, are set equal to 0. Moreover, the void interaction parameters (i.e., q_1, q_2 and q_3) are set equal to 1. The FLDs are predicted for both cases of associative and non-associative plastic flow rule. The Hill'48 anisotropy parameters for both the yield surface and the plastic potential are listed in Table 2.8.

Table 2.8. Hill'48 anisotropy coefficients for non-associative plasticity.

F_Y	G_Y	H_Y	L_Y	M_Y	N_Y	F_P	G_P	H_P	L_P	M_P	N_P
0.251	0.297	0.703	1.5	1.5	1.29	0.215	0.347	0.653	1.5	1.5	1.32

Fig. 2.7 shows the corresponding FLDs predicted by using the four bifurcation criteria. Note that, strain localization does not occur in the right-hand side of the FLD (i.e., for positive biaxial strain-path ratios). Indeed, in the works of Mansouri et al. (2014) and Chalal and Abed-Meraim (2015), it has been shown that, using the bifurcation theory along with phenomenological models and smooth yield surface, the occurrence of strain localization for positive biaxial strain-path ratios requires the critical hardening modulus to be strongly negative, which can be achieved by the consideration of damage induced softening. Moreover, from the comparison of Fig. 2.7a and Fig. 2.7b, it can be clearly observed that the consideration of non-associative plasticity, which results in a non-symmetric analytical elastic–plastic tangent modulus, leads to the prediction of quite distinct necking limit strains for the four bifurcation-based plastic instability criteria.

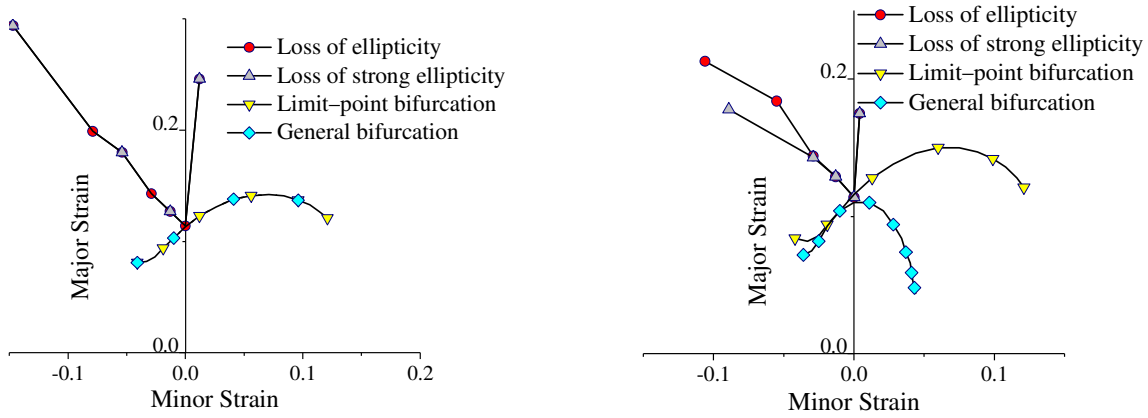

Figure 2.7. FLDs predicted by the four bifurcation-based instability criteria coupled with the undamaged elastic–plastic model. Case of associative plasticity (left) and case of non-associative plasticity (right).

2.4.2 Associative plasticity

2.4.2.1 Case of strain-controlled nucleation

In this section, the GTN damage model with strain-controlled nucleation and associative plasticity is considered for the prediction of FLDs. Void nucleation amplitudes are $A_N > 0$ and $B_N = 0$. In this case of associative plasticity, the plastic potential Φ_P is taken the same as the yield surface Φ_Y, which leads to the classical normal plastic flow rule. This implies that:

$$\mathbf{M} = \frac{\partial \Phi_Y}{\partial \boldsymbol{\Sigma}} = \frac{\partial \Phi_P}{\partial \boldsymbol{\Sigma}} = \mathbf{V}_p \tag{2.23}$$

and

$$\mathbf{C}^{ep} = \mathbf{C}^{e} - \tau \frac{\left(\mathbf{C}^{e} : \mathbf{M}\right) \otimes \left(\mathbf{M} : \mathbf{C}^{e}\right)}{H_\lambda} \tag{2.24}$$

It is interesting to note that the analytical elastic–plastic tangent modulus $\mathbf{C}^{ep}$ becomes symmetric in this special case. However, the localization tangent modulus $\mathbf{L}$ remains non-symmetric, since large strain framework in considered, which involves non-zero values of convective stress components. The GTN damage parameters used in the simulations, which

correspond to two fictitious materials, i.e. M1 and M2, are reported in Table 2.9. The Hill'48 anisotropy parameters for both materials are $F = G = H = 0.5$ and $L = M = N = 1.5$, which corresponds to von Mises isotropic plasticity.

Table 2.9. GTN damage parameters for strain-controlled nucleation.

Material	f_0	f_N	ε_N	s_N	q_1	q_2	q_3	f_{cr}	δ_{GTN}
M1	0.01	0.1	0.3	1.5	1.5	1	2.15	0.0601	20
M2	0.02	0.2	0.35	1.5	1.5	1	2.15	0.04	22

Figure 2.8 shows the predicted FLDs for the studied materials M1 and M2, using the four instability criteria. It is noteworthy that only two distinct FLDs are observed, which correspond to diffuse necking (predicted by GB and LPB criteria), and localized necking (predicted by LOSE and LOE criteria). Similar results have been reported by Abed-Meraim et al. (2014) and Bouktir et al. (2018), using the CDM approach and associative plasticity. The reason behind this observation is that the non-symmetric part of the tangent modulus $\mathbf{L}$, which is due to the convective stress components, is not significant enough to provide separate FLDs for localized necking (as predicted by LOE and LOSE criteria), and diffuse necking (as predicted by GB and LPB criteria). Nevertheless, the theoretical classification established in the previous section is well respected. More specifically, the GB criterion represents a lower bound to all the bifurcation criteria, in terms of necking prediction, while the LOE criterion provides an upper bound.

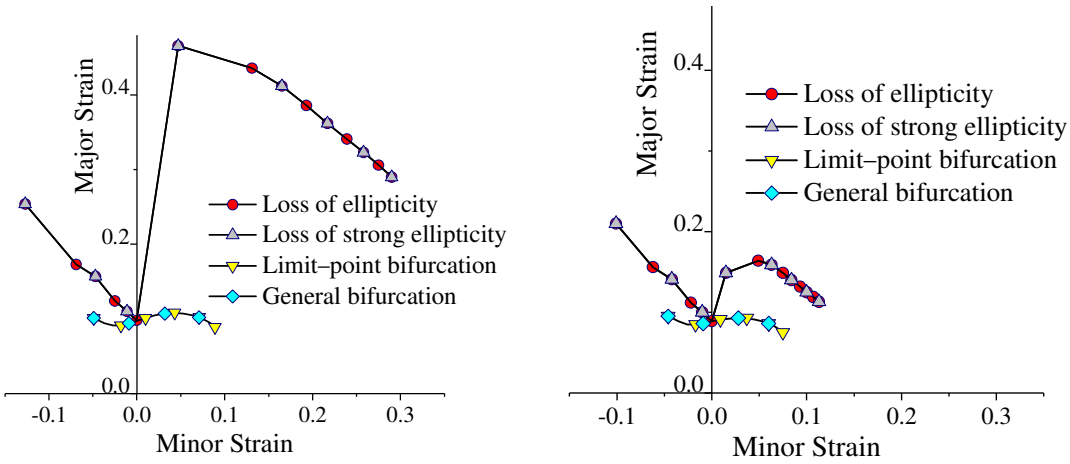

Figure 2.8. FLDs predicted by the four bifurcation-based instability criteria coupled with the GTN damage model and strain-controlled nucleation. Case of associative plasticity: material M1 (left), and material M2 (right).

In order to further analyze the above predictions, the true stress–strain curves and the porosity evolution curves are plotted in Fig. 2.9, for three strain loading paths corresponding to uniaxial tension (UT), plane-strain tension (PST), and balanced biaxial tension (BBT). Note that, for conciseness, only results corresponding to material M1 are shown. It can be seen, from the comparison of the strain levels involved in Figs. 2.8 and 2.9, that diffuse necking, predicted by the GB and LPB criteria, takes place in the positive hardening regime, well before the onset of the coalescence stage for the three strain loading paths. With regard to localized necking, the latter also occurs in the positive hardening regime for the UT and PST loading paths, while negative hardening modulus is required for the BBT loading path. These observations are consistent with the available literature.

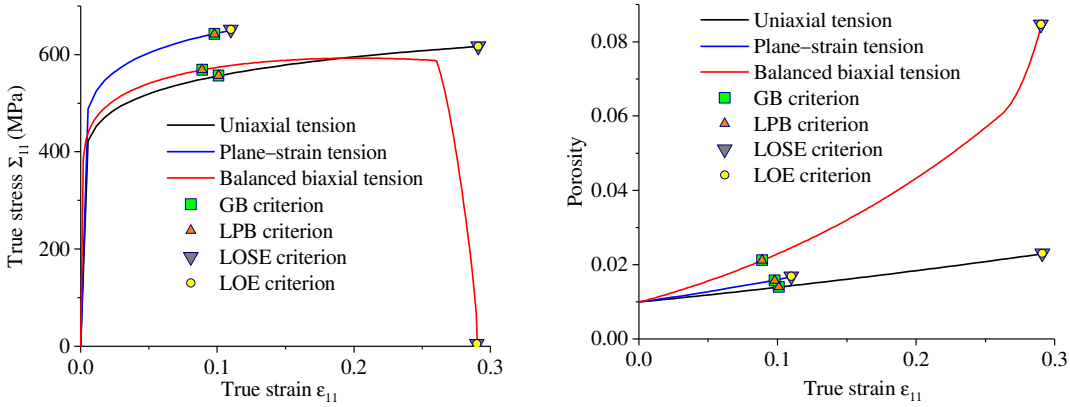

Figure 2.9. True stress–strain curves (left) and porosity evolution (right), for material M1 under UT, PST and BBT, using the GTN damage model with strain-controlled nucleation and associative plasticity.

2.4.2.2 Case of stress-controlled nucleation

In this section the GTN damage model with stress-controlled nucleation and associative plasticity is considered. In this case, the void nucleation amplitudes are $A_N = 0$ and $B_N > 0$. Note that the yield surface and the plastic potential are similar, i.e., $\Phi_Y = \Phi_P$. However, the stress-controlled nucleation leads to some sort of non-normality in the plastic flow, which results in a non-symmetric analytical elastic–plastic tangent modulus $\mathbf{C}^{ep}$ (see Eq. (2.12)). The GTN damage parameters for fictitious material used in the simulations are summarized in Table 2.10.

Table 2.10. GTN damage parameters for stress-controlled nucleation.

f_0	f_N	σ_N (MPa)	s_N	q_1	q_2	q_3	f_{cr}	δ_{GTN}
0.01	0.1	850	1.5	1.5	1	2.15	0.0601	20

Figure 2.10 depicts the FLDs predicted by the four bifurcation-based instability criteria, where four distinct FLDs are obtained. Indeed, in contrast to the first studied case of strain-controlled nucleation and associative plasticity, the predicted limit strains are well distinct in the left-hand side of the FLDs, for diffuse necking criteria (i.e., GB and LPB) as well as for localized necking criteria (i.e., LOSE and LOE). However, in the right-hand side of the FLDs, the limit strains coincide for both localized necking criteria, which has been also observed in the case of strain-controlled nucleation and associative plasticity. Note that the GB and LPB criteria predict the occurrence of diffuse necking at different limit strains for all of the strain paths considered, except for the BBT strain path loading, where the limit strains coincide for both diffuse necking criteria. On the whole, the hierarchical order of the FLDs is well respected with regard to the established theoretical one (see Section 1.5).

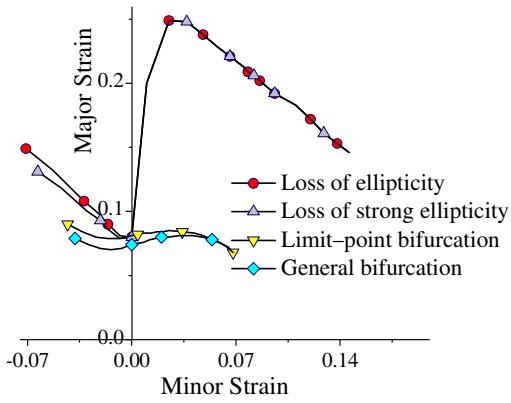

Figure 2.10. FLDs predicted by the four bifurcation-based instability criteria coupled with the GTN damage model and stress-controlled nucleation. Case of associative plasticity.

In order to provide better insight into the plastic instability phenomena for the four bifurcation theories, Fig. 2.11 exhibits the logarithmic plots for minimum values of determinants of the acoustic tensor $\mathbf{Q}$, tangent modulus $\mathbf{L}^{B}$, and their symmetric parts ($\mathbf{Q}^{sym}$ and $\mathbf{L}^{B^{sym}}$, respectively), for three typical strain loading paths i.e., UT, PST, and BBT. The non-bifurcation condition according to the GB criterion requires all the eigenvalues of the symmetric part of the

tangent modulus $\mathbf{L}^{\mathrm{B}^{\mathrm{sym}}}$ to be positive. This condition amounts here to the positiveness of the determinant of the tangent modulus $\mathbf{L}^{\mathrm{B}^{\mathrm{sym}}}$. Similarly, the non-localization condition given by the LOSE criterion requires positive definiteness of the acoustic tensor $\mathbf{Q}$, which implies that, for a non-localization state, $\det\left(\mathbf{Q}^{\mathrm{sym}}\right) > 0$. Recalling also that LPB and LOE predict diffuse and localized necking, respectively, when $\det\left(\mathbf{L}^{\mathrm{B}}\right) = 0$ and $\det\left(\mathbf{Q}\right) = 0$. Therefore, the different bifurcation criteria predict plastic instability when their associated minimum determinant of the tensor quantity, as discussed above, tends to zero (see Fig. 2.11).

It is interesting to note that, when the tangent modulus $\mathbf{L}^{\mathrm{B}}$ is symmetric, or when the non-symmetric part is negligibly small, then $\mathbf{L}^{\mathrm{B}} \approx \mathbf{L}^{\mathrm{B}^{\mathrm{sym}}}$ and $\mathbf{Q} \approx \mathbf{Q}^{\mathrm{sym}}$. In this case, the GB and the LOSE criteria become equivalent to the LPB and the LOE criteria, respectively (see Fig. 2.8). However, in Fig. 2.11, since the tangent modulus $\mathbf{L}^{\mathrm{B}}$ is non-symmetric, it can be clearly seen that the occurrence of plastic instabilities with the GB and the LOSE criteria can be predicted earlier than the LPB and the LOE criteria, respectively.

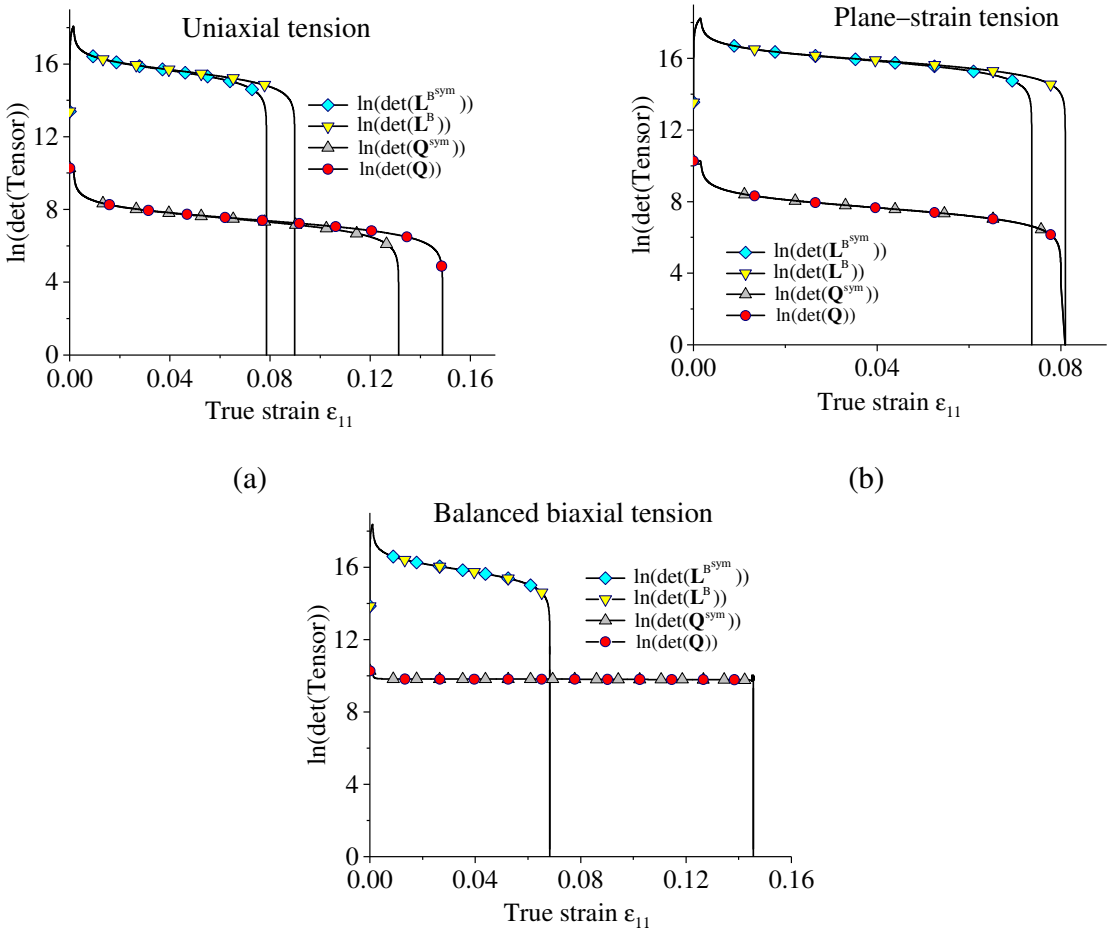

Figure 2.11. Logarithmic plots of minimum determinants of the tangent modulus $\left(\mathbf{L}^{\mathrm{B}}\right)$, acoustic tensor $\mathbf{Q}$, and their symmetric parts ($\mathbf{L}^{\mathrm{B}^{\mathrm{sym}}}$ and $\mathbf{Q}^{\mathrm{sym}}$) for (a) uniaxial tension, (b) plane-strain tension, and (c) balanced biaxial tension.

2.4.3 Non-associative plasticity

2.4.3.1 Case of strain-controlled nucleation

In this subsection, non-associative plasticity is coupled with the GTN damage model using the Hill'48 plastic anisotropy. With this consideration, the analytical elastic–plastic tangent modulus $\mathbf{C}^{\mathrm{ep}}$ is non-symmetric (see Eq. (2.12)), with the following relation for tensor $\mathbf{M}$:

$$\mathbf{M} = \frac{\partial \Phi_{\mathrm{Y}}}{\partial \boldsymbol{\Sigma}}. \tag{2.25}$$

In this section, only one material is simulated, which corresponds to the fictitious material M1 used in the previous section (see Tables 2.7 and 2.9 for the elasto-plasticity and damage material parameters, respectively). The Hill'48 anisotropy parameters for both the yield function and the plastic potential surface are reported in Table 2.8.

The predicted FLDs using the non-associative GTN damage model with strain-controlled nucleation are shown in Fig. 2.12. It can be observed that the consideration of non-associative plasticity, which results in a non-symmetric analytical elastic–plastic tangent modulus, leads to the prediction of quite distinct necking limit strains for the four bifurcation-based instability criteria. More specifically, in the left-hand side of the FLDs, the lowest and highest ductility limits are predicted by GB criterion and LOE criterion, respectively. LOSE criterion appears to be more conservative than the LOE criterion, while the LPB criterion is less conservative than the GB theory. In the right-hand side of the FLDs, the order of prediction for diffuse necking is similar to that obtained in the left-hand side of the FLDs, while for both LOSE and LOE criteria, the same limit strains for localized necking are predicted. Overall, this hierarchical order of the predicted FLDs is well consistent with the theoretical classification (see Section 1.5).

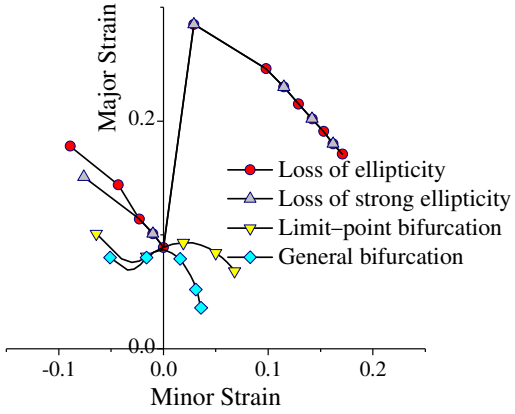

Figure 2.12. FLDs predicted by the four bifurcation-based instability criteria coupled with the GTN damage model and strain-controlled nucleation. Case of non-associative plasticity.

As to the stress–strain curves and porosity evolution, Fig. 2.13 depicts the material responses for three typical strain paths: UT, PST and BBT. The obtained curves are similar to the case of associative plasticity, with the occurrence of localized necking in the positive hardening

regime for the UT and PST loading paths, while for the BBT loading path, negative hardening modulus is required for localized necking.

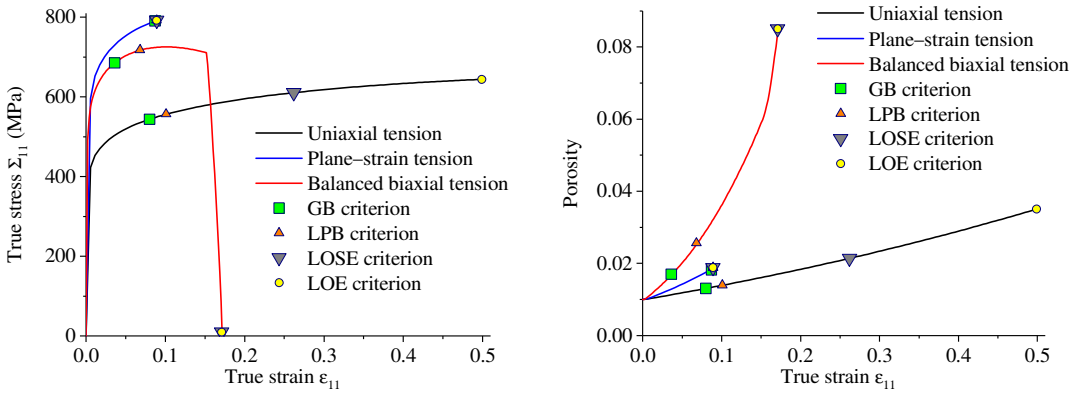

Figure 2.13. True stress–strain curves (left) and porosity evolution (right), under UT, PST and BBT, using the GTN damage model with strain-controlled nucleation and non-associative plasticity.

2.4.3.2 Case of stress-controlled nucleation

In this section, two destabilizing mechanisms are combined simultaneously within the constitutive equations, i.e., non-associative plasticity and stress-controlled nucleation, which induce some sort of non-normality in the plastic flow. More specifically, the anisotropic GTN damage model with stress-controlled nucleation is coupled with the four bifurcation theories for the prediction of FLDs. Moreover, the yield surface and the plastic potential are different with regard to the Hill'48 anisotropy coefficients. The anisotropy coefficients for the yield surface and the plastic potential as well as the GTN damage parameters used in the simulations are those used in the previous sections (see Tables 2.8 and 2.10). The FLDs predicted by the resulting approach are shown in Fig. 2.14. In the left-hand side of the FLDs, the consideration of both mechanisms, i.e., non-associative plasticity and stress-controlled nucleation, seems not to destabilize the prediction of diffuse and localized necking, as in the case of associative plasticity and strain-controlled nucleation (see Fig. 2.8). However, in the right-hand side of the FLDs, these destabilizing mechanisms lead to distinct limit strains for diffuse necking criteria (i.e., GB and LPB). Similar to the previous combinations of destabilizing mechanisms, the hierarchical order

of prediction of FLDs, in this case, is once again well consistent with regard to the established theoretical one (see Section 1.5).

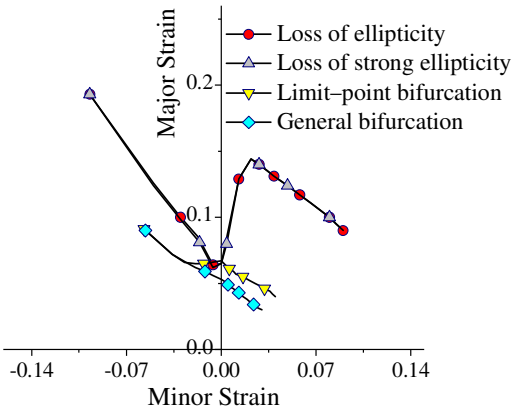

Figure 2.14. FLDs predicted by the four bifurcation-based instability criteria coupled with the GTN damage model and stress-controlled nucleation. Case of non-associative plasticity.

2.4.4 Comparison of associative and non-associative plasticity

In this section, the FLDs predicted by the associative GTN damage model (AFR GTN) are compared to those obtained using the non-associative GTN damage model (NAFR GTN), in the case of strain-controlled nucleation. Note that, from Fig. 2.15, the FLDs predicted by considering the NAFR GTN damage model are lower than those predicted by the AFR GTN damage model for all strain paths. The reason behind this observation is that the introduction of NAFR in the constitutive model brings more destabilizing effects, which promotes early occurrence of plastic instability.

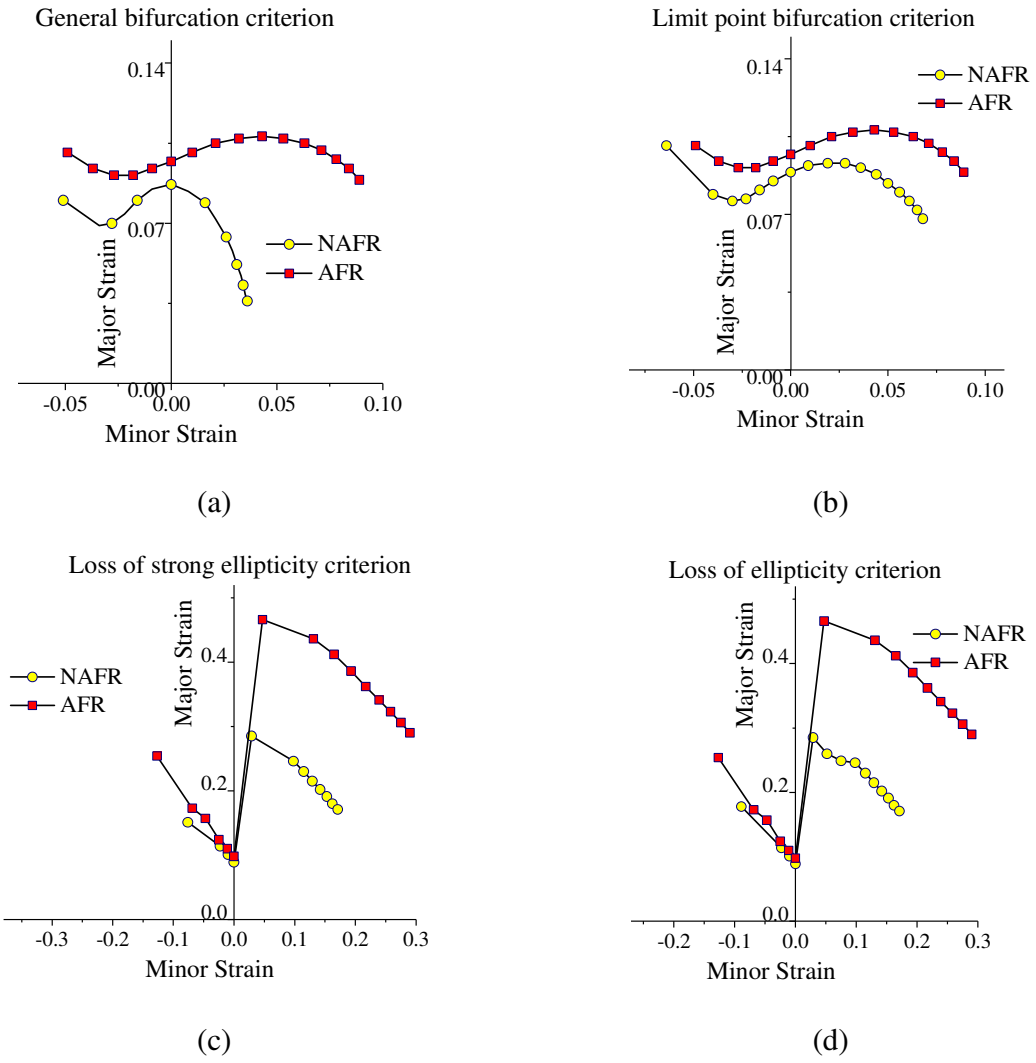

Figure 2.15. Comparison of the FLDs predicted by the associative and non-associative GTN damage model with strain-controlled nucleation and (a) GB criterion, (b) LPB criterion, (c) LOSE criterion and (d) LOE criterion.

2.4.5 Orientations of the localization bands

The orientation of the localization band, as predicted by LOSE and LOE criteria, is investigated in this section. Note that the band orientation is only defined by a single in-plane angle, since the framework of plane-stress conditions is adopted in this work (see Fig. 1.31). Fig. 2.16 shows the orientations of the localization bands, as predicted by LOSE and LOE criteria for different values of the strain-path ratio. The localization band orientations are also compared with the analytical band orientations given by the Hill (1952) localized necking criterion. For the

considered variants of the GTN model, it can be seen that the predicted localization band orientations are in excellent agreement with the Hill'52 analytical formula (i.e., $\theta = \tan^{-1}\left(\sqrt{-\rho}\right)$, where ρ is the strain-path ratio), for both LOSE and LOE criteria. It is worth noting that because the Hill'52 criterion is only applicable to the left-hand side of the FLD, the comparison in the range of positive biaxial stretching (i.e., $\rho > 0$) only involves the LOSE and LOE criteria, which predict equivalent band orientations.

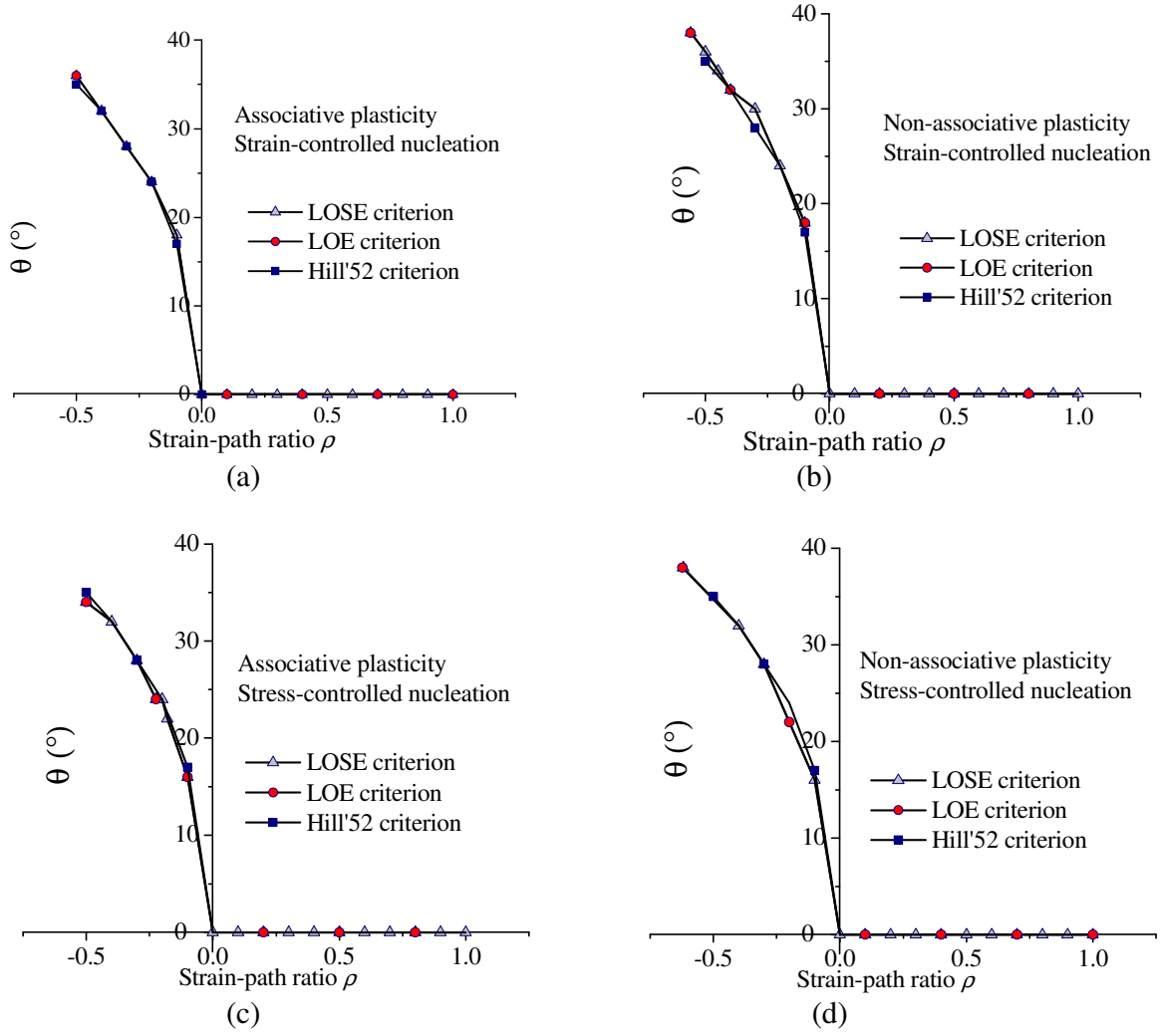

Figure 2.16. Orientations of the localization bands, predicted with the LOSE, LOE and Hill'52 localized necking criteria.

2.5 Conclusion

In this chapter, the GTN damage model has been coupled with four bifurcation-based plastic instability criteria for the prediction of forming limit diagrams. Two of these plastic instability criteria, i.e., general bifurcation criterion (GB) and limit-point bifurcation criterion (LPB), predict diffuse necking; whereas the two others, i.e., loss of strong ellipticity criterion (LOSE) and loss of ellipticity criterion (LOE), predict localized necking. The constitutive equations together with the four plastic instability criteria have been implemented into the finite element code ABAQUS/standard via user-defined material behavior (UMAT) and user-defined output variables (UVARM) subroutines. The constitutive equations have been formulated in a fully three-dimensional framework; however, plane-stress conditions have been considered while applying the plastic instability criteria, since the intended application of the present contribution is the prediction of ductility limits in thin sheet metals. Various linear strain loading paths, corresponding to in-plane biaxial stretching, have been applied on a single finite element so that all structural (geometric) instabilities are excluded. These strain loading paths cover different loading conditions, including uniaxial tension, plane-strain tension, and balanced biaxial tension, for the purpose of predicting FLDs.

Two destabilizing mechanisms have been introduced within the constitutive equations, i.e., non-associative plasticity and stress-controlled nucleation inducing some sort of non-normality in the plastic flow. First, the FLDs have been predicted by the GTN damage model with strain-controlled nucleation and associative plasticity. The analytical elastic–plastic tangent modulus is symmetric in this case, while the localization tangent modulus is non-symmetric due to the large strain framework. In this case, the GB and the LPB criteria predict the same critical strains for diffuse necking, while the LOSE and LOE criteria predict the same limit strains for localized necking. Then, stress-controlled nucleation is considered, which results in a non-symmetric analytical elastic–plastic tangent modulus. For this case, the GB criterion predicts limit strains lower than those obtained with the LPB criterion for all of the strain loading paths considered except balanced biaxial tension. As to localized necking, the LOSE criterion predicts limit strains lower than the LOE criterion only for the left-hand side of the FLD, while both LOSE and LOE predictions coincide for the right-hand side of the FLD. Similar destabilizing effects on diffuse and localized necking have also been observed when considering non-associative plasticity.

Throughout all studied cases, the hierarchical order of the predicted FLDs has been shown to be consistent with the preliminarily established theoretical classification, which states that the GB criterion is a lower bound to all the bifurcation criteria, in terms of necking prediction, while the LOE criterion provides an upper bound.

Chapter 3

Comparative analysis between the M–K imperfection approach and the loss of ellipticity criterion

3.1 Introduction

In the previous Chapter 2, the critical limit strains were predicted using bifurcation-based plastic instability criteria, while in the present Chapter, the prediction of FLDs is based on the Marciniak and Kuczyński (M–K) imperfection approach. The latter is combined with the Gurson–Tvergaard–Needleman (GTN) damage model. The M–K imperfection approach is implemented into the MATLAB program within the framework of plane-stress conditions. FLDs are predicted by assuming both geometric (thickness) as well as material initial imperfections in the M–K approach. An analogy is established between the M–K imperfection approach and the loss of ellipticity (Rice's bifurcation) criterion for the prediction of localized necking in thin sheet metals. Moreover, FLDs for a real AA2024 aluminum material are determined by using different types of initial imperfections in the M–K approach and compared with experimental results.

The remainder of the present Chapter is organized as follows. First, the M–K imperfection approach for the prediction of localized necking is presented. Then, a theoretical link is established between the M–K approach and the Rice bifurcation theory. Following this, the numerical implementation and validations of the developed numerical tool in presented. Finally, the numerical results in terms of FLDs are presented and discussed.

3.2 M–K imperfection approach for localized necking

In this section, the Marciniak and Kuczyński (M–K) imperfection approach (see Marciniak and Kuczyński, 1967) which is used hereafter for the prediction of localized necking in thin sheet metals, is presented under the plane-stress framework. In this approach, an initial imperfection is assumed within the sheet in the form of a narrow band. The initial imperfection may be taken as a narrow band of reduced thickness (considered here as geometric imperfection), an imperfection band with slightly degraded mechanical properties (considered here as material imperfection), or

the combination of both geometric and material imperfections. In the original M–K imperfection approach), the imperfection band has been assumed perpendicular to the major principal stress axis, which ultimately leads to unrealistically high values of forming limit strains on the left-hand side of the FLD (i.e., negative minor strains). However, experimental observations have shown that the localization band is not perpendicular to the major principal stress axis for the strain paths that cover the left-hand side of the FLD. Therefore, Marciniak (1968) introduced the band inclination angle, which enables the M–K model to predict realistic limit strains on the left-hand side of the FLD. In this enhanced approach, the normal to the imperfection band is assumed at an angle θ_0 from the major principal stress axis. The initial orientation θ_0 of the localization band is searched in the plane of the sheet metal in order to minimize the limit strains. Since the imperfection band is considered weaker than the homogeneous zone, therefore during in-plane biaxial stretching, the strains in the imperfection band always remain larger than those in the homogeneous zone. At a critical loading point, the plastic strains in the imperfection band evolve drastically as compared to those in the homogeneous zone. Localization is assumed to take place when the ratio of equivalent plastic strain rate inside the imperfection band to the homogeneous zone, i.e., $\dot{\bar{\varepsilon}}^{pB} / \dot{\bar{\varepsilon}}^{pH}$, exceeds a critical value. The latter is commonly set equal to 10 in the literature.

Fig. 3.1 depicts the schematic illustration of the imperfection band present inside the homogeneous zone. Both material and geometric imperfections are illustrated in Fig. 3.1. The material imperfection is represented in this figure by an increased void volume fraction inside the imperfection band, while the geometric imperfection is represented by a reduced thickness of the imperfection band. The initial geometric imperfection factor is defined as:

$$f_0 = \frac{h_i^B}{h_i^H}, \tag{3.1}$$

where the superscripts *B* and *H* represent the quantities inside and outside the imperfection band, respectively. The key components of M–K imperfection approach are as follows:

- Definition of the constitutive equations for both zones.
- Kinematic compatibility of strains between the imperfection band and the homogeneous zone.
- The equilibrium of forces across the imperfection band.

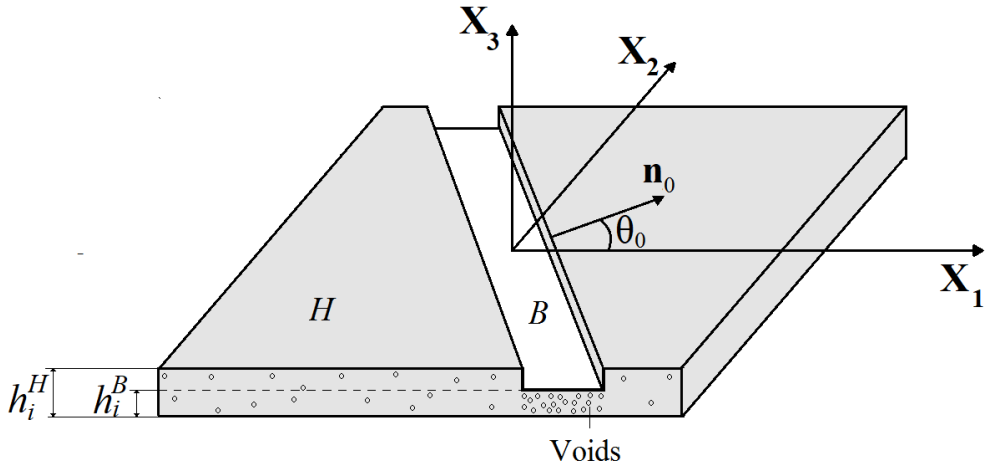

Figure 3.1. Schematic representation of the initial imperfection band in the M–K imperfection approach.

In the present Chapter, the elastic–plastic–damage GTN model, presented in the previous Chapter 2, is assumed to be applicable for both zones *H* and *B*. Following the condition of kinematic compatibility, the velocity gradients in the imperfection band $\mathbf{G}^B$ and in the homogeneous zone $\mathbf{G}^H$ are related as:

$$\mathbf{G}^B = \mathbf{G}^H + \dot{\boldsymbol{\gamma}} \otimes \mathbf{n}, \tag{3.2}$$

where $\dot{\boldsymbol{\gamma}}$ is the jump amplitude vector, and $\mathbf{n}$ is the unit vector normal to the imperfection band. The homogeneous zone is subjected to various linear strain paths under in-plane biaxial stretching for the prediction of FLD. The strain-path ratio is defined as:

$$\rho = \frac{\dot{\varepsilon}_{22}^H}{\dot{\varepsilon}_{11}^H} = \frac{G_{22}^H}{G_{11}^H} \;\; ; \;\; -0.5 \le \rho \le 1, \tag{3.3}$$

where the particular values $\rho = -0.5$ and $\rho = 1$ represent the uniaxial tension and balanced biaxial tension, respectively. Therefore, the velocity gradient tensor in the homogeneous zone is given as:

$$\mathbf{G}^H = \begin{bmatrix} \dot{\varepsilon}_{11}^H & 0 & 0 \\ 0 & \rho\,\dot{\varepsilon}_{11}^H & 0 \\ 0 & 0 & G_{33}^H \end{bmatrix}. \tag{3.4}$$

By substituting Eq. (3.4) into Eq. (3.2), the velocity gradient tensor inside the imperfection band is calculated as:

$$\mathbf{G}^B = \begin{bmatrix} \dot{\varepsilon}_{11}^H + \dot{\gamma}_1 \mathrm{n}_1 & \dot{\gamma}_1 \mathrm{n}_2 & 0 \\ \dot{\gamma}_2 \mathrm{n}_1 & \rho\,\dot{\varepsilon}_{11}^H + \dot{\gamma}_2 \mathrm{n}_2 & 0 \\ 0 & 0 & G_{33}^B \end{bmatrix}. \tag{3.5}$$

The components G_{33}^H and G_{33}^B of the velocity gradients are calculated so that the plane-stress conditions (i.e., $\Sigma_{33}^H = 0$ and $\Sigma_{33}^B = 0$) are satisfied. The equilibrium of forces across the imperfection band can be expressed by the following equation:

$$\left(\mathrm{f}\,\boldsymbol{\Sigma}^B - \boldsymbol{\Sigma}^H\right) \cdot \mathbf{n} = \mathbf{0}, \tag{3.6}$$

where "f" is the value of the geometric imperfection factor in the deformed configuration, which can be calculated as:

$$\mathrm{f} = \frac{h^B}{h^H} = \frac{h_i^B e^{\varepsilon_{33}^B}}{h_i^H e^{\varepsilon_{33}^H}} = \mathrm{f}_0 e^{\varepsilon_{33}^B - \varepsilon_{33}^H}, \tag{3.7}$$

where f_0 is the initial value of the geometric imperfection factor.

Note that the imperfection band rotates during the applied loading. The evolution of the band inclination angle θ is given according to Nanson's formula:

$$\tan(\theta) = \tan(\theta_0)\, e^{\varepsilon_{11}^H - \varepsilon_{22}^H}, \tag{3.8}$$

where θ_0 is the initial orientation of the imperfection band with respect to the global axis.

3.2.1 Analogy between the M–K imperfection approach and Rice's bifurcation criterion

In this subsection, a theoretical link is established between the M–K imperfection approach and the Rice bifurcation criterion. By following an updated Lagrangian approach, the equilibrium equation stated in Eq. (3.6) can be rewritten in the following equivalent rate form:

$$\mathbf{n}\cdot\left(\mathrm{f}\,\dot{\mathbf{N}}^{B}-\dot{\mathbf{N}}^{H}\right)=\mathbf{0}, \tag{3.9}$$

where $\dot{\mathbf{N}}$ is the nominal stress rate tensor, which is related to the velocity gradient tensor $\mathbf{G}$ as follows:

$$\dot{\mathbf{N}}=\mathbf{L}:\mathbf{G}, \tag{3.10}$$

where $\mathbf{L}$ is a fourth-order tangent modulus, which is related to the elastic–plastic tangent modulus $\mathbf{C}^{\mathrm{ep}}$ by Eq. (2.20). The elastic–plastic tangent modulus $\mathbf{C}^{\mathrm{ep}}$ for the GTN damage model is given by Eq. (2.12).

By substituting Eq. (3.10) into Eq. (3.9), the equilibrium equations can be written in terms of the velocity gradients:

$$\mathbf{n}\cdot\left(\mathrm{f}\left(\mathbf{L}^{B}:\mathbf{G}^{B}\right)-\left(\mathbf{L}^{H}:\mathbf{G}^{H}\right)\right)=\mathbf{0}. \tag{3.11}$$

Finally, by considering the compatibility condition given by Eq. (3.2), the above equation can be expanded as:

$$\mathbf{n}\cdot\left[\left(\mathrm{f}\,\mathbf{L}^{B}-\mathbf{L}^{H}\right):\mathbf{G}^{H}\right]+\mathrm{f}\left(\mathbf{n}\cdot\mathbf{L}^{B}\cdot\mathbf{n}\right)\cdot\dot{\boldsymbol{\gamma}}=\mathbf{0}. \tag{3.12}$$

In the case when no material imperfection is introduced, and in the absence of geometric imperfection (i.e., $\mathrm{f}=\mathrm{f}_0=h_i^B/h_i^H=1$), meaning that the material properties within the band remain identical to those in the homogeneous zone (i.e., $\mathbf{L}^B=\mathbf{L}^H=\mathbf{L}$), Eq. (3.12) simplifies to:

$$\left(\mathbf{n}\cdot\mathbf{L}\cdot\mathbf{n}\right)\cdot\dot{\boldsymbol{\gamma}}=\mathbf{0}. \tag{3.13}$$

The non-trivial solution for Eq. (3.13) corresponds to the Rice loss of ellipticity criterion. More specifically, the critical condition for bifurcation, which corresponds to the occurrence of localized necking, can be expressed as the singularity of the acoustic tensor $\mathbf{Q} = \mathbf{n} \cdot \mathbf{L} \cdot \mathbf{n}$:

$$\det\left(\mathbf{Q}\right) = \det\left(\mathbf{n} \cdot \mathbf{L} \cdot \mathbf{n}\right) = 0 . \tag{3.14}$$

Therefore, from the above equations, it can be concluded that when no geometric and material imperfections are considered, the M–K imperfection approach becomes equivalent to the Rice bifurcation criterion.

3.2.2 Numerical implementation and validations

The resulting numerical tool by coupling the GTN damage model with the M–K imperfection approach is implemented into MATLAB user subroutines for the prediction of FLDs. The homogeneous zone of the sheet metal, as illustrated in Fig. 3.1, is subjected to proportional in-plane biaxial strains, with a strain-path ratio ρ. For each strain-path ratio considered between –0.5 and 1, the initial band orientation angle θ_0 is varied from 0° to 90°. For the given values of the initial band angle θ_0 and the strain-path ratio ρ, the stress–strain as well as the internal variables are updated for each loading increment, according to an explicit time integration scheme. The simulation is stopped when the ratio of equivalent plastic strain rate inside the imperfection band to the homogeneous zone (i.e., $\dot{\bar{\varepsilon}}^{pB} / \dot{\bar{\varepsilon}}^{pH}$) exceeds the threshold value of 10. The corresponding values of the principal strains in the homogeneous zone, i.e. ε_{11}^{H} and $\varepsilon_{22}^{H} = \rho\varepsilon_{11}^{H}$, are the critical strains for the selected value of θ_0. This procedure is repeated for all possible values of the initial band angle θ_0, and the smallest values of the critical strains are considered as the forming limit strains for the considered strain-path ratio ρ. Note that the numerical simulations are considered to be strain driven. The equivalent plastic strain rate inside the imperfection band is considered as a prescribed quantity and, throughout the loading, its value is set equal to 1:

$$\dot{\bar{\varepsilon}}^{pB} - 1 = 0 . \tag{3.15}$$

All of the variables at the beginning and at the end of the loading increment are designated with subscript "n" and "n+1", respectively. The evolution of the geometric imperfection factor and the imperfection band angle (see Eqs. (3.7)-(3.8)) can be expressed in their incremental forms as follows:

$$\mathrm{f}_{n+1} = \mathrm{f}_n e^{\Delta t\,(G_{33}^B - G_{33}^H)}, \tag{3.16}$$

and

$$\tan(\theta_{n+1}) = \tan(\theta_n) e^{\Delta t(1-\rho)\dot{\varepsilon}_{11}^H} \quad . \tag{3.17}$$

The unit vector $\mathbf{n}_{n+1}$ normal to the imperfection band lies in the plane of the sheet, and its components can be updated as:

$$\mathbf{n}_{n+1} = \left[\cos\left(\theta_{n+1}\right) \;\; \sin\left(\theta_{n+1}\right) \;\; 0\right]^{\mathrm{T}}. \tag{3.18}$$

Applying the plane-stress conditions and exploiting the fact that the third component of the normal vector $\mathbf{n}_{n+1}$ is equal to zero, the equilibrium equation stated in Eq. (3.6) can be expanded in the following form:

$$\begin{aligned} &\left(\mathrm{f}_{n+1}\,\Sigma_{11,n+1}^B - \Sigma_{11,n+1}^H\right)\mathrm{n}_{1,n+1} + \left(\mathrm{f}_{n+1}\,\Sigma_{12,n+1}^B - \Sigma_{12,n+1}^H\right)\mathrm{n}_{2,n+1} = 0, \\ &\left(\mathrm{f}_{n+1}\,\Sigma_{12,n+1}^B - \Sigma_{12,n+1}^H\right)\mathrm{n}_{1,n+1} + \left(\mathrm{f}_{n+1}\,\Sigma_{22,n+1}^B - \Sigma_{22,n+1}^H\right)\mathrm{n}_{2,n+1} = 0. \end{aligned} \tag{3.19}$$

For a given strain-path ratio ρ and an initial imperfection band angle θ_0, the velocity gradients in the imperfection band and in the homogeneous zone only depend on three unknowns: $\dot{\varepsilon}_{11}^H$, $\dot{\gamma}_1$ and $\dot{\gamma}_2$ (see Eqs. (3.4)-(3.5)). By combining Eq. (3.15) with Eq. (3.19), a non-linear system of three scalar equations is obtained:

$$\begin{aligned} &\mathcal{R}_1(\dot{\varepsilon}_{11}^H, \dot{\gamma}_1, \dot{\gamma}_2) = \left(\mathrm{f}_{n+1}\,\Sigma_{11,n+1}^B - \Sigma_{11,n+1}^H\right)\mathrm{n}_{1,n+1} + \left(\mathrm{f}_{n+1}\,\Sigma_{12,n+1}^B - \Sigma_{12,n+1}^H\right)\mathrm{n}_{2,n+1} = 0, \\ &\mathcal{R}_2(\dot{\varepsilon}_{11}^H, \dot{\gamma}_1, \dot{\gamma}_2) = \left(\mathrm{f}_{n+1}\,\Sigma_{21,n+1}^B - \Sigma_{21,n+1}^H\right)\mathrm{n}_{1,n+1} + \left(\mathrm{f}_{n+1}\,\Sigma_{22,n+1}^B - \Sigma_{22,n+1}^H\right)\mathrm{n}_{2,n+1} = 0, \\ &\mathcal{R}_3(\dot{\varepsilon}_{11}^H, \dot{\gamma}_1, \dot{\gamma}_2) = \dot{\bar{\varepsilon}}^{\mathrm{p}B} - 1 = 0. \end{aligned} \tag{3.20}$$

The above system of non-linear equations is solved iteratively at each loading increment to determine the three unknowns $\dot{\varepsilon}_{11}^{H}$, $\dot{\gamma}_1$ and $\dot{\gamma}_2$. As to the internal variables involved in the GTN damage model (i.e., porosity f, yield stress $\overline{\sigma}$, equivalent plastic strain $\overline{\varepsilon}^{\mathrm{p}}$, and Cauchy stress tensor $\boldsymbol{\Sigma}$), they can be expressed in a general differential equation of the form:

$$\dot{\boldsymbol{y}} = \boldsymbol{g}_y(\boldsymbol{y}), \tag{3.21}$$

where the vector $\boldsymbol{y}$ encompasses all of the GTN model variables to be updated at the end of each loading increment. This vector $\boldsymbol{y}$ is updated using an explicit time integration scheme. The complete algorithm for the M–K approach coupled with the GTN model is outlined in Fig. 3.2.

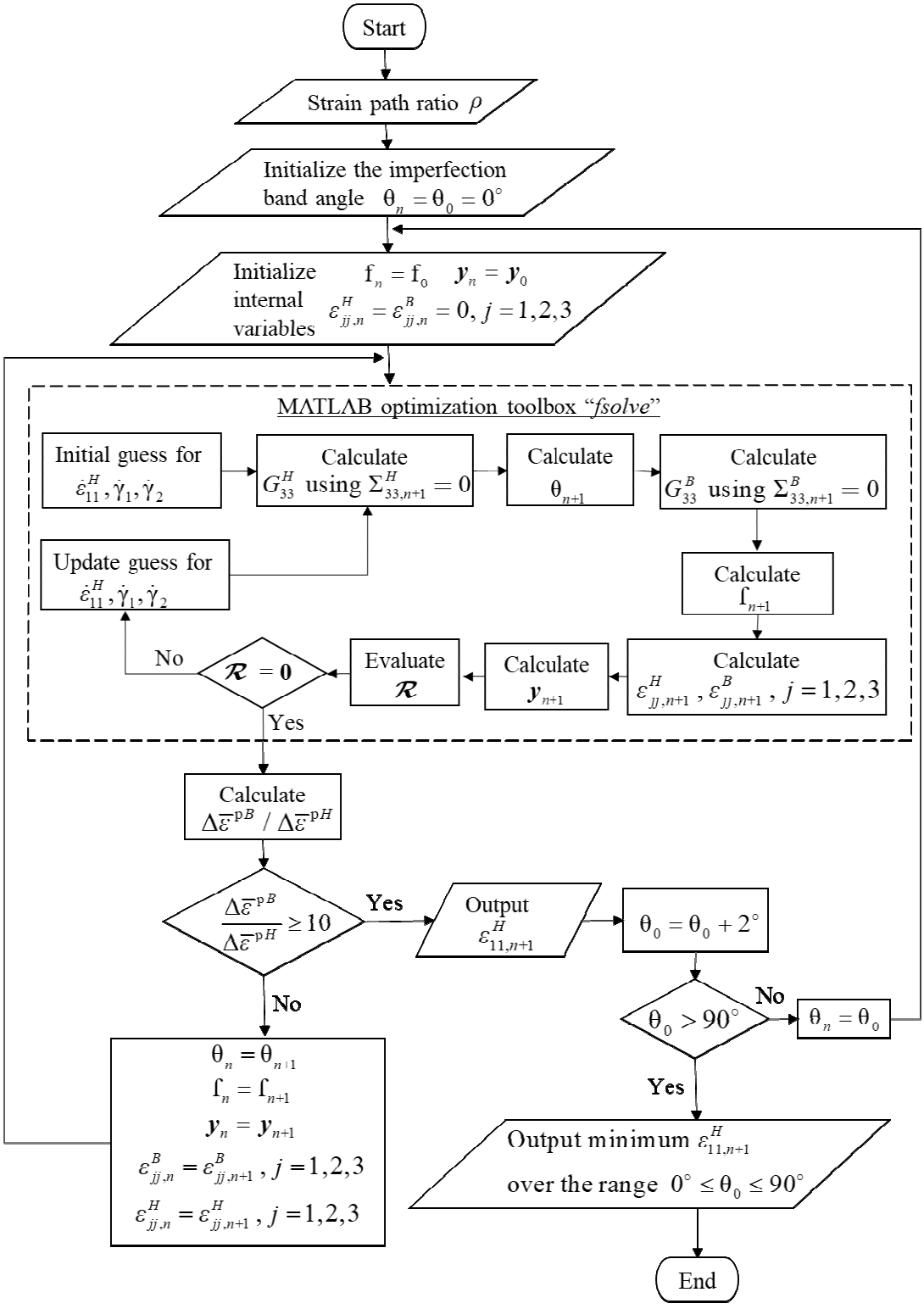

Figure 3.2. Flow diagram for the M–K–GTN algorithm.

In order to numerically validate the implementation of the constitutive equations into the MATLAB software, some preliminary simulations are first performed, and the results obtained from the MATLAB user subroutine are compared with the corresponding results obtained from the built-in Gurson-based damage model available in ABAQUS/Standard. It is worth noting that the complete GTN damage model, with growth, nucleation and coalescence mechanisms, is not available in ABAQUS/Standard, which restricts the following comparisons to only growth and nucleation of voids. The elastic properties, Swift's isotropic hardening parameters and damage parameters used in the simulations are listed in Tables 3.1 and 3.2. Fig. 3.3 provides the true stress–strain curves under uniaxial tension obtained from the MATLAB user subroutine and the built-in Gurson damage model available in ABAQUS/Standard. Fig. 3.3 shows that the numerical results obtained with the developed algorithm in MATLAB software are in excellent agreement with the reference results provided by the built-in ABAQUS model.

Table 3.1. Elastic properties and isotropic hardening parameters used in the simulations.

E (GPa)	ν	K (MPa)	n	ε_0
70	0.33	371.2	0.17	0.00324

Table 3.2. Growth and nucleation parameters used in the simulations.

f_0	f_N	ε_N	s_N	q_1	q_2	q_3
0.001	0.27	0.27	0.1	1.5	1	2.15

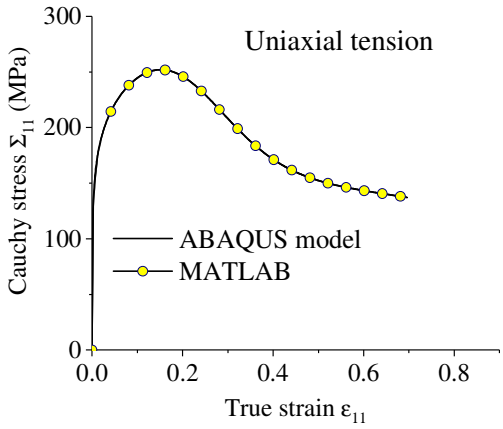

Figure 3.3. Comparison of the uniaxial stress–strain curves obtained with the built-in ABAQUS model and the developed MATLAB program.

In order to further evaluate the accuracy of the developed algorithm under in-plane biaxial loading, Fig. 3.4 shows the true stress–strain curve for balanced biaxial tension, as obtained from the developed MATLAB program along with the reference solution obtained from the built-in ABAQUS model. This figure shows that the numerical results given by the developed MATLAB program are in excellent agreement with those obtained with the built-in ABAQUS model, which validates the numerical implementation of the present model.

It is worth noting that, in the case of the M–K imperfection approach, shear stresses and strains may develop inside the imperfection band, although the homogeneous zone is subjected to in-plane biaxial stretching. To validate the accuracy of the developed numerical tool with respect to the shear behavior, Fig. 3.5 depicts the shear stress–strain curve and the porosity evolution curve for pure shear loading. This figure reveals once again that the numerical results obtained with the developed MATLAB program are in excellent agreement with the reference results provided by the built-in ABAQUS model.

The final set of simulations are specifically intended to validate the loading and unloading response. For this purpose, the considered material is subjected to cyclic loading under pure shear, and the shear stress–strain response is plotted in Fig. 3.6. From this figure, it can be observed that the stress–strain curve given by the developed MATLAB program coincides with that provided by the built-in ABAQUS model.

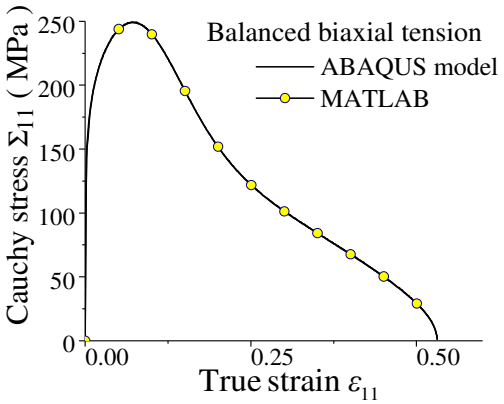

Figure 3.4. Comparison of stress–strain curves obtained with the built-in ABAQUS model and the developed MATLAB program, for balanced biaxial tension.

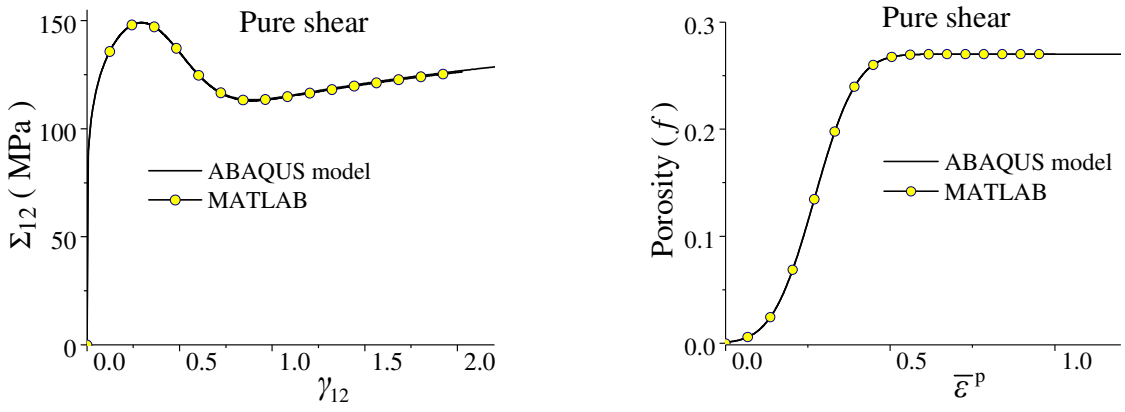

(a) (b)

Figure 3.5. Comparison of the stress–strain curves (left) and porosity evolution (right) obtained with the built-in ABAQUS model and the developed MATLAB program, for pure shear loading.

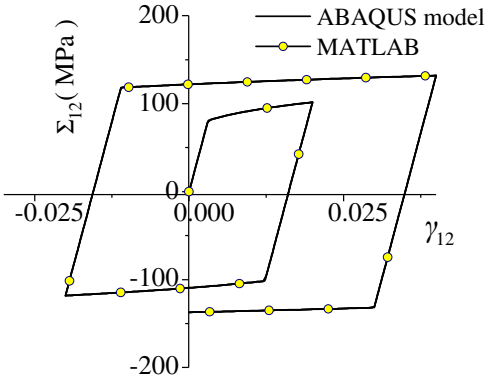

Figure 3.6. Comparison of the stress–strain curve obtained with the built-in ABAQUS model and the developed MATLAB program, for pure shear cyclic loading.

3.3 Prediction of localized necking using the M–K imperfection approach and the loss of ellipticity criterion

In this section, the elastic–plastic-damage GTN model is combined with two distinct classes of plastic instability criteria: the Rice bifurcation theory and the M–K initial imperfection approach, for the prediction of FLDs. The previously established theoretical link between both plastic instability criteria is thoroughly investigated in this section through numerical simulations. First, the FLDs are predicted for a fictitious material, which is similar to an aluminum alloy,

using the geometric imperfection in M–K approach. Then, by considering various types of material imperfections, a parameter sensitivity study is conducted in order to determine the most influential parameters on strain localization. The FLDs predicted with the M–K approach are systematically compared with the FLD obtained using the Rice bifurcation criterion. Finally, the FLDs for a real AA2024 aluminum material are determined by using different types of initial imperfections in the M–K imperfection approach.

The material parameters for the fictitious material used in what follows are listed in Tables 3.3 and 3.4.

Table 3.3. Elastic properties and isotropic hardening parameters used in the simulations.

E (GPa)	ν	K (MPa)	n	ε_0
70	0.33	500	0.17	0.00324

Table 3.4. GTN damage parameters used in the simulations.

f_0	f_N	ε_N	s_N	q_1	q_2	q_3	f_{cr}	δ_{GTN}
0.001	0.035	0.27	0.1	1.5	1	2.15	0.00213	10

3.3.1 Geometric imperfection

This subsection outlines the predicted FLDs when the initial imperfection in the M–K approach is assumed in the form of reduced thickness in the localization band, as compared to the thickness in the homogeneous zone. Note that, in the Rice bifurcation approach, no initial imperfection is required to predict localized necking. For different values of the initial thickness imperfection factor, the FLDs predicted by the M–K approach are shown in Fig. 3.7, along with the FLD obtained by the Rice bifurcation criterion. It can be seen that when the initial geometric imperfection factor increases (i.e., a reduction in the imperfection size), an increase in the limit strains is observed. Furthermore, when the initial geometric imperfection factor becomes equal to 1 (i.e., thickness of the imperfection band becomes equal to that of the homogeneous zone), the FLD obtained with the M–K approach coincides with that given by the Rice bifurcation criterion. Consequently, the Rice bifurcation criterion provides an upper bound to the limit strains predicted by the M–K approach. This finding is fully consistent with the observations reported in the literature, in which similar analogy between the M–K approach and the Rice bifurcation

criterion has been established within the framework of J_2 deformation theory of plasticity (see Yoshida and Kuroda, 2012; Ben Bettaieb and Abed-Meraim, 2015) and continuum damage mechanics models (see Abed-Meraim et al., 2014).

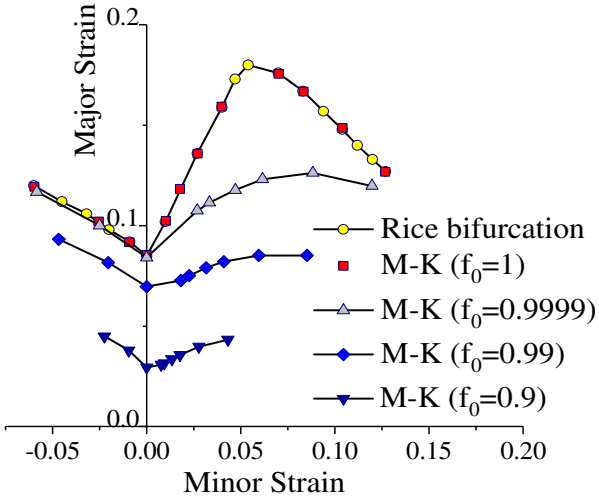

Figure 3.7. FLDs obtained with the M–K approach (using initial thickness imperfection) and with the Rice bifurcation criterion.

The evolution of the minimum value of the determinant of the acoustic tensor is presented in Fig. 3.8 along with the evolution of the ratio $\dot{\bar{\varepsilon}}^{pB} / \dot{\bar{\varepsilon}}^{pH}$ for the initial imperfection factor $f_0 = 1$. From this figure, it can be observed that the ratio of the equivalent plastic strain rate, for the M–K approach with no initial imperfection, remains equal to 1 as long as the determinant of the acoustic tensor, for the Rice bifurcation criterion, remains positive. When the condition of loss of ellipticity is met (i.e., $\det(\mathbf{Q}) = 0$), the ratio of the equivalent plastic strain rate suddenly becomes very high, as shown in Fig. 3.8 for the strain path of balanced biaxial tension. Note that similar trends are observed for other strain paths, which are not shown for conciseness.

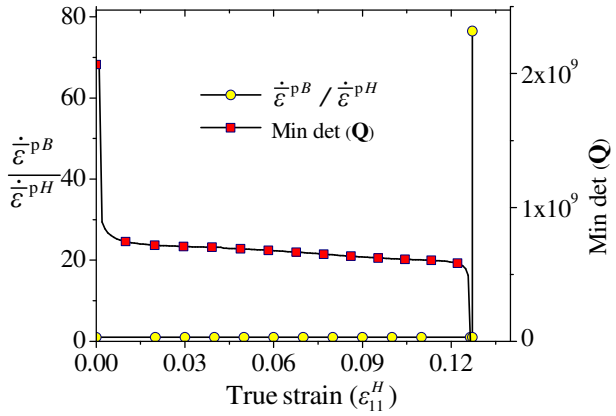

Figure 3.8. Evolution of the equivalent plastic strain rate ratio for the M–K approach with initial imperfection factor $f_0 = 1$, along with the minimum determinant of the acoustic tensor for the Rice bifurcation criterion, under balanced biaxial tension.

3.3.2 Material imperfection

In contrast to the original M–K approach, which considers an initial geometric imperfection (i.e., thickness imperfection), Yamamoto (1978) has proposed in his pioneering study the introduction of an initial imperfection within the sheet in the form of material imperfection, and more specifically, as an initial porosity imperfection. In this subsection, only material-type imperfections are considered, such as initial porosity imperfection, void nucleation imperfection, void coalescence imperfection and hardening imperfection. The material parameters adopted in the following simulations are the same as those listed in Tables 3.3 and 3.4 in both the homogeneous zone and the localization band. However, in order to account for a specific initial material imperfection, only one material parameter is varied at a time within the localization band.

3.3.2.1 Initial porosity imperfection

An imperfection band with slightly increased initial porosity, as compared to the homogeneous zone, is considered here for the M–K approach. The initial material imperfection factor in this case is represented by the difference in initial porosity between the imperfection band and the homogeneous zone, i.e., $\Delta f_0 = f_0^B - f_0^H$. In order to illustrate the effect of the initial porosity imperfection on the material behavior, Fig. 3.9a depicts the material response under uniaxial tension within the imperfection band for four different values of Δf_0. Higher values of

initial porosity are associated with weaker material. As can be seen, higher values of initial porosity imperfection tend to accelerate the porosity evolution, leading to early softening. The corresponding FLDs obtained with the M–K approach are shown in Fig. 3.9b, along with the FLD predicted with the Rice bifurcation criterion. It is interesting to note that when $\Delta f_0 = 0$ (i.e., identical initial porosity both in the imperfection band and in the homogeneous zone), the FLD predicted with the M–K approach coincides with that given by the Rice bifurcation criterion, which is consistent with the previous predictions using initial geometric imperfection. On the other hand, when Δf_0 is increased, the initial porosity in the imperfection band is greater than that in the homogeneous zone, which ultimately lowers the FLDs. These results are fully consistent with the earlier studies reported in Yamamoto (1978) and Needleman and Triantafyllidis (1978), in which it has been concluded that the overall shape of the predicted FLD mainly depends on the difference in initial porosity Δf_0, and not on the individual initial porosity in each zone (i.e., f_0^B and f_0^H).

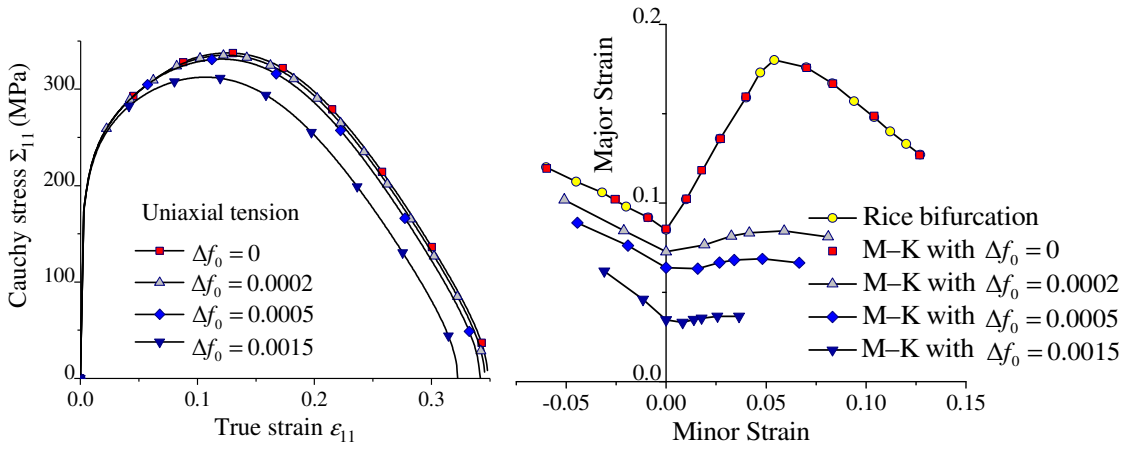

(a) (b)

Figure 3.9. Uniaxial stress–strain curves (left) for different values of initial porosity imperfection, and FLDs (right) predicted with the M–K approach and the Rice bifurcation criterion.

3.3.2.2 Void nucleation imperfection

Nucleation of voids is considered here as a material imperfection in the M–K approach. To achieve this, the Gaussian amplitude f_N (see Eq. (1.29)), which represents the total volume

fraction of cavities that are likely to nucleate, is considered slightly higher inside the imperfection band, as compared to the homogeneous zone. The material imperfection factor in this case is expressed as $\Delta f_N = f_N^B - f_N^H$, where f_N^B and f_N^H represent the Gaussian amplitudes inside the imperfection band and the homogeneous zone, respectively. Fig. 3.10a shows the true stress–strain curve under uniaxial tension within the imperfection band, for four different values of Δf_N. Note that the softening regime starts earlier for higher values of Δf_N, which is consistent with the physical significance of the nucleation parameter f_N. The corresponding FLDs are presented in Fig. 3.10b. It can be observed that the limit strains obtained with the M–K approach are lowered as the considered material imperfection Δf_N increases. Moreover, the FLDs predicted with the M–K approach tend to the FLD obtained with the Rice bifurcation criterion when the size of material imperfection Δf_N tends to zero, which is consistent with the previous numerical results.

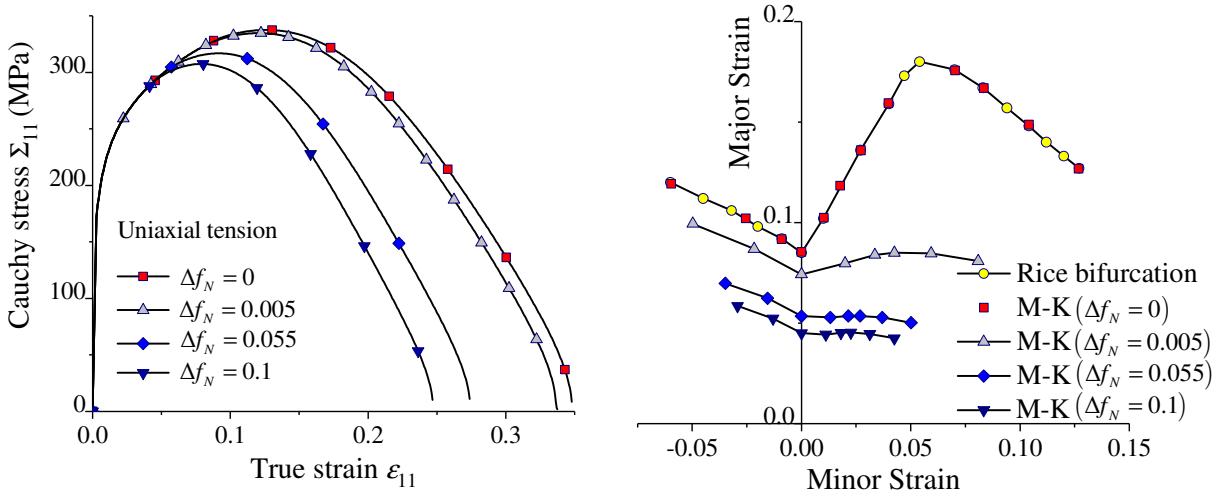

Figure 3.10. Uniaxial stress–strain curves (left) for different values of void nucleation imperfection, and FLDs (right) predicted with the M–K approach and the Rice bifurcation criterion.

3.3.2.3 Void coalescence imperfection

Similar to the previous studies, the effect of void coalescence imperfection on the prediction of FLDs is investigated here. Both the critical porosity parameter f_{cr} and the accelerating factor δ_{GTN}, involved in the coalescence mechanism, are considered as separate void coalescence imperfections. Figs. 3.11a and 3.11c illustrate the effect of the critical porosity and

the accelerating factor imperfections, respectively, on the true stress–strain response within the imperfection band under uniaxial tension. As can be seen, significant influence of these coalescence parameters on the softening regime is observed. The corresponding FLDs obtained with the M–K approach are shown in Figs. 3.11b and 3.11d, for the considered void coalescence imperfections. It is interesting to note that the overall shapes and trends of the predicted FLDs are similar to what has been obtained with the previous types of material imperfections (see Figs. 3.9b and 3.10b).

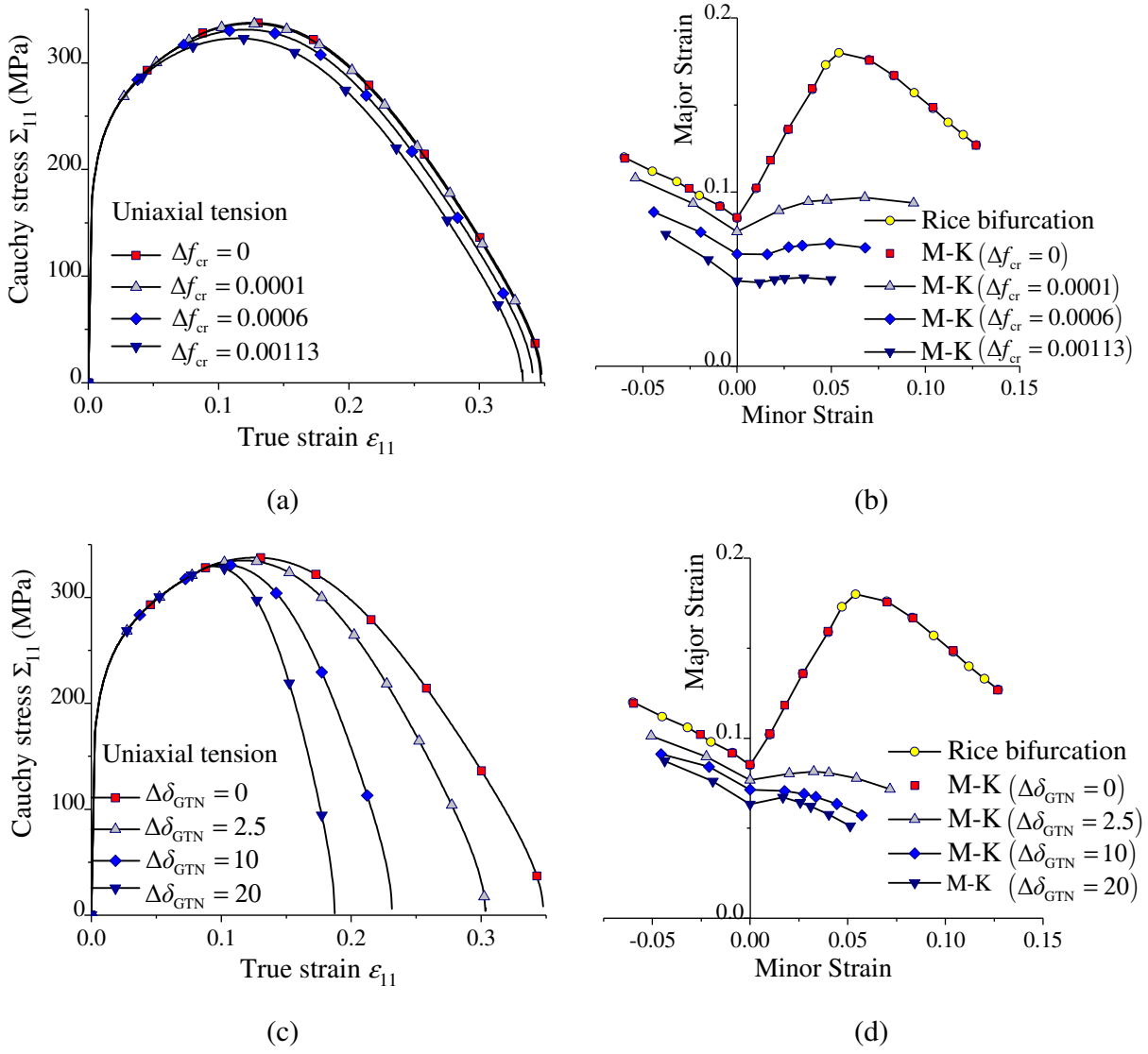

Figure 3.11. Uniaxial stress–strain curves (left) for different values of (a) critical porosity imperfection and (c) accelerating factor imperfection, with the associated FLDs (right) predicted with the M–K approach and the Rice bifurcation criterion.

3.3.2.4 Hardening imperfection

In the earlier work of Needleman and Triantafyllidis (1978), it has been shown that qualitatively equivalent FLDs are obtained when either hardening imperfection or initial porosity imperfection is considered in the M–K approach. In order to further investigate this observation, the imperfection band in the M–K approach is assumed with slightly reduced value of Swift's hardening coefficient K, as compared to the homogeneous zone. Accordingly, the material imperfection factor in this case is expressed as $\Delta K = K^H - K^B$, where K^H and K^B represent the Swift hardening coefficient in the homogeneous zone and inside the imperfection band, respectively. Fig. 3.12a clearly shows the effect of the hardening imperfection ΔK on the true stress–strain response within the imperfection band under uniaxial tension. The corresponding FLDs are shown in Fig. 3.12b. It can be seen that the FLDs are lowered as the initial material imperfection ΔK increases, which is fully consistent with the previous predictions using various types of imperfections. Moreover, the FLD predicted with the M–K approach becomes equivalent to that obtained with the Rice bifurcation criterion when the hardening imperfection vanishes (i.e., $\Delta K = 0$).

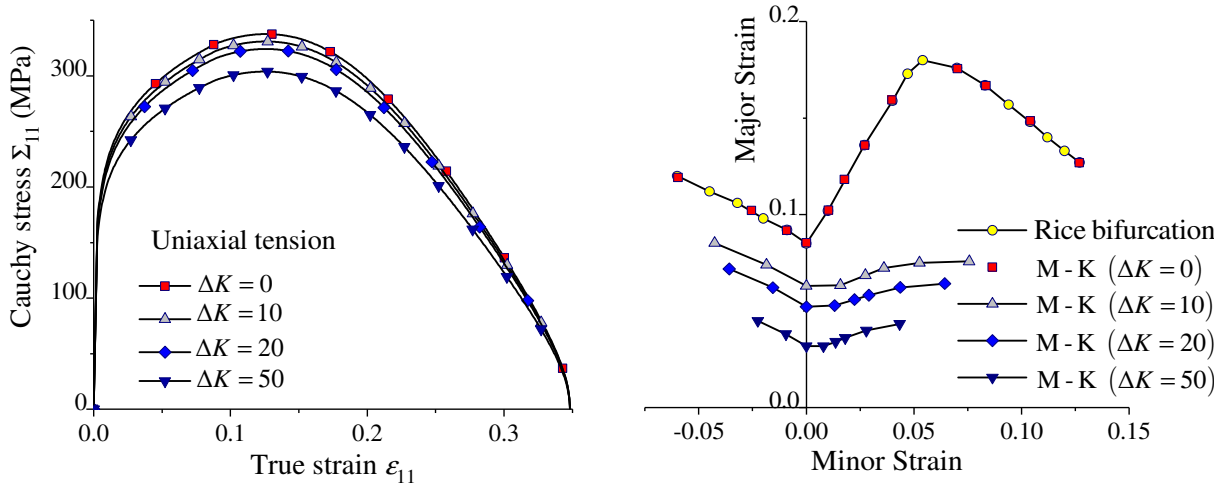

(a) (b)

Figure 3.12. Uniaxial stress–strain curves (left) for different values of hardening imperfection and FLDs (right) predicted with the M–K approach and the Rice bifurcation criterion.

3.3.3 Comparison of the FLDs obtained by using different initial imperfections in the M–K model

From the previous study, it can be clearly concluded that the limit strains are lowered when the size of initial imperfection is increased, whatever the type of initial imperfection. However, in order to determine the most influential initial imperfection factors, and to identify those having a key destabilizing role in triggering plastic flow localization, a comparative study is conducted in Fig. 3.13. This Fig. 3.13 illustrates the variation of the normalized major critical strain, predicted with the M–K approach at localization, as a function of the percentage of increase in the initial imperfection factor ϑ. Note that, for conciseness, the results are reported for only three particular strain-path ratios, i.e., –0.5, 0 and 1. For the geometric imperfection (i.e., thickness imperfection), the initial imperfection factor ϑ is defined as:

$$\vartheta_{f_0}(\%) = \frac{\Delta h_i}{h_i^H} \times 100 = \frac{h_i^H - h_i^B}{h_i^H} \times 100 \text{ with } h_i^H \neq 0 \text{ and } h_i^B \leq h_i^H \,. \tag{3.22}$$

Similar to Eq. (3.22), the initial imperfection factors associated with the material imperfections are defined as follows:

$$\begin{aligned}
&\vartheta_{f_0}(\%) = \frac{\Delta f_0}{f_0^H} \times 100 = \frac{f_0^B - f_0^H}{f_0^H} \times 100; \text{ with } f_0^H \neq 0 \text{ and } f_0^B \geq f_0^H \\
&\vartheta_{f_N}(\%) = \frac{\Delta f_N}{f_N^H} \times 100 = \frac{f_N^B - f_N^H}{f_N^H} \times 100; \text{with } f_N^H \neq 0 \text{ and } f_N^B \geq f_N^H \\
&\vartheta_{f_{cr}}(\%) = \frac{\Delta f_{cr}}{f_{cr}^H} \times 100 = \frac{f_{cr}^H - f_{cr}^B}{f_{cr}^H} \times 100; \text{ with } f_{cr}^H \neq 0 \text{ and } f_{cr}^B \leq f_{cr}^H \\
&\vartheta_{\delta_{GTN}}(\%) = \frac{\Delta \delta_{GTN}}{\delta_{GTN}^H} \times 100 = \frac{\delta_{GTN}^B - \delta_{GTN}^H}{\delta_{GTN}^H} \times 100; \text{ with } \delta_{GTN}^H \neq 0 \text{ and } \delta_{GTN}^B \geq \delta_{GTN}^H \\
&\vartheta_K(\%) = \frac{\Delta K}{K^H} \times 100 = \frac{K^H - K^B}{K^H} \times 100; \text{ with } K^H \neq 0 \text{ and } K^B \leq K^H
\end{aligned} \,. \tag{3.23}$$

From Fig. 3.13, the following conclusions can be drawn:

- The critical strains are lowered with the percentage of increase in the initial imperfection factor for all of the considered strain-path ratios. However, the decrease in the critical strains for balanced biaxial tension is comparatively more significant than for the uniaxial tension and plane-strain tension, which is in accordance with the available literature (see, e.g., Hu et al., 1998; Ben Bettaieb and Abed-Meraim, 2015).

- The initial imperfections associated with the thickness and the isotropic hardening have similar effects on the predicted critical strains for all of the strain-path ratios. Additionally, rapid decrease in the critical strains is observed when the initial imperfection ratios ϑ_{f_0} and ϑ_K are increased, as compared to the damage-related material imperfections. Therefore, it can be concluded that the critical strains, and thus the FLDs, are more sensitive to the initial imperfections associated with the thickness and the isotropic hardening.

- As to the GTN damage-related material imperfections, the effect of the critical porosity imperfection on the predicted critical strains is the most significant, which reveals that the critical porosity is the most influential parameter on the prediction of FLD among the GTN damage parameters.

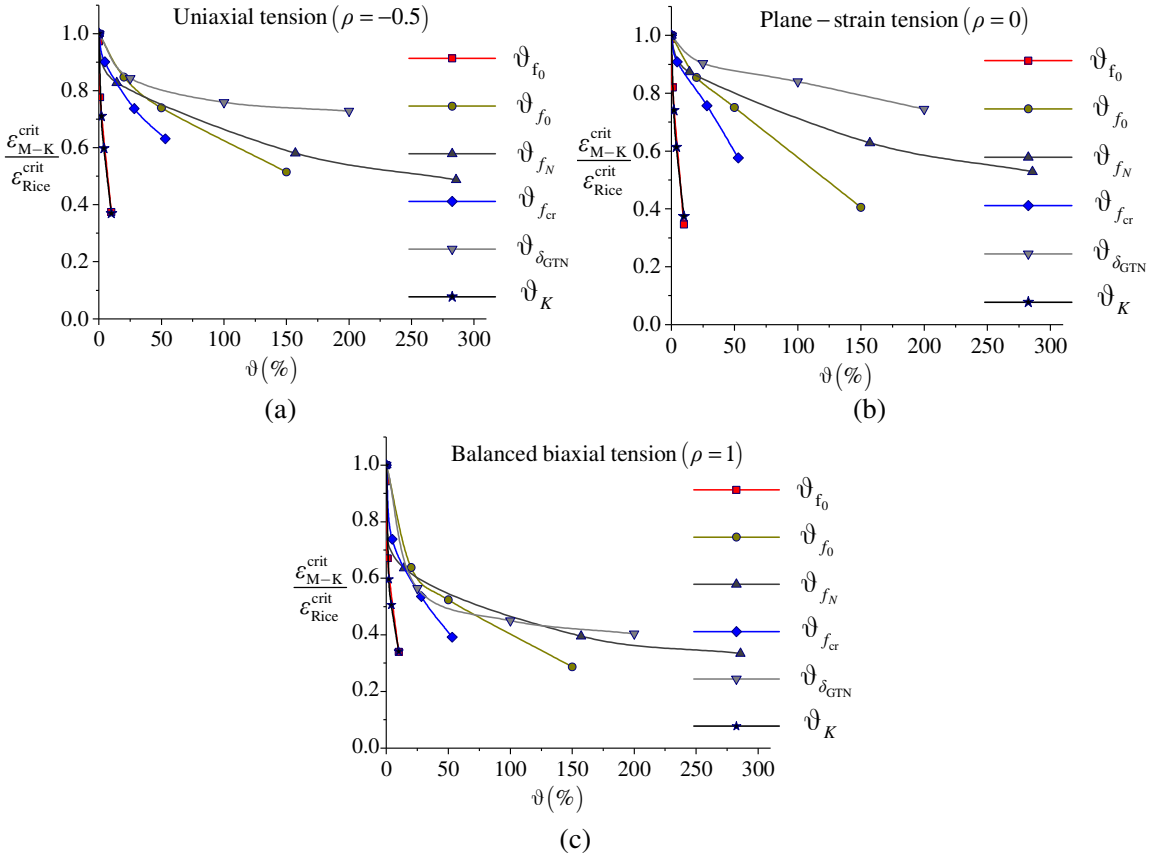

Figure 3.13. Normalized major critical strain at localization, as a function of percentage of increase in initial imperfection factor: (a) uniaxial tension (UT), (b) plane-strain tension (PS), and (c) balanced biaxial tension (BBT).

3.3.4 FLD prediction for AA2024 aluminum material

In this section, the developed numerical tool based on the M–K imperfection approach and GTN damage model is used to predict FLD for AA2024 aluminum material. The predicted FLDs are also compared with the experimental FLD reported in Janbakhsh et al. (2012). The elastic properties, Swift's isotropic hardening parameters and GTN damage parameters for the studied AA2024 aluminum material have been provided by Wu et al. (2019) and are listed in Tables 3.5 and 3.6.

Table 3.5. Elastic properties and isotropic hardening parameters for AA2024 aluminum material.

E (GPa)	ν	K (MPa)	n	ε_0
71.5	0.33	962.14	0.0109	0.1993

Table 3.6. GTN damage parameters for AA2024 aluminum material.

f_0	f_N	ε_N	s_N	q_1	q_2	q_3	f_{cr}	δ_{GTN}
0.00	0.025	0.122	0.198	1.5	1	2.15	0.014	18.19

Figure 3.14 shows the FLDs predicted using three different types of M–K initial imperfections: thickness, isotropic hardening and critical porosity initial imperfections. These three specific initial imperfections are the most influential parameters on the prediction of FLD, as concluded from the previous investigation (see Section 3.3.3). For each imperfection type, different initial values are considered for the prediction of FLD. Compared to the experimental FLD taken from Janbakhsh et al. (2012), Fig. 3.14a shows that an initial thickness imperfection factor of $\mathrm{f}_0 = 0.995$ leads to excellent agreement with the experimental limit strains. Similar to the consideration of initial thickness imperfection, Fig. 3.14b shows that the FLD predicted with an initial hardening imperfection of $\Delta K = 7\,\mathrm{MPa}$ is in good agreement with the experimental one. The effect of critical porosity imperfection on the prediction of FLD is also investigated in Fig. 3.14c. In contrast with the effect of initial thickness and hardening imperfections on the prediction of FLDs, the critical porosity imperfection has a significant effect on the overall shape of the predicted FLDs (see Fig. 3.14c). In addition, the predicted limit strains are comparatively closer to the experimental ones for $\Delta f_{cr} = 0.003$. On the whole, it can be concluded that the above three initial imperfection factors play a crucial role in the prediction of FLD, and their

magnitudes should be determined carefully. Also, the experimental identification of these initial imperfections must be combined with that of the material parameters, in order to provide accurate predictions of limit strains.

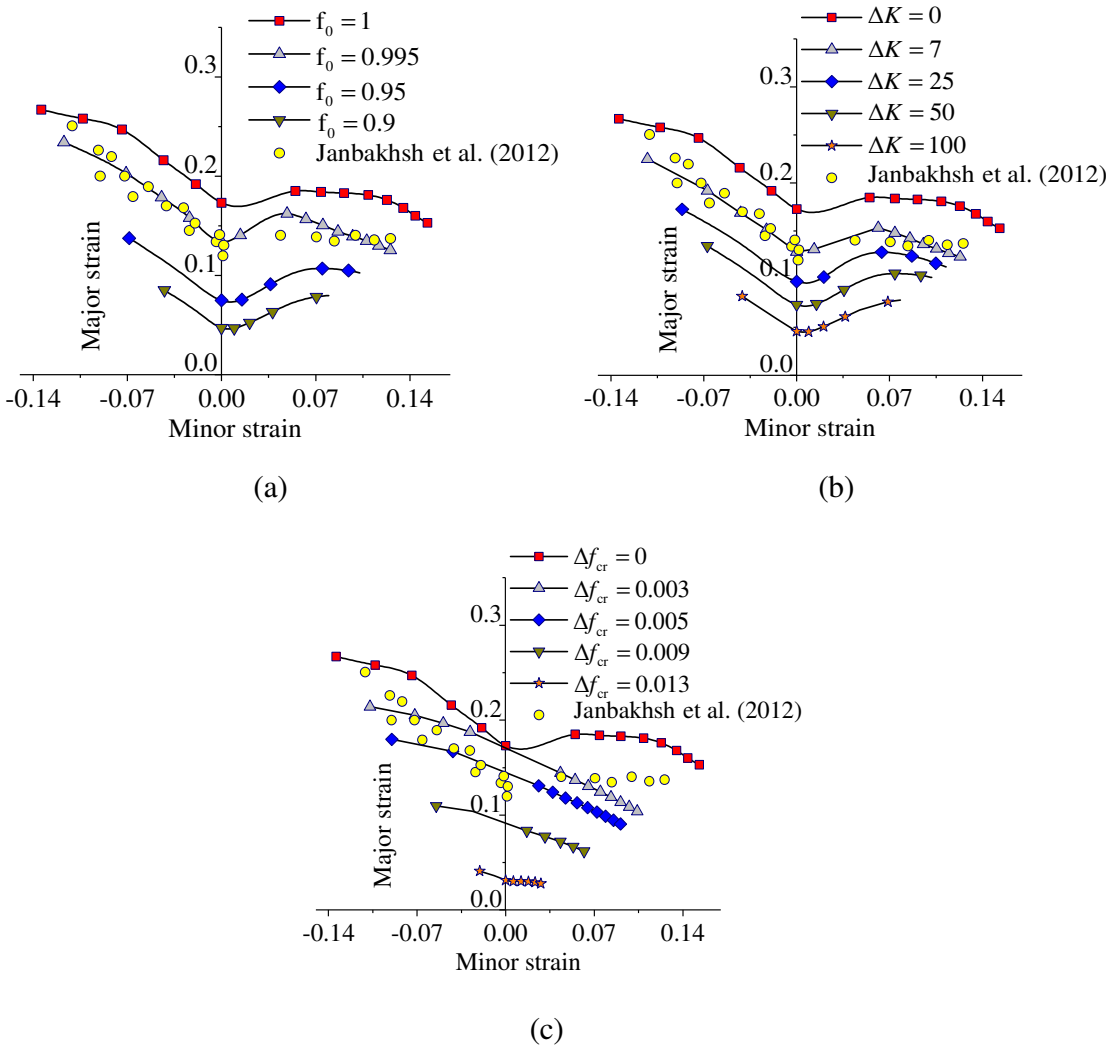

Figure 3.14. Predictions of the forming limit diagram for AA2024 aluminum material using: (a) initial thickness imperfection, (b) hardening imperfection and (c) critical porosity imperfection, in the M–K imperfection approach.

3.4 Conclusion

In the present Chapter, a numerical tool has been developed to predict forming limit diagrams (FLDs) by combining the GTN damage model with the Marciniak–Kuczyński (M–K)

imperfection approach. For the M–K imperfection approach, the effects of thickness-based geometric imperfection as well as various types of material imperfections on the prediction of FLDs have been investigated for a fictitious material. The predicted limit strains have been systematically compared to those obtained with the Rice bifurcation criterion, for which no initial imperfection is required. It has been shown that when the geometric or material imperfection tends to zero (i.e., vanishing initial imperfection), the FLD predicted with the M–K approach tends to that obtained with the Rice bifurcation criterion. Moreover, the limit strains are lowered when the initial imperfection magnitudes are increased for the M–K approach, which is consistent with the basic foundation of this criterion. Accordingly, the Rice bifurcation criterion provides an upper bound for the prediction of localized necking, as compared to the M–K approach. A parameter sensitivity study has also been conducted in order to identify the most influential initial imperfection factors on the prediction of limit strains with the M–K approach. It has been shown that the thickness-based imperfection type as well as the hardening imperfection type have a significant impact on the prediction of limit strains, as compared to damage-based imperfections. As to the latter damage-related material imperfections, the effect of the critical porosity imperfection on the predicted FLDs is the most significant, which highlights the importance of the critical porosity parameter in the interaction between damage evolution and strain localization. The present approach has additionally been used for the prediction of the FLD of the AA2024 aluminum material. It has been shown that a careful selection of the initial imperfection factor leads to excellent agreement between the predicted limit strains and the experimental ones. These initial imperfection factors, which can be regarded as additional material parameters, could be determined experimentally within an identification procedure including the intrinsic material parameters (see, e.g., Liu et al., 2015)..

Chapter 4

Effect of void size on the prediction of FLDs for porous materials

4.1 Introduction

In the previous two chapters, the Gurson–Tvergaard–Needleman (GTN) model has been coupled with the bifurcation-based plastic instability criteria and multi-zone approach, respectively, for the prediction of ductility limits. However, the effect of void size on the prediction of FLDs has not been considered, which is taken into account in the present Chapter. The scientific literature has shown the strong effect of void size on material response. Several yield functions have been developed to incorporate the void size effects in ductile porous materials. In the present Chapter, the void-size dependent constitutive model proposed by Dormieux and Kondo (2010) is combined with the loss of ellipticity criterion to predict FLDs of sheet metals. The constitutive equations as well as the bifurcation-based localization criterion are implemented into the finite element code ABAQUS/Standard within the framework of large plastic deformations. The resulting numerical tool is applied to the prediction of FLDs for an aluminum material.

This chapter first addresses the state of the art and the applications of void-size dependent yield functions, developed in the literature over the past decades. Then, the constitutive equations and the calculation of the elastic–plastic tangent modulus for the Dormieux and Kondo (2010) parametric yield surface are presented. Following this, the algorithm for the numerical implementation of the parametric yield surface is discussed and its numerical validations are presented. Finally, the numerical results in terms of FLDs for Al5754 aluminum, obtained with the proposed approach, are presented and discussed along with some concluding remarks.

4.2 Void-size dependent models: state of the art

For describing the mechanical behavior of porous metallic materials, the Gurson model involves only one microstructural variable, i.e., porosity (void volume fraction), for the analysis of void growth. The original Gurson model does not incorporate the void size in the yield surface. However, this model has been applied to materials with micron void sizes as well as submicron

void sizes. Due to the mechanism of dislocation motion, plasticity depends upon internal length scale factor, and when the cavity size is equal to or less than the order of internal length scale, application of the original Gurson model is no more justified (see Hutchinson, 2000). The underlying motive for this non-applicability of the Gurson damage model is that higher strength is associated with smaller cavity sizes. In this context, it has been shown in the literature that the yield surface is larger as compared to the original Gurson yield surface for void sizes in the range of micron and submicron (see, e.g., Wen et al., 2005). Experimental investigations have also revealed the void size effects on the material behavior (see, e.g., Fleck et al., 1994; Schlu et al., 1996; Begley and Hutchinson, 1998; Nix and Gao, 1998; Stölken and Evans, 1998; Khraishi et al., 2001; Kawasaki et al., 2005; Fu and Chan, 2011; Chentouf et al., 2017; Li et al., 2018). In particular, the experimental studies carried out by Biener et al. (2005, 2006) and Hakamada and Mabuchi (2007) on nano-porous materials revealed that the decrease in void size causes an increase in material strength. Similarly, Xu et al. (2014, 2015, 2019) experimentally investigated the relationship between the size effects, material hardening, and forming limit diagrams (FLDs). Their observations have shown that small grain size, and thus small void size, leads to an increase in strain hardening and forming limits. Concurrently, several numerical and unit cell studies have equally shown the void size effects (see, e.g., Liu et al., 2003; Mi et al., 2011; Monchiet and Bonnet, 2013; Brach et al., 2016). Mi et al. (2011) pointed out, through their atomistic simulations, the need for enhancement of the Gurson model to incorporate the void size in the yield function. Their simulations show that, for the same value of initial porosity, smaller voids result in increased material strength.

Several void-size dependent yield functions have recently been developed in the literature. For instance, Wen et al. (2005) and Monchiet and Bonnet (2013) have proposed yield functions for micron and sub-micron void sizes, based on the Taylor dislocation theory and strain gradient plasticity theory, respectively. Li and Huang (2005) and Li and Steinmann (2006) combined the strain gradient plasticity theory with the Gologanu-Leblond-Devaux (GLD) yield function and proposed a modified yield surface, which incorporates the combined effects of the void size and the void shape. Another category of void-size dependent yield functions is based on the existence of interface stresses between the nano-voids and the matrix material. Dormieux and Kondo (2010) accounted these interface stresses in the yield function by considering a hypothetical membrane surrounding the spherical nano-voids. Dormieux and Kondo (2010) developed a

Gurson-type macroscopic yield function, which involves a non-dimensional parameter depending on the void size and the membrane strength. Monchiet and Kondo (2013) further extended this yield function by introducing the concept of interface stresses in the GLD model. Unlike the limit analysis, Dormieux and Kondo (2013) and Brach et al. (2017) developed the void-size dependent yield functions by following the non-linear homogenization techniques. Brach et al. (2018) also proposed a closed form yield function, which incorporates the void size effects and all the three invariants of the Cauchy stress tensor. Recently, Niordson and Tvergaard (2019) and Holte et al. (2019) proposed a simplified approach to capture the void size effect by the calibration of the q-parameters in the Gurson damage model.

4.3 Dormieux–Kondo (D–K) void-size dependent model

4.3.1 Constitutive equations

Dormieux and Kondo (2010) extended the original Gurson model by considering a hypothetical membrane surrounding a spherical void present inside a spherical representative volume element (RVE), as depicted in Fig. 4.1. The membrane around the void is acted on by a surface tension, which produces surface stresses around the voids. The strength of the membrane follows the von Mises criterion, with k_{int} (N/m) being the cavity interface strength. A non-dimensional parameter Γ is introduced to characterize the void size effects, which depends on the membrane strength k_{int}, void size a and the yield strength $\overline{\sigma}$ of the fully dense matrix material:

$$\Gamma = \frac{k_{\text{int}}}{a\overline{\sigma}}. \tag{4.1}$$

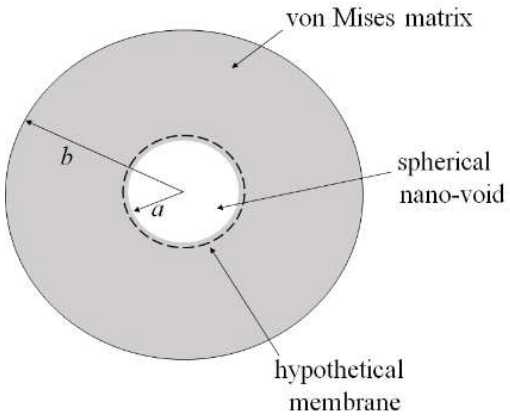

Figure 4.1. Spherical representative volume element with a spherical nano-void and hypothetical membrane.

The D–K yield function is expressed in the form of the following parametric equations:

$$\Phi\left[\Sigma_{eq}(\xi),\Sigma_{m}(\xi)\right]=0,$$
$$3\Sigma_{m}=\mathrm{tr}(\boldsymbol{\Sigma})=\bar{\sigma}\left(2\left(\sinh^{-1}(\xi)-\sinh^{-1}(f\xi)\right)+\Gamma\frac{6\xi}{\sqrt{\xi^{2}+3/5}}\right), \tag{4.2}$$
$$\Sigma_{eq}=\bar{\sigma}\left(\sqrt{1+f^{2}\xi^{2}}-f\sqrt{1+\xi^{2}}+\Gamma\frac{9f}{5\sqrt{\xi^{2}+3/5}}\right),$$

where $\xi=\dfrac{2\mathrm{D}_{m}}{f\ \mathrm{D}_{eq}}$ is a dimensionless parameter defined as a function of the mean part D_{m} and the equivalent part D_{eq} of the macroscopic strain rate tensor $\mathbf{D}$. In Eq. (4.2), $\boldsymbol{\Sigma}$ is the Cauchy stress tensor, $\bar{\sigma}$ is the yield stress of the fully dense matrix, $f=\left(\dfrac{a}{b}\right)^{3}$ is the void volume fraction, $\Sigma_{eq}=\sqrt{\dfrac{3}{2}\boldsymbol{\Sigma}':\boldsymbol{\Sigma}'}$ is the macroscopic equivalent stress, with $\boldsymbol{\Sigma}'$ and Σ_{m} the deviatoric and hydrostatic part of the Cauchy stress tensor, respectively.

For illustration purposes, the above parametric yield function is plotted in Fig. 4.2 for $\Gamma=0,\ 0.2$ and 0.43, along with the original Gurson model (i.e., without void size effect). It is worth noting that the Gurson model is recovered from the Dormieux and Kondo (2010) model

(D–K model) when $\Gamma = 0$. Note that owing to the symmetry of the parametric yield surface with respect to $\frac{\Sigma_{eq}}{\bar{\sigma}}$ axis, only the first quadrant is plotted.

From Fig. 4.2, it can be seen that the yield locus becomes larger for smaller void sizes (i.e., larger values of Γ). As the void size increases (i.e., smaller values of Γ), the size dependency of the D–K model becomes negligible, while for $\Gamma = 0$ (i.e., very large void sizes), the Gurson model is recovered, as shown in Fig. 4.2. In addition, two linear stress paths, corresponding to constant stress triaxiality of $T = 0.333$ (i.e., uniaxial tension) and $T = 0.667$ (balanced biaxial tension) are highlighted in Fig. 4.2. Note that, in sheet metal forming applications, the range of stress triaxiality lies typically between 0.333 and 0.667. In this range of stress triaxiality, it can be observed that the parametric yield locus is sensitive to void size.

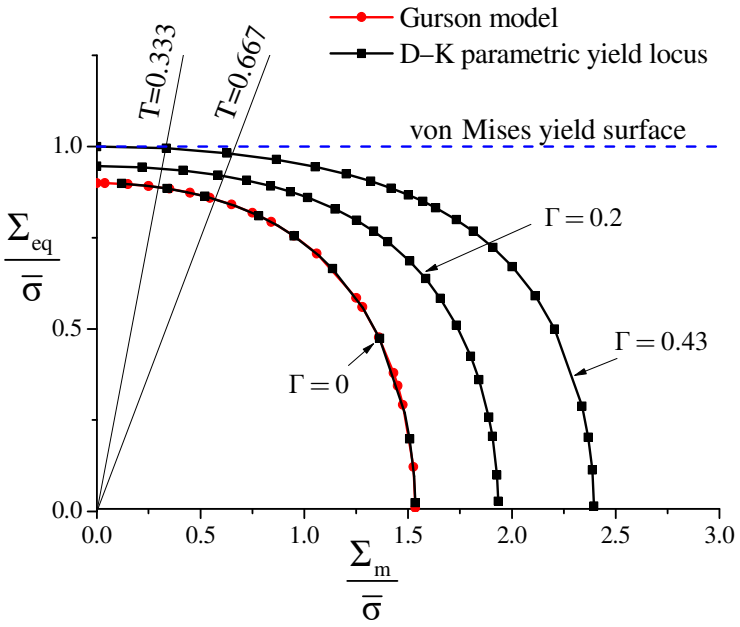

Figure 4.2. D–K parametric yield locus for $f = 0.1$ and $\Gamma = 0, 0.2$ and 0.43.

Morin et al. (2015) have numerically implemented the D–K model by using the heuristic extension of Gurson's model for isotropic hardening. The yield stress $\bar{\sigma}$, which was considered as a constant value in the D–K model (i.e., without hardening), is actually a function of the cumulated equivalent plastic strain $\bar{\varepsilon}^p$, which allows modeling isotropic hardening. The commonly used isotropic hardening laws have been presented in Chapter 1 (see Eq. (1.22)). In

the present Chapter, Swift's law and power-hardening law will be used in conjunction with D–K model. From the equivalence principle of the plastic work rate, the equivalent plastic strain rate $\dot{\bar{\varepsilon}}^{\mathrm{p}}$ and the macroscopic plastic strain rate tensor $\mathbf{D}^{\mathrm{p}}$ are related as (see Eq. (1.23)):

$$\dot{\bar{\varepsilon}}^{\mathrm{p}} = \frac{\boldsymbol{\Sigma} : \mathbf{D}^{\mathrm{p}}}{(1-f)\bar{\sigma}}, \tag{4.3}$$

where $\mathbf{D}^{\mathrm{p}}$ represents the macroscopic plastic strain rate tensor. The time derivative of the yield stress (i.e., $\dot{\bar{\sigma}}$) can be evaluated as:

$$\dot{\bar{\sigma}} = \frac{\partial \bar{\sigma}}{\partial \bar{\varepsilon}^{\mathrm{p}}} \dot{\bar{\varepsilon}}^{\mathrm{p}} = h(\bar{\varepsilon}^{\mathrm{p}}) \dot{\bar{\varepsilon}}^{\mathrm{p}}, \tag{4.4}$$

where $h(\bar{\varepsilon}^{\mathrm{p}}) = \partial \bar{\sigma} / \partial \bar{\varepsilon}^{\mathrm{p}}$ is the plastic hardening slope of the fully dense matrix material, which depends on the isotropic strain hardening law considered in the constitutive equations. Morin et al. (2015) have implemented into the D–K model the evolution of the porosity due to growth, based on the matrix incompressibility (see, Eq. (1.21)):

$$\dot{f} = \dot{f}_{\mathrm{g}} = (1-f)\mathrm{tr}\left(\mathbf{D}^{\mathrm{p}}\right). \tag{4.5}$$

The evolution of the void size (i.e., $\dot{a}$) has been modeled by Morin et al. (2015) by considering that for a spherical void of volume ω, present inside a spherical RVE of volume Ω, the volume constancy of the matrix material implies that $\dot{\omega} = \dot{\Omega}$. As the porosity is defined by $f = \dfrac{\omega}{\Omega}$, the evolution equation for the porosity and thus for the void size writes:

$$\begin{aligned} \dot{f} &= \frac{\mathrm{d}}{\mathrm{d}t}\left(\frac{\omega}{\Omega}\right) = \frac{\Omega\dot{\omega} - \omega\dot{\Omega}}{\Omega^2} = \frac{\dot{\omega}}{\omega}\left(\frac{\omega}{\Omega} - \frac{\omega^2\dot{\Omega}}{\Omega^2\dot{\omega}}\right) = 3\frac{\dot{a}}{a}\left(f - f^2\right), \\ \dot{a} &= \frac{a}{3f(1-f)}\dot{f}. \end{aligned} \tag{4.6}$$

The evolution of the non-dimensional parameter Γ can be expressed by taking the time derivative of Eq. (4.1) as:

$$\dot{\Gamma} = \frac{\mathrm{d}}{\mathrm{d}t}\left(\frac{k_{\mathrm{int}}}{a\bar{\sigma}}\right) = \frac{-k_{\mathrm{int}}}{\left(a\bar{\sigma}\right)^2}\left(a\dot{\bar{\sigma}} + \dot{a}\bar{\sigma}\right). \tag{4.7}$$

In order to determine the elastic–plastic tangent modulus for the D–K model, the plastic multiplier $\dot{\lambda}$ and the yield function Φ can be combined in the form of the following Kuhn–Tucker relation:

$$\Phi \le 0,\ \ \dot{\lambda} \ge 0,\ \ \Phi\dot{\lambda} = 0. \tag{4.8}$$

The above expression shows that no plastic flow occurs (i.e., $\dot{\lambda} = 0$) when $\Phi < 0$, while a strict plastic loading (i.e., $\dot{\lambda} > 0$) necessarily implies $\dot{\Phi} = 0$. The latter condition, called consistency condition, is used to derive the elastic–plastic tangent modulus as follows:

$$\dot{\Phi}\left(\boldsymbol{\Sigma}, f, \Gamma, \bar{\sigma}\right) = \mathbf{V}_{\boldsymbol{\Sigma}} : \dot{\boldsymbol{\Sigma}} + \mathrm{V}_{\bar{\sigma}}\dot{\bar{\sigma}} + \mathrm{V}_{\Gamma}\dot{\Gamma} + \mathrm{V}_f \dot{f} \ = 0, \tag{4.9}$$

where $\mathbf{V}_{\boldsymbol{\Sigma}}, \mathrm{V}_{\bar{\sigma}}, \mathrm{V}_{\Gamma}$ and V_f are the partial derivatives of the yield function Φ with respect to $\boldsymbol{\Sigma}$, $\bar{\sigma}$, Γ and f, respectively. Their expressions are derived as follows:

$$\mathbf{V}_{\boldsymbol{\Sigma}} = \frac{\partial \Phi}{\partial \boldsymbol{\Sigma}} = \frac{\partial \Phi}{\partial \Sigma_{\mathrm{m}}}\frac{\partial \Sigma_{\mathrm{m}}}{\partial \boldsymbol{\Sigma}} + \frac{\partial \Phi}{\partial \Sigma_{\mathrm{eq}}}\frac{\partial \Sigma_{\mathrm{eq}}}{\partial \boldsymbol{\Sigma}}, \tag{4.10}$$

where the partial derivative terms i.e., $\dfrac{\partial \Phi}{\partial \Sigma_{\mathrm{m}}}$ and $\dfrac{\partial \Phi}{\partial \Sigma_{\mathrm{eq}}}$ are given as (see Morin et al., 2015):

$$\begin{aligned} \frac{\partial \Phi}{\partial \Sigma_{\mathrm{m}}} &= -\mathrm{C}^2\frac{\mathrm{d}\Sigma_{\mathrm{eq}}}{\mathrm{d}\xi}, \\ \frac{\partial \Phi}{\partial \Sigma_{\mathrm{eq}}} &= \mathrm{C}^2\frac{\mathrm{d}\Sigma_{\mathrm{m}}}{\mathrm{d}\xi}, \end{aligned} \tag{4.11}$$

where C is a real constant, which depends on the parameter ξ. By using Eq. (4.11), $\mathbf{V}_{\boldsymbol{\Sigma}}$ can be expressed as:

$$\mathbf{V}_{\boldsymbol{\Sigma}} = -\mathrm{C}^2\frac{\mathrm{d}\Sigma_{\mathrm{eq}}}{\mathrm{d}\xi}\frac{\partial \Sigma_{\mathrm{m}}}{\partial \boldsymbol{\Sigma}} + \mathrm{C}^2\frac{\mathrm{d}\Sigma_{\mathrm{m}}}{\mathrm{d}\xi}\frac{\partial \Sigma_{\mathrm{eq}}}{\partial \boldsymbol{\Sigma}}, \tag{4.12}$$

where the partial derivatives involved in Eq. (4.12) can be evaluated as:

$$\begin{aligned}\frac{\partial \Sigma_{\mathrm{m}}}{\partial \boldsymbol{\Sigma}} &= \frac{1}{3}\mathbf{I},\\ \frac{\partial \Sigma_{\mathrm{eq}}}{\partial \boldsymbol{\Sigma}} &= \frac{3}{2}\frac{\boldsymbol{\Sigma}'}{\Sigma_{\mathrm{eq}}},\end{aligned} \tag{4.13}$$

where $\mathbf{I}$ is the second-order identity tensor. By taking the derivative of the parametric yield function given by Eq. (4.2) with respect to parameter ξ, we obtain:

$$\begin{aligned}\frac{\mathrm{d}\Sigma_{\mathrm{eq}}}{\mathrm{d}\xi} &= \overline{\sigma}\left\{\frac{f^2\xi}{\sqrt{1+f^2\xi^2}} - \frac{f\xi}{\sqrt{1+\xi^2}} - \frac{9f\Gamma\xi}{5}\left(\xi^2+\frac{3}{5}\right)^{-\frac{3}{2}}\right\},\\ \frac{\mathrm{d}\Sigma_{\mathrm{m}}}{\mathrm{d}\xi} &= \frac{\overline{\sigma}}{3}\left\{2\left\{\frac{1}{\sqrt{1+\xi^2}} - \frac{f}{\sqrt{1+f^2\xi^2}}\right\} + 6\Gamma\left\{-\xi^2\left(\xi^2+\frac{3}{5}\right)^{-\frac{3}{2}} + \left(\xi^2+\frac{3}{5}\right)^{-\frac{1}{2}}\right\}\right\}.\end{aligned} \tag{4.14}$$

Finally, by using Eq. (4.14), $\mathbf{V}_{\boldsymbol{\Sigma}}$ in Eq. (4.12) writes:

$$\mathbf{V}_{\boldsymbol{\Sigma}} = \mathrm{C}^2\left\{-\frac{\mathrm{d}\Sigma_{\mathrm{eq}}}{\mathrm{d}\xi}\frac{1}{3}\mathbf{I} + \frac{\mathrm{d}\Sigma_{\mathrm{m}}}{\mathrm{d}\xi}\frac{3}{2}\frac{\boldsymbol{\Sigma}'}{\Sigma_{\mathrm{eq}}}\right\} = \mathrm{C}^2\mathbf{V}_{\boldsymbol{\Sigma}_{\mathrm{N}}}. \tag{4.15}$$

By following similar steps, the general expressions of the partial derivatives $\mathrm{V}_{\overline{\sigma}}, \mathrm{V}_{\Gamma}$ and V_f can be obtained as follows:

$$\begin{aligned}\mathrm{V}_{\overline{\sigma}} &= \frac{\partial\Phi}{\partial\overline{\sigma}} = \frac{\partial\Phi}{\partial\Sigma_{\mathrm{m}}}\frac{\partial\Sigma_{\mathrm{m}}}{\partial\overline{\sigma}} + \frac{\partial\Phi}{\partial\Sigma_{\mathrm{eq}}}\frac{\partial\Sigma_{\mathrm{eq}}}{\partial\overline{\sigma}},\\ \mathrm{V}_f &= \frac{\partial\Phi}{\partial f} = \frac{\partial\Phi}{\partial\Sigma_{\mathrm{m}}}\frac{\partial\Sigma_{\mathrm{m}}}{\partial f} + \frac{\partial\Phi}{\partial\Sigma_{\mathrm{eq}}}\frac{\partial\Sigma_{\mathrm{eq}}}{\partial f},\\ \mathrm{V}_{\Gamma} &= \frac{\partial\Phi}{\partial\Gamma} = \frac{\partial\Phi}{\partial\Sigma_{\mathrm{m}}}\frac{\partial\Sigma_{\mathrm{m}}}{\partial\Gamma} + \frac{\partial\Phi}{\partial\Sigma_{\mathrm{eq}}}\frac{\partial\Sigma_{\mathrm{eq}}}{\partial\Gamma},\end{aligned} \tag{4.16}$$

and more specifically:

$$
\begin{aligned}
V_{\bar{\sigma}} &= C^2\left\{-\frac{d\Sigma_{eq}}{d\xi}\frac{\partial\Sigma_m}{\partial\bar{\sigma}}+\frac{d\Sigma_m}{d\xi}\frac{\partial\Sigma_{eq}}{\partial\bar{\sigma}}\right\}=C^2V_{\bar{\sigma}_N},\\
V_f &= C^2\left\{-\frac{d\Sigma_{eq}}{d\xi}\frac{\partial\Sigma_m}{\partial f}+\frac{d\Sigma_m}{d\xi}\frac{\partial\Sigma_{eq}}{\partial f}\right\}=C^2V_{f_N},\\
V_\Gamma &= C^2\left\{-\frac{d\Sigma_{eq}}{d\xi}\frac{\partial\Sigma_m}{\partial\Gamma}+\frac{d\Sigma_m}{d\xi}\frac{\partial\Sigma_{eq}}{\partial\Gamma}\right\}=C^2V_{\Gamma_N}.
\end{aligned}
\tag{4.17}
$$

The macroscopic plastic strain rate tensor $\mathbf{D}^p$ is defined using the following classical plastic flow rule (normality law):

$$
\mathbf{D}^p=\dot{\lambda}\mathbf{V}_{\boldsymbol{\Sigma}}. \tag{4.18}
$$

By substituting Eq. (4.15) in the above equation, the macroscopic plastic strain rate tensor becomes:

$$
\mathbf{D}^p=\dot{\lambda}C^2\mathbf{V}_{\boldsymbol{\Sigma}_N}=\dot{\lambda}_N\mathbf{V}_{\boldsymbol{\Sigma}_N}, \tag{4.19}
$$

where

$$
\dot{\lambda}_N=\dot{\lambda}C^2. \tag{4.20}
$$

The macroscopic Cauchy stress rate tensor is expressed, in the co-rotational material frame, by the following hypoelastic law:

$$
\dot{\boldsymbol{\Sigma}}=\mathbf{C}^e:\left(\mathbf{D}-\mathbf{D}^p\right)=\mathbf{C}^{ep}:\mathbf{D}, \tag{4.21}
$$

where $\mathbf{D}$ is the macroscopic strain rate tensor, $\mathbf{C}^e$ is the fourth-order tensor of elasticity constants, and $\mathbf{C}^{ep}$ is the elastic–plastic tangent modulus, which needs to be determined. By using all of the above-described partial derivatives of the yield function and considering Eqs. (4.19) and (4.21), the consistency condition (4.9) can be developed as follows:

$$
\mathbf{V}_{\boldsymbol{\Sigma}_N}:\mathbf{C}^e:\mathbf{D}-\dot{\lambda}_N\mathbf{V}_{\boldsymbol{\Sigma}_N}:\mathbf{C}^e:\mathbf{V}_{\boldsymbol{\Sigma}_N}+V_{\bar{\sigma}_N}\dot{\bar{\sigma}}+V_{\Gamma_N}\dot{\Gamma}+V_{f_N}\dot{f}=0. \tag{4.22}
$$

Then, substituting Eqs. (4.3–4.7) and (4.19) into the above consistency condition, the expression of the plastic multiplier is derived as follows:

$$\dot{\lambda}_{\mathrm{N}} = \frac{\mathbf{V}_{\boldsymbol{\Sigma}_{\mathrm{N}}} : \mathbf{C}^{\mathrm{e}} : \mathbf{D}}{\mathrm{H}_{\lambda}}, \tag{4.23}$$

where

$$\mathrm{H}_{\lambda} = \mathbf{V}_{\boldsymbol{\Sigma}_{\mathrm{N}}} : \mathbf{C}^{\mathrm{e}} : \mathbf{V}_{\boldsymbol{\Sigma}_{\mathrm{N}}} - h\frac{\boldsymbol{\Sigma} : \mathbf{V}_{\boldsymbol{\Sigma}_{\mathrm{N}}}}{(1-f)\bar{\sigma}}\left\{\mathrm{V}_{\bar{\sigma}_{\mathrm{N}}} - \mathrm{V}_{\Gamma_{\mathrm{N}}}\frac{k_{\mathrm{int}}}{a\bar{\sigma}^{2}}\right\} - (1-f)(\mathbf{V}_{\boldsymbol{\Sigma}_{\mathrm{N}}} : \mathbf{I})\left\{\mathrm{V}_{f_{\mathrm{N}}} - \frac{k_{\mathrm{int}}\mathrm{V}_{\Gamma_{\mathrm{N}}}}{3f(1-f)a\bar{\sigma}}\right\}. \tag{4.24}$$

By substituting Eqs. (4.19) and (4.23) into Eq. (4.21), the final expression for the elastic–plastic tangent modulus $\mathbf{C}^{\mathrm{ep}}$ is derived as:

$$\mathbf{C}^{\mathrm{ep}} = \mathbf{C}^{\mathrm{e}} - \frac{\left(\mathbf{C}^{\mathrm{e}} : \mathbf{V}_{\boldsymbol{\Sigma}_{\mathrm{N}}}\right) \otimes \left(\mathbf{V}_{\boldsymbol{\Sigma}_{\mathrm{N}}} : \mathbf{C}^{\mathrm{e}}\right)}{\mathrm{H}_{\lambda}}. \tag{4.25}$$

4.3.2 Numerical implementation and validation

The constitutive equations described above have been implemented into the finite element code ABAQUS/Standard in the framework of large strains and three-dimensional approach. In order to maintain the frame invariance for the rate constitutive equations, objective derivatives of the tensor variables are used. More specifically, the Jaumann objective rate of the Cauchy stress tensor is considered in the present investigation, which is also consistent with the approach used in the finite element code ABAQUS/Standard. The simulations are performed by considering a single finite element with only one Gauss integration point, which is then subjected to various boundary conditions depending on the required values of strain-path ratio or stress triaxiality ratio. For each loading increment, the stress state is updated using a predictor-corrector approach, following the numerical procedure proposed by Morin et al. (2015). The resulting numerical algorithm is detailed in Table 4.1.

Table 4.1. Algorithm for the predictor-corrector approach used for the numerical implementation of the D–K model.

For t=0, initialization of all state variables ($\boldsymbol{\Sigma}=\mathbf{0}$, $\overline{\varepsilon}^{\mathrm{p}}=0$, $\overline{\sigma}=\overline{\sigma}_0$, $f=f_0$, $\mathrm{a}=\mathrm{a}_0$)

Compute elastic predictor $\boldsymbol{\Sigma}_{\mathrm{n+1}}^{\mathrm{elast}}=\boldsymbol{\Sigma}_{\mathrm{n}}+\mathbf{C}^{\mathrm{e}}:\Delta\boldsymbol{\varepsilon}_{\mathrm{n+1}}$

Determine the parameter $\xi_{\mathrm{n+1}}$ by solving the nonlinear equation $\mathrm{T}\left(\xi_{\mathrm{n+1}},f_{\mathrm{n}},\Gamma_{\mathrm{n}}\right)-\mathrm{T}_{\mathrm{n+1}}^{\mathrm{elast}}=0$, in which T is the triaxiality ratio (i.e., $\mathrm{T}=\dfrac{\Sigma_{\mathrm{m}}}{\Sigma_{\mathrm{eq}}}$)

Compute $\mathrm{F}=\left[\left(\Sigma_{\mathrm{m}}^{\mathrm{elast}}\right)_{\mathrm{n+1}}^{2}+\left(\Sigma_{\mathrm{eq}}^{\mathrm{elast}}\right)_{\mathrm{n+1}}^{2}\right]-\left[\left(\Sigma_{\mathrm{m}}\left(\xi_{\mathrm{n+1}}\right)\right)_{\mathrm{n+1}}^{2}+\left(\Sigma_{\mathrm{eq}}\left(\xi_{\mathrm{n+1}}\right)\right)_{\mathrm{n+1}}^{2}\right]$

Plastic yield condition:

- If $\mathrm{F}<0$ then (elastic loading)

  $\boldsymbol{\Sigma}_{\mathrm{n+1}}=\boldsymbol{\Sigma}_{\mathrm{n+1}}^{\mathrm{elast}}$, $\Delta\overline{\varepsilon}^{\mathrm{p}}=0$, $\Delta\overline{\sigma}=0$, $\Delta f=0$ and $\Delta\Gamma=0$

  Tangent modulus $\mathbf{C}^{\mathrm{ep}}=\mathbf{C}^{\mathrm{e}}$

- Else (plastic loading)

  Compute $\Delta\lambda_{\mathrm{N,n}}$ and $\xi_{\mathrm{n+1}}$ using the plastic correction

  Compute the corrected $\boldsymbol{\Sigma}_{\mathrm{n+1}}$

  Update the internal variables $\overline{\varepsilon}_{\mathrm{n+1}}^{\mathrm{p}}$, $\overline{\sigma}_{\mathrm{n+1}}$, $f_{\mathrm{n+1}}$ and $\Gamma_{\mathrm{n+1}}$

  Compute the tangent modulus $\mathbf{C}^{\mathrm{ep}}=\mathbf{C}^{\mathrm{e}}-\dfrac{\left(\mathbf{C}^{\mathrm{e}}:\mathbf{V}_{\boldsymbol{\Sigma}_{\mathrm{N}}}\right)\otimes\left(\mathbf{V}_{\boldsymbol{\Sigma}_{\mathrm{N}}}:\mathbf{C}^{\mathrm{e}}\right)}{\mathrm{H}_{\lambda}}$

- End if

Return $\boldsymbol{\Sigma}_{\mathrm{n+1}}$ and $\mathbf{C}^{\mathrm{ep}}$ to ABAQUS for solving the equilibrium equations.

In order to numerically validate the algorithm described in Table 4.1 for D–K model, simulations are performed by considering an RVE subjected to two values of constant stress triaxiality ratio (i.e., T=1 and T=3). The power-hardening law, as given by Eq. (1.22d), is used for the description of isotropic hardening. The material parameters used in the simulations are summarized in Table 4.2 (see Morin et al., 2015). The numerical results in terms of normalized equivalent stress and porosity with respect to equivalent strain, obtained with the developed D–K UMAT subroutine, are shown in Figs. 4.3–4.6, along with the reference results provided by Morin et al. (2015).

Table 4.2. Material parameters used in the simulations.

E (GPa)	ν	$\overline{\sigma}_0$ (MPa)	n	f_0	k_{int} (N/m)	Γ_0
200	0.3	400	0.1	[0.01, 0.001]	1	[0., 0.5, 1.25, 2.5]

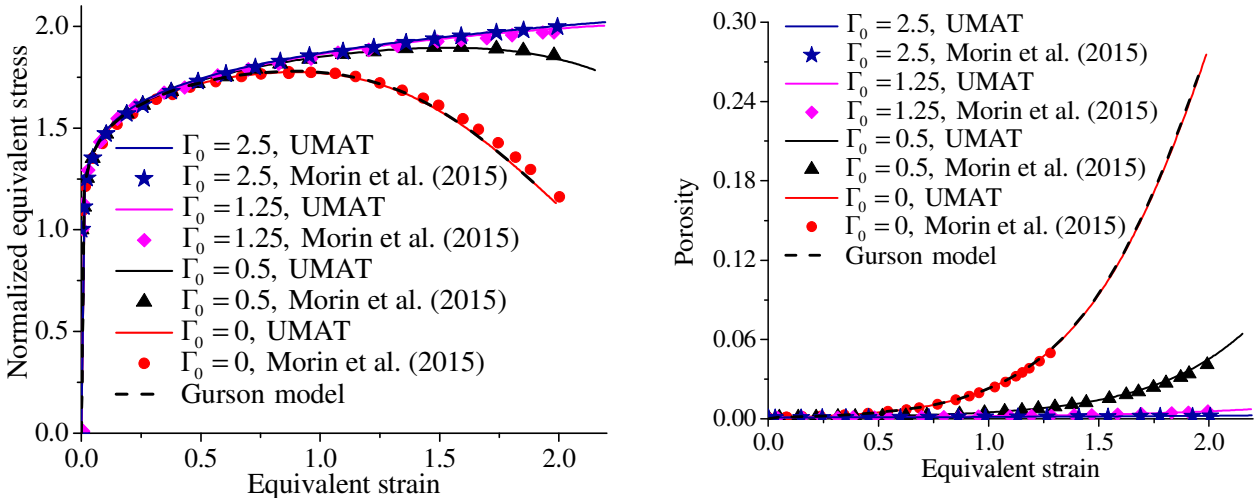

(a) (b)

Figure 4.3. Evolution of: (a) normalized equivalent stress, and (b) porosity, for stress triaxiality T=1 and initial porosity $f_0 = 0.001$.

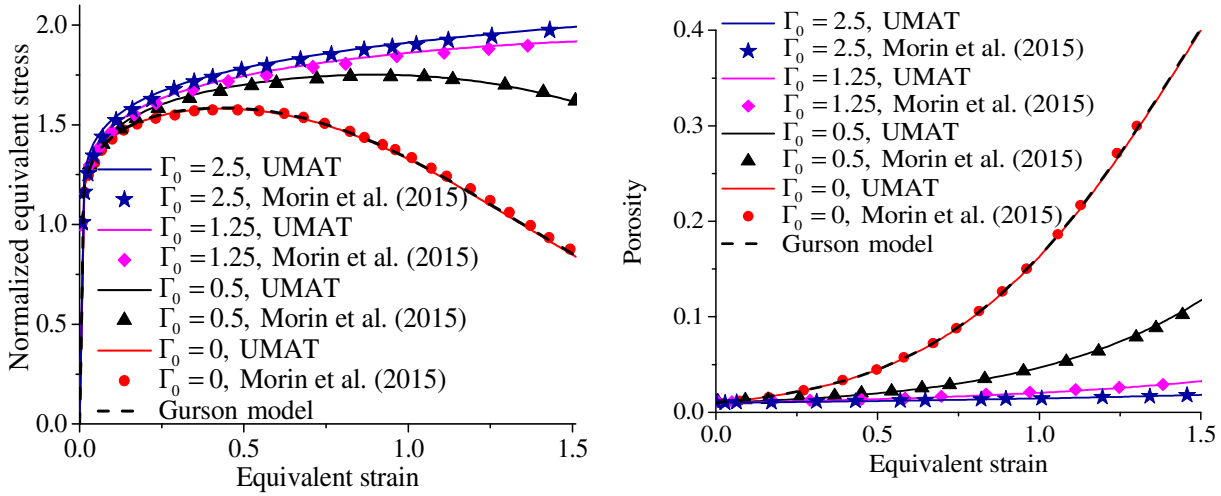

(a) (b)

Figure 4.4. Evolution of: (a) normalized equivalent stress, and (b) porosity, for stress triaxiality T=1 and initial porosity $f_0 = 0.01$.

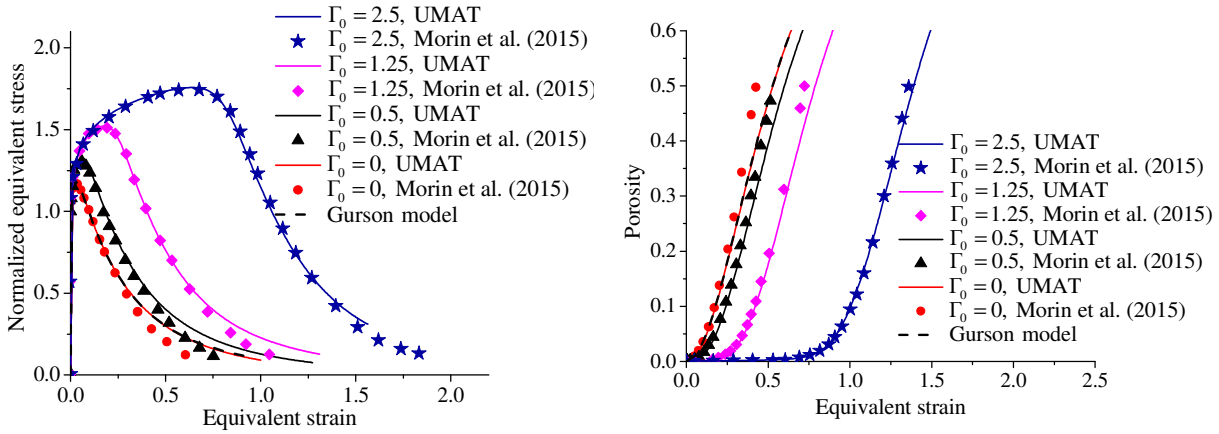

(a) (b)

Figure 4.5. Evolution of: (a) normalized equivalent stress, and (b) porosity, for stress triaxiality T=3 and initial porosity $f_0 = 0.001$.

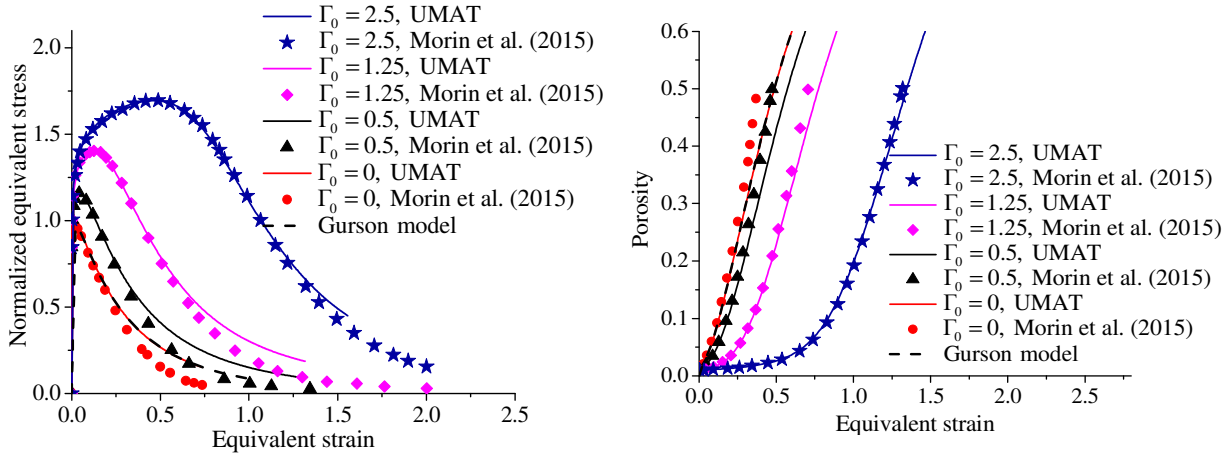

(a) (b)

Figure 4.6. Evolution of: (a) normalized equivalent stress, and (b) porosity, for stress triaxiality T=3 and initial porosity $f_0 = 0.01$.

It is recalled here that the original Gurson model is recovered from the D–K model when $\Gamma_0 = 0$. In this case, the numerical results obtained with the developed D–K UMAT subroutine can be compared with those predicted by the Gurson model, which is available in ABAQUS/Standard. When the void-size independent model is considered (i.e., D–K model with

$\Gamma_0 = 0$), all the results predicted using the developed UMAT subroutine coincide with their counterparts obtained with the Gurson model, which is fully consistent. As to the case of void-size dependent model (i.e., D–K model with $\Gamma_0 \neq 0$), it can be observed a significant difference between the results predicted by the Gurson model and those provided by the D–K model, which includes the void size effect. More specifically, for small initial porosity and moderate stress triaxiality (i.e., $f_0 = 0.001$ and T=1, respectively), a softening regime is predicted by the Gurson model, starting from an equivalent strain of about 1, while no softening regime is shown by the D–K model for high values of Γ_0 (i.e., from $\Gamma_0 = 1.25$ and more in this case, see Fig. 4.3a). However, stress softening is observed for small values of Γ_0, which is due to the rapid evolution of the porosity in this range of small initial non-dimensional parameter Γ_0 (see Fig. 4.3b). Similar trends are also observed for $f_0 = 0.01$ and T=1 (see Fig. 4.4). For moderate initial porosity as well as high stress triaxiality (i.e., $f_0 = 0.01$ and T=3, respectively), the developed UMAT subroutine for the D–K model predicts the same trends as above for both stress and porosity evolutions, which are consistent with the reference predictions provided by Morin et al. (2015).

4.4 Prediction of FLDs using the D–K model and bifurcation analysis

In this section, the D–K model is coupled with the loss of ellipticity criterion (i.e., Rice bifurcation criterion) for the prediction of localized necking in terms of FLD. According to the loss of ellipticity criterion, localized necking is predicted when the acoustic tensor ($\mathbf{Q} = \mathbf{n} \cdot \mathbf{L} \cdot \mathbf{n}$) becomes singular (see Chapter 1, Eq. (1.64)). The fourth-order tangent modulus $\mathbf{L}$ is related to the analytical elastic–plastic tangent modulus $\mathbf{C}^{ep}$ by the following expression:

$$\mathbf{L} = \mathbf{C}^{ep} + \mathbf{C}_1 - \mathbf{C}_2 - \mathbf{C}_3, \tag{4.26}$$

where the analytical elastic–plastic tangent modulus $\mathbf{C}^{ep}$ is given by Eq. (4.25), while $\mathbf{C}_1$, $\mathbf{C}_2$ and $\mathbf{C}_3$ are composed of convective stress components, which are induced by the large strain framework. Their expressions depend only on Cauchy stress components (see Chapter 2, Eq. (2.21)).

In order to investigate plastic instabilities that are inherent to the material alone, the same strategy used in Chapter 2 and 3 is applied here. It consists of the use of a single finite element with one integration point in the simulations, which results in a homogenous strain state in the material prior to the occurrence of plastic instability.

The effect of void size on the prediction of FLDs is presented for Al5754 aluminum, for which the material parameters are taken from Mansouri et al. (2014), and are summarized in Table 4.3. The additional parameter Γ_0, which incorporates the void size effect is varied here to analyze its effect on the prediction of localized necking.

Table 4.3. Material parameters for the Al5754 aluminum.

Elastic properties		Swift's hardening parameters			Initial porosity
E (GPa)	ν	K (MPa)	ε_0	n	f_0
70	0.33	309.1	0.00173	0.177	0.001

The FLDs predicted with the loss of ellipticity criterion are presented in Fig. 4.7a for the Al5754 aluminum material for three values of the initial non-dimensional parameter (i.e., $\Gamma_0 = 0$, 1.5 and 2.5). It is worth recalling that the original Gurson model, which only describes the elastic–plastic behavior with damage due to porosity growth, can be recovered from the D–K model when $\Gamma_0 = 0$. Therefore, for comparison purposes, the FLD predicted with the original Gurson model and the loss of ellipticity criterion is also presented in Fig. 4.7a. From this figure, it can be seen that the effect of the initial non-dimensional parameter on strain localization is not perceptible when only the void growth mechanism is considered in the D–K model. Moreover, strain localization does not occur in the right-hand side of the FLD (i.e., for positive biaxial strain-path ratios) due to the low values of porosity in this range of strain paths (i.e., right-hand side of FLD, see Fig. 4.7b). Indeed, in the works of Mansouri et al. (2014) and Chalal and Abed-Meraim (2015), it has been shown that, using the bifurcation theory coupled with Gurson-type models, the occurrence of strain localization for positive biaxial strain-path ratios requires the critical hardening modulus to be strongly negative.

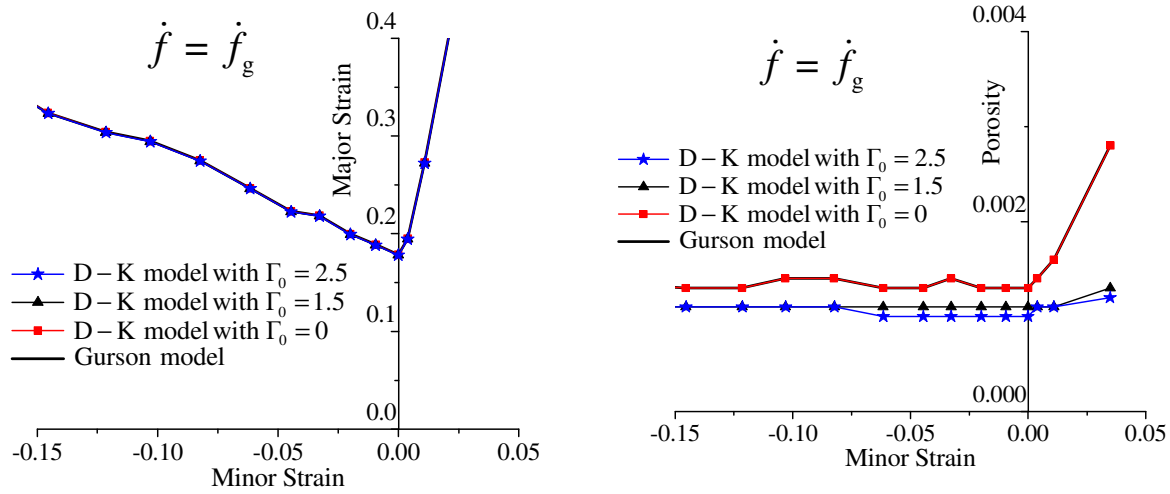

(a) (b)

Figure 4.7. FLDs (left) and porosity at localization (right) for Al5754 aluminum.

In order to further investigate the insensitivity of the strain localization predictions to the different values of the initial non-dimensional parameter (see Fig. 4.7a), the yield surface for Al5754 is illustrated in Fig. 4.8. In addition, two linear stress paths, corresponding to the extreme left (uniaxial tension) and right (balanced biaxial tension) strain paths of FLD, i.e. constant stress triaxialities of $T = 0.333$ and $T = 0.667$, respectively, are highlighted in this Fig. 4.8. Note that, within this narrow range of stress triaxiality ratio, the yield surface points corresponding to different values of initial non-dimensional parameter are almost indistinguishable, which explains the insensitivity of the predicted FLDs to the initial non-dimensional parameter, as observed in Fig. 4.7a.

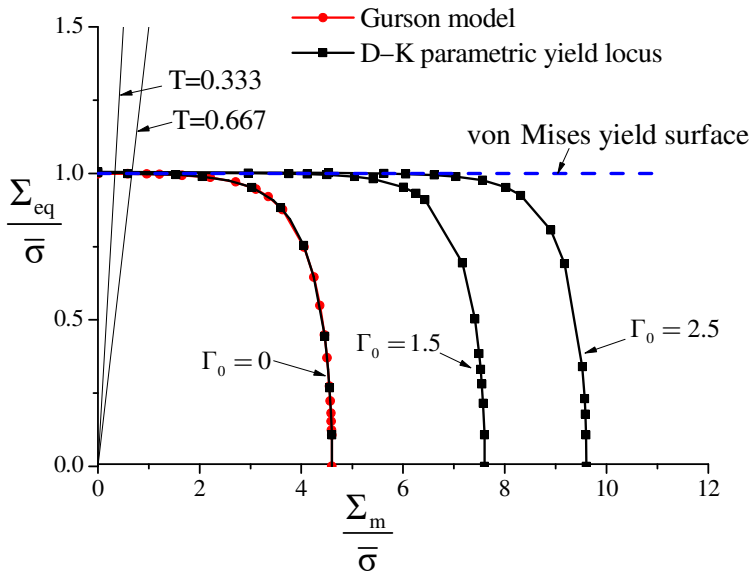

Figure 4.8. Parametric yield surface for Al5754 aluminum and $\Gamma_0 = 0$, 1.5 and 2.5 .

To better highlight the effect of the void size on strain localization, nucleation of new voids is considered in what follows, in addition to the void growth mechanism, for both the D–K model and the Gurson model. Accordingly, the evolution of porosity, with an initial value of f_0, is due to void nucleation and growth, and the porosity rate can then be partitioned as follows:

$$\dot{f} = \dot{f}_{\mathrm{g}} + \dot{f}_{\mathrm{n}}, \tag{4.27}$$

where $\dot{f}_{\mathrm{g}}$ and $\dot{f}_{\mathrm{n}}$ represent the rates of the porosity due to void growth and void nucleation, respectively. Void nucleation is considered here to be strain-controlled (i.e., $A_N \neq 0$ and $B_N = 0$, see Chapter 1, Eqs. (1.28-1.30)). The material parameters for the void nucleation mechanism, i.e., f_N , s_N and ε_N are reported in Table 4.4 for Al5754 aluminum. The corresponding FLDs are presented in Fig. 4.9a, for which the porosity evolution due to nucleation and growth of voids is considered.

Table 4.4. Nucleation parameters for the Al5754 aluminum.

Material	f_N	s_N	ε_N
Al5754	0.034	0.1	0.320

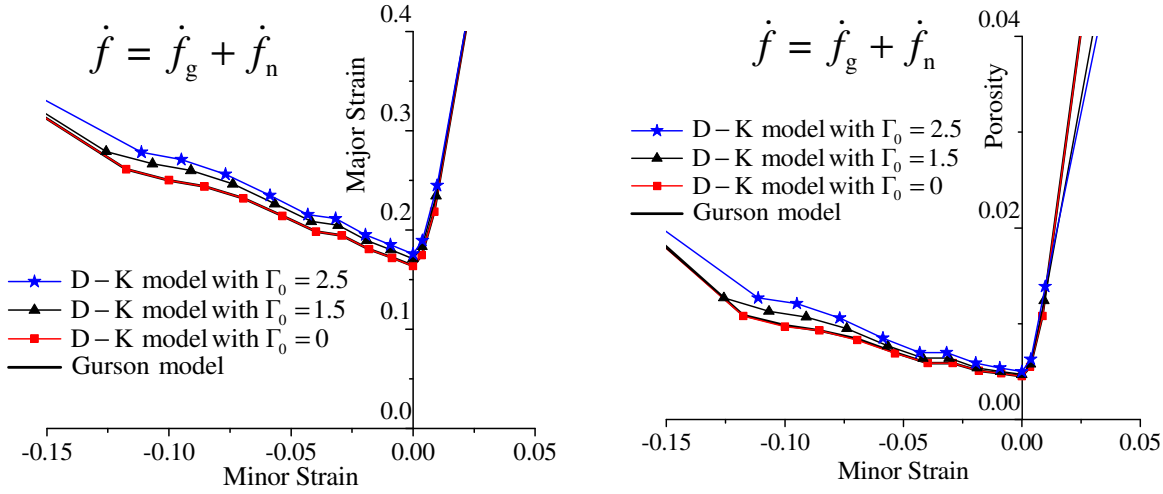

(a) (b)

Figure 4.9. FLDs (left) and porosity at localization (right) for Al5754 aluminum. Porosity evolution is due to growth and nucleation.

In contrast to the FLDs obtained with porosity evolution only due to growth (i.e., D–K model and Gurson model, see Fig. 4.7a), Fig. 4.9a shows that the effect of void size on strain localization is more perceptible when both growth and nucleation of porosity are considered. More specifically, the smaller values of the initial non-dimensional parameter induce rapid softening (see the stress–strain curves in Figs. 4.3-4.6), thereby promoting early plastic flow localization. This expectation is also confirmed by Fig. 4.9a, which shows that the predicted FLDs are lowered as the initial non-dimensional parameter Γ_0 decreases. This trend is confirmed by Fig. 4.9b, which also shows the effect of the initial non-dimensional parameter on the values of porosity at localization. Note that when $\Gamma_0 = 0$, the FLD predicted by the D–K model coincides with that of the Gurson model, which is also consistent with the theoretical expectation for this particular case (i.e., the Gurson model is recovered from the D–K model when $\Gamma_0 = 0$).

In addition to growth and nucleation of voids during plastic deformation in ductile materials, coalescence of voids can also be introduced to model the rapid decay of the material

stress carrying capacity. Tvergaard and Needleman (1984) have modified the original Gurson model to account for the complete kinetics of voids within the material (i.e., nucleation, growth and coalescence), which corresponds to the well-known Gurson–Tvergaard–Needleman (GTN) model. Using the GTN model, the actual void volume fraction f in the expression of the yield surface is replaced by the effective porosity f^*, which is given by Eq. (1.32). The parameters associated with the coalescence regime, i.e., f_{cr} and δ_{GTN} for the Al5754 aluminum material are reported in Table 4.5. The elastic–plastic and nucleation parameters are kept the same as those used in Tables 4.3 and 4.4.

Table 4.5. Coalescence parameters for the Al5754 aluminum.

Material	f_{cr}	δ_{GTN}
Al5754	0.00284	7

The corresponding FLDs obtained with the developed approach are presented in Fig. 4.10a. As discussed above, coalescence causes sudden loss of the stress carrying capacity and, therefore, the hardening modulus becomes strongly negative. It has been shown in Mansouri et al. (2014) that the prediction of strain localization using the loss of ellipticity criterion requires strongly negative hardening modulus in the right-hand side of the FLD (i.e., for biaxial stretching loading paths), which can be reached by considering the coalescence mechanism. Consequently, it can be observed in Fig. 4.10a that more localization points are obtained in the right-hand side of the FLD, as compared to the FLDs in Figs. 4.7a and 4.9a, thanks to the consideration of the void coalescence mechanism. Note that the experimental FLD, which is taken from Brunet et al. (1998), is also shown in Fig. 4.10a for qualitative comparison.

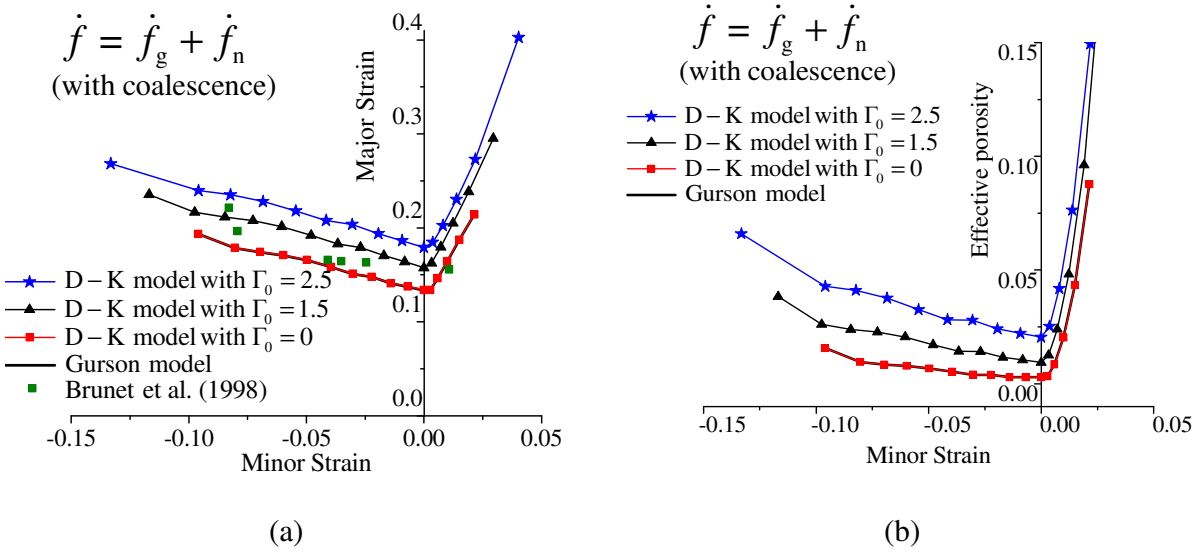

(a) (b)

Figure 4.10. FLDs (left) and effective porosity at localization (right) for Al5754 aluminum. Porosity evolution is due to growth, nucleation and coalescence.

Analogous to the previous FLDs, obtained using only growth and nucleation of voids, the FLDs in Fig. 4.10a are clearly sensitive to variation of the initial non-dimensional parameter, with lowered FLDs for smaller values of the initial non-dimensional parameter. Note also that for $\Gamma_0 = 0$, the FLD predicted by the D–K model coincides with that of the GTN model, for which the q-parameters for the void interactions are set equal to 1. Furthermore, the yield surfaces for different values of initial non-dimensional parameter are presented in Fig. 4.11, in which the evolution of porosity is attributed to growth, nucleation and coalescence. In contrast to Fig. 4.8, with porosity evolution only due to growth, Fig. 4.11 depicts distinct yield surfaces for different initial values of non-dimensional parameter, and for all possible values of stress triaxiality ratio, which leads in turn to a more perceptible effect on the prediction of FLDs.

In Fig. 4.11, the von Mises yield surface is also illustrated. It is noteworthy that when the initial non-dimensional parameter is increased (i.e., void size is decreased), an increase in the material strength is observed (i.e., expansion of the yield surface). However, the strength of porous material cannot be larger than the strength of the sound material (i.e., undamaged material). This requires that the initial non-dimensional parameter Γ_0 must vary within a physically admissible range, i.e. $0 \le \Gamma_0 \le \Gamma_0^{\lim}$, in which the parametric D–K yield surface must

lie between the Gurson yield surface (i.e., $\Gamma_0 = 0$) and the undamaged elastic–plastic yield surface. This physical range of initial non-dimensional parameter Γ_0 can be identified by comparing the parametric D–K yield surface for various values of Γ_0 with the particular cases of Gurson yield surface (i.e., $\Gamma_0 = 0$) and von Mises yield surface (i.e., undamaged isotropic elastic–plastic model), as illustrated in the above Fig. 4.11. This figure reveals that the physical upper bound of the non-dimensional parameter Γ_0 is 2.5, for which the ratio between the equivalent stress and the yield stress of the fully dense matrix is lower or equal to 1 (i.e., $\frac{\Sigma_{eq}}{\overline{\sigma}} \leq 1$).

It is worth noting that the coalescence criterion used in the present model does not take the effect of void size into account. Other coalescence criteria including the effect of void size can be combined with the present approach. Among them, the constitutive model for nanoporous materials proposed by Gallican and Hure (2017), in which the effect of void size on the coalescence regime has been considered.

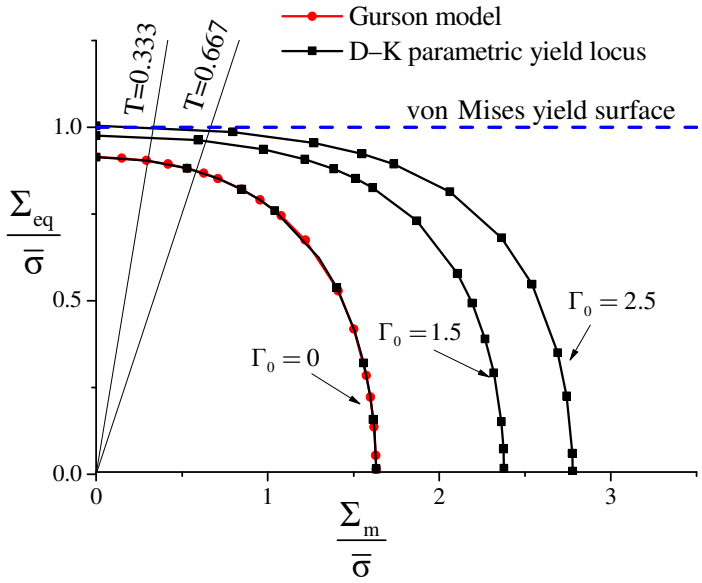

Figure 4.11. Parametric yield surface for Al5754 aluminum and $\Gamma_0 = 0, 1.5$ and 2.5. Porosity evolution is due void growth, void nucleation and void coalescence.

It has been found out by Wen et al. (2005) that the effect of void size on the material response is more pronounced for higher values of initial porosity. In order to further investigate

this observation, the effect of void size on the ductility limits for high initial porosity is also investigated hereafter. Note that, in the previous simulations, the initial porosity for the Al5754 aluminum material has been identified by Brunet et al. (1998) to a value of 0.001. To reveal the effect of void size on strain localization for larger values of initial porosity, Fig. 4.12 provides the FLDs predicted by the D–K model for different values of initial non-dimensional parameter, when the initial porosity is set to 0.01. The simulation results reported in Fig. 4.12 are obtained with the D–K model, in which the porosity evolution takes into account all three mechanisms of growth, nucleation and coalescence of voids. As previously discussed for Gurson-type models in general, and for the D–K model in particular, porosity is the most important parameter for the sensitivity of FLDs to the void size. As shown in Fig. 4.12, for high initial porosity (i.e., $f_0 = 0.01$), the effect of the initial non-dimensional parameter on strain localization is more significant than in the case of smaller initial porosity (i.e., $f_0 = 0.001$, see Fig. 4.10a). Indeed, increasing the initial non-dimensional parameter (i.e., decreasing the void size) will increase the number of voids within the material, in order to keep the same actual porosity, which will increase in turn the number of interfaces between voids and the dense matrix. Therefore, material strain hardening will be increased in this case in the same way as material ductility. This observation has also been found by Wen et al. (2005), who concluded that the void size effects on material response is more significant for higher initial porosity.

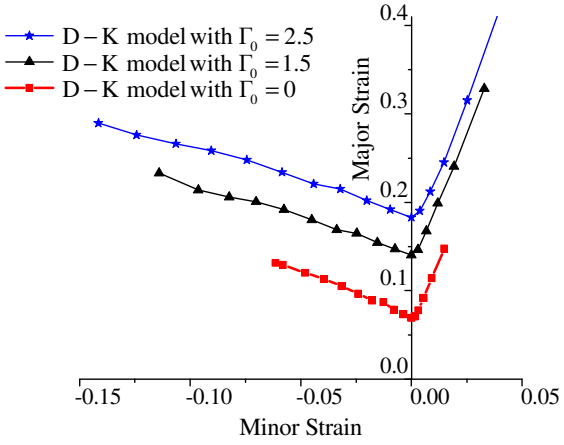

Figure 4.12. FLDs for Al5754 aluminum alloy with $f_0 = 0.01$. Porosity evolution is due to growth, nucleation and coalescence of voids.

4.5 Conclusion

In this chapter, the phenomenological model proposed by Dormieux and Kondo (2010) for ductile porous materials accounting for void size effects has been combined with the loss of ellipticity criterion to predict strain localization in thin sheet metals. The constitutive equations have been implemented together with the loss of ellipticity criterion into the finite element code ABAQUS/Standard within the framework of large strains and fully three-dimensional approach. However, the localization bifurcation criterion has been reformulated within the plane-stress framework, as classically done for the prediction of localized necking in thin sheet metals. Linear in-plane biaxial stretching loading paths have been applied for the prediction of FLDs for the Al5754 aluminum material.

Recall that the Dormieux and Kondo (2010) model, which is an extension of the original Gurson model, has been developed by performing a limit analysis for a spherical void inside a spherical RVE, and by considering a membrane with surface stresses around the void. The resulting yield function depends on the void size through a non-dimensional parameter. Considering at first only the porosity evolution due to void growth, the FLDs predicted with the present approach show no sensitivity to the void size, due to the fact that the porosity at localization remains very small. However, when successively nucleation and coalescence are considered in the evolution of porosity, FLDs exhibit more sensitivity to the void size. More specifically, it is found that the ductility limits are lowered as the initial non-dimensional parameter is decreased (i.e., when the void size is increased). In other words, decreasing the void size has a beneficial effect on formability. These findings are consistent with what has been reported in the literature regarding the void size effects on material response. Nonetheless, there is an upper bound for the initial non-dimensional parameter Γ_0 (i.e., lower bound for the void size), which is physically admissible. This upper bound, which depends on the material parameters, is identified so that the parametric D–K yield surface must lie between the Gurson yield surface and the undamaged elastic–plastic yield surface (i.e., sound material with no void). Moreover, it is found that the FLD predicted using the D–K model with an initial non-dimensional parameter $\Gamma_0 = 0$ coincides with that obtained with the Gurson model, which is also consistent with the material response for this particular case. Finally, the investigation of the combined effect of void size and initial porosity shows that smaller void sizes lead to an increase

in the ductility limits, and this trend becomes more significant for high initial porosity, due to the increase of void-matrix interface strength within the material.

Conclusions and future work

5.1 Conclusions

Various approaches have been developed in the literature for the characterization of the formability of thin sheet metals using the concept of forming limit diagrams (FLDs). Among these approaches, the experimental methods for the determination of FLDs, numerical approaches based on finite element method, and theoretical criteria for the prediction of diffuse and localized necking are worth mentioning. In the present thesis, plastic instabilities such as diffuse and localized necking have been predicted, based on the bifurcation analyses and multi-zone approach. Concerning the material mechanical behavior, the present work focuses on the implementation of elastic–plastic–damage Gurson-based models within the framework of large strains and fully three-dimensional approach. The resulting constitutive equations have been formulated in an incremental form in order to simplify their numerical implementations into finite element code. The resulting numerical tool, combining several Gurson-based models with various instability criteria, has been implemented into the finite element code ABAQUS/Standard via user defined material (UMAT) subroutines, and validated before being used for the prediction of plastic instabilities. The assumption of plane-stress conditions has been considered in the formulation of the plastic instability criteria, since the intended application of the present work is the prediction of ductility limits of thin sheet metals.

Among the bifurcation-based plastic instability criteria, the general bifurcation criterion (GB) and limit-point bifurcation criterion (LPB) predict diffuse necking, while the loss of strong ellipticity criterion (LOSE) and loss of ellipticity criterion (LOE) predict localized necking. These four bifurcation criteria have been combined in the first part of the thesis with the GTN model for the prediction of FLDs. The effects of non-associative plasticity and stress-controlled nucleation, which induce non-normality in the plastic flow, on the occurrence of diffuse and localized necking have been investigated. The predicted results show that, for all the studied variants of the GTN model, the hierarchical order of the FLDs is consistent with the established

theoretical classification, which states that the GB criterion is a lower bound to all the bifurcation criteria, in terms of necking prediction, while the LOE criterion provides an upper bound.

The comparative analysis between the LOE criterion and M–K initial imperfection approach, in terms of prediction of localized necking, shows that when the geometric or material imperfection tends to zero (i.e., no initial imperfection), the FLD predicted with the M–K approach tends to that obtained with the LOE criterion. More specifically, the limit strains are lowered when the initial imperfection factors are increased for the M–K approach. Accordingly, it is concluded that the LOE criterion provides an upper bound for the prediction of strain localization, as compared to the M–K approach. Moreover, it has been shown that the thickness-based imperfection as well as the hardening-based imperfection have a significant destabilizing effect on the prediction of limit strains, as compared to damage-based imperfections.

In order to investigate the effect of void size on the FLDs, the Dormieux and Kondo (2010) yield function for ductile porous materials accounting for void size effects has been combined with the LOE criterion to predict strain localization for Al5754 aluminum. The FLDs predicted with the developed numerical approach show no sensitivity to the void size when the porosity evolution is considered only due to void growth. The reason for this observation is that the porosity at localization remains very small. However, when successively void nucleation and void coalescence are considered in the evolution of porosity, FLDs exhibit more sensitivity to the void size. More specifically, it is found that the necking limit strains are lowered when the void size is increased. In other words, decreasing the void size has a beneficial effect on formability. It has also been found out that the void size effect on the FLDs becomes more significant for high initial porosity. These findings are consistent with what has been reported in the literature regarding the void size effects on the material response.

5.2 Future work

After the conclusions from the main results detailed in the present thesis, the following aspects will be pursued in future work:

- In order to take into account the effect of material initial anisotropy, only one anisotropic yield surface (i.e., Hill'48) has been coupled with the GTN damage model in the present

thesis. Indeed, the yield surface curvature significantly affects the ductility limits of the material. Therefore, consideration of other non-quadratic anisotropic yield surfaces, such as Karafillis and Boyce (1993), Bron and Besson (2004), Barlat et al. (2005), Banabic et al. (2005), Aretz and Barlat (2013), Cazacu (2018) with the GTN damage model will definitely turn out to be an interesting investigation.

- In order to model the softening regime in the material mechanical response, two classes of damage theories have been developed in the literature, i.e. micromechanics-based damage models, such as the Gurson–Tvergaard–Needleman (GTN) model (adopted in this work), and the Continuum Damage Mechanics (CDM). A comparative analysis of these two classes of constitutive models for the FLD prediction of different materials will be an important study in order to determine the most suitable approach for a given material. This comparative study should also be accompanied by the material parameter identification of each model based on the same experimental data (see, e.g., Incandela et al., 2004; Teaca et al., 2010; Cao et al., 2013, 2015).

- The conventional Gurson-based models assume that the void shape remains spherical throughout the plastic deformation. Indeed, this assumption is valid under high values of stress triaxiality ratio. However, for low values of stress triaxiality ratio, experiments have revealed that the void shape changes from spherical to general spheroids. In this regard, the implementation of void shape dependent yield surfaces, such as the Gologanu–Leblond–Devaux (GLD) model (see Gologanu et al. (1993, 1994) and Madou and Leblond (2012a, 2012b, 2013)), should be made in future studies to investigate the void shape effects on the prediction of FLDs.

- In the present work, the void-size dependent constitutive model proposed by Dormieux and Kondo (2010) has been implemented to investigate the void size effects on the material ductility limits. However, the Dormieux and Kondo (2010) model is limited to void sizes of the order of nanometer (10^{-9} m). In order to investigate the effect of micron-sized voids, the yield surface proposed by Wen et al. (2005) could serve as an alternative to Dormieux and Kondo (2010) model for microvoids. Moreover, future work should deal with the implementation of Monchiet and Kondo (2013) yield surface, which serves as the

combination of Dormieux and Kondo (2010) yield function and the GLD model. Therefore, the combined effect of the void size and void shape on the FLD could be investigated.

- Experimental observations have revealed that the through-thickness shear and normal loads have a non-negligible effect on the material ductility limits, especially in the incremental forming and hydroforming processes. Therefore, future work should also focus on the effects of through-thickness normal and shear stresses on the prediction of FLDs.

Part II : Résumé en français de la thèse

Introduction

Le contexte

Avec les récents progrès réalisés dans le domaine des procédés de fabrication, la mise en forme des tôles minces est devenue un procédé d'importance majeure dans de nombreuses industries, telles que l'automobile, l'emballage, l'aérospatiale, la fabrication d'appareils électroménagers, d'ustensiles de cuisine, etc. Dans ce contexte de mise en forme des tôles minces, la forme finale souhaitée est obtenue en appliquant à la matière première de grandes déformations plastiques, sans enlèvement de matière. Presque toute la matière première est utilisée dans ce précédé de mise en forme, avec un taux de production très élevé. Par conséquent, ce précédé est bien adapté à la production de masse, et peut être entièrement automatisé. L'augmentation des coûts des matières premières et les grandes préoccupations mondiales de réduction des gaz à effet de serre conduisent les industriels à fabriquer des structures de plus en plus légères. La concurrence accrue entre les entreprises de construction automobile conduit, d'une part, au développement de matériaux plus avancés et plus légers et nécessite, d'autre part, des procédés et des outils de formage efficaces pour que le produit fini puisse être fabriqué sans défauts. Par conséquent, la compréhension approfondie de ces défauts et leur prédiction précoce lors du processus de déformation plastique sont cruciales afin d'augmenter la productivité des procédés de mise en forme.

Objectifs de la thèse

Dans le cadre de la mise en forme des tôles minces, l'utilisation du concept de courbes limites de formage (CLF) est importante. Le tracé de ces CLFs permet de fournir les limites des déformations que la tôle peut supporter sans amorçage de défauts indésirables. La détermination expérimentale des CLFs est un processus coûteux et long, et les résultats souffrent souvent d'un manque de reproductibilité. Les objectifs de la thèse relèvent du domaine des prédictions théoriques et numériques des CLFs. Pour cela, la thèse vise, dans un premier temps, à modéliser le comportement mécanique des matériaux ductiles couramment utilisés dans les procédés de mise en forme des tôles minces. L'accent sera mis sur le modèle d'endommagement de Gurson, qui est basé sur l'analyse micromécanique des milieux poreux. Diverses extensions du modèle d'endommagement de Gurson, telles que l'incorporation des effets de l'anisotropie du matériau,

de la taille des cavités, de la nucléation des cavités, de la coalescence des cavités et de la plasticité non associée, seront considérées, et leur impact sur la formabilité des tôles sera étudié et discuté. Quant à la prédiction des instabilités plastiques, les critères de striction diffuse et localisée, basés sur la théorie de bifurcation et l'approche multi-zones (imperfection initiale), seront mis en œuvre et comparés les uns aux autres. L'outil numérique résultant pourra être utilisé dans le cadre de l'élaboration de nouvelles nuances de matériaux métalliques aux propriétés mécaniques améliorées (i.e., résistance et ductilité), tout en respectant les nouvelles règlementations liées aux émissions de CO_2.

Organisation du manuscrit

Le manuscrit est organisé en cinq chapitres dont le contenu est détaillé ci-dessous :

Dans le premier chapitre, un aperçu général des procédés de mise en forme des tôles minces, de leurs applications et des principaux défauts susceptible d'apparaître lors de ces procédés sont présentés. Ensuite, le concept et le contexte historique de courbes limites de formage (CLFs) sont rappelés. De plus, le chapitre 1 inclut également un état de l'art des théories de l'endommagement ductile et des différents critères d'instabilités plastiques pouvant être utilisés pour la prédiction de la striction diffuse et localisée.

Le deuxième chapitre est consacré au couplage du modèle d'endommagement de Gurson–Tvergaard–Needleman (GTN) avec quatre critères de bifurcation pour la prédiction des CLFs. Les effets de certains mécanismes déstabilisants, relatifs à la plasticité non associée et à la non-normalité de la règle d'écoulement plastique, sur la prédiction des CLFs sont étudiés.

Le troisième chapitre traite de l'analyse comparative de la théorie de bifurcation et de l'approche multi-zone (imperfection initiale) dans la prédiction de la striction localisée. Le modèle d'endommagement GTN est utilisé en conjonction avec l'approche d'imperfection initiale. Deux types d'imperfections initiales sont considérés : imperfection géométrique et imperfection matérielle. L'outil numérique développé est également appliqué à la prédiction des limites de formabilité de l'aluminium Al2024.

Le quatrième chapitre traite de la mise en œuvre d'une version étendue du modèle d'endommagement GTN, prenant en compte l'effet de la taille des cavités. Ce dernier modèle, dépendant de la taille des cavités, est couplé à la théorie de bifurcation afin de prédire les CLFs et

d’étudier l’effet de taille sur les prédictions de formabilité. Comme pour le chapitre précédent, ce modèle étendu sera appliqué à l’étude des limites de ductilité de l'aluminium Al5754.

Enfin, les différents travaux présentés dans ce manuscrit sont synthétisés dans une conclusion générale, suivie de quelques perspectives sur les travaux futurs.

Chapitre 1. État de l’art sur les limites de formabilité des tôles minces

La mise en forme par déformation plastique des tôles minces est l’un des procédés de fabrication les plus utilisés. Dans ce type de procédés, une tôle mince, initialement plane, est déformée plastiquement à l'aide d'un ou plusieurs outils massifs (e.g., poinçon, matrice). Les opérations de mise en forme des tôles minces peuvent être généralement classées en trois catégories : découpage, pliage, et emboutissage. Un autre procédé similaire à l’emboutissage est l’hydroformage, dans lequel la tôle est déformée plastiquement à l'aide d'un fluide sous pression. Ce procédé s'avère particulièrement bien adapté à la mise en forme de pièces tubulaires. Les progrès récents dans les procédés de mise en forme ont conduit au développement d'un procédé plutôt nouveau, connu sous le nom de procédé de formage incrémental (IF). Le procédé de formage incrémental à un point (SPIF) consiste à déplacer un outil hémisphérique sur l'ensemble de l'échantillon en plusieurs passes pour obtenir la forme finale souhaitée. Les figures 1.1 et 1.2 illustrent quelques opérations de mise en forme de tôles minces.

Défauts courants rencontrés en mise en forme des tôles minces

Les procédés de mise en forme des tôles minces ont généralement des cadences de production très élevées. Cependant, les défauts produits au cours de ces procédés sont la principale cause de rebut des pièces formées. Le plissement, la striction et la rupture sont les défauts les plus courants observés lors de la déformation plastique de la tôle. Des plis peuvent apparaître dans la bride, le mur ou sur le corps principal de la pièce emboutie, comme illustré sur la Fig. 1.5. La rupture se produit lors du formage de la tôle, lorsque les déformations dépassent la déformation critique de rupture. La striction se produit en raison de l'instabilité plastique au sein de la pièce, due à une diminution brutale et locale de l'épaisseur. La striction peut être classée en deux types : striction diffuse et striction localisée. La striction diffuse peut être interprétée comme l'évolution progressive d'un état de déformation homogène vers un état de déformation quasi-

homogène ou hétérogène. La striction diffuse est souvent précurseur de la striction localisée, qui est considérée comme plus critique que la précédente. La striction localisée est caractérisée par la diminution locale de l'épaisseur de la tôle sous forme d'une bande localisée. La striction localisée est généralement suivie de la rupture finale de la structure, sous forme d'une fissure apparente à l'intérieur de la bande localisée.

Concept de courbe limite de formage

Afin de caractériser la formabilité des tôles minces, plusieurs chercheurs ont mis au point différents tests expérimentaux en laboratoire (voir, par exemple, Erichsen (1914) et Ghosh (1975)). Cependant, Gensamer (1946) a été le premier à établir les bases du tracé d'une courbe limite, basée sur les mesures des déformations locales. Par la suite, Keeler et Backofen (1963) ont mis en place une procédure similaire basée sur les déformations ε_1 et ε_2 à rupture d'une tôle soumise à l'expansion biaxiale (i.e., $\varepsilon_1 > 0$ et $\varepsilon_2 > 0$). Les déformations principales ε_1 et ε_2 sont communément appelées déformation majeure et mineure, respectivement. Plus tard, Goodwin (1968) a étendu le concept de courbe limite de formage (CLF) pour des déformations principales mineures négatives (i.e., $\varepsilon_2 < 0$ et $\varepsilon_1 > 0$). La CLF complète obtenue par Goodwin (1968) est représentée sur la Fig. 1.11b. Dans le cas d'une CLF typique, les déformations limites sont mesurées au moment de l'apparition d'une striction diffuse ou localisée. D'autres concepts de courbe limite à rupture (CLR) ou de courbe limite de plissement ont également été introduits par d'autres chercheurs, pour lesquels les déformations limites sont mesurées au moment de l'apparition d'une fissure ou d'un plissement, respectivement. La Fig. 1.12 représente les formes typiques de CLF ou CLR. Aussi, il a été montré dans la littérature que les CLFs, basées sur la mesure des déformations, sont très sensibles aux changements de trajets de chargement (voir, par exemple, Hiwatashi et al., 1998; Kuroda et Tvergaard, 2000). À cette fin, plusieurs chercheurs (voir, e.g., Arrieux, 1995, 1997; Stoughton, 2000) ont proposé une transformation des CLFs de l'espace des déformations principales vers l'espace des contraintes principales.

Détermination expérimentale des CLFs

Depuis l'introduction du concept de CLF par Keeler et Goodwin, plusieurs procédures expérimentales ont été proposées pour déterminer les CLFs des tôles minces. Parmi ces

procédures, des essais de traction uniaxiale, des essais de gonflement hydraulique, et des essais de poinçonnage sont d'une importance capitale. Dans le cas des essais de traction uniaxiale, des éprouvettes rectangulaires sont utilisées, comme illustré sur la Fig. 1.14. Pour les essais de gonflement hydraulique, une pression hydraulique est appliquée pour déformer plastiquement les éprouvettes à travers des matrices elliptiques (voir Fig. 1.15). Contrairement au test du gonflement hydraulique, les tests de Keeler, de Marciniak, de Nakazima et de Hasek sont basés sur des éprouvettes à géométrie rectangulaire, qui sont déformées plastiquement à l'aide d'un poinçon. Dans le cas du test de Keeler, un poinçon sphérique est utilisé pour déformer les éprouvettes. Dans le cas du test de Marciniak, une entretoise intermédiaire trouée est placée entre l'éprouvette et le poinçon plat creux afin de réduire les frottements (voir illustration dans la Fig. 1.17). Dans le test de Nakazima, un poinçon hémisphérique est utilisé pour déformer des éprouvettes rectangulaires à travers une matrice circulaire (voir, par exemple, Nakazima et Kikuma, 1967 ; Nakazima et al., 1968 ; Garcia et al., 2006). La Fig. 1.18a donne une illustration schématique de l'essai d'emboutissage de Nakazima, tandis que la géométrie des éprouvettes recommandée par la norme ISO 12004-2 (2008) est présentée dans la Fig. 1.18b. Hasek (1973) a proposé d'utiliser des flancs circulaires au lieu d'une géométrie rectangulaire, comme le montre la Fig. 1.19, pour les matériaux qui présentent un phénomène de plissement lors de l'emboutissage. La Fig. 1.20 compare les formes typiques des CLFs obtenues en utilisant les différentes procédures expérimentales décrites ci-dessus. L'utilisation de l'essai Marciniak ou celui du gonflement hydraulique est adaptée pour les situations où le frottement entre le poinçon et la tôle est la cause principale de rupture.

En dépit de tous les progrès et les efforts réalisés pour la détermination expérimentale des CLFs, ces méthodes sont rarement utilisées dans l'industrie en raison de leurs inconvénients majeurs, tels que le coût élevé des essais et une faible reproductibilité des résultats. Cependant, ces méthodes sont largement utilisées dans les laboratoires de recherche en tant que référence pour valider les outils numériques nouvellement mis au point pour la prédiction théorique et numérique de la formabilité des tôles minces.

Prédiction théorique des CLFs

La prédiction théorique des CLFs nécessite l'utilisation de deux ingrédients essentiels à savoir, la loi de comportement du matériau et un critère d'instabilité plastique. Le couplage de la

loi de comportement et du critère d'instabilité plastique pour la prédiction des CLFs est schématiquement représenté sur la Fig. 1.22. Tout d'abord, un modèle de comportement est sélectionné, qui dépend du matériau étudié. Ensuite, le matériau est soumis à divers chemins de chargement proportionnels allant de la traction uniaxiale à la traction équibiaxiale. A la fin de chaque incrément de chargement, le critère d'instabilité plastique est évalué. Si le critère est satisfait, la simulation est arrêtée, et les valeurs des déformations principales à cet incrément de chargement sont considérées comme les déformations limites utilisées pour tracer la CLF. En revanche, si le critère n'est pas satisfait, le matériau est soumis à l'incrément de chargement suivant et les calculs sont à nouveau effectués.

Modèles d'endommagement ductile : état de l'art

La modélisation du comportement des matériaux métalliques joue un rôle important dans la simulation numérique des procédés de mise en forme. Les modèles de comportement permettent de décrire différents phénomènes physiques observés expérimentalement lors de la déformation du matériau, tels que l'écrouissage, l'anisotropie, l'endommagement, etc. Le phénomène d'endommagement, qui traduit la dégradation progressive des propriétés mécaniques du matériau, joue un rôle important dans la prédiction des instabilités plastiques. Dans ce contexte, deux théories d'endommagement ont été développées dans la littérature au cours des dernières décennies, à savoir les modèles d'endommagement micromécaniques, et les modèles d'endommagement continu.

Modèles d'endommagement micromécanique (modèle de Gurson)

Gurson (1977) a développé une surface de charge macroscopique pour les matériaux ductiles poreux en suivant la théorie de l'homogénéisation. La fonction de charge pour le modèle de Gurson est donnée par l'équation (1.19), qui n'implique qu'une seule variable microstructurale, à savoir la porosité. L'évolution de la porosité est donnée par l'Eq. (1.21). L'utilisation d'une seule variable microstructurale, c'est-à-dire la porosité, est généralement suffisante pour la modélisation de l'endommagement dans un matériau isotrope. Cependant, pour un matériau fortement anisotrope en grandes déformations, l'incorporation d'autres paramètres microstructuraux, tels que les formes des cavités et leurs orientations, est nécessaire. Afin de mettre en œuvre le modèle de Gurson dans les codes de calcul par éléments finis, et d'établir une

bonne représentation entre l'expérimental et les résultats simulés, plusieurs extensions heuristiques du modèle de Gurson ont été développées. Ces extensions sont décrites dans ce qui suit.

1) Considération de l'écrouissage de la matrice

Afin d'incorporer le phénomène d'écrouissage de la matrice dans le modèle de Gurson, la limite d'élasticité constante est remplacée de manière heuristique par une fonction $\overline{\sigma}\left(\overline{\varepsilon}^{\mathrm{p}}\right)$, où $\overline{\varepsilon}^{\mathrm{p}}$ est la déformation plastique équivalente du matériau constituant la matrice. Les lois d'écrouissage isotrope les plus utilisées sont présentées dans l'Eq. (1.22). Les analyses effectuées par Koplik et Needleman (1988) sur une cellule unitaire ont montré l'effet du durcissement (écrouissage) de la matrice sur l'évolution de la porosité. A cet effet, Leblond et al. (1995) et Lacroix et al. (2016) ont étendu le modèle original de Gurson en incorporant deux variables internes (Σ_1 et Σ_2) au lieu d'une seule variable ($\overline{\sigma}$), pour définir l'écrouissage isotrope (voir, Éq. (1.24)). L'expression de la fonction de charge a été de nouveau modifiée par Morin et al. (2017) pour intégrer l'écrouissage cinématique en plus de l'écrouissage isotrope.

2) Facteurs de correction

Sur la base des analyses micromécaniques de la répartition périodique des cavités sphériques et cylindriques, Tvergaard (1981) a introduit dans le modèle original de Gurson des coefficients supplémentaires, qui modélisent les interactions des cavités (i.e., q_1 , q_2 et q_3) (voir, Eq. (1.25)). Les valeurs typiques de ces coefficients d'interaction des cavités sont $q_1 = 1.5$, $q_2 = 1$ et $q_3 = q_1^2 = 2.25$. Cependant, certains chercheurs calibrent ces paramètres en fonction de l'écrouissage (voir Faleskog et al., 1998), ou de la triaxialité des contraintes et du paramètre de Lode (voir, par exemple, Vadillo et Fernández-Sáez, 2009; Vadillo et al., 2016).

3) Nucléation des cavités

Lors de la déformation plastique des matériaux poreux, de nouvelles cavités se forment en raison de la rupture des particules ou de la décohésion de l'interface particule-matrice. En traitant la nucléation des cavités comme un mécanisme non directement lié à la croissance des cavités, l'évolution de la porosité $\dot{f}$ peut être représentée comme la somme de l'évolution de la porosité

due à la croissance des cavités $\dot{f}_{\mathrm{g}}$ et celle due à la nucléation des cavités $\dot{f}_{\mathrm{n}}$. Needleman et Rice (1978) et Chu et Needleman (1980) ont proposé une approche statistique pour modéliser la nucléation des cavités. Ce modèle statistique est largement utilisé en conjonction avec le modèle d'endommagement de Gurson, et est exprimé par l'Eq. (1.28).

4) Coalescence des cavités

En raison des mécanismes de nucléation et de croissance des cavités pendant la déformation plastique, les cavités qui sont proches les unes des autres tendent à réduire l'espacement inter-vides pour fusionner en une seule cavité. Ce phénomène est connu sous le nom de coalescence des cavités. Il existe trois modes couramment observés de coalescence des cavités, à savoir la coalescence sous forme de couches, la coalescence sous forme de colonnes et l'apparition de bandes de micro-cisaillement. Ces trois modes de coalescence des cavitéssont représentés sur la Fig. 1.28.

Tvergaard (1982) et Tvergaard et Needleman (1984) ont proposé un modèle phénoménologique de coalescence des cavités en introduisant le concept de porosité effective ($f^{*}\left(f\right)$) dans le modèle d'endommagement de Gurson. Par conséquent, la surface de charge de Gurson est modifiée de manière heuristique en remplaçant la porosité par une porosité effective. La surface de charge de Gurson modifiée et l'expression de la porosité effective sont données par les équations (1.31-1.33)

Thomason (1985) a proposé un modèle phénoménologique de coalescence sous forme de couches. Pardoen et Hutchinson (2000) ont étendu le critère de coalescence de Thomason (1985) pour le cas général d'une cavité sphéroïdale. Le critère de coalescence de Thomason ne permet pas de prédire le début de coalescence pour des cavités plates. A cet effet, Benzerga (2002) a proposé un critère de coalescence en supposant un élément de volume représentatif cylindrique ayant une cavité sphéroïdale. Keralavarma et Chockalingam (2016) ont incorporé l'anisotropie plastique et les effets de forme pour le développement d'un critère de coalescence à l'aide du modèle de Gurson. Gallican et Hure (2017) ont proposé un critère de coalescence qui intègre également l'effet de la taille des cavités. Récemment, Torki et al. (2017) ont proposé un critère de

coalescence pour des chargements arbitraires, qui fournit également une borne supérieure pour les cas qui impliquent des chargements de cisaillement.

Malgré tous les travaux de recherche menés dans la littérature pour l'élaboration de critères de coalescence, la pratique actuelle repose souvent sur le critère de coalescence phénoménologique proposé par Tvergaard et Needleman (1984), car dans ce dernier, les paramètres matériaux sont relativement faciles à calibrer. Lorsque ce modèle de coalescence phénoménologique est combiné au modèle d'endommagement de Gurson, le modèle résultant est connu sous le nom du modèle d'endommagement de Gurson–Tvergaard–Needleman (GTN).

5) Forme des cavités

Le modèle original de Gurson a été développé en considérant une cavité sphérique présente à l'intérieur d'un élément de volume représentatif sphérique. De plus, les cavités sont supposées rester sphériques même après la déformation plastique. Par conséquent, le modèle de Gurson n'incorpore qu'une seule variable microstructurale, à savoir la porosité. En effet, cette hypothèse est valable pour des valeurs élevées du rapport de triaxialité des contraintes. Cependant, pour de faibles valeurs du rapport de triaxialité des contraintes, des expériences ont révélé que les formes des cavités passent de sphéroïdes sphériques à sphéroïdes générales. À cet égard, Gologanu et al. (1993, 1994) ont proposé des surfaces de charge macroscopiques en considérant des cavités ellipsoïdales allongées et aplaties dans des éléments de volume représentatifs confocaux. Contrairement au modèle d'endommagement de Gurson, leurs surfaces de charge incorporent trois variables microstructurales, c'est-à-dire le rapport d'aspect de la cavité, la porosité et l'orientation de l'axe principal de la cavité ellipsoïdale. Récemment, Madou et Leblond (2012a, 2012b, 2013) et Madou et al. (2013) ont encore étendu cette approche à des formes générales sphéroïdales de cavités.

6) Taille des cavités

Puisque la porosité est la seule variable microstructurale dans le modèle original de Gurson, la surface de charge du modèle de Gurson ne dépend donc pas de la taille des cavités. Dormieux et Kondo (2010) ont étendu le modèle d'endommagement de Gurson pour prendre en compte l'effet de la taille des cavités en considérant une membrane hypothétique entourant la nano-cavité. Dormieux et Kondo (2013) et Brach et al. (2017) ont étendu davantage la surface de charge

dépendant de la taille des cavités pour les matériaux métalliques poreux en utilisant les techniques d'homogénéisation non linéaire. De même, Monchiet et Kondo (2013) ont étendu le modèle en incorporant l'effet de la forme de la cavité en plus de sa taille. Monchiet et Bonnet (2013) ont également proposé un modèle basé sur le modèle original de Gurson, qui incorpore l'effet de taille des cavités en utilisant l'approche de plasticité à gradient de déformation. Sur la base du modèle de plasticité des dislocations de Taylor, Wen et al. (2005) ont proposé une surface de charge dépendante de la taille des cavités pour des tailles de cavités micrométriques et submicroniques.

7) Anisotropie

Dans le modèle de Gurson, le comportement plastique de la matrice correspond à celui défini par la théorie incrémentale classique de la plasticité isotrope. Afin d'étendre le modèle de Gurson aux matériaux plastiques anisotropes, Benzerga et Besson (2001) ont considéré le modèle de plasticité de Hill'48 (voir Hill, 1948) pour modéliser la plasticité du matériau constituant la matrice. Le modèle de Gurson a également été étendu de manière heuristique pour des matériaux anisotropes par d'autres auteurs, en remplaçant simplement le terme de contrainte équivalente (Σ_{eq}) dans l'expression de la fonction de charge de Gurson par la fonction de contrainte équivalente associée à un matériau anisotrope. Par exemple, Morin et al. (2018a) ont incorporé la fonction de contrainte équivalente non quadratique Yld2004-18p (voir Barlat et al., 2005) pour un matériau anisotrope dans le modèle d'endommagement GTN.

Modèles constitutifs phénoménologiques

Selon la théorie phénoménologique d'endommagement continu (appelée en anglais « Continuum Damage Mechanics (CDM) »), une variable d'endommagement est introduite dans les équations constitutives élastiques–plastiques, ce qui entraîne un adoucissement progressif de la réponse contrainte–déformation du matériau. Ce concept a été initialement proposé par Kachanov (1958), puis étendu par la suite par Rabotnov (1969), Lemaître (1992), Maire et Chaboche (1997), Brünig (2002), Bouchard et al. (2011) et Doghri (2013). La variable d'endommagement est définie comme la densité surfacique de fissures, qui sont supposées exister à la surface d'un élément de volume représentatif (EVR). En fonction de l'anisotropie et du comportement adoucissant, la variable d'endommagement peut être scalaire ou tensorielle. La

Fig. 1.30 représente un EVR considéré dans la théorie CDM pour la description de la variable d'endommagement. L'expression de la variable d'endommagement est définie par l'Eq. (1.42). La contrainte effective et la fonction de charge proposées par Lemaitre (1971) sont présentées dans les équations (1.43-1.44). Dans le modèle d'endommagement de Lemaitre, l'évolution de la variable d'endommagement dépend du taux de restitution de densité d'énergie de déformation, qui est calculé par les équations (1.46-1.47).

Prédiction de l'apparition de la striction : état de l'art

Différents critères d'instabilités plastiques théoriques et numériques ont été proposés dans la littérature au cours des dernières décennies. Ces critères peuvent prédire l'apparition de la striction diffuse ou localisée. Les critères d'instabilités plastiques peuvent globalement être classés en quatre catégories :

1) Principe de force maximale

La première catégorie est basée sur le critère de force maximale proposé par Considère (1885) pour la prédiction de la striction diffuse dans le cas particulier de la traction uniaxiale. Selon ce critère, la striction diffuse est détectée lorsque le point d'effort maximal est atteint lors de l'essai de traction uniaxiale. Le critère de Considère a ensuite été étendu au cas de chargements biaxiaux dans le plan par Swift (1952). Parallèlement, Hill (1952) a proposé un critère alternatif pour la prédiction de la striction localisée, également connu sous le nom de la théorie de l'extension nulle de Hill. Hora et al. (1996), et plus tard Mattiasson et al. (2006), ont étendu les critères de Considere et de Swift aux chargements tenant compte des changements de trajets de déformation.

2) Théories de bifurcation

La deuxième catégorie des critères d'instabilités plastiques est basée sur la théorie de bifurcation. Drucker (1956), et plus tard Hill (1958), ont jeté les bases de la théorie générale de la bifurcation pour la prédiction de la striction diffuse. Cette théorie nécessite la positivité du travail de second ordre pour un état de non-bifurcation. Un critère similaire pour la prédiction de la striction diffuse, connu sous le nom de bifurcation par point limite, a été proposé par Valanis (1989). Ce critère prédit l'apparition de la striction diffuse, qui correspond à la stationnarité du

premier tenseur des contraintes de Piola–Kirchhoff. Sur la base de la théorie de bifurcation, Rudnicki et Rice (1975), Stören et Rice (1975) et Rice (1976) ont développé un critère d'instabilité plastique pour la prédiction de la striction localisée sous la forme d'une bande de localisation. Ce critère de localisation correspond à la perte d'ellipticité des équations aux dérivées partielles régissant le problème des valeurs aux limites associé. Par la suite, Bigoni et Hueckel (1991) et Neilsen et Schreyer (1993) ont proposé un critère de striction localisée plus conservatif que le précédent, à savoir le critère de perte d'ellipticité forte. L'inconvénient majeur des critères d'instabilités plastiques basés sur la théorie de bifurcation est que ces critères ne s'appliquent qu'aux matériaux indépendants de la vitesse de déformation.

3) Approche multi-zones (imperfection initiale)

La troisième catégorie de critères d'instabilités plastiques a été popularisée par Marciniak et Kuczyński (1967), et est généralement connu sous le nom de l'approche M–K. Dans cette approche, une région hétérogène initiale est supposée exister à l'intérieur de la tôle avec des propriétés mécaniques légèrement dégradées par rapport au reste de la tôle. Par conséquent, dans l'approche M–K, la tôle est modélisée en deux zones distinctes : une zone homogène et une zone contenant le défaut (imperfection) initial. Dans l'approche originale M–K, l'hétérogénéité initiale était supposée sous la forme d'une bande étroite d'épaisseur réduite (ce qui sera considéré plus tard comme une imperfection géométrique) (voir, e.g., Mesrar et al., 1998 ; Ding et al., 2015). Cependant, Yamamoto (1978) a introduit le concept d'hétérogénéité initiale en termes de propriétés mécaniques (ce qui sera considéré plus tard comme une imperfection matérielle) à l'intérieur de la zone contenant le défaut initial. Lors de la déformation plastique, les contraintes, les déformations et les propriétés géométriques sont évaluées à la fois dans la zone homogène comme dans la bande d'imperfection. L'apparition de la striction localisée est détectée lorsque la déformation plastique à l'intérieur de la bande localisée devient très grande devant celle de la zone homogène. Un examen approfondi de l'approche M–K et de son couplage avec diverses formes de contraintes équivalentes, de surfaces de charge polycristallines et de modèles d'endommagement ductile a récemment été présenté par Banabic (2010a) et Banabic et al. (2019).

4) Théorie de perturbations linéaires

La dernière catégorie des critères d'instabilités plastiques est basée sur la théorie linéarisée de la stabilité et l'analyse de perturbations. La théorie de la perturbation linéaire peut être utilisée pour prédire à la fois la striction diffuse ou localisée, et constitue une bonne alternative à la théorie de bifurcation dans le cas particulier de matériaux dépendant de la vitesse de déformation (voir, par exemple, Fressengeas et Molinari, 1987; Dudzinski et Molinari, 1991; Toth et al., 1996). Il convient de noter que la théorie de la perturbation linéaire est moins utilisée pour la prédiction des CLFs par rapport à la théorie de bifurcation ou l'approche M–K, en raison des difficultés liées à ses implémentations numériques.

Modélisation des critères de striction basée sur la théorie de bifurcation

Critère de bifurcation générale (GB)

Drucker (1956) et Hill (1958) ont proposé un critère général pour un état de non-bifurcation pour la classe des matériaux indépendants de la vitesse de déformation. Ceci nécessite la positivité de toutes les valeurs propres associées à la partie symétrique du module tangent $\mathbf{L}^{\mathrm{B}}$. En pratique, l'apparition d'une striction diffuse est détectée numériquement lorsque la valeur propre minimale associée à la partie symétrique du module tangent $\mathbf{L}^{\mathrm{B}}$ devient non positive.

Critère de bifurcation par point limite (LPB)

Comme alternative au critère GB ci-dessus, Valanis (1989) a introduit un critère moins conservatif, appelé critère de bifurcation par point limite (LPB). Selon ce critère, la striction diffuse a lieu lorsque le premier tenseur des contraintes de Piola–Kirchhoff atteint une valeur stationnaire, ce qui suggère que la bifurcation est associée à la singularité du module tangent $\mathbf{L}^{\mathrm{B}}$, c'est-à-dire $\det\left(\mathbf{L}^{\mathrm{B}}\right)=0$, ou de manière équivalente, lorsque l'une de ses valeurs propres devient égale à zéro.

Critère de perte d'ellipticité (LOE)

Stören et Rice (1975) et Rice (1976) ont étudié l'apparition de la striction localisée sous la forme d'une bande de localisation, au passage de laquelle le gradient de vitesse est discontinu. En

pratique, la localisation est prédite numériquement lorsque la valeur minimale du déterminant du tenseur acoustique, pour toutes les orientations possibles de la normale à la bande de localisation, devient non positive. L'expression du tenseur acoustique est donnée par l'équation (1.64).

Critère de perte d'ellipticité forte (LOSE)

Semblable au critère de perte d'ellipticité ci-dessus, Bigoni et Zaccaria (1992) et Bigoni (1996) ont proposé le critère de perte d'ellipticité forte pour la prédiction de la striction localisée. On peut démontrer que ce critère de perte d'ellipticité forte est un cas particulier du critère de bifurcation générale. En pratique, la perte de condition d'ellipticité forte nécessite la positivité de toutes les valeurs propres de la partie symétrique du tenseur acoustique.

Classification théorique des critères de bifurcation

Il a été montré dans la littérature (voir, par exemple, Abed-Meraim, 1999) que les parties réelles des valeurs propres d'une matrice quelconque sont bornées par les valeurs propres minimale et maximale de la partie symétrique de cette matrice. En utilisant cette propriété mathématique, on peut montrer que la singularité du module tangent $\mathbf{L}^{B}$ ne peut pas se produire avant la perte de définie positivité de la partie symétrique de ce module tangent $\mathbf{L}^{B}$, ce qui implique que, pour la prédiction de la striction diffuse, le critère GB est plus conservatif que le critère LPB. De même, il peut être démontré que la singularité du tenseur acoustique $\mathbf{Q}$ ne peut pas se produire avant la perte de définie positivité de la partie symétrique de ce tenseur acoustique $\mathbf{Q}$. En d'autres termes, pour la prédiction de striction localisée, le critère LOSE est plus conservatif que le critère LOE.

Cadre des contraintes planes

Il convient de rappeler que la présente thèse est principalement consacrée à la prédiction de la formabilité des tôles minces. Par conséquent, les critères d'instabilités plastiques, discutés dans les sections précédentes, doivent être reformulés en tenant compte de l'hypothèse des contraintes planes. Pour cela, le module tangent élastique–plastique $\mathbf{L}$, qui est requis dans la formulation de divers critères de bifurcation, est réécrit dans le cadre d'une formulation en contraintes planes (voir équation (1.77)). Il est à noter que dans ce cas, la normale à la bande de localisation se

trouve dans le plan de la tôle et est définie par un seul angle d'orientation de la bande (voir Fig. 1.31).

Conclusion

Ce chapitre permet de dresser une vue d'ensemble des procédés de mise forme des tôles minces. Parmi les défauts observés en mise en forme des tôles minces, on peut noter l'apparition de la striction diffuse et de la striction localisée pendant la déformation plastique, ce qui limite la formabilité. Afin de caractériser la formabilité des tôles minces, quelques méthodes expérimentales et théoriques ont été présentées pour la détermination des courbes limites de formage (CLFs). Il a été démontré que la prédiction théorique/numérique des CLFs est une alternative intéressante par rapport à l'expérience. À cet égard, l'accent principal est mis sur le modèle d'endommagement de Gurson, ainsi que certaines de ses principales extensions qui ont été proposées ces dernières décennies. Quant à la prédiction des instabilités plastiques, une classification des divers critères de striction diffuse et localisée est présentée. Deux critères de bifurcation, i.e. critère de bifurcation générale et critère de bifurcation par point limite, ont été présentés pour la prédiction de la striction diffuse. Aussi, le critère de perte d'ellipticité et le critère de perte d'ellipticité forte ont été présentés pour la prédiction de la striction localisée. Une classification théorique des critères de bifurcation a également été mise en place. Cette classification a montré que le critère de bifurcation générale est plus conservatif que le critère de bifurcation par point limite, et fournit une borne inférieure à l'apparition de tout type de striction. De plus, le critère de perte d'ellipticité est moins conservatif que le critère de perte d'ellipticité forte, et fournit une borne supérieure à l'apparition d'une striction.

Chapitre 2. Modèle de Gurson–Tvergaard–Needleman (GTN) couplé à la théorie de la bifurcation

Dans ce chapitre, quatre critères d'instabilités plastiques, basés sur la théorie de bifurcation, sont couplés au modèle d'endommagement GTN pour la prédiction de la striction diffuse et de la striction localisée. Ce chapitre se concentre sur l'effet de certains mécanismes déstabilisants, dus à la plasticité non associée et à la règle d'écoulement plastique non normale, sur la prédiction des CLFs. Plusieurs variantes du modèle GTN sont combinées aux critères de bifurcation pour la

prédiction des CLFs pour des matériaux fictifs. L'ordre de prédiction des CLFs à l'aide des quatre critères de bifurcation est comparé à la classification théorique établie au chapitre 1.

Equations constitutives du modèle GTN pour les matériaux anisotropes

Dans cette section, la surface de charge quadratique de Hill (1948), qui est l'extension directe de la théorie de l'écoulement J_2 pour un matériau anisotrope, a été utilisée conjointement avec la surface de charge du modèle GTN. L'expression de la contrainte équivalente de Hill'48 est présentée dans l'équation (2.1). Dans le cadre d'une règle d'écoulement non associée, l'écoulement plastique est supposé contrôlé par un potentiel plastique Φ_P, différent de la surface de charge Φ_Y. La forme mathématique du potentiel plastique Φ_P est similaire à celle de la partie non endommagée de la surface de charge Φ_Y (i.e., $\Phi_P = \left(\frac{\Sigma_{peq}}{\overline{\sigma}}\right)^2 - 1 \leq 0$). En utilisant la condition de cohérence et les taux de porosité, de la limite élastique et du tenseur des contraintes de Cauchy, ainsi que la règle d'écoulement, les expressions du multiplicateur plastique et du module tangent élastique–plastique sont calculées. Leurs expressions sont données par les équations. (2.9-2.12). Il est à noter que, dans les cas de la plasticité non associée et d'un mécanisme de nucléation des cavités contrôlé en contrainte, le module tangent élastique–plastique est non symétrique.

Implémentation et validation numériques

Schéma d'intégration des équations différentielles

Les équations constitutives du modèle d'endommagement de GTN sont implémentées dans le code de calcul par éléments finis ABAQUS/Standard à l'aide d'une subroutine utilisateur (UMAT). Le cadre des grandes déformations et une approche tridimensionnelle sont considérés dans la formulation. La dérivée objective de Jaumann du tenseur de contraintes de Cauchy est utilisée afin de garantir l'objectivité de la loi de comportement. Un schéma d'intégration explicite, et en particulier la méthode de Runge–Kutta du $4^{ème}$ ordre, est adopté pour l'intégration numérique des équations différentielles du modèle. Avec un tel schéma d'intégration explicite, un compromis raisonnable peut être trouvé en termes de précision, du temps de calcul et de la convergence des simulations (voir Mansouri et al., 2014).

Validations numériques

La validation numérique de l'implémentation du modèle GTN dans ABAQUS/standard s'effectue en deux étapes. En premier, les résultats numériques correspondant à un chargement de traction uniaxiale, obtenus avec le modèle GTN implémenté, sont comparés à ceux obtenus à partir du modèle GTN disponible dans ABAQUS/Standard. Ensuite, l'implémentation numérique du comportement plastique anisotrope sans endommagement est validée par des comparaisons aux résultats de référence disponibles dans la littérature.

Les courbes de contrainte–déformation ainsi que d'évolution de la porosité sont illustrées par la Fig. 2.1, issues de l'UMAT développée et du modèle disponible dans ABAQUS. Comme observé, les résultats prédits avec l'UMAT sont en excellent accord avec ceux du modèle disponible dans ABAQUS, ce qui permet de valider l'implémentation numérique du modèle GTN isotrope. Afin de valider l'implémentation numérique du comportement plastique anisotrope, les résultats prédits en termes de contraintes d'écoulement normalisées et des coefficients *r* de Lankford, en fonction de l'orientation du matériau par rapport à la direction de laminage, sont présentés sur la Fig. 2.4, ainsi que les résultats de référence obtenus par Neto et al. (2018). On peut voir sur cette Fig. 2.4 que les résultats prédits sont en excellent accord avec ceux de référence, ce qui valide l'implémentation numérique du comportement anisotrope.

Prédiction de striction à l'aide du modèle GTN et des critères de bifurcation

Afin d'étudier les instabilités plastiques inhérentes au matériau seul, en excluant tous les effets structuraux (géométriques), un seul élément fini avec un point d'intégration est utilisé dans les simulations, ce qui entraîne un état de déformation homogène dans le matériau jusqu'à l'apparition de l'instabilité plastique. Des conditions aux limites correspondant à un chargement biaxial dans le plan sont appliquées à l'élément fini, afin de générer divers chargements proportionnels allant de la traction uniaxiale à la traction équibiaxiale. Le module tangent du quatrième ordre $\mathbf{L}$, impliqué dans la formulation des critères de bifurcation, est relié au module tangent élastique–plastique analytique $\mathbf{C}^{ep}$ par l'équation (2.20). Les critères d'instabilité sont implémentés dans ABAQUS via une subroutine spécifique (UVARM).

Modèle élastique–plastique anisotrope sans endommagement

Dans cette section, le modèle GTN anisotrope est paramétré de sorte à ne garder que la partie élastique–plastique sans endommagement, afin de prédire les CLFs. Les CLFs sont prédites pour les deux cas de la règle d'écoulement : plasticité associée et non associée. La Fig. 2.7 montre les CLFs prédites en utilisant les quatre critères de bifurcation. Notez que la localisation de la déformation ne se produit pas dans le côté droit de la CLF (c'est-à-dire pour les rapports de déformation positifs). En effet, il a été montré dans la littérature que, en utilisant la théorie de bifurcation avec des modèles phénoménologiques et une surface de charge lisse, l'apparition de la localisation de la déformation en expansion biaxiale nécessite un module tangent critique fortement négatif, ce qui peut être obtenu par la prise en compte du phénomène d'adoucissement. De plus, à partir de la comparaison de la Fig. 2.7a et de la Fig. 2.7b, il peut être clairement observé que la prise en compte de la plasticité non associée conduit à la prédiction de déformations limites de striction bien distinctes pour les quatre critères d'instabilités plastiques.

Plasticité associée

1) Cas de la nucléation contrôlée par la déformation

Dans cette section, la variante du modèle d'endommagement GTN incluant une nucléation contrôlée par la déformation et la plasticité associée est considérée pour la prédiction des CLFs. Il est intéressant de noter que, dans le cas de cette variante du modèle GTN, le module tangent analytique élastique–plastique $\mathbf{C}^{ep}$ est symétrique. Cependant, le module tangent de localisation $\mathbf{L}$ reste non symétrique, dû au cadre des grandes transformations considéré. La Fig. 2.8 montre les CLFs prédites en utilisant les quatre critères de bifurcation. Il est à noter que seules deux CLFs distinctes sont observées, qui correspondent à une striction diffuse (prédite par les critères GB et LPB) et une striction localisée (prédite par les critères LOSE et LOE). La raison derrière cette observation est que la partie non symétrique du module tangent $\mathbf{L}$, qui est due aux termes convectifs de contraintes, n'est pas significative pour fournir des CLFs distinctes pour la striction localisée (comme prévu par les critères LOE et LOSE), ainsi que pour la striction diffuse (comme prévu par les critères GB et LPB).

2) Cas de la nucléation contrôlée par la contrainte

Dans cette section, la variante du modèle d'endommagement GTN incluant une nucléation contrôlée par la contrainte et la plasticité associée est considérée. Notez que la nucléation contrôlée par la contrainte conduit à une non-normalité de l'écoulement plastique, ce qui se traduit par un module tangent analytique élastique–plastique $\mathbf{C}^{ep}$ non symétrique (voir équation (2.12)). La Fig. 2.10 montre les CLFs prédites par les quatre critères de bifurcation, où quatre CLFs bien distinctes sont obtenues. De plus, l'ordre hiérarchique des CLFs est bien respecté par rapport à celui établi théoriquement.

Plasticité non associée

1) Cas de la nucléation contrôlée par la déformation

Les CLFs prédites à l'aide de la variante du modèle d'endommagement GTN non associée incluant la nucléation contrôlée par la déformation sont présentées sur la Fig. 2.12. On constate que la prise en compte de la plasticité non associée, qui se traduit par un module tangent élastique–plastique analytique non symétrique, conduit à une prédiction des déformations limites de striction bien distinctes pour les quatre critères de bifurcation. Dans l'ensemble, l'ordre hiérarchique des CLFs est bien cohérent avec la classification théorique des quatre critères.

2) Cas de la nucléation contrôlée par la contrainte

Dans cette section, deux mécanismes déstabilisants sont combinés simultanément au sein des équations constitutives, à savoir la plasticité non associée et la nucléation contrôlée par la contrainte induisant une non-normalité de l'écoulement plastique. Plus précisément, le modèle d'endommagement GTN anisotrope avec une nucléation contrôlée par la contrainte est couplé aux quatre critères de bifurcation pour la prédiction des CLFs. Les CLFs prédites par cette variante du modèle GTN sont illustrées par la Fig. 2.14. Dans la partie gauche des CLFs, la prise en compte des deux mécanismes, c'est-à-dire la plasticité non associée et la nucléation contrôlée par la contrainte, ne semble pas déstabiliser la prédiction de la striction diffuse et localisée. Cependant, dans le côté droit des CLFs, ces mécanismes déstabilisants conduisent à des déformations limites distinctes pour les critères de striction diffuse (c'est-à-dire GB et LPB). Semblable aux

combinaisons précédentes de mécanismes déstabilisants, l'ordre hiérarchique de la prédiction des CLFs, dans ce cas, est à nouveau bien cohérent par rapport à la classification théorique.

Comparaison des prédictions issues des variantes du modèle GTN avec plasticité associée et non associée

La Fig. 2.15 compare les CLFs prédites par le modèle GTN tenant compte des variantes avec une plasticité associée (AFR GTN) et non associée (NAFR GTN), couplées à une nucléation contrôlée par la déformation. On constate que les CLFs prédites en considérant le modèle NAFR GTN sont inférieures à celles prédites par le modèle AFR GTN pour tous les trajets de déformation considérés. La raison derrière cette observation est que l'introduction d'une non-normalité dans le modèle GTN (i.e., modèle NAFR GTN) apporte des effets plus déstabilisants, ce qui favorise l'apparition précoce de l'instabilité plastique.

Orientations des bandes de localisation

L'orientation de la bande de localisation, telle que prédite par les critères LOSE et LOE pour différents trajets de déformation, est analysée sur la Fig. 2.16. Les orientations des bandes de localisation sont également comparées à celles calculées analytiquement par le critère de striction localisée de Hill (1952). Pour les variantes considérées du modèle GTN, on peut voir que les orientations de la bande de localisation prédites sont en excellent accord avec la formule analytique de Hill'52 (c'est-à-dire $\theta = \tan^{-1}\left(\sqrt{-\rho}\right)$, où ρ est le rapport des composantes du taux de déformation mineure et majeure), pour les critères LOSE et LOE.

Conclusion

Dans ce chapitre, le modèle d'endommagement GTN a été couplé à quatre critères d'instabilités plastiques basés sur l'analyse de bifurcation pour la prédiction des CLFs. Deux de ces critères d'instabilités plastiques, c'est-à-dire le critère de bifurcation générale (GB) et le critère de bifurcation par point limite (LPB), prédisent l'apparition de la striction diffuse, tandis que les deux autres critères, c'est-à-dire le critère de perte d'ellipticité forte (LOSE) et le critère de perte d'ellipticité (LOE), prédisent l'apparition de la striction localisée. Dans un premier temps, les CLFs ont été prédites par la première variante du modèle d'endommagement GTN, combinant une nucléation contrôlée par la déformation et la plasticité associée. Dans le cas de cette variante

du modèle GTN, le module tangent analytique élastique–plastique est symétrique, tandis que le module tangent de localisation est non symétrique en raison du cadre des grandes transformations. Dans ce cas, les critères GB et LPB prédisent les mêmes déformations critiques pour la striction diffuse, tandis que les critères LOSE et LOE prédisent les mêmes déformations limites pour la striction localisée. Ensuite, une deuxième variante du modèle GTN, incluant la nucléation contrôlée par la contrainte, est considérée, ce qui se traduit par un module tangent analytique non symétrique. Dans ce cas, le critère GB prédit des déformations limites inférieures à celles obtenues avec le critère LPB. En ce qui concerne la striction localisée, le critère LOSE prédit des déformations limites inférieures à celles données par le critère LOE. Des effets déstabilisants similaires sur la striction diffuse et localisée ont également été observés en considérant une autre variante du modèle GTN, incluant la plasticité non associée. Dans tous les cas étudiés, l'ordre hiérarchique de prédiction des CLFs s'est avéré cohérent avec la classification théorique établie au préalable, qui révèle que le critère GB est une borne inférieure de tous les critères de bifurcation, en termes de prédiction de striction, tandis que le critère LOE fournit une borne supérieure.

Chapitre 3. Analyse comparative entre l'approche d'imperfection M–K et le critère de perte d'ellipticité

Contrairement au précédent chapitre, qui traite des prédictions des CLFs à l'aide de différents critères de bifurcation, ce chapitre traite de la prédiction des CLFs par le critère d'imperfection de Marciniak et Kuczyński (M–K) combiné au modèle GTN. Les CLFs sont prédites en supposant des imperfections initiales géométriques (épaisseur) et/ou matérielles. Un lien théorique est également établi entre l'approche d'imperfection M–K et le critère de perte d'ellipticité (critère de bifurcation de Rice) pour la prédiction de la striction localisée. Ensuite, en considérant différents types d'imperfections initiales, une étude de sensibilité par rapport aux paramètres est menée afin de déterminer les paramètres les plus influents sur la localisation des déformations. L'outil numérique développé est également utilisé pour prédire les CLFs d'un aluminium AA2024, qui sont ensuite comparées aux résultats expérimentaux.

Approche d'imperfection M–K pour la prédiction de la striction localisée

Dans l'approche d'imperfection de Marciniak et Kuczyński (M–K), une imperfection initiale est supposée exister dans la tôle sous la forme d'une bande étroite. L'imperfection initiale peut être considérée comme une bande étroite d'épaisseur réduite (imperfection géométrique), une bande d'imperfection aux propriétés mécaniques légèrement dégradées (imperfection matérielle), ou la combinaison d'imperfections géométrique et matérielle. La Fig. 3.1 montre l'illustration schématique d'une bande d'imperfection présente à l'intérieur de la zone homogène. Le facteur d'imperfection géométrique initial est défini dans l'Eq. (3.1). L'orientation initiale θ_0 de la bande de localisation est modifié successivement, avec un balayage complet du plan de la tôle, afin de sélectionner les déformations critiques minimales. L'évolution de l'orientation de la bande θ et du facteur d'imperfection géométrique sont donnés par les équations (3.7-3.8). La localisation est supposée avoir lieu lorsque le rapport des taux de déformation plastique équivalente à l'intérieur de la bande d'imperfection et dans la zone homogène, c'est-à-dire $\dot{\bar{\varepsilon}}^{pB} / \dot{\bar{\varepsilon}}^{pH}$, dépasse une valeur critique. Cette dernière est généralement égale à 10 dans la littérature. Il est à noter que dans le cas où aucune imperfection géométrique et/ou matérielle n'est considérée, l'approche d'imperfection M–K devient équivalente au critère de bifurcation de Rice.

Implémentation numérique et validations

L'outil numérique résultant du couplage du modèle GTN avec l'approche d'imperfection M−K est implémenté dans MATLAB pour la prédiction des CLFs. La zone homogène de la tôle, comme illustrée sur la Fig. 3.1, est soumise à des trajets proportionnels de déformation dans le plan. Pour chaque trajet de déformation considéré, l'angle initial d'orientation de la bande θ_0 varie de 0° à 90°. Pour l'ensemble des valeurs de l'angle initial de la bande et du trajet de chargement, l'état de contrainte ainsi que les variables internes sont mis à jour pour chaque incrément de chargement, selon un schéma d'intégration explicite. Il convient de noter que les gradients de vitesse dans la bande de l'imperfection et dans la zone homogène ne dépendent que de trois inconnues : $\dot{\varepsilon}_{11}^{H}$, $\dot{\gamma}_1$ et $\dot{\gamma}_2$. Ces trois inconnues sont calculées en résolvant le système de trois équations simultanées données par le système d'équations (3.20). L'algorithme complet de l'approche M−K couplée au modèle GTN est présenté sur la Fig. 3.2.

Afin de valider numériquement l'implémentation des équations constitutives dans le logiciel MATLAB, quelques simulations préliminaires sont d'abord effectuées, et les résultats obtenus à partir du logiciel MATLAB sont comparés aux résultats obtenus à partir du modèle GTN disponible dans ABAQUS/Standard. Les résultats présentés dans les Figs. 3.3-3.6, pour une sollicitation de traction uniaxiale, de cisaillement pur et de traction équibiaxiale, montrent que les résultats numériques issus de l'algorithme développé dans le logiciel MATLAB sont en excellent accord avec les résultats de référence fournis par le modèle GTN ABAQUS. Ceci permet de valider numériquement l'implémentation de l'outil utilisé.

Prédiction de la striction localisée à l'aide de l'approche d'imperfection M−K et du critère de perte d'ellipticité

Imperfection géométrique

L'imperfection initiale dans l'approche M−K est supposée ici géométrique sous forme d'épaisseur réduite dans la bande de localisation, par rapport à l'épaisseur dans la zone homogène. On peut voir sur la Fig. 3.7 que lorsque le facteur d'imperfection géométrique initiale est augmenté, une augmentation des déformations critiques est observée. De plus, lorsque le facteur

d'imperfection géométrique initiale devient égal à 1 (c'est-à-dire que l'épaisseur de la bande d'imperfection devient égale à celle de la zone homogène), la CLF obtenue avec l'approche M–K coïncide avec celle prédite par le critère de bifurcation de Rice. Par conséquent, le critère de bifurcation de Rice fournit une limite supérieure aux déformations critiques prédites par l'approche M–K.

Imperfection matérielle due à la porosité initiale

Une bande d'imperfection avec une porosité initiale légèrement supérieure à celle de la zone homogène est considérée ici dans l'approche M–K. Le facteur d'imperfection initiale du matériau dans ce cas est représenté par la différence de la porosité initiale entre la bande d'imperfection et la zone homogène, c'est-à-dire $\Delta f_0 = f_0^B - f_0^H$. Les CLFs obtenues avec quatre valeurs différentes Δf_0 sont illustrées par la Fig. 3.9b. Il est intéressant de noter que lorsque $\Delta f_0 = 0$, la CLF prédite par l'approche M–K coïncide avec celle donnée par le critère de bifurcation de Rice, ce qui est cohérent avec les prédictions précédentes utilisant l'imperfection géométrique initiale. D'autre part, lorsque Δf_0 augmente, les déformations critiques diminuent. Ce résultat est tout à fait cohérent avec les études antérieures rapportées dans Yamamoto (1978) et Needleman et Triantafyllidis (1978), dans lesquelles il a été conclu que la forme globale des CLFs dépend principalement de la différence de porosité initiale Δf_0, et non pas de la valeur de la porosité initiale dans chaque zone (c'est-à-dire f_0^B et f_0^H).

Imperfection matérielle due à la nucléation des cavités

Dans cette section, l'amplitude gaussienne f_N, qui représente la fraction volumique totale des cavités susceptibles de nucléer, est considérée comme légèrement plus élevée dans la bande d'imperfection, par rapport à celle de la zone homogène. Le facteur d'imperfection matérielle dans ce cas est exprimé par $\Delta f_N = f_N^B - f_N^H$. Les CLFs obtenues avec quatre valeurs différentes du facteur d'imperfection Δf_N sont présentées sur la Fig. 3.10b. On peut observer que les déformations critiques obtenues avec l'approche M–K sont sensibles à ce facteur. De plus, la CLF prédite avec l'approche M–K tend vers la CLF obtenue avec le critère de bifurcation de Rice

lorsque le facteur d'imperfection initiale Δf_N tend vers 0, ce qui est cohérent avec les résultats numériques précédents.

Imperfection matérielle due à la coalescence des cavités

L'effet de l'imperfection matérielle, due à la coalescence des cavités, sur la prédiction des CLFs est étudié. La porosité critique f_{cr} et le facteur d'accélération δ_{GTN}, impliqués dans le modèle de coalescence des cavités, sont considérés comme des imperfections initiales de coalescence séparées. Les CLFs obtenues avec l'approche M–K sont présentées sur les Fig. 3.11b et 3.11d. Il est intéressant de noter que, globalement, l'effet de ces facteurs d'imperfection initiale sur la prédiction de CLFs est similaire à celui observé dans les précédentes études sur les imperfections matérielles.

Imperfection matérielle due à l'écrouissage

Dans les travaux antérieurs de Needleman et Triantafyllidis (1978), il a été démontré que, dans le cas de l'approche M–K, des CLFs qualitativement équivalentes peuvent être obtenues en calibrant deux catégories différentes d'imperfection initiale : imperfection initiale due à l'écrouissage, et imperfection initiale due à la porosité initiale. Afin d'approfondir ici cette observation, la bande d'imperfection dans l'approche M–K est supposée avoir un coefficient d'écrouissage K de la loi de Swift légèrement plus petit que celui de la zone homogène. Par conséquent, le facteur d'imperfection initiale dans ce cas est exprimé par $\Delta K = K^H - K^B$. Les CLFs obtenues pour quatre valeurs différentes de ΔK sont présentées sur la Fig. 3.12b. On peut observer que les déformations critiques sont plus faibles lorsque le facteur d'imperfection initiale ΔK est augmenté, ce qui est parfaitement cohérent avec les prédictions précédentes utilisant divers types d'imperfections. De plus, la CLF prédite avec l'approche M–K devient équivalente à celle obtenue avec le critère de bifurcation de Rice lorsqu'il n'y a pas d'imperfection d'écrouissage dans la bande (i.e., $\Delta K = 0$).

Comparaison des CLFs obtenues en utilisant différentes imperfections initiales

Afin de déterminer les facteurs d'imperfections initiales les plus influents, et pour identifier ceux qui jouent un rôle clé dans l'apparition de la localisation des déformations, une étude

comparative entre les différents facteurs d'imperfection initiale, présentés plus haut, est menée. La Fig. 3.13 illustre la variation de la déformation critique majeure normalisée, prédite avec l'approche M–K, en fonction du pourcentage d'augmentation du facteur d'imperfection initiale ϑ, qui est défini par les équations (3.22-3.23) pour différents types d'imperfections. De cette étude comparative, les conclusions suivantes peuvent être tirées :

- Les déformations critiques sont faibles lorsque le pourcentage de variation du facteur d'imperfection initiale est grand, et ce pour l'ensemble des types d'imperfection initiale considérés. Cet effet du type d'imperfection initiale sur les déformations critiques est plus important pour des trajets de chargement proches de la traction équibiaxiale que de la traction uniaxiale.

- À la différence des imperfections matérielles liées aux paramètres d'endommagement, les déformations critiques, et donc les CLFs, sont plus sensibles aux imperfections initiales associées à l'épaisseur et à l'écrouissage.

- En ce qui concerne les imperfections matérielles liées à l'endommagement, l'effet de l'imperfection initiale due à la porosité critique sur la prédiction des déformations critiques est le plus significatif, ce qui révèle que la porosité critique est le paramètre le plus influent sur la prédiction des CLFs parmi les paramètres d'endommagement.

Application à la prédiction de CLF pour l'aluminium AA2024

L'outil numérique développé dans ce chapitre est maintenant utilisé pour prédire la formabilité de l'alliage d'aluminium AA2024. Les CLFs prédites sont également comparées à la CLF expérimentale rapportée dans Janbakhsh et al. (2012). La Fig. 3.14 montre les CLFs prédites en utilisant trois différents types d'imperfections initiales dans l'approche d'imperfection M–K, c'est-à-dire l'imperfection géométrique, l'imperfection due à l'écrouissage et l'imperfection due à la porosité critique. Notez que les CLFs sont en excellent accord avec la CLF expérimentale lorsque le facteur d'imperfection initiale géométrique est $f_0 = 0.995$, ou lorsque celui dû à l'écrouissage est $\Delta K = 7\text{MPa}$, ou alors lorsque celui dû à la porosité critique est $\Delta f_{cr} = 0.003$. Dans l'ensemble, on peut conclure que pour l'aluminium AA2024, l'imperfection géométrique

initiale et l'imperfection due à l'écrouissage sont considérées comme les plus pertinents pour la prédiction des CLFs en utilisant l'approche d'imperfection initiale M–K.

Conclusion

Dans ce chapitre, un outil numérique a été développé pour prédire les CLFs en combinant le modèle d'endommagement GTN avec l'approche d'imperfection initiale de Marciniak–Kuczyński (M–K). Pour l'approche M–K, l'effet de l'imperfection initiale géométrique, basée sur la variation d'épaisseur ainsi que d'autres types imperfections matérielles, sur la prédiction des CLFs a été étudié pour un matériau fictif. Il a été montré que les limites de ductilité prédites sont abaissées à mesure que le niveau d'imperfection initiale est augmenté. Il a été montré aussi que le type d'imperfection géométrique (i.e. épaisseur) ainsi que le type d'imperfection initiale due à l'écrouissage ont un effet déstabilisant significatif sur la prédiction des déformation critiques. En ce qui concerne les imperfections matérielles basées sur les paramètres d'endommagent, l'effet de l'imperfection initiale due à la porosité critique sur la prédiction des CLFs est le plus significatif. La CLF pour un alliage d'aluminium AA2024 est également estimée en considérant l'imperfection initiale géométrique (épaisseur) ainsi que les imperfections matérielles (i.e., due à l'écrouissage et à la porosité critique).

Chapitre 4. Effet de la taille des cavités sur la prédiction des CLFs

La littérature scientifique a révélé le fort effet de la taille des cavités sur la réponse d'un matériau poreux. Plusieurs surfaces de charge ont été développées pour incorporer les effets de taille des cavités dans les matériaux poreux ductiles. Dans ce chapitre, le modèle constitutif dépendant de la taille des cavités, proposé par Dormieux et Kondo (2010), est combiné avec le critère de perte d'ellipticité de Rice pour prédire les CLFs. L'outil numérique résultant est appliqué à la prédiction des CLFs de l'alliage d'aluminium Al5754.

Modèle dépendant de la taille des cavités de Dormieux–Kondo (D–K)

Dormieux et Kondo (2010) ont étendu le modèle original de Gurson en considérant une membrane hypothétique entourant une cavité sphérique présente à l'intérieur d'un élément volumique représentatif (EVR) sphérique, comme illustré sur la Fig. 4.1. Un paramètre non dimensionnel Γ est introduit dans la surface de charge, qui est inversement proportionnel à la

taille des cavités. Les équations paramétriques de la surface de charge D−K sont présentées par l'équation (4.2). En considérant l'incompressibilité de la matrice entourant la cavité, l'évolution de la taille de la cavité a été modélisée par Morin et al. (2015), et est donnée par l'équation (4.6). En utilisant la condition de cohérence, et en exprimant les dérivées partielles de la surface de charge par rapport aux variables internes, le multiplicateur plastique et le module tangent analytique sont calculés. Leurs expressions finales sont données par les équations (4.23-4.25).

Implémentation et validation numériques

Les équations constitutives du modèle D−K ont été implémentées dans le code de calcul par éléments finis ABAQUS/Standard dans le cadre des grandes déformations. Pour chaque incrément de chargement, l'état de contrainte est mis à jour à l'aide d'une approche prédiction−correction, suivant la procédure numérique proposée par Morin et al. (2015). L'algorithme numérique résultant est détaillé dans le Tableau 4.1. Afin de valider l'implémentation numérique du modèle D−K, des simulations sont effectuées en considérant un EVR soumis à deux valeurs constantes de rapport de triaxialité des contraintes (c'est-à-dire T = 1 et T = 3). Les résultats numériques, en termes de contrainte équivalente normalisée et de porosité par rapport à la déformation équivalente, sont présentés sur les Fig. 4.3-4.6, ainsi que les résultats de référence fournis par Morin et al. (2015). On peut observer à partir de ces figures que les prédictions issues de l'implémentation du modèle D−K dans ABAQUS sont très proches des résultats de référence fournis par Morin et al. (2015).

Prédiction des CLFs à l'aide du modèle D–K et de l'analyse de bifurcation

Dans la présente étude, le modèle D−K a été couplé au critère de bifurcation de Rice pour la prédiction de la striction localisée. L'effet de la taille des cavités sur la prédiction des CLFs est présenté pour l'aluminium Al5754, pour lequel les paramètres matériau sont tirés de Mansouri et al. (2014). Les CLFs obtenues sont présentées sur la Fig. 4.7a. Cette figure montre que l'effet de la taille initiale des cavités sur la localisation des déformations n'est pas perceptible lorsque seul le mécanisme de croissance des cavités est pris en compte dans le modèle D−K. Pour mieux mettre en évidence l'effet de la taille des cavités sur la localisation des déformations, le mécanisme de nucléation des cavités est considéré dans ce qui suit, en plus du mécanisme de croissance des cavités. Les CLFs correspondantes sont présentées sur la Fig. 4.9a. Contrairement au cas précédent avec un seul mécanisme de croissance des cavités, la Fig. 4.9a montre que l'effet

de la taille initiale des cavités sur la localisation des déformations est plus perceptible lorsque la croissance et la nucléation des cavités sont considérées. Plus spécifiquement, les valeurs plus petites du paramètre non dimensionnel induisent un adoucissement plus rapide de la réponse mécanique, favorisant ainsi la localisation précoce des déformations. En plus de la croissance et de la nucléation des cavités lors de la déformation plastique, la coalescence des cavités peut également être introduite pour accélérer l'évolution de la porosité. Le modèle de coalescence des cavités de Tvergaard et Needleman (1984) a été considéré conjointement avec le modèle D–K. Les CLFs correspondantes obtenues avec l'approche développée sont présentées sur la Fig. 4.10a. De manière analogue aux prédictions précédentes, obtenues en utilisant uniquement la croissance et la nucléation des cavités, les CLFs correspondantes (voir Fig. 4.10a) sont clairement sensibles à la variation du paramètre non dimensionnel.

Il a été montré par Wen et al. (2005) que l'effet de la taille des cavités sur la réponse du matériau est plus prononcé pour des valeurs plus élevées de la porosité initiale. Afin d'approfondir cette observation, l'effet de la taille des cavités sur les limites de ductilité pour une porosité initiale élevée est également étudié. Pour révéler l'effet de la taille des cavités sur la localisation des déformations pour des valeurs plus importantes de la porosité initiale, la Fig. 4.12 fournit les CLFs prédites par le modèle D–K pour différentes valeurs de la taille initiale des cavités, lorsque la porosité initiale est fixée à 0.01. La Fig. 4.12 révèle que lorsque la porosité initiale est élevée (par exemple, $f_0 = 0.01$), l'effet de la taille initiale des cavités sur la localisation est plus important que dans le cas d'une porosité initiale faible (i.e., $f_0 = 0.001$, voir Fig. 4.10a).

Conclusion

Dans ce chapitre, le modèle phénoménologique proposé par Dormieux et Kondo (2010) pour les matériaux poreux ductiles tenant compte des effets de la taille des cavités a été combiné avec le critère de perte d'ellipticité de Rice pour prédire la localisation des déformations dans les tôles minces. Considérant, dans un premier temps, seulement l'évolution de la porosité due à la croissance des cavités, les CLFs prédites avec la présente approche ne montrent pas de sensibilité à la taille des cavités, du fait que la porosité au moment de la localisation reste très faible. Cependant, lorsque successivement la nucléation et la coalescence sont considérées dans l'évolution de la porosité, les CLFs présentent une plus grande sensibilité à la taille des cavités.

Plus spécifiquement, on constate que les limites de ductilité sont plus basses lorsqu'on augmente la taille initiale des cavités. En d'autres termes, la diminution de la taille des cavités a un effet bénéfique sur la formabilité. De plus, cette tendance devient plus significative pour une porosité initiale élevée, en raison de l'augmentation de la résistance des interfaces vide-matrice dans le matériau.

Conclusions générales et perspectives

Conclusions

Dans la présente thèse, les instabilités plastiques associées à l'apparition de la striction diffuse et localisée ont été prédites en utilisant la théorie de bifurcation et l'approche multi-zone. Parmi les critères d'instabilités plastiques basés sur la bifurcation, le critère de bifurcation générale (GB) et le critère de bifurcation par point limite (LPB) prédisent la striction diffuse ; tandis que le critère de perte d'ellipticité forte (LOSE) et le critère de perte d'ellipticité (LOE) prédisent l'apparition de la striction localisée. Ces quatre critères de bifurcation ont été combinés avec plusieurs variantes du modèle GTN pour la prédiction des CLFs des tôles minces. Les résultats numériques montrent que l'ordre hiérarchique des CLFs est cohérent avec la classification théorique, qui établit que le critère GB est une borne inférieure de tous les critères de bifurcation, en termes de prédiction de la striction, alors que le critère LOE fournit une borne supérieure. L'analyse comparative entre le critère LOE et l'approche d'imperfection initiale M–K montre que, lorsque l'imperfection géométrique ou matérielle tend vers zéro, les CLFs prédites avec l'approche M–K tendent vers celle obtenue avec le critère LOE. De plus, les déformations limites associées à l'apparition de la striction localisée sont plus faibles lorsque les facteurs d'imperfection initiale sont augmentés pour l'approche M–K. En conséquence, le critère LOE fournit une limite supérieure pour la prédiction de la localisation des déformations, par rapport à l'approche M–K. Il a été également montré que le type d'imperfection basé sur l'épaisseur ainsi que l'imperfection initiale due à l'écrouissage ont un effet déstabilisant significatif sur la prédiction des déformations limites, par rapport aux imperfections initiales basées sur les paramètres d'endommagement. Afin d'étudier l'effet de la taille des cavités sur la prédiction des CLFs, la surface de charge de Dormieux et Kondo (2010), tenant compte de l'effet de la taille des cavités, a été combinée avec le critère de bifurcation de Rice (LOE) pour prédire la localisation

des déformations de l'alliage d'aluminium Al5754. Les CLFs prédites ne montrent pas de sensibilité à la taille des cavités lorsque seul le mécanisme de croissance des cavités est considéré. Cependant, lorsque successivement la nucléation des cavités et leur coalescence sont considérées dans l'évolution de la porosité, les CLFs présentent une plus grande sensibilité à la taille des cavités. Aussi, les résultats numériques ont permis de révéler que l'effet de la taille des cavités sur la prédiction des CLFs devient plus significatif lorsque la porosité initiale est élevée.

Perspectives

Après les conclusions des principaux résultats détaillés dans la présente thèse, les aspects suivants seront poursuivis dans les futurs travaux :

- Afin de prendre en compte l'effet de l'anisotropie initiale du matériau sur les limites de ductilité, une seule surface de charge anisotrope (i.e., Hill'48) a été couplée au modèle d'endommagement GTN dans ce travail. En effet, la courbure de la surface de charge peut affecter significativement la formabilité du matériau. Par conséquent, la prise en compte d'autres surfaces de charge anisotropes non quadratiques, telles que Karafillis et Boyce (1993), Bron et Besson (2004), Barlat et al. (2005), Banabic et al. (2005), Artez et Barlat (2013), Cazacu (2018), dans le modèle d'endommagement GTN constituera certainement une perspective intéressante.

- Afin de modéliser le régime d'adoucissement dans la réponse mécanique du matériau, deux classes de théories d'endommagement ont été développées dans la littérature, à savoir les modèles d'endommagement basés sur la micromécanique, tels que le modèle de Gurson–Tvergaard–Needleman (GTN) (adopté dans ce travail), et le modèle d'endommagement continu (CDM). Une analyse comparative de ces deux classes de modèles d'endommagement pour la prédiction des CLFs de différents matériaux pourra être une contribution importante afin de déterminer l'approche la plus appropriée pour un matériau donné. Cette étude comparative devrait également être accompagnée d'une procédure d'identification des paramètres matériaux de chaque modèle à partir des mêmes données expérimentales (see, e.g., Incandela et al., 2004; Teaca et al., 2010; Cao et al., 2013, 2015).

- Les modèles conventionnels basés sur le modèle original de Gurson supposent que la forme des cavités reste sphérique au cours de la déformation plastique. En effet, cette hypothèse est valable pour des valeurs élevées du rapport de triaxialité des contraintes. Cependant, pour les faibles valeurs du rapport de triaxialité des contraintes, des expériences ont révélé que la forme des cavités passe de sphéroïde sphérique à sphéroïde générale. Dans ce contexte, la mise en œuvre de surfaces de charge dépendantes de la forme des cavités, telles que le modèle de Gologanu–Leblond–Devaux (GLD) (voir Gologanu et al., 1993,1994) et Madou et Leblond (2012a, 2012b, 2013), peuvent apporter des prédictions plus proches de l'expérience en termes de limites de ductilité.

- Dans le présent travail, le modèle constitutif dépendant de la taille des cavités proposé par Dormieux et Kondo (2010) a été combiné au critère de striction localisée de Rice pour étudier les effets de la taille des cavités sur les limites de ductilité des matériaux. Cependant, le modèle de Dormieux et Kondo (2010) est limité à des tailles de cavité de l'ordre du nanomètre (10^{-9} m). Afin d'étudier l'effet des cavités de l'ordre du micromètre, la surface de charge proposée par Wen et al. (2005) pourrait servir d'alternative au modèle de Dormieux et Kondo (2010) pour les microcavités. Aussi, la surface de charge développée dans les travaux de Monchiet et Kondo (2013) permet une combinaison des effets liés à la taille des cavités et à l'évolution de leurs formes, comme c'est le cas dans le modèle de Dormieux et Kondo (2010) et le modèle GLD, respectivement.

- Des observations expérimentales ont révélé que le cisaillement dans l'épaisseur ainsi que les contraintes normales à la surface de la tôle peuvent avoir des effets non négligeables sur les limites de ductilité des matériaux, en particulier dans le cas du formage incrémental et de l'hydroformage. Par conséquent, les futurs travaux devraient également se pencher sur l'effet de ces contraintes dans l'épaisseur sur la prédiction des CLFs.

References

Abed-Meraim F, Balan T, Altmeyer G. Investigation and comparative analysis of plastic instability criteria: application to forming limit diagrams. The International Journal of Advanced Manufacturing Technology 2014;71(5-8):1247-62.

Abed-Meraim F. Quelques problèmes de stabilité et de bifurcation des solides visqueux. PhD Thesis, Ecole Polytechnique, Palaiseau, France 1999.

Aretz H, Barlat F. New convex yield functions for orthotropic metal plasticity. International Journal of Non-Linear Mechanics 2013;51:97-111.

Arrieux R. Determination and use of the forming limit stress diagrams in sheet metal forming. Journal of Materials Processing Technology 1995;53(1-2):47-56.

Arrieux R. Determination and use of the forming limit stress surface of orthotropic sheets. Journal of Materials Processing Technology 1997;64(1-3):25-32.

Babout L, Brechet Y, Maire E, Fougeres R. On the competition between particle fracture and particle decohesion in metal matrix composites. Acta Materialia 2004;52(15):4517-25.

Ballay M, Monoši M. Selected aspects of the relationship between scientific-technological development of structures of passenger cars of the recovery and hydraulic equipment fire and rescue corps used in rescue operations. Procedia Engineering 2017;192:16-21.

Banabic D, Aretz H, Comsa DS, Paraianu L. An improved analytical description of orthotropy in metallic sheets. International Journal of Plasticity 2005;21(3):493-512.

Banabic D, Kami A, Comsa DS, Eyckens P. Developments of the Marciniak-Kuczynski model for sheet metal formability: A review. Journal of Materials Processing Technology 2019:116446.

Banabic D. A review on recent developments of Marciniak-Kuczynski model. Computer Methods in Materials Science 2010a;10:225-37.

Banabic, D. Sheet metal forming processes: constitutive modelling and numerical simulation. Springer Science and Business Media 2010.

Barlat F, Aretz H, Yoon JW, Karabin ME, Brem JC, Dick RE. Linear transformation-based anisotropic yield functions. International Journal of Plasticity 2005;21(5):1009-39.

Becker R, Needleman A, Richmond O, Tvergaard V. Void growth and failure in notched bars. Journal of the Mechanics and Physics of Solids 1988;36(3):317-51.

Becker R, Needleman A. Effect of yield surface curvature on necking and failure in porous plastic solids. Journal of Applied Mechanics 1986;108: 491-499.

Begley MR, Hutchinson JW. The mechanics of size-dependent indentation. Journal of the Mechanics and Physics of Solids 1998;46(10):2049-68.

Ben Bettaieb M, Abed-Meraim F. Investigation of localized necking in substrate-supported metal layers: Comparison of bifurcation and imperfection analyses. International Journal of Plasticity 2015;65:168-90.

Benzerga AA, Besson J. Plastic potentials for anisotropic porous solids. European Journal of Mechanics and Solids 2001;20(3):397-434.

Benzerga AA, Leblond JB. Ductile fracture by void growth to coalescence. Advances in Applied Mechanics 2010;44:169-305.

Benzerga AA. Micromechanics of coalescence in ductile fracture. Journal of the Mechanics and Physics of Solids 2002;50(6):1331-62.

Benzerga, AA. Rupture ductile des tôles anisotropes. PhD thesis, Ecole Nationale Supérieure des Mines de Paris, France 2000.

Beremin FM. Cavity formation from inclusions in ductile fracture of A508 steel. Metallurgical Transactions A 1981;12(5):723-31.

Bhaduri A. Mechanical Properties and Working of Metals and Alloys. Springer Singapore 2018:693-719.

Biener J, Hodge AM, Hamza AV, Hsiung LM, Satcher Jr JH. Nanoporous Au: A high yield strength material. Journal of Applied Physics 2005;97(2):024301.

Biener J, Hodge AM, Hayes JR, Volkert CA, Zepeda-Ruiz LA, Hamza AV, Abraham FF. Size effects on the mechanical behavior of nanoporous Au. Nano Letters 2006;6(10):2379-82.

Bigoni D, Hueckel T. Uniqueness and localization–I. Associative and non-associative elastoplasticity. International Journal of Solids and structures 1991;28(2):197-213.

Bigoni D, Zaccaria D. Loss of strong ellipticity in non-associative elastoplasticity. Journal of the Mechanics and Physics of Solids 1992;40(6):1313-31.

Bigoni D. On smooth bifurcations in non-associative elastoplasticity. Journal of the Mechanics and Physics of Solids 1996;44(8):1337-51.

Bouchard PO, Bourgeon L, Fayolle S, Mocellin K. An enhanced Lemaitre model formulation for materials processing damage computation. International Journal of Material Forming 2011;4(3):299-315.

Bouktir Y, Chalal H, Abed-Meraim F. Prediction of necking in thin sheet metals using an elastic–plastic model coupled with ductile damage and bifurcation criteria. International Journal of Damage Mechanics 2018;27(6):801-39.

Brach S, Anoukou K, Kondo D, Vairo G. Limit analysis and homogenization of nanoporous materials with a general isotropic plastic matrix. International Journal of Plasticity 2018;105:24-61.

Brach S, Dormieux L, Kondo D, Vairo G. A computational insight into void-size effects on strength properties of nanoporous materials. Mechanics of Materials 2016;101:102-17.

Brach S, Dormieux L, Kondo D, Vairo G. Strength properties of nanoporous materials: A 3-layered based non-linear homogenization approach with interface effects. International Journal of Engineering Science 2017;115:28-42.

Bron F, Besson J. A yield function for anisotropic materials application to aluminum alloys. International Journal of Plasticity 2004;20(4-5):937-63.

Brown LM, Embury JD. Initiation and growth of voids at second-phase particles. Microstructure and Design of Alloys 1973;1(33):164-169.

Brunet M, Mguil S, Morestin F. Analytical and experimental studies of necking in sheet metal forming processes. Journal of Materials Processing Technology 1998;80:40-46.

Brünig M. Numerical analysis and elastic–plastic deformation behavior of anisotropically damaged solids. International Journal of Plasticity 2002;18(9):1237-70.

Cao TS, Gaillac A, Montmitonnet P, Bouchard PO. Identification methodology and comparison of phenomenological ductile damage models via hybrid numerical-experimental analysis of fracture experiments conducted on a zirconium alloy. International Journal of Solids and Structures 2013;50(24):3984-3999.

Cao TS, Bobadilla C, Montmitonnet P, Bouchard PO. A comparative study of three ductile damage approaches for fracture prediction in cold forming processes. Journal of Materials Processing Technology 2015;216:385-404.

Cazacu O. New yield criteria for isotropic and textured metallic materials. International Journal of Solids and Structures 2018;139:200-10.

Chalal H, Abed-Meraim F. Hardening effects on strain localization predictions in porous ductile materials using the bifurcation approach. Mechanics of Materials 2015;91:152-66.

Chentouf SM, Belhadj T, Bombardier N, Brodusch N, Gauvin R, Jahazi M. Influence of pre deformation on microstructure evolution of super plastically formed Al 5083 alloy. The International Journal of Advanced Manufacturing Technology 2017;88(9-12):2929-37.

Chien WY, Pan J, Tang SC. A combined necking and shear localization analysis for aluminum sheets under biaxial stretching conditions. International Journal of Plasticity 2004;20(11):1953-81.

Chu CC, Needleman A. Void nucleation effects in biaxially stretched sheets. Journal of Engineering Materials and Technology 1980;102:249-256

Col A. Emboutissage des tôles - Importance des modes de déformation. Techniques de l'ingénieur 2011.

Considère A. Mémoire sur l'emploi du fer et de l'acier dans les constructions. Ann. Ponts et Chaussées 1885;9:574-775.

Dæhli LE, Morin D, Børvik T, Hopperstad OS. A Lode-dependent Gurson model motivated by unit cell analyses. Engineering Fracture Mechanics 2018;190:299-318.

Devaux J, Gologanu M, Leblond JB, Perrin G. On continued void growth in ductile metals subjected to cyclic loadings. International Union of Theoretical and Applied Mechanics Symposium on nonlinear analysis of fracture, Dordrecht 1997:299-310.

Ding J, Zhang C, Chu X, Zhao G, Leotoing L, Guines D. Investigation of the influence of the initial groove angle in the M-K model on limit strains and forming limit curves. International Journal of Mechanical Sciences 2015;98:59-69.

Doghri I, Billardon R. Investigation of localization due to damage in elasto-plastic materials. Mechanics of Materials 1995;19(2-3):129-49.

Doghri I. Mechanics of deformable solids: linear, nonlinear, analytical and computational aspects. Springer Science and Business Media 2013.

Doraivelu SM, Gegel HL, Gunasekera JS, Malas JC, Morgan JT, Thomas Jr JF. A new yield function for compressible PM materials. International Journal of Mechanical Sciences 1984 ;26(9-10):527-35.

Dormieux L, Kondo D. An extension of Gurson model incorporating interface stresses effects. International Journal of Engineering Science 2010;48(6):575-81.

Dormieux L, Kondo D. Non linear homogenization approach of strength of nanoporous materials with interface effects. International Journal of Engineering Science 2013;71:102-10.

Drucker DC. On uniqueness in the theory of plasticity. Quarterly of Applied Mathematics 1956;14(1):35-42.

Dudzinski D, Molinari A. Perturbation analysis of thermo viscoplastic instabilities in biaxial loading. International Journal of Solids and Structures 1991;27(5):601-28.

Erichsen AM. A new test for thin sheets. Stahl und Eisen 1914;34:879-882.

Faleskog J, Gao X, Shih CF. Cell model for nonlinear fracture analysis–I. Micromechanics Calibration. International Journal of Fracture 1998;89(4):355-73.

Fleck NA, Muller GM, Ashby MF, Hutchinson JW. Strain gradient plasticity: theory and experiment. Acta Metallurgica et Materialia 1994;42(2):475-87.

Fressengeas C, Molinari A. Instability and localization of plastic flow in shear at high strain rates. Journal of the Mechanics and Physics of Solids 1987;35:185–211.

Fu MW, Chan WL. Geometry and grain size effects on the fracture behavior of sheet metal in micro-scale plastic deformation. Materials and Design 2011;32(10):4738-46.

Fukui S. Researches on the deep-drawing process. Scientific papers of the Institute of Physical and Chemical Research 1938;34,1422-1527.

Gagov V, Yankov E, Radev R. Some features of the sheet metals testing by hydraulic bulging. In14th International Conference of METAL 2005.

Gallican V, Hure J. Anisotropic coalescence criterion for nanoporous materials. Journal of the Mechanics and Physics of Solids 2017;108:30-48.

García C, Celentano D, Flores F, Ponthot JP, Oliva O. Numerical modelling and experimental validation of steel deep drawing processes: Part II: Applications. Journal of Materials Processing Technology 2006;172(3):461-471.

Gensamer M. Strength and ductility. Transactions of the American Society for Metals 1946;36:30-60.

Ghosh AK. The effect of lateral drawing-in on stretch formability. Metals Engineering 1975;15:53-64.

Gologanu M, Leblond JB, Devaux J. Approximate models for ductile metals containing non-spherical voids—case of axisymmetric prolate ellipsoidal cavities. Journal of the Mechanics and Physics of Solids 1993;41(11):1723-54.

Gologanu M, Leblond JB, Devaux J. Approximate models for ductile metals containing nonspherical voids—case of axisymmetric oblate ellipsoidal cavities. Journal of Engineering Materials and Technology 1994;116(3):290-97.

Gologanu M, Leblond JB, Devaux J. Theoretical models for void coalescence in porous ductile solids. II. Coalescence "in columns". International Journal of Solids and Structures 2001b;38(32-33):5595-604.

Gologanu M, Leblond JB, Perrin G, Devaux J. Recent extensions of Gurson's model for porous ductile metals. Continuum Micromechanics 1997:61-130.

Gologanu M, Leblond JB, Perrin G, Devaux J. Theoretical models for void coalescence in porous ductile solids. I. Coalescence "in layers". International Journal of Solids and Structures 2001a;38(32-33):5581-94.

Goodwin GM. Application of strain analysis to sheet metal forming problems in the press shop. Society of Automotive Engineers 1968:380-387.

Gurson AL. Continuum theory of ductile rupture by void nucleation and growth: Part I—Yield criteria and flow rules for porous ductile media. Journal of Engineering Materials and Technology 1977;99(1):2-15.

Guyot J. Deep-drawability of thin sheets. Dunod, Paris 1962.

Hakamada M, Mabuchi M. Mechanical strength of nanoporous gold fabricated by dealloying. Scripta Materialia 2007;56(11):1003-6.

Harrison NR, Ilinich A, Friedman PA, Singh J, Verma R. Optimization of high-volume warm forming for lightweight sheet. Society of Automotive Engineers, Technical paper 2013;1:1170.

Hasek V. On the strain and stress states in drawing of large un-regular sheet metal components. Berichte aus dem Institut für Umformtechnik, Universität Stuttgart 1973;25.

Hasek V. Research and theoretical description concerning the influences on the FLDs. Blech Rohre Profile 1978; 25:213–220, 285–292, 493–499, 617–627.

Hecker SS. A cup test for assessing stretchability. Metals Engineering 1974;14:30-36.

Hill R. A general theory of uniqueness and stability in elastic-plastic solids. Journal of the Mechanics and Physics of Solids 1958;6(3):236-49.

Hill R. A theory of the yielding and plastic flow of anisotropic metals. Proceedings of the Royal Society: Mathematical, Physical and Engineering Sciences 1948;193:281-297.

Hill R. On discontinuous plastic states, with special reference to localized necking in thin sheets. Journal of the Mechanics and Physics of Solids 1952;1(1):19-30.

Hiwatashi S, Van Bael A, Houtte P, Teodosiu C. Prediction of forming limit strains under strain-path changes: application of an anisotropic model based on texture and dislocation structure. International Journal of Plasticity 1998;14(7):647-669.

Holte I, Niordson CF, Nielsen KL, Tvergaard V. Investigation of a gradient enriched Gurson-Tvergaard model for porous strain hardening materials. European Journal of Mechanics and Solids 2019;75:472-84.

Hora P, Tong L, Reissner J. A prediction method for ductile sheet metal failure in FE-simulation. In Proceedings of NUMISHEET 1996;96:252-256.

Hosseini ME, Hosseinipour SJ, Bakhshi-Jooybari M. Theoretical FLD Prediction Based on MK Model using Gurson's Plastic Potential Function for Steel Sheets. Procedia Engineering 2017;183:119-24.

Hotz W. European efforts in standardization of FLC. Numerical and experimental methods in prediction of forming limits in sheet forming and tube hydroforming processes. ETH Zürich 2006;24-25.

Hu J, Jonas JJ, Zhou Y, Ishikawa T. Influence of damage and texture evolution on limit strain in biaxially stretched aluminum alloy sheets. Materials Science and Engineering 1998;251(1-2):243-50.

Hu P, Liu W, Ying L, Zhang J, Wang D. A thermal forming limit prediction method considering material damage for 22MnB5 sheet. The International Journal of Advanced Manufacturing Technology 2017;92(1-4):627-38.

Huang HM, Pan J, Tang SC. Failure prediction in anisotropic sheet metals under forming operations with consideration of rotating principal stretch directions. International Journal of Plasticity 2000;16(6):611-33.

Hutchinson JW, Neale KW. Sheet necking-II. Time-independent behavior. Mechanics of sheet metal forming 1978;127-153.

Hutchinson JW. Plasticity at the micron scale. International Journal of Solids and Structures 2000;37(1-2):225-38.

Incandela O, Tabourot L, Porret P, Balland P, Arrieux R, Ducher F. Modelling and analysis of a deep-drawing operation: Key factors for successful comparisons between experimental and simulated results. Journal of Materials Processing Technology 2004;155-156(1-3):1105-1110.

ISO 12004-1. International Organization for Standardization, Metallic Materials –Sheet and Strip – Determination of Forming-Limit Curves, Part 1: Measurement and application of forming-limit diagrams in the press shop, Switzerland 2008.

ISO 12004-2. International Organization for Standardization, Metallic Materials –Sheet and Strip – Determination of Forming-Limit Curves, Part 2: Determination of Forming-Limit Curves in the Laboratory, Switzerland 2008.

Janbakhsh M, Djavanroodi F, Riahi M. A comparative study on determination of forming limit diagrams for industrial aluminium sheet alloys considering combined effect of strain path, anisotropy and yield locus. The Journal of Strain Analysis for Engineering Design 2012;47(6):350-61.

Jovignot C. Method and testing device for the study the fracture of the sheet metals. Revue de Metallurgie 1930;27:287-291.

Kachanov LM. On creep rupture time. Izv. Acad. Nauk SSSR, Otd. Techn. Nauk 1958;8:26-31.

Karafillis AP, Boyce MC. A general anisotropic yield criterion using bounds and a transformation weighting tensor. Journal of the Mechanics and Physics of Solids 1993;41(12):1859-86.

Kawasaki M, Xu C, Langdon TG. An investigation of cavity growth in a superplastic aluminum alloy processed by ECAP. Acta Materialia 2005;53(20):5353-64.

Keeler SP, Backofen WA. Plastic instability and fracture in sheets stretched over rigid punches. Transactions of the American Society for Metals 1963;56:25-48.

Keeler SP. Determination of forming limits in automotive stampings. Society of Automotive Engineers Technical paper 1965:1-9.

Kelly PA. Mechanics lecture notes: An introduction to solid mechanics 2019;25.

Keralavarma SM, Chockalingam S. A criterion for void coalescence in anisotropic ductile materials. International Journal of Plasticity 2016;82:159-76.

Khraishi TA, Khaleel MA, Zbib HM. A parametric-experimental study of void growth in superplastic deformation. International Journal of Plasticity 2001;17(3):297-315.

Koplik J, Needleman A. Void growth and coalescence in porous plastic solids. International Journal of Solids and Structures 1988;24(8):835-53.

Kuroda M, Tvergaard V. Effect of strain path change on limits to ductility of anisotropic metal sheets. International Journal of Mechanical Sciences 2000;42(5):867-887.

Lacroix R, Leblond JB, Perrin G. Numerical study and theoretical modelling of void growth in porous ductile materials subjected to cyclic loadings. European Journal of Mechanics and Solids 2016;55:100-9.

Lankford WT. New criteria for predicting the performance of deep drawing sheets. Transactions of American Society for Metals 1950;42:1197.

Leblond JB, Perrin G, Devaux J. An improved Gurson-type model for hardenable ductile metals. European Journal of Mechanics and Solids 1995;14(4):499-527.

Lee EH. Elastic-Plastic Deformation at Finite Strains. Journal of Applied Mechanics 1969;36:1-6.

Lemaitre J. A Course on Damage Mechanics. Springer Science and Business Media 1992.

Lemaitre J. Evaluation of dissipation and damage in metals. In: Mechanical behavior of materials, Proceedings of the International Conference on Mechanical Behavior 1971;1:15-20.

Li S, Jin S, Huang Z. Cavity Behavior of Fine-Grained 5A70 Aluminum Alloy during Superplastic Formation. Metals 2018;8(12):1065.

Li S, Wang G. Introduction to micromechanics and nanomechanics. World Scientific Publishing Company 2008.

Li Z, Huang M. Combined effects of void shape and void size–oblate spheroidal microvoid embedded in infinite non-linear solid. International Journal of Plasticity 2005;21(3):625-50.

Li Z, Steinmann P. RVE-based studies on the coupled effects of void size and void shape on yield behavior and void growth at micron scales. International Journal of Plasticity 2006;22(7):1195-216.

Liu B, Qiu X, Huang Y, Hwang KC, Li M, Liu C. The size effect on void growth in ductile materials. Journal of the Mechanics and Physics of Solids 2003;51(7):1171-87.

Liu J, Wang Z, Meng Q. Numerical investigations on the influence of superimposed double-sided pressure on the formability of biaxially stretched AA6111-T4 sheet metal. Journal of Materials Engineering and Performance 2012;21(4):429-36.

Liu W, Guines D, Leotoing L, Ragneau E. Identification of sheet metal hardening for large strains with an in-plane biaxial tensile test and a dedicated cross specimen. International Journal of Mechanical Sciences 2015;101-102:387-398.

Loret B, Rizzi E. Anisotropic stiffness degradation triggers onset of strain localization. International Journal of Plasticity 1997a;13(5):447-59.

Loret B, Rizzi E. Qualitative analysis of strain localization. Part II: Transversely isotropic elasticity and plasticity. International Journal of Plasticity 1997b;13(5):501-19.

Loxley EM, Swift HW. The wedge drawing test. Engineering 1945;159:38-40.

Madou K, Leblond JB, Morin L. Numerical studies of porous ductile materials containing arbitrary ellipsoidal voids–II: Evolution of the length and orientation of the void axes. European Journal of Mechanics and Solids 2013;42:490-507.

Madou K, Leblond JB. A Gurson-type criterion for porous ductile solids containing arbitrary ellipsoidal voids—I: Limit-analysis of some representative cell. Journal of the Mechanics and Physics of Solids 2012a;60(5):1020-36.

Madou K, Leblond JB. A Gurson-type criterion for porous ductile solids containing arbitrary ellipsoidal voids—II: Determination of yield criterion parameters. Journal of the Mechanics and Physics of Solids 2012b;60(5):1037-58.

Madou K, Leblond JB. Numerical studies of porous ductile materials containing arbitrary ellipsoidal voids–I: Yield surfaces of representative cells. European Journal of Mechanics and Solids 2013;42:480-89.

Maire JF, Chaboche JL. A new formulation of continuum damage mechanics (CDM) for composite materials. Aerospace Science and Technology 1997;1(4):247-57.

Mansouri LZ, Chalal H, Abed-Meraim F. Ductility limit prediction using a GTN damage model coupled with localization bifurcation analysis. Mechanics of Materials 2014;76:64-92.

Marciniak Z, Kuczyński K, Pokora T. Influence of the plastic properties of a material on the forming limit diagram for sheet metal in tension. International Journal of Mechanical Sciences 1973;15(10):789-800.

Marciniak Z, Kuczyński K. Limit strains in the processes of stretch-forming sheet metal. International Journal of Mechanical Sciences 1967;9(9):609-20.

Marciniak Z. Analysis of necking preceding fracture of sheet metal under tension. Met. Ital. 1968;60(8):701-9.

Marciniak Z. Stability of plastic shells under tension with kinematic boundary condition. Archives of Mechanics 1965;17:577-592.

Marino B, Mudry F, Pineau A. Experimental study of cavity growth in ductile rupture. Engineering Fracture Mechanics 1985;22(6):989-96.

Marron G, Moinier L, Patou P, Celeski JC. A new necking criterion for the forming limit diagrams. Revue de Metallurgie, Cahiers d'Informations Techniques 1997;94(6): 837-845.

Martins PAF, Bay N, Tekkaya AE, Atkins AG. Characterization of fracture loci in metal forming. International Journal of Mechanical Sciences 2014;83:112-123.

Mattiasson K, Sigvant M, Larson M. Methods for forming limit prediction in ductile metal sheets. In Proceedings of IDDRG 2006;6:1-9.

McClintock FA. Erratum:A Criterion for Ductile Fracture by the Growth of Holes. Journal of Applied Mechanics 1968;35:363-371.

Mesrar R, Fromentin S, Makkouk R, Martiny M, Ferron G. Limits to the ductility of metal sheets subjected to complex strain-paths. International Journal of Plasticity 1998;14(4-5):391-411.

Mi C, Buttry DA, Sharma P, Kouris DA. Atomistic insights into dislocation-based mechanisms of void growth and coalescence. Journal of the Mechanics and Physics of Solids 2011;59(9):1858-71.

Mohamed MS, Ismail A. Review on sheet metal forming process of aluminum alloys. In 17th International Conference on Applied Mechanics and Mechanical Engineering 2016;129-141.

Monchiet V, Bonnet G. A Gurson-type model accounting for void size effects. International Journal of Solids and Structures 2013;50(2):320-7.

Monchiet V, Kondo D. Combined voids size and shape effects on the macroscopic criterion of ductile nanoporous materials. International Journal of Plasticity 2013;43:20-41.

Morin D, Fourmeau M, Børvik T, Benallal A, Hopperstad OS. Anisotropic tensile failure of metals by the strain localization theory: An application to a high-strength aluminium alloy. European Journal of Mechanics and Solids 2018a;69:99-112.

Morin D, Hopperstad OS, Benallal A. On the description of ductile fracture in metals by the strain localization theory. International Journal of Fracture 2018b;209(1-2):27-51.

Morin L, Kondo D, Leblond JB. Numerical assessment, implementation and application of an extended Gurson model accounting for void size effects. European Journal of Mechanics and Solids 2015;51:183-92.

Morin L, Michel JC, Leblond JB. A Gurson-type layer model for ductile porous solids with isotropic and kinematic hardening. International Journal of Solids and Structures 2017;118:167-78.

Nahshon K, Hutchinson JW. Modification of the Gurson model for shear failure. European Journal of Mechanics and Solids 2008;27(1):1.

Nakazima K, Kikuma T, Hasuka K. Study on the formability of steel sheets. Yawata Technical Reports 1968;264:8517-8530.

Nakazima K, Kikuma T. Forming limits under biaxial stretching of sheet metals. Testu-to Hagane 1967;53:455-458.

Needleman A, Rice JR. Limits to ductility set by plastic flow localization. Mechanics of Sheet Metal Forming 1978:237-267.

Needleman A, Triantafyllidis N. Void growth and local necking in biaxially stretched sheets. Journal of Engineering Materials and Technology 1978;100:164-169.

Neilsen MK, Schreyer HL. Bifurcations in elastic-plastic materials. International Journal of Solids and Structures 1993;30(4):521-44.

Neto DM, Martins JM, Cunha PM, Alves JL, Oliveira MC, Laurent H, Menezes LF. Thermo-mechanical finite element analysis of the AA5086 alloy under warm forming conditions. International Journal of Solids and Structures 2018;151:99-117.

Nguyen VD, Pardoen T, Noels L. A nonlocal approach of ductile failure incorporating void growth, internal necking, and shear dominated coalescence mechanisms. Journal of the Mechanics and Physics of Solids 2020;137:103891.

Niordson CF, Tvergaard V. A homogenized model for size-effects in porous metals. Journal of the Mechanics and Physics of Solids 2019;123:222-33.

Nix WD, Gao H. Indentation size effects in crystalline materials: a law for strain gradient plasticity. Journal of the Mechanics and Physics of Solids 1998;46(3):411-25.

Olsen TY. Machines for ductility testing. Proceedings of the American Society for Testing and Materials 1920;20:398-403.

Pan J, Saje M, Needleman A. Localization of deformation in rate sensitive porous plastic solids. International Journal of Fracture 1983;21(4):261-78.

Pardoen T, Hutchinson JW. An extended model for void growth and coalescence. Journal of the Mechanics and Physics of Solids 2000;48(12):2467-512.

Pearce R. Sheet metal testing – From the 19th century until now. Sheet Metal Forming and Formability, Proceedings of 10th Biennial Congress of The International Deep Drawing Research Group (IDDRG) Warwick 1978;355-362.

Quaak G. Biaxial testing of sheet metal: An experimental-numerical analysis. Eindhoven University of Technology, Department of Mechanical Engineering, Computational and Experimental Mechanics. 2008;1-33.

Rabotnov YN. Creep problems in structural members. North-Holland Publishing Company 1969.

Ragab AR, Saleh C, Zaafarani NN. Forming limit diagrams for kinematically hardened voided sheet metals. Journal of Materials Processing Technology 2002;128(1-3):302-12.

Ragab AR, Saleh CA. Effect of void growth on predicting forming limit strains for planar isotropic sheet metals. Mechanics of Materials 2000;32(2):71-84.

Raghavan KS. A simple technique to generate in-plane forming limit curves and selected applications. Metallurgical and Materials Transactions 1995;26(8):2075-2084.

Rice JR, Tracey DM. On the ductile enlargement of voids in triaxial stress fields. Journal of the Mechanics and Physics of Solids 1969;17(3):201-17.

Rice, JR. The localization of plastic deformation. Theoretical and Applied Mechanics 1976;207-227.

Rizzi E, Loret B. Qualitative analysis of strain localization. Part I: Transversely isotropic elasticity and isotropic plasticity. International Journal of Plasticity 1997;13(5):461-99.

Rudnicki JW, Rice JR. Conditions for the localization of deformation in pressure-sensitive dilatant materials. Journal of the Mechanics and Physics of Solids 1975;23(6):371-94.

Sachs G. A new testing device for deep-drawing. Metallwirtschaft 1930;9:213-218.

Saje M, Pan J, Needleman A. Void nucleation effects on shear localization in porous plastic solids. International Journal of Fracture 1982;19(3):163-82.

Sánchez PJ, Huespe AE, Oliver J. On some topics for the numerical simulation of ductile fracture. International Journal of Plasticity 2008;24(6):1008-38.

Schlu N, Grimpe F, Bleck W, Dahl W. Modelling of the damage in ductile steels. Computational Materials Science 1996;7(1-2):27-33.

Shima S, Oyane M. Plasticity theory for porous metals. International Journal of Mechanical Sciences 1976;18(6):285-91.

Silva MB, Skjødt M, Martins PA, Bay N. Single point incremental forming of metal sheets. In Annual Winter Meeting of Danish Society for Metallurgy, Jutland, Denmark 2009;1-14.

Simha CH, Grantab R, Worswick MJ. Computational analysis of stress-based forming limit curves. International Journal of Solids and Structures 2007;44(25-26):8663-84.

Son HS, Kim YS. Prediction of forming limits for anisotropic sheets containing prolate ellipsoidal voids. International Journal of Mechanical Sciences 2003;45(10):1625-43.

Song X, Leotoing L, Guines D, Ragneau E. Characterization of forming limits at fracture with an optimized cruciform specimen: Application to DP600 steel sheets. International Journal of Mechanical Sciences 2017;126:35-43.

Sorce FS, Ngo S, Lowe C, Taylor AC. Quantification of coating surface strains in Erichsen cupping tests. Journal of Materials Science 2019;54(10):7997-8009.

Stölken JS, Evans AG. A microbend test method for measuring the plasticity length scale. Acta Materialia 1998;46(14):5109-15.

Stören S, Rice JR. Localized necking in thin sheets. Journal of the Mechanics and Physics of Solids 1975;23(6):421-41.

Stoughton TB. A general forming limit criterion for sheet metal forming. International Journal of Mechanical Sciences 2000;42(1):1-27.

Swift H. Plastic instability under plane stress. Journal of the Mechanics and Physics of Solids 1952;1(1):1-8.

Teaca M, Charpentier I, Martiny M, Ferron G. Identification of sheet metal plastic anisotropy using heterogeneous biaxial tensile tests. International Journal of Mechanical Sciences 2010;52(4):572-580.

Tekoglu C. Void coalescence in ductile solids containing two populations of voids. Engineering Fracture Mechanics 2015;147:418-30.

Thomason PF. A three-dimensional model for ductile fracture by the growth and coalescence of microvoids. Acta Metallurgica 1985;33(6):1087-95.

Tisza M. Recent development trends in sheet metal forming. International Journal of Microstructure and Materials Properties 2013;8(1/2): 125-140.

Torki ME, Tekoglu C, Leblond JB, Benzerga AA. Theoretical and numerical analysis of void coalescence in porous ductile solids under arbitrary loadings. International Journal of Plasticity 2017;91:160-81.

Toth LS, Dudzinski D, Molinari A. Forming limit predictions with the perturbation method using stress potential functions of polycrystal viscoplasticity. International Journal of Mechanical Sciences 1996;38(8-9):805-24.

Tvergaard V, Needleman A. Analysis of the cup-cone fracture in a round tensile bar. Acta Metallurgica 1984;32(1):157-69.

Tvergaard V. Influence of voids on shear band instabilities under plane strain conditions. International Journal of Fracture 1981;17(4):389-407.

Tvergaard V. Material failure by void coalescence in localized shear bands. International Journal of Solids and Structures 1982;18(8):659-72.

Vadillo G, Fernández-Sáez J. An analysis of Gurson model with parameters dependent on triaxiality based on unitary cells. European Journal of Mechanics and Solids 2009;28(3):417-27.

Vadillo G, Reboul J, Fernández-Sáez J. A modified Gurson model to account for the influence of the Lode parameter at high triaxialities. European Journal of Mechanics and Solids 2016;56:31-44.

Valanis KC. Banding and stability in plastic materials. Acta Mechanica 1989;79(1-2):113-41.

Weck A, Wilkinson DS, Toda H, Maire E. Second and third visualization of ductile fracture. Advanced Engineering Materials 2006;8(6):469-72.

Wen J, Huang Y, Hwang KC, Liu C, Li M. The modified Gurson model accounting for the void size effect. International Journal of Plasticity 2005;21(2):381-95.

Wu H, Xu W, Shan D, Jin BC. An extended GTN model for low stress triaxiality and application in spinning forming. Journal of Materials Processing Technology 2019;263:112-28.

Xu Z, Peng L, Yi P, Lai X. An investigation on the formability of sheet metals in the micro/meso scale hydroforming process. International Journal of Mechanical Sciences 2019;150:265-76.

Xu ZT, Peng LF, Fu MW, Lai XM. Size effect affected formability of sheet metals in micro/meso scale plastic deformation: experiment and modeling. International Journal of Plasticity 2015;68:34-54.

Xu ZT, Peng LF, Lai XM, Fu MW. Geometry and grain size effects on the forming limit of sheet metals in micro-scaled plastic deformation. Materials Science and Engineering 2014;611:345-53.

Xue L. Constitutive modeling of void shearing effect in ductile fracture of porous materials. Engineering Fracture Mechanics 2008;75(11):3343-66.

Yamamoto H. Conditions for shear localization in the ductile fracture of void-containing materials. International Journal of Fracture 1978;14(4):347-65.

Yoshida K, Kuroda M. Comparison of bifurcation and imperfection analyses of localized necking in rate-independent polycrystalline sheets. International Journal of Solids and Structures 2012;49(15-16):2073-84.

Zadpoor AA, Sinke J, Benedictus R. Formability prediction of high strength aluminum sheets. International Journal of Plasticity 2009;25(12):2269-97.

Zhang KS, Bai JB, Francois D. Numerical analysis of the influence of the Lode parameter on void growth. International Journal of Solids and Structures 2001;38(32-33):5847-56.

Zhang ZL, Niemi E. A new failure criterion for the Gurson-Tvergaard dilational constitutive model. International Journal of Fracture 1994b;70(4):321-34.

Zhang ZL, Niemi E. Analyzing ductile fracture using dual dilational constitutive equations. Fatigue and Fracture of Engineering Materials and Structures 1994a;17(6):695-707.

Zhang ZL, Thaulow C, Ødegård J. A complete Gurson model approach for ductile fracture. Engineering Fracture Mechanics 2000;67(2):155-68.

Zhou J, Gao X, Sobotka JC, Webler BA, Cockeram BV. On the extension of the Gurson-type porous plasticity models for prediction of ductile fracture under shear-dominated conditions. International Journal of Solids and Structures 2014;51(18):3273-91.

Muhammad Waqar NASIR

Etude des interactions endommagement ductile-striction dans les tôles minces : application à la prédiction de la formabilité

Résumé

La mise en forme des tôles minces est sans aucun doute l'un des procédés de fabrication les plus utilisés de nos jours dans divers secteurs industriels, tels que l'automobile, l'aérospatiale, l'électroménager et l'industrie alimentaire. Divers défauts dans la tôle peuvent apparaître durant sa mise en forme par déformation plastique, tels que le plissement, la striction ou la rupture. Plus précisément, ce travail de thèse se concentre sur l'étude de l'apparition des instabilités plastiques inhérentes au matériau lui-même, telles que la striction diffuse et la striction localisée, limitant ainsi sa formabilité. Le concept de courbes limites de formage (CLF) fournit les limites de déformations que les tôles peuvent supporter sans l'apparition de défauts indésirables. Ce présent travail contribue au développement d'outils théoriques et numériques pour la prédiction des CLF, ce qui permet de fournir une approche complémentaire aux essais expérimentaux à des fins de caractérisation de la formabilité des tôles minces. Pour cela, des modèles constitutifs phénoménologiques, basés sur le modèle original de Gurson, sont considérés dans la présente contribution. Concernant la prédiction des instabilités plastiques, plusieurs critères de striction diffuse et localisée, basés sur la théorie de la bifurcation et l'approche multi-zone (imperfection initiale), sont combinés aux modèles de comportement. Ces critères sont analysés et hiérarchisés en termes d'ordre de prédiction de la striction. Globalement, les résultats numériques montrent que, pour l'ensemble des lois de comportement considérées, le critère de bifurcation générale constitue une borne inférieure à tous les critères de bifurcation, en termes de prédiction de la striction. En ce qui concerne la prédiction de la striction localisée, le critère de perte d'ellipticité apparaît comme une borne supérieure à tous les critères de bifurcation, ainsi qu'à l'approche d'imperfection initiale.

Mots clés : Endommagement ductile, Matériaux poreux, Plasticité, Striction, Mise en forme, Tôles minces, Formabilité.

Résumé en anglais

Sheet metal forming is undoubtedly a manufacturing process that has massive applications in numerous industrial sectors, such as automotive, aerospace, home appliance and food industry. Various defects may occur during the forming processes, such as wrinkling, and those inherent to material plastic instabilities, such as necking, which are responsible for limiting the formability. Therefore, controlling such plastic instabilities results in enhanced productivity and high quality of products during the manufacturing process. The concept of forming limit diagram (FLD) provides the limits to the deformations that sheet metals can withstand without the occurrence of undesirable defects. The current work contributes to the development of theoretical and numerical tools for the predictions of FLDs, which leads to a complementary approach to experimental tests. For this purpose, phenomenological Gurson-based damage constitutive models are considered in the present contribution. For the prediction of plastic instabilities, both diffuse and localized necking criteria, which are based on the bifurcation theory and multi-zone (initial imperfection) approach, have been implemented and compared to each other in terms of their order of prediction of critical necking strains. It has been found that the critical strains are lowered when the void size is increased for porous materials. In other words, decreasing the void size has a beneficial effect on the material formability. The predicted FLDs show that for all the considered constitutive models, the general bifurcation criterion is a lower bound to all the bifurcation criteria, in terms of necking prediction. As to the prediction of strain localization, the loss of ellipticity criterion provides an upper bound as compared to the initial imperfection approach and other bifurcation criteria.

Keywords : Ductile damage, Porous materials, Plasticity, Necking, Forming, Sheet metals, Formability.